Damage Detection in Reinforced Concrete and Self-Healing Concrete Structures using Non-Destructive Testing Techniques

Yu Wang

B.Sc., M.Sc.

A thesis submitted in partial fulfilment for

the degree of *Doctor of Philosophy*

Cardiff University Structural Performance Laboratory
Cardiff School of Engineering
Cardiff University

December 2020

Contents

Summary of thesis

Candidate's Name: Yu Wang
Candidate's for the Degree of: PHD
Institution at which study pursued: School of Engineering, Cardiff University
Full title of Thesis: Damage Detection in Reinforced Concrete and Self-Healing Concrete Structures using Non-Destructive Testing Techniques

This thesis mainly contains the investigation of the role of Acoustic Emission (AE) and Acousto-Ultrasonics (AU) as the Non-Destructive Testing (NDT) techniques for concrete structure. Further the techniques applied in this work explored the application and feasibility of AE to monitor and characterise the behaviour of the recently developed self-healing concrete structure. Experimental studies were conducted on a range of specimen in different scale, focusing on the development and application of experimental techniques and data analysis methods for source characterisation, damage detection, location and assessment of AE. The four main topics and findings are as follows:

1. Characterisation of basic failure mode on concrete member
Considering the complexity of AE signals of concrete structure, a fundamental study on the source characterisation of two basic failure mode of concrete is conducted using a combined method of parametric analysis and waveform analysis. The maximum amplitude and corresponding characteristic instantaneous frequency are extracted as two indicators of basic failure mode to characterise the complex damage source in concrete.

2. Characterisation of AE source using Moment Tensor Analysis (MTA)
A detailed experimental investigation of Moment Tensor Analysis (MTA) is conducted on a concrete cube to elucidate the SiGMA procedure performed by the H-N source. Then the MTA results obtained from a bending testing on a RC beam shows a promising agreement with results obtained via the conventional parameter-based method. Comparison between different methods is discussed and concluded.

3. Laboratory investigations on AE monitoring of self-healing behaviours
The applicability of AE techniques to monitor the whole damage and healing process of the vascular-network based self-healing system is evaluated and was found that the Kaiser effect and Felicity ratio could be applied as an indicator to assess the healing efficiency. Principal Component Analysis and unsupervised pattern recognition techniques are adopted to differentiate between concrete fracture signals and other sources.

4. Crack size monitoring and measurement using ultrasonic testing method
Experimental studies are conducted using Acousto-Ultrasonics on a range of different size specimen to monitor and measure the crack development. The prospect and potential application of the AU technique investigating impact of healing agent of vascular network-based system were explored.

Key Words:
Acoustic Emission, Damage Detection, Reinforced Concrete, Self-healing Concrete, Moment Tensor Analysis, Acousto-Ultrasonics, Crack Development Monitoring.

Acknowledgements

There are too many people that I owe a great debt of gratitude for their support and endless help during my study and living in the UK. Without them, none of this would be possible.

First of all, I would like to express my sincere gratitude to all my supervisors, Dr Matthew Pearson, Professor Karen Holford, Professor Rhys Pullin and Dr Robert Davies. This work was completed under the careful guidance and help from them since the very beginning, from research proposal to experiments design, from technical problems solving to my English language checking. Every single sentence, figure and table in this thesis is involved with their time and hard work. Your endless support, encouragement, optimism and enthusiasm had inspired and helped me through not only my PhD journey but my life in the UK all the time. It has been a great honour and privilege to be supervised by all of you, inspired and immersed by your professionalism, academic pursuit and leadership. Those critical and great values mean a lot and will have an impact to my whole life.

I would like to thank all the academics in the CUSP Lab, Dr John McCrory, Dr Hayley Wyatt, Dr Ryan Marks, Dr Stephen Grigg, Dr Mark J Eaton, Dr Davide Crivelli and Dr Alastair Clarke and for all the support and advice through my study. I benefit a lot from the presentations and discussions at the bi-weekly group meeting, which expands my horizons widely and deeply in different research areas and always inspired me to pick up new skills.

I would like to thank my colleagues, Faisel Almudaihesh, Kiriaki Gkaliou, Pim Sangha, Frederick Purcell, Benjamin Fisher, Stephen Ball, Paul Revill, William Britton. We started the journey at different time but we spent most of the time together at work. Thanks for all your company, joyfulness spread and all cups of tea we had together in the CUSP lab all along.

I would like to highly appreciate the excellent technical assistance and countless help from technicians Carl Wadsworth, Ian King, Richard Thomas, Jack Morgan and Harry Lane at the School of Engineering department in Cardiff University. Thanks for always helping me out and taking good care of me.

I would like thank Professor Robert Lark for being the reviewer of my annual reviews and all those suggestion and advice. And thanks to the Resilient Materials 4 Life (RM4L) group for providing me a great opportunity to be participated in this forefront research project.

I also would like to thank my supervisor Dr Robert Davies and Dr Aled Davies for their guide in teaching and demonstrating activities. Those experience and skills are extremely valuable and important to my future path.

Besides, I am also grateful to Tim Bradshaw and Apostolos Tsimogiannis from MISTRAS Group Ltd. for their massive technical support and help throughout, especially during the COVID-19 pandemic.

Apart from work, thanks also to my friend Dr Tharmesh Selvarajoo, Dr Brubeck Freeman, Dr Cristina De Nardi, Professor Liu Simeng, Professor Rongling Zhang and Castor Cai for encouragements, sharing and spreading positivity all the time. I hope everything goes well for you and I won't forget those experience we shared in Cardiff.

I would also like to express my deepest appreciation to my parents and all my family for their unconditional love and support all the time. Thank you all for always standing by me at my best, and at my worst. No matter what happens, I know there is always a place called home being my only harbour forever.

In the end, I would like to primarily acknowledge the joint sponsorship from China Scholarship Council and Cardiff University School of Engineering. Thanks for providing me this great opportunity which left me an indelible and particular memories in life.

Due to the COVID-19 pandemic in 2020, I finished most of writing at my apartment and thanks to all my supervisors, colleagues, friends, and those who always there being accompanying physically or remotely, sharing joys and failures all the time during the final few months of writing.

Yu Wang

24th December 2020

Glossary

Many of the following Acoustic Emission(AE)-related terms can be found in ASTM E610 (ASTM 1982) and ASTM E1316 (ASTM 2011);

1. AE-related Terminology

Acoustic Emission (AE): the class of phenomena whereby transient elastic waves are generated by the rapid release of energy from localized sources within a material, or the transient waves so generated.

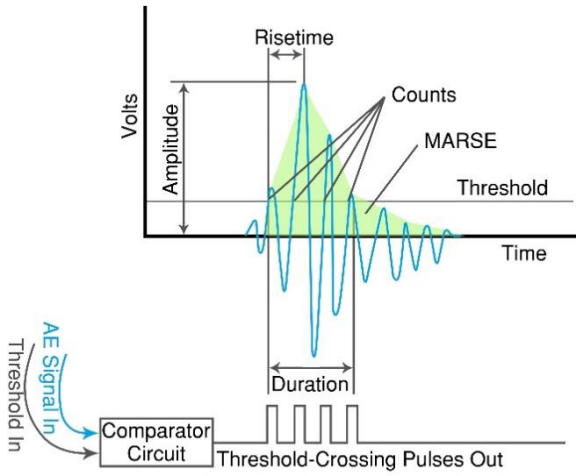

Figure i. AE Waveform Features, figure reproduced from Pearson (2013)

Acoustic emission signal: The electrical signal obtained through the detection of acoustic emission.

AE Features: This refers to the features of an AE waveform such as amplitude, duration, rise time, decay and counts, as shown in Figure i, which are frequently used during the analysis of AE data.

Hit: A hit is the term used to indicate that a given AE channel has detected and processed an acoustic emission transient.

Threshold: A pre-set voltage level, which has to be exceeded before an AE signal is recorded and processed. The following terms are made with reference to the threshold (as shown in Figure i).

Duration: The interval between the first and last time the threshold was exceeded by the signal (as shown in Figure i).

Peak Amplitude: Maximum signal amplitude within the duration of the signal (as shown in Figure i).

Counts: Number of times the signal amplitude exceeds the threshold (as shown in Figure i).

Rise Time: The interval between the first threshold crossing and the maximum amplitude of the signal (as shown in Figure i).

Initiation Frequency: The average frequency of the waveform from the initial threshold crossing to the peak of the AE waveform.

Energy (Absolute): The integral of the squared voltage signal divided by the reference resistance (10kΩ) over the duration of the AE waveform packet.

Event: An event is the group of AE hits that were received from a single source.

Source: A mechanical mechanism that produces AE signals.

Transducer: Device that converts the physical parameters of the wave into an electrical signal.

Couplant: Substance providing an acoustic coupling between the propagation medium and the transducer.

2. Wave propagation-related Terminology

Wave Mode: The type of waves propagating in a material as characterized by the particle motion (for example, longitudinal, transverse, etc.).

Mode conversion: Phenomenon by which an ultrasonic wave that is propagating in one mode can form ultrasonic wave(s) of other modes; typically due to the interaction of the original wave with an interface.

Attenuation: The rate at which signal amplitude reduces with distance of propagation.

Dispersion: The phenomenon whereby wave velocity varies with frequency.

Hsu-Nielson (H-N) Source: An artificial source of AE generated by breaking a mechanical pencil lead on the surface of a structure.

Time of Arrival (TOA): This is the conventional AE source location algorithm used to locate AE sources in a structure. It uses the difference in arrival times between transducers and a defined wave velocity to estimate the location of an AE event.

3. Experimental Terminology

Digital Image Correlation (DIC): An optical technique that allows for the full field measurement of contour deformation, vibration and strain by tracking the movement of a black and white speckle pattern applied to the specimen.

Moment Tensor Analysis (MTA): A powerful technique of waveform analysis to quantitatively characterise a seismic source such as an earthquake or an explosion.

Scanning Electron Microscope (SEM): A type of electron microscope that produces images of a sample by scanning the surface with a focused beam of electrons.

4. Material-related Terminology

Smart Materials: A designed materials that have one or more properties that can be significantly changed by an external condition, such as temperature, light, pressure, electricity, voltage, pH, or chemical compounds, to react accordingly in their environment.

Self-healing Materials: An artificial or synthetically-created substances that have the built-in ability to automatically repair damages to themselves without any external diagnosis of the problem or human intervention.

Reinforced Concrete (RC) structure: A composite material in which concrete's relatively low tensile strength and ductility are counteracted by the inclusion of reinforcement having higher tensile strength or ductility.

Prestressed Concrete (PC) structure: A form of concrete used in construction. It is

substantially "prestressed" (compressed) during production, in a manner that strengthens it against tensile forces which will exist when in service.

Alkali-Silica Reaction (ASR): A deleterious swelling reaction that occurs over time in concrete between the highly alkaline cement paste and the reactive amorphous (i.e., non-crystalline) silica found in many common aggregates, given sufficient moisture.

Asphalt Concrete (AC): A composite material commonly used to surface roads, parking lots, airports, and the core of embankment dams. It consists of mineral aggregate bound together with asphalt, laid in layers, and compacted.

Ultra-High-Performance Concrete (UHPC): Generally defined as the cementitious concrete material with a compressive strength greater than 150 MPa with specified durability, tensile ductility and toughness requirements.

5. Signal processing-related Terminology

Kaiser effect: The absence of detectable AE until the previous maximum applied stress level has been exceeded.

Felicity ratio: The measurement of the Felicity effect. Defined as the ratio between the applied load at which the AE reappears during the next application of loading and the previous maximum applied load.

Akaike Information Criterion (AIC): An estimator of out-of-sample prediction error and thereby relative quality of statistical models for a given set of data.

Fourier transform (FT): A mathematical transform that decomposes functions depending on space or time into functions depending on spatial or temporal frequency.

Fast Fourier transform (FFT): A common algorithm for Fourier transforms that computes the Discrete Fourier transform (DFT) of a sequence, or its inverse (IDFT) more efficient.

The Hilbert–Huang transform (HHT): Signal processing technique which decompose a signal into so-called intrinsic mode functions (IMF) along with a trend and obtain

instantaneous frequency data.

Empirical mode decomposition (EMD): The fundamental part of the Hilbert–Huang transform which break down the signals into a finite and often small number of components.

Intrinsic mode functions (IMF): A generally simple oscillatory mode as a counterpart to the simple harmonic function.

Hilbert spectral analysis (HSA): A method for examining each IMF's instantaneous frequency as functions of time, presented in a frequency-time distribution of signal amplitude (or energy), designated as the Hilbert spectrum,.

Wavelet Transform (WT): Signal processing technique which decomposes a transient signal in order to release a time-frequency representation of a wave.

Ultrasonic Pulse Velocity (UPV): A non-destructive testing method using ultrasonic waves to normally check the quality of concrete or natural rocks.

Apparent Velocity: The velocity is measured directly from the travel time plot, uncorrected for any refractor dip relative to the surface.

List of Figures

List of Tables

Chapter 1 Introduction

1.1 Background

The safety during operation of most infrastructures and major engineering structures such as long-span bridges, large-scale water conservancy facilities, large-span spatial structures, high buildings, and deep-sea drilling platforms directly affects people's lives, property and safety, as well as national economic development and social stability.

However, during the service life period of several decades or even hundreds of years, the effects of environmental erosion, material aging, natural disasters, etc. will lead to the accumulation of structural damage, performance degradation, and even catastrophic accidents in extreme cases. For example, recently in October 2019, a highway bridge in Wuxi city of Jiangsu Province, China suddenly collapsed at the peak of rush hour and fell on three cars below, killing three people in two of the vehicles (shown in Figure 1-1). After the investigation by the city and transport ministry officials, it was confirmed that this accident was caused by overloaded vehicles passing by and the bridge resonance induced, resulting in collapse (Tracy 2019). Such kind of catastrophic tragedies have never stopped happening today.

Figure 1-1. Highway bridge collapsed in Wuxi, Jiangsu province, China (October 2019)

Take bridges, one of the most important infrastructure forms, as an example, Table 1-1 lists the bridge failure events that have occurred around the world in the past two years (2019 - 2020).

Table 1-1. List of bridge failures from 2018 to 2020 (Wikipedia, Available at:

https://en.wikipedia.org/wiki/List_of_bridge_failures#cite)

Bridge	Location	Country	Date	Construction type, use of bridge	Reason	Casualties	Damage
Ponte Morandi motorway bridge collapse	Genoa – Liguria	Italy	14 August 2018	Viaduct incorporating a cable-stayed bridge		43 dead	210-metre (690 ft) section of the bridge collapsed
Dale Bend Bridge	Ola, Arkansas	United States	30-Jan-2019 (Rddad 2019)	Truss	Overweight truck	/	/
CST Foot over bridge	Mumbai	India	14-Mar-2019 (MumbaiMarch 15 et al. 2019)	Concrete Foot Over bridge	The structural audit has been conducted in an irresponsible and negligent manner.	6 dead, 30 injured	Partial Collapse
Ponte sobre o rio Moju, Bridge over the river Moju collapse	Moju, State of Pará	Brazil	7-Apr-2019 (BBC News 2019)	Concrete	Middle sections of the bridge collapsed after ferryboat crash	Unknown	200 metres (660 ft) section of the bridge collapsed
Bishopsford Road Bridge	Mitcham, London	England	14-Jun-2019	Road bridge (Fully demolished in July 2020, due to be rebuilt)	Bridge scour caused by jack posts installed 4 days earlier caused instability and led to the partial collapse of the northern arch	0 dead, 0 injured (the bridge was closed to traffic at the time)	Partial collapse (northern arch)
Nanfang'ao Bridge	Su'ao, Yilan County, Taiwan	China	1-Oct-2019 (Keoni Everington 2019)	Road bridge	/	4 dead, 10 injured	Total collapse
Wuxi National Route 312 Overpass	Wuxi, Jiangsu Province	China	10-Oct-2019 (Reuters Staff 2019)	Concrete highway bridge	overweight (186t) truck	3 dead, 2 injured	200 metres (660 ft) section of the elevated road toppled
Pont de Mirepoix	Mirepoix-sur-Tarn	France	18-Nov-2019 (Dominique Alzéari 2019)	Concrete-steel bridge	overweight truck	2 dead, 5 injured	150m long bridge collapsed
Viadotto Madonna del Monte on A6 Highway (Savona-Torino)	Savona	Italy	24-Nov-2019 (Jerrold Colten and Sonia Sirletti 2019)	Concrete bridge	heavy rain, landslide	0 dead, 0 injured	30 long highway bridge collapsed
Ponte sul Magra a Caprigliola	Aulla	Italy	8-Apr-2020 (Landini 2020)	Concrete bridge	/	0 dead, 2 injured	260m long provincial road bridge collapsed
Bridge over Kola near Murmansk	Murmansk	Russia	1-Jun-2020 (Staff 2020)	Steel bridge	/	0 dead	railway bridge collapsed after foundations were washed away by strong water
Tittle Bridge	Canso, Nova Scotia	Canada	7-Jul-2020 (Alexander Quon 2020)	Truss road bridge	Overweight truck	0 killed, 1 injured	Total failure of bridge

These catastrophic accidents have aroused widespread attention and made governments and scientific research institutions aware of the increasing urgency of structural health diagnosis and corresponding timely maintenance with remedies. Studies (Mobley 2002; Reddy et al. 2020; Sun et al. 2020) have shown that early structural damage detection, warning and timely maintenance during service can greatly reduce the possibility of catastrophic accidents and the maintenance and repair costs of the whole life cycle. Therefore, ensuring the structure safety and extending their service life as much as possible is the key mission for maintenance. It is well known that the structural health monitoring (SHM) technology is of great potential to achieve such goal.

A unified definition and concept of SHM has not yet been formed, but based on the extensive literature that has developed on SHM over the last 30 years, it can be argued that this field has matured to the point where several fundamental axioms, or general principles, have emerged (Worden et al. 2007). Aktan et al. (2000) described SHM as follows: health monitoring is the measurement of the operating and loading environment and the critical responses of a structure to track and evaluate the symptoms of operational incidents, anomalies, and/or deterioration or damage indicators that may affect operation, serviceability, or safety reliability. Catbas et al. (2008) described SHM as the process of monitoring the condition of a structure and detection of damage occurring in the structure over the time. They indicated that damage is referred as any structural or material change that affects the behaviour of the structure adversely and shortens its operational life. Farrar et al. (1999) and Sohn et al. (2001) described the SHM as a statistical pattern recognition process to implement a damage detection strategy for aerospace, civil and mechanical engineering infrastructure. Further they elaborated it as a four-part process, i.e. operational evaluation, data acquisition and cleansing, feature extraction, and statistical model development. Eaton (2007) and Pearson (2013) summarized the application of piezoelectric transducer technologies for SHM in recent years and detailed discussed the conventional piezoceramic transducers application for Acoustic

Emission (AE) and Acousto-Ultrasonics (AU) based SHM system.

After years of development, on this basis of online monitoring of the structure status and evaluation of its health and safety, the identification and treatment of early damage has been recognised as an important measure to improve the safety, extend the service life and reduce maintenance costs.

In recent years, the health monitoring of large-scale civil engineering structures has become a study hotspot where countries all over the world are vying to invest abundant manpower, material and financial resources for research. Since 1997, Stanford University has held regular International Workshop on Structural Health Monitoring (IWSHM) every two years. Van der Auweraer and Peeters (2003) presented a detailed introduction to SHM research institutions, important projects and international cooperation in the Europe. Ou and Li (2010), and Li et al. (2016) provided an overview of recent advances and development on intelligent health monitoring systems specializing in civil infrastructure systems in China.

As early as 1999, scholars had reached a consensus at the Second International Workshop on Structural Health Monitoring (IWSHM 1999) that future efforts and focuses should be concentrated on the analysis and interpretation of collected data (Yao and Wong 2012). This point leads to two key problems to be solved in the theoretical research and practical application of SHM – Damage identification and corresponding repair methods. From the perspective of structure design, the durability and stability are of great importance to the infrastructure. In the meanwhile, the material properties and performance have to be improved and enhanced as well to meet the needs of construction industry nowadays.

There are obvious differences between civil engineering, aerospace engineering and mechanical engineering (for example, bridge structures and most other civil structures are large in size and volume, boundary conditions are complicated, have low natural frequency and vibration response etc.). Moreover, the dynamic response of the structure is extremely easily affected by non-structural factors, which is often

misjudged as damage. Therefore, the damage identification of structures become more challenging.

Non-destructive Testing & Evaluation (NDT&E) methods play a key role in the success of SHM applications. Modern NDT&E techniques include Acoustic Emission (AE), Acousto-Ultrasonics (AU), Ultrasonics (UT), Digital Image Correlation (DIC) and Infrared Thermography (IRT), which are broadly applied for damage monitoring and detection on civil structures.

From the view of materials, the ongoing problem of the deterioration of concrete is still a major concern in the construction industry. More seriously, even though micro-cracking in reinforced concrete structures does not result in short-term collapse, the accumulation of damage over time can lead to excessive cracking and result in an unforeseeable major failure eventually.

In recent years, the investigation of ‘smart material’ and development of self-healing cementitious materials could be a solution to the problem of cracking and material degradation. Researchers are inspired by nature and developed the self-healing cementitious materials (SHCMs) which have the ability to adapt and respond to a changing environment in such a way that they recover some of their performance after being exposed to damage (Selvarajoo 2020). As those newly developed materials and technologies appear promising, there are still pressing challenges and problems needing to be solved. In the UK, a research project called ‘Resilient Materials for Life’, a programme grant funded by EPSRC, is being carried out by the Universities of Cardiff, Bath, Cambridge and Bradford to investigate the development of self-healing cementitious construction materials. Progress towards large scale applications in a construction environment has already been achieved (Davies et al. 2018).

1.2 Aims and objectives

The overall motivation for this thesis is derived from the need to improve the safety and extend the service life of infrastructure made from concrete material. To approach and achieve this goal, this research aims to build a bridge between ‘Diagnose’ and

‘Treatment’ of construction materials. More specifically, this work is inspired to be a connection of taking the advantages of NDT&E techniques from widely applied SHM systems and the newly developed self-repairing techniques to provide the information necessary and to be beneficial for the design and development of associated methods to improve the durability and performance of structures. The self-healing technique selected for the case study in this thesis is a vascular network based system, where a healing agent is delivered to the damage location through a network of channels in the concrete. These techniques were developed by the RM4L group in Cardiff University. Further details are given in Chapter 5.

The objectives of this research work are as follows:

I. Investigate the characterisation of AE sources within concrete and explore appropriate signal processing methods based on conventional parameter-based analysis.

II. Determine the reliability of Moment Tensor Analysis (MTA) as a well-recognized method to quantitatively identify and characterise source mechanisms of AE signals, and validate the effectiveness comparing to other methods.

III. Explore the potential application of NDT&E methods to provide extra information on the realisation of ‘self-sensing’, ‘self-diagnosing’ and ‘self-repairing’ goals for the investigation of self-healing mechanisms in cementitious materials.

1.3 Thesis organisation and structure

The thesis is presented in seven chapters, with Chapter 1 being an introduction to the background of the status quo of concrete-built infrastructure and the need of the implementation of NDT&E techniques and development of smart materials.

Chapter 2 provides a literature review and background around important areas including AE theories, development of NDT&E applications both on reinforced concrete and recently designed and developed innovative type of concrete.

Chapter 3 presents a fundamental study of source characterisation on two basic

failure mode of concrete structure through a combined method of parametric analysis and waveform analysis. Two extracted indexes are introduced to evaluate the source type and severity of damage.

Chapter 4 describes a detailed experimental investigation of MTA analysis on quantitative characterisation of AE sources. A preliminary study on a concrete cube is conducted followed by a reinforced concrete (RC) beam test to further present the SiGMA procedure applied.

In Chapter 5 a case study of the application of AE monitoring on vascular network based self-healing concrete is presented.

Chapter 6 the focus shifts towards the Acousto-Ultrasonics (AU) testing on the monitoring of crack development. Future directions of application related to self-healing properties are pointed out in the end.

Finally, Chapter 7 provides a summary of the findings of the thesis and discusses future work.

A glossary of all terms appeared throughout this work is attached at the start of the thesis.

1.4 Novelty Statement

This study conducted four experimental investigation on the application of Acoustic Emission (AE) techniques and Acousto-Ultrasonics (AU) techniques on both concrete and self-healing concrete. The key areas of novelty are listed below.

- Given the complexity of AE source of concrete structures in damage detection, an investigation strategy from fundamental damage to complex damage is proposed to realize the quantitative characterisation of AE signal.
- Two parameters, the maximum amplitude A_{mi} and characteristic instantaneous frequency f_c are extracted and determined through the Hilbert–Huang transform (HHT) to be introduced as two indicators to characterise the nature of AE source mechanism efficiently and intuitively.

- Detailed experimental investigation of the source mechanism from artificial Hsu-Nielson (H-N) source using Moment Tensor Analysis.
- Robustness validation for the feasibility of the Moment Tensor Analysis on a four-point bending test of RC beam. The predesignated damage mode is successfully located and determined through performing the SiGMA procedure.
- AE monitoring test on the whole damage and healing process of a vascular-network based self-healing concrete structures.
- Application of Kaiser effect and Felicity ratio as criterion to evaluate healing efficiency of the vascular-network based self-healing system.
- Using Principal Component Analysis and unsupervised pattern recognition techniques to differentiate between concrete fracture signals and those relating to the healing process included further damage.
- Characterisation and representation of crack development and defected areas using apparent velocity methods directly obtained from the Acousto-Ultrasonics signal transmission. Exploration testing on the impact of healing agent in self-healing concrete structure.

1.5 Publications

The work from Chapter 5 formed the basis of the conference publication below:

- Wang, Yu, Pullin, Rhys, Pearson, Matthew, Davies, Robert, & Holford, Karen. M. 2020. Detection and Evaluation of Vascular Network Based Self-healing Concrete Using Acoustic Emission. In: Shen, G. et al. eds. Advances in Acoustic Emission Technology. Proceedings of the World Conference on Acoustic Emission-2019. Springer International Publishing. doi: 10.1007/978-981-15-9837-1.

Author presented the following work at the 12th BSSM (the British Society for Strain Measurement) Conference in Sheffield, UK in 2017 on behalf of the first author, Dr Simeng Liu.

• Liu, Simeng, Pearson, Matthew R., Eaton, Mark and Pullin, Rhys 2017. Correlation between acoustic emission distribution and stress variation through the depth of RC beam cross sections. Construction and Building Materials 150 , pp. 634-645. 10.1016/j.conbuildmat.2017.06.001

Chapter 2 Literature Review

2.1 Overview of Non-Destructive Testing (NDT) methods

Infrastructure of a country is related to the national economy and people's livelihood. Reinforced concrete structure as it combines the advantages of both steel and concrete, it has become the most widely used structure in the world and plays an extremely important role in infrastructure construction. With the continuous expansion of the scale of infrastructure construction, the safety and maintenance of structures has become a major requirement for ensuring the sustainable development of society and economy. In order to ensure the normal operation of facilities and avoid the formation of major disasters, early identification of structural damage and planned maintenance of facilities have to be carried out beforehand to ensure the economic resources can be used more efficiently. Therefore, the development of new structural Non-Destructive Testing theory and technology has become a research focus for scientists and technicians nowadays.

Commonly used NDT&E techniques in reinforced concrete structures include ultrasonic testing, impact-echo, Acoustic Emission (AE), Acousto-Ultrasonics (AU), infrared testing, microwave technology and radar method. Except for AE detection, the above-mentioned other methods are all active detection methods, and their detection range is limited to the local range where the energy input can reach. Therefore, it is laborious and time-consuming with those active methods to implement damage detection in large structures such as huge and complex bridges, high-rise buildings, underground projects and dams, etc. In addition, some key parts of the structure are often hidden by protective layers or coverings, making damage detection more challenging. The AE method collects elastic waves emitted when damage occurs in the structure. It is only required to ensure the sensor array is well arranged to realize the monitoring of the entire structure. It not only overcomes the detection difficulties of large structures, but also has unique features such as real-time, dynamic and online detection.

The Acoustic Emission (AE) is defined in ASTM E1316 (2011) as the class of phenomena whereby transient elastic waves are generated by the rapid release of energy from localized sources within a material, or the transient waves so generated. AE is a common physical phenomenon. The frequency range of AE signals of different materials is very wide from infrasound frequencies of only a few hertz, to acoustic frequencies of 20Hz-20kHz, to ultrasonic frequencies of several mega-hertz. The signal amplitude varies largely as well ranging from a microscopic displacement of an order of magnitude of 10^{-13} m to a seismic wave of an order of magnitude of 1m. Therefore, the AE method is sensitive so that the damage can be found early before it is visible. The energy detected by AE comes from the material itself, not provided by non-destructive testing equipment like ultrasonic or radiographic testing methods. The AE technology can provide real-time or continuous information of defects with external parameters such as load, time, temperature, etc., therefore it is suitable for online real-time structural health monitoring of for those structures under service. Nowadays AE detection has become an important way for evaluating structural damage caused in fibre composite materials, reinforced concrete, and prestressed reinforced concrete, etc.

2.1.1 Brief history of AE

The beginning of modern AE technology is marked by the research work of Kaiser in Germany in the early 1950s. Kaiser observed that many metals and alloys have the AE during the deformation process. One of the most significant findings is the irreversible effect of AE events during the process of material deformation. That is, when the material is reloaded, there are no AE signals generated before the stress value reaches the maximum stress at the last time. This kind of irreversible phenomenon of material is called “Kaiser effect” (Kaiser 1950).

Tatro (1971) conducted a study on the physical mechanism of AE. Tatro found that the AE events of metal plastic deformation are mainly caused by a large number of dislocation motion. For the first time, he presented that the AE technology can be used as a tool to study the performance of engineering materials, and it has a unique

advantage and application prospect in NDT methods.

In the early 1960s, a wide range of research work on AE had been conducted in the United States and Japan where a lot of researchers tried to apply AE technology to the field of non-destructive testing of actual structure of engineering. In 1960s, Dunegan, for the first time, applied AE technology in the pressure vessel detection (Dunegan et al. 1968; Harris and Dunegan 1972). In 1964, Green et al. applied the AE technology to the non-destructive testing of the rocket engine casing (Green et al. 1964).

However, the early AE equipment and AE detection were limited to the audio range. So it is difficult to eliminate noise interference. Dunegan and Kanuss set up the first AE company in the United States in 1969 and carried out the development of modern AE equipment (Muravin 2009). They put the experimental frequency up to 100kHz-1MHz range to avoid the interference of audible noise, which is a significant progress of AE experiment technology. The development of modern AE equipment had created the condition for the AE technology from the laboratory material research to the integrated large-scale structure monitoring of working field. The Acoustic Emission Working Group (AEWG) was established in the United States in 1967. Subsequently, the European Working Group on Acoustic Emission (EWGAE) and the Japanese Committee on Acoustic Emission (JCAE) were both established in 1969.

With the emergence of modern AE instruments, people have carried out extensive and systematic research work throughout the 1970s and early 1980s from AE source generation mechanism, wave propagation to AE signal analysis. It has also been widely used in field of production sites, especially in the aspects of chemical containers, nuclear containers and welding processes control. In 1979, Drouillard has compiled and published a list all of the known literature on AE before 1979 in a single volume (Drouillard 1979). According to its statistics, more than 5000 papers on AE had been published in the world by the end of 1986.

In the early 1980s, the American Physical Acoustics Corporation (PAC) introduced

modern micro-processor computer technology into the AE detection system and designed a second-generation source localization AE detection instrument with smaller size and lighter weight. Due to the portable size and weight of the second-generation AE instrument, it promoted the extensive application of AE technology for field testing in the 1980s. Meanwhile, due to the introduction of 286 processor with more advanced micro-processing computers and multi-functional detection and analysis software, the speed of collecting and processing AE signals is significantly improved, and the information storage capacity of the instrument is hugely expanded, thereby the AE source localisation function and accuracy of damage detection have been greatly improved as well.

In the 1990s, the PAC and the German Vallen Company successively developed and produced the third-generation digital multi-channel AE detection and analysis system with a higher degree of computerization, much smaller size and lighter weight. In addition to real-time measurement of AE parameters and location of AE sources, these systems are able to directly record, display and analyse waveforms.

In the early 2000, a breakthrough in AE applications occurred as shown in Figure 2-1. At that moment, more sophisticated AE analysis tools were developed that permit effective monitoring of damage even in complex concrete composite structures or elaborate external loadings (Ida and Meyendorf 2019).

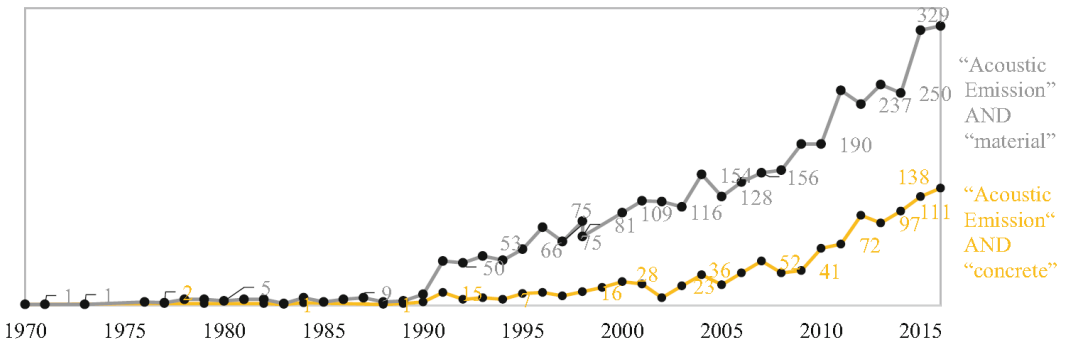

Figure 2-1. The scientific interest in AE monitoring of materials performance progressively increases since 1990 (Ida and Meyendorf 2019)

After entering the 21st century, as a mature Non-Destructive Testing method, AE

technology has been widely used in many fields in the world mainly including the following aspects:

(1) Petrochemical industry: detection and structural integrity evaluation of various pressure vessels, pressure pipelines and offshore oil platforms, leak detection of the bottom of atmospheric storage tanks, various valves and buried pipelines, etc.

(2) Electric power industry: detection and leakage monitoring of high-pressure steam drums, pipelines and valves, detection of steam turbine blades, monitoring of turbine bearing operating conditions, and detection of partial discharge of transformers.

(3) Aerospace industry: inspection and structural integrity evaluation of aircraft shells and main components, aircraft aging test, fatigue test inspection and online continuous monitoring during operation, etc.

(4) Transportation industry: inspection of long tube trailers, highway and railway tank cars, crack detection of railway materials and structures, inspection and structural integrity evaluation of bridges and tunnels, and condition monitoring of ball bearings and journal bearings of trucks and trains, fracture detection of train wheels and bearings, etc.

(5) Machinery manufacturing industry: detection of tool wear and fracture, detection of contact between grinding wheels or shaping devices and workpieces, verification of repair and shaping, quality control of metal processing, monitoring of welding processes, vibration detection, forging testing, and processing Collision detection and prevention, etc.

(6) Civil engineering industry: inspection, monitoring and structural integrity evaluation of buildings, bridges, cranes, large amusement facilities, passenger ropeways, tunnels, dams, continuous monitoring of cracks expansions of cement and concrete structures, etc.

(7) Scientific research and material testing industry: performance testing, fracture testing, fatigue testing, corrosion monitoring and friction testing of various materials,

magneto-acoustic emission testing of ferromagnetic materials, etc.

(8) Others: interference detection of hard disk, drought stress monitoring of crops and trees, wear and friction monitoring, rock detection, geological and seismic applications, engine condition monitoring, online process monitoring of rotating machinery, crack detection of steel rolling silver, monitoring of the strengthening process of automobile bearings, monitoring of the casting process, monitoring of battery charging and discharging, testing of friction, force and destruction characteristics of human bones, monitoring of bone and joint conditions, etc.

2.1.2 Principles of AE

The principle of AE detection is shown in Figure 2-2. The elastic wave emitted from the AE source eventually propagates through material to structure surface, causing a surface displacement that can be detected by AE sensors. These detectors convert the mechanical vibration of material into electrical signals, which then will be amplified, processed and recorded. The change of internal stress in solid materials produces AE signals and there are many factors that can cause changes in internal stress during material processing and application, such as dislocation movement, crack initiation and propagation, fracture, and non-diffusion phases change, magnetic domain wall motion, thermal expansion and contraction, changes in applied load, etc. According to the observed AE signals, the mechanism of AE source can be analysed and investigated.

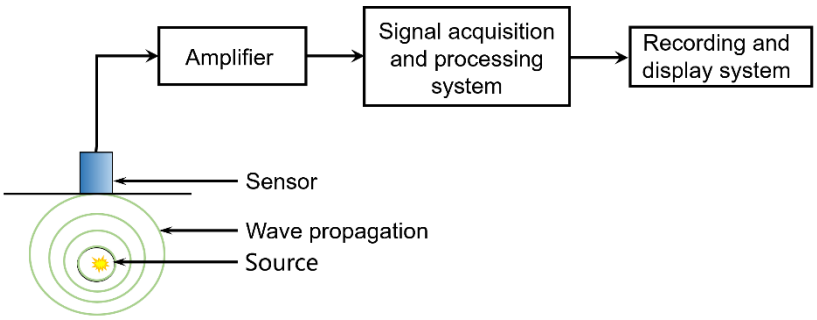

Figure 2-2. Schematic diagram of AE detection principle

The main purposes of AE detection are to: (1) Determine the location of the AE source; (2) Assess the activity and intensity of the AE source; (3) Analyse the nature

of the AE source; (4) Determine the time and load when the AE occurs. Generally, for active AE sources, other Non-Destructive Testing (NDT) methods such as the use of Acousto-Ultrasonics(AU) testing, magnetic particles, penetrant, or radiation, should be applied for local re-examination to accurately determine the nature and size of the defect area.

2.1.3 AE sources of different materials

After many years of research, it has been ascertained that there are many mechanisms in materials that can produce AE sources. The energy of AE is generally provided by external load, latent heat of phase change, external magnetic field, etc. At present, a large number of AE source models proposed can be roughly divided into two categories: One is that the source is regarded as an energy emitter, and the macroscopic parameters such as stress and strain can be used to obtain a stable solution to this problem, that is, the steady-state source model; the other one is to use the time-varying stress-strain field near the source to calculate the dynamic changes related to the behaviour of the source, that is, the dynamic source model.

Figure 2-3 shows the energy distribution process of an AE source from a crack propagation event of a steady-state source model. For an event such as crack growth, only part of the released energy is transformed into elastic wave energy, and most of the rest is transformed into lattice strain energy, surface energy and thermal energy. It can be seen from Figure 2-3 that if the elastic wave energy emitted by the source event can be measured and the energy distribution function can be determined, then the energy of the source event can be reversely calculated, which will provide a method for understanding the microscopic fracture process of the material. However, due to the influence of the surrounding environment of the source, the rate of energy release, the differences between the material's P wave and S wave propagation speeds and the dispersion of surface Rayleigh waves (Full details are given in the following section 2.1.4), the distribution function of each source is different and the elastic wave energy measured by the sensor could hugely vary with different positions.

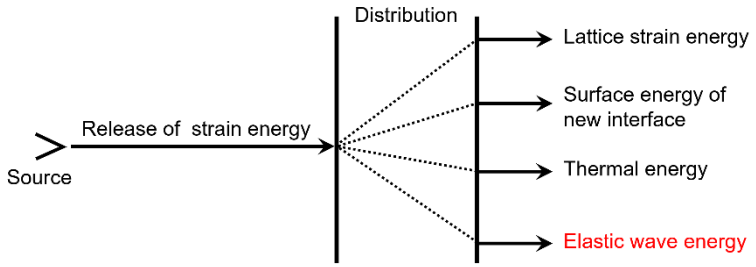

Figure 2-3. Distribution process of released strain energy during crack propagation

2.1.3.1 Transient and continuous AE signals

The AE signal generated in the material has a wide dynamic range. Its amplitude can range from less than 10^{-15}m to 10^{-9}m, reaching a level of 10^{6} magnitude (120dB). In addition, the generation rate of AE signals is also volatile. According to the description of Vallen (2002), AE signals are currently artificially categorised into transient (or burst) and continuous types as shown below in Figure 2-4.

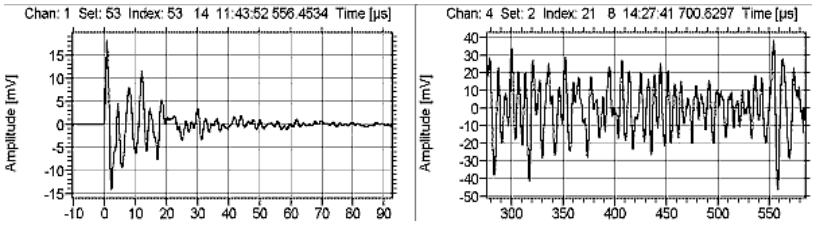

Figure 2-4. Transient (left) and continuous (right) AE signal (Vallen-Systeme GmbH 2002)

If the AE event signal is transient, intermittent and can be separated in time, then this signal is called a burst AE signal; if a large number of AE events occur at the same time and being indistinguishable in time, then these signals are continuous AE signals. In fact, continuous AE signals are also composed of a large number of small burst-type signals but too dense to be distinguished individually.

2.1.3.2 AE sources in metallic materials

After more than 60 years of research since early 1950s, AE sources in metal materials have been studied and identified. In this section, as the AE sources in metallic materials is not the focus in this work so a summary are given below in Figure 2-5. (Shen Gongtian 2015)

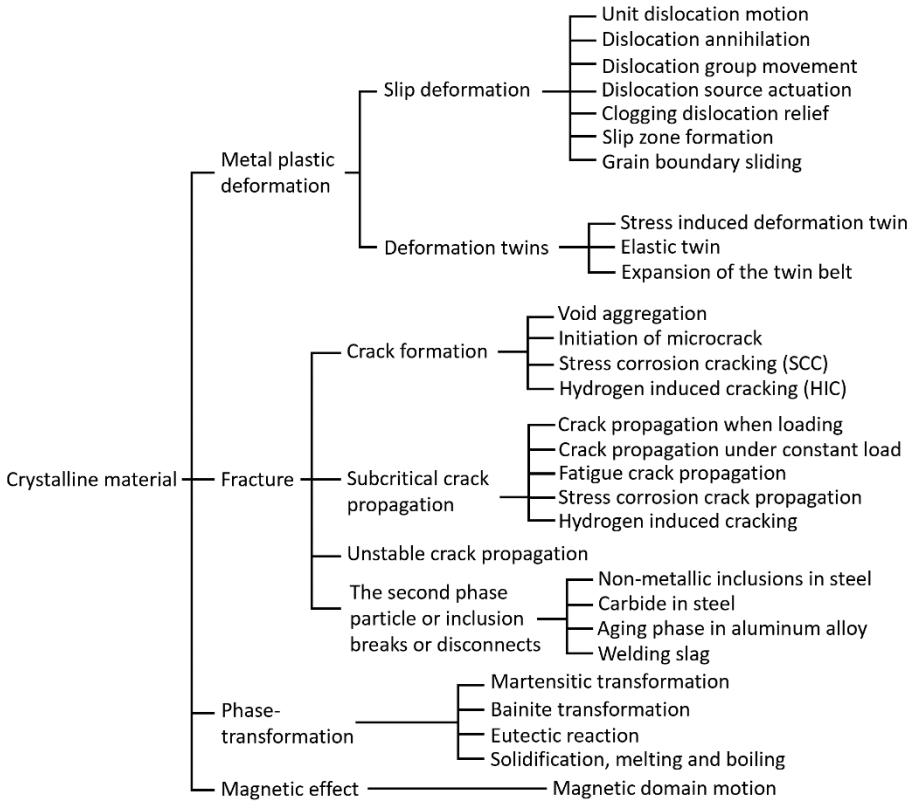

Figure 2-5. AE sources in metallic materials

2.1.3.3 AE sources in non-metallic materials

Most of AE studies on non-metallic materials are mainly focused and applied on rock, concrete, glass and ceramics. Because those materials are all brittle and with high strength but poor ductility, the vast majority of AE sources come from the initiation of micro-cracks and formation and propagation of macro-cracks. The specific application of AE on concrete structure is covered in the following section 2.2 and 2.3.

2.1.3.4 Other AE sources

Other AE sources often encountered in the AE testing are listed below:

- Delamination, fibre failure, etc. in composite materials;
- Leakage of fluid medium;
- Cracking of oxide or oxide layer;
- Cracking of slag inclusion;
- Friction source;
- Liquefaction and solidification;
- Loose and intermittent components contact;

2.1.4 Wave propagation

For electromagnetic waves, propagation may occur in a vacuum as well as in a material medium. But for other types of waves they cannot propagate through a vacuum and need a transmission medium to exist. AE signals, as one of the typical elastic waves, have to undergo the propagation process in the medium from the generation of a source to reception. Due to the physical characteristics and geometric characteristics of the transmission medium, there is a significant impact on the wave propagation and further on the analysis and evaluation of the signal. Therefore, it is particularly important to know and understand the propagation characteristics of AE signals.

2.1.4.1 Different modes of wave propagation

The wave propagation of AE signals in the medium are in different modes according to the direction of the oscillation relative to the propagation direction. Much of the fundamental research into AE wave propagation are well documented started from the work conducted by Pollock (1986) and Rindorf (1981). Their work alongside other works and development afterwards has been widely discussed such as by Pearson (2013), Marks (2016) and McCrory (2016). Therefore only a brief summary of fundamentals is presented here.

In infinite solid media, there only exist two types of wave which propagates: longitudinal wave and transverse waves. Longitudinal wave is also called P wave (Primary wave), whose direction of particle motion is parallel to the wave propagation direction; transverse wave is also called S wave (Secondary wave), whose particle motion is perpendicular to the wave propagation direction. When the transverse wave propagates in the medium, the medium will produce corresponding shear deformation accordingly. After the wave reaches the solid surface, the vibration of the medium surface elements become a combination of longitudinal and transverse waves, forming a surface wave or known as Rayleigh wave. Figure 2-6 gives the schematic diagrams of the characteristics of particle motion for the two body waves (P wave and S wave) and the Rayleigh (surface) wave.

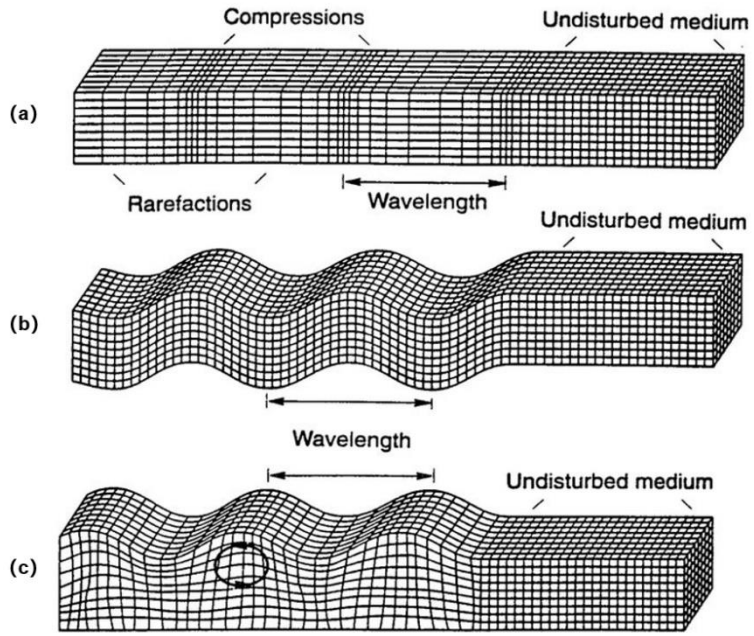

Figure 2-6. Displacement characteristics of body waves: (a) P wave, (b) S wave and (c) Rayleigh (surface) wave (Nam et al. 2013)

When the solid medium is in plate-like and the plate thickness is sufficiently limited to a certain extent (corresponding to the wavelength), then these waves couple together into more complex surface waves known as Lamb waves. Figure 2-7 shows two fundamental modes of Lamb wave in the plate-like medium which are the symmetric or extensional (S_0) mode and the asymmetric or flexural mode (A_0). The occurrence of these modes depends on the plate thickness and the particle motion characteristics and they occur for every excitation frequency. And different modes possess different wavelengths and propagation velocities as well.

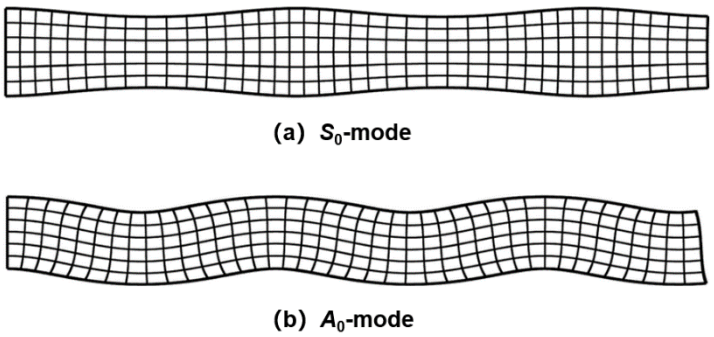

Figure 2-7. Lamb wave modes in plate-like medium (Willberg et al. 2015)

The use of Lamb waves for SHM applications also has difficulties as the propagating modes are dispersive in nature and can convert into each other in the

presence of damages or other changes. One way to explicitly describe the dispersion behaviour of Lamb waves is to compute the solution of the dispersion equation for each frequency. And the Lamb's homogenous equations are used to produce dispersion curves which describe the wave velocity of each mode as a product of the frequency and plate thickness (Pearson 2013). Figure 2-8 gives an example of dispersion curves for a 3.2mm thick aluminium of two basic wave modes.

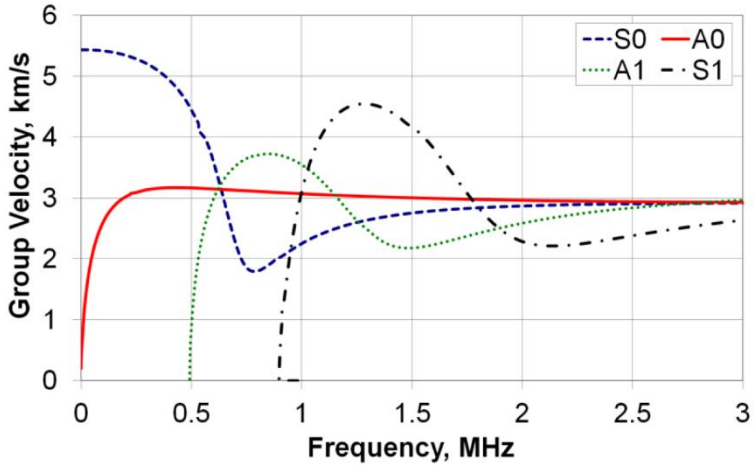

Figure 2-8. Example of dispersion curve for the aluminium material (thickness = 3.2mm) (Pearson 2013)

2.1.4.2 Reflection, refraction and mode conversion

In an elastic solid medium, two propagation modes, longitudinal wave and transverse wave, are both generated at the AE source. When they propagate to the interface of different materials, the wave reflection, refraction and mode conversion occur as shown in Figure 2-9. In addition to their own reflecting (or refracting) P waves and S waves of the two incident waves, they can also be converted into surface waves on the free surface of a semi-infinite body. The Rayleigh waves can be generated in a thin plate with a thickness close to the wavelength. In a thick-walled structure with a thickness far greater than the wavelength, the wave propagation becomes more complicated as shown in Figure 2-10.

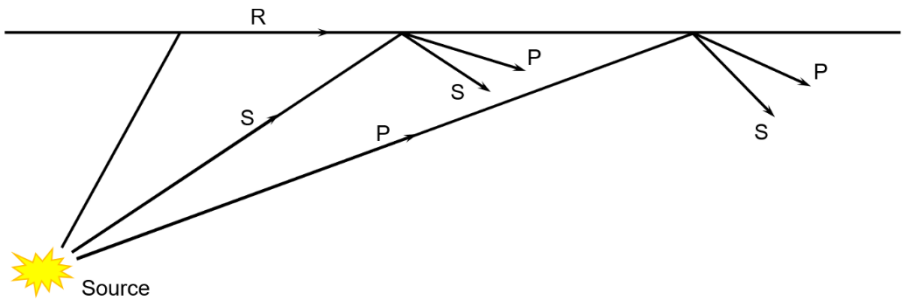

Figure 2-9. Wave reflection, refraction and mode conversion

P - P wave; S - S wave; R - Rayleigh wave.

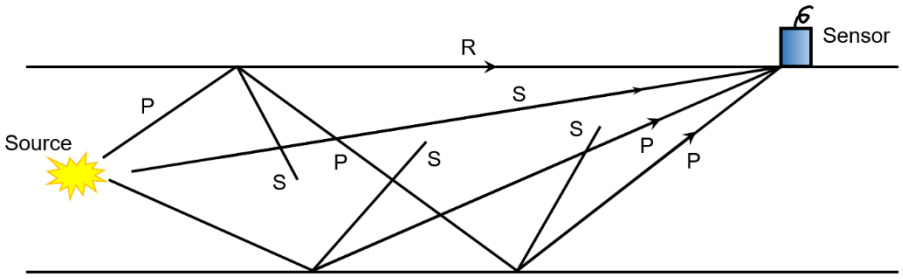

Figure 2-10. Wave propagation in thick plate

P - P wave; S - S wave; R - Rayleigh wave.

2.1.4.3 Wave velocity in material

The wave propagation velocity is a material characteristic which is related to the elastic modulus and density of the medium. It can vary widely in different materials. In a certain material, different propagation modes also have different propagation velocities. In a homogeneous medium, the velocities of longitudinal wave (P wave) and transverse wave (S wave) can be expressed by the following equations:

$$v_l = \sqrt{\frac{E}{\rho}\frac{1-v}{\rho(1+v)(1-2v)}} \tag{2.1}$$

$$v_t = \sqrt{\frac{E}{\rho}\frac{1}{2(1+v)}} = \sqrt{\frac{G}{\rho}} \tag{2.2}$$

Where

v_l is the longitudinal wave velocity;

v_t is the transverse wave velocity;

v is the Poisson's ratio;

E is the Young's modulus;

G is the shear modulus;

ρ is the material density.

In the same material, there is a certain relationship between the wave velocities of different modes. For example, the velocity of transverse waves is about 60% of the velocity of longitudinal waves, and the velocity of Rayleigh waves is about 90% of the velocity of transverse waves (Graff 2012). The speed of longitudinal wave, transverse wave, and Rayleigh wave is not related to the frequency of the wave, while the speed of Lamb wave is highly related to the frequency contents of the wave as due to the existence of dispersion phenomenon, which is approximately distributed between the speed of longitudinal wave and transverse wave. In the actual structures, the propagation velocity is also affected by many factors such as material type, anisotropy, geometry and scale of structure, etc.

2.1.4.4 Attenuation

Attenuation is a general term that refers to the reduction in the strength or energy of a signal, which is natural consequence and inevitable of signal transmission over long distances. Therefore, attenuation controls the detectability of the source at different distances. For AE monitoring, it is a key factor in determining the sensor location and spacing.

There are several factors causing wave attenuation, especially related to those physical parameters that determine the wave amplitude. There are also different attenuation mechanisms that cause a reduction in wave amplitude, but not all attenuation mechanisms necessarily cause energy loss. Some only cause propagation mode changes and energy redistribution without actual energy loss. The following are the main factors causing attenuation of wave propagation (Shen Gongtian 2015):

(1) Geometric attenuation

When a wave is generated by a local source, the wave will propagate in all directions from the source. Even in a lossless medium, the energy of the entire wavefront remains unchanged, but it is spread over the entire wavefront sphere. As

the propagation distance of the wave increases, the wave amplitude must decrease.

(2) Dispersion attenuation

Dispersion is a phenomenon caused by the change of wave velocity with different frequency. Since the actual AE signal includes multiple frequency components, and the velocity of Lamb waves is related to the frequency of the wave, the components of different frequencies in the wave packet will propagate at different speeds in the medium. The amplitude of each wave packet decreases as the wave propagation distance increases.

(3) Scattering and diffraction attenuation

Waves propagating in media with complex boundaries or discontinuities (such as cavities, cracks, inclusions, etc.) will interact with these geometric discontinuities, leading to scattering and diffraction phenomenon. Both scattering and diffraction of waves can cause the reduction of amplitude and lead to wave attenuation.

(4) Attenuation caused by energy loss mechanism (internal friction)

In the wave attenuation mechanism discussed above, if the transmission solid is an elastic medium, theoretically the total energy of all waves (original wave, reflected wave, scattered wave, diffracted wave, dispersion, etc.) remains the same. However, in reality, the total mechanical energy of wave propagation cannot remain constant, but gradually attenuate. Due to the thermoelastic effect, mechanical energy can be converted into thermal energy over propagation. If the stress exceeds the elastic limit of the medium, plastic deformation can occur and cause a loss of mechanical energy as well. Crack propagation converts the mechanical energy of the wave into new surface energy, and the interaction between the wave and the dislocation in the medium can also cause energy loss and attenuation. The viscous behaviour of plastic materials, the friction between the interface and the incompletely combined inclusions or fibres in the composite material can cause the energy loss and attenuation. Furthermore, magneto-elastic interactions, electronic interactions in metals, paramagnetic electrons or nucleus spin mechanisms, etc. can cause energy loss and

attenuation of waves as well. No matter which of the above mechanisms causes the reduction of mechanical energy, the amplitude of the wave will decrease as the wave propagates through the medium in any case.

Figure 2-11 below gives an example of the attenuation curves in a reinforced concrete structure for different frequency bands. The figure shows a continuous reduction of the overall AE signal amplitude in each frequency band as the propagation distance increases.

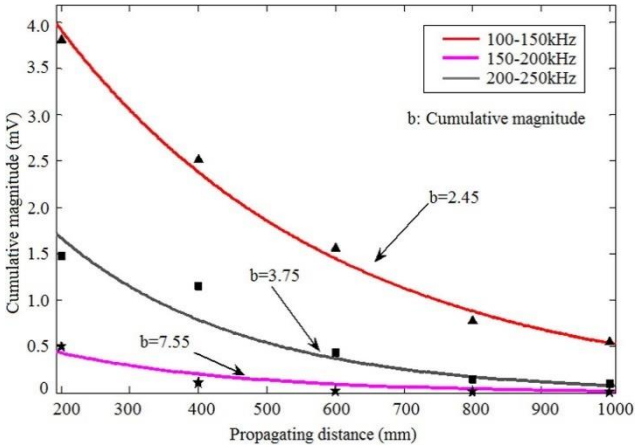

Figure 2-11. The attenuation of different frequency bands in a reinforced concrete beam (Feng and Yi 2017)

2.1.5 Kaiser effect and Felicity effect

Generally, the loading path history of the material has an important impact on the AE characteristics during the repeated loading. The Kaiser effect was put forward by the German scholar Kaiser in the first place (Kaiser 1953). It was discovered in a test of loading metal materials. The Kaiser effect is manifested and defined as the absence of AE signals (or no obvious AE signals) at loads not exceeding the previous maximum load level when material undergoes repetitive loading. In other words, material has a memory for the historical load with respect to the presence of AE phenomenon. Conversely, if the material gives off significant AE signals at a lower load than the one previously reached in an increasing repeated loading, then this phenomenon is defined as the Felicity effect.

Rusch and Van Amerongen (1960), Mccabeetal et al. (1976) have proved through

experiments that the Kaiser effect exists in concrete, rock and masonry materials as well. Watanabe et al (2007) found that the Kaiser effect has a certain relationship with the strength of concrete. The more obvious Kaiser effect could be observed in higher strength concrete. Große and Schumacher (2013) found that Kaiser effect depends on the highest stress level reached by the previous loading. When the stress level exceeds a certain range (e.g. when the irreversible plastic deformation occurs) during the previous loading stage, the Kaiser effect disappears.

Hongguang and Zaoding (1997) verified the existence of the Kaiser effect and Felicity effect during the cyclic loading process of concrete materials through a series of studies and the relationship between Kaiser effect and Felicity ratio is studied in detail. It is found that the Kaiser effect of the concrete material has both the upper stress limit (about 70% - 80% of the ultimate stress) and the lower stress limit (about 30% - 40% of the ultimate stress). The upper limit of stress is determined by the failure mechanism of the concrete, and the lower limit of stress is determined by the structural characteristics of the concrete material itself.

The Kaiser effect and Felicity effect have a number of applications in AE detection technology and especially play an important role in the areas below:

- Regular AE detection of new cracks in active components under overload;
- Estimation of the original maximum stress on rock mass structure;
- AE detection of fatigue crack initiation and propagation;
- Eliminate the noise interference of loading pin hole through pre-loading measures;
- Identification of the common reversible friction noise during the loading process.

2.1.6 Source mechanism identification

A major issue in successful AE monitoring is to distinguish the nature of the source. Mainly there are two different methods which are based on waveform and parameter respectively. The first one is the Moment Tensor Analysis (MTA), which is derived from

the seismic engineering application of structural materials. The second method is a statistical method which is based on AE signal features.

2.1.6.1 Moment Tensor Analysis (MTA)

Moment tensor analysis (MTA) is a post-processing analysis method for cracking mechanism identification based on acoustic signals. It is known that cracking mechanisms related to AE generation include crack dynamics and crack kinematics. Crack dynamics can be determined by deconvolution analysis, but it is worth noting that MTA has only been successfully applied in really limited cases because of the nature of this method and the material it applied on. To intrinsically investigate the damage mechanism and understand the cracking progress in fracture tests, a powerful technique using the simplified Green's functions for Moment Tensor Analysis (SiGMA) procedure which is capable of quantitatively determining the crack kinematics of located sources, crack types and orientations has been proposed by Ohtsu (1991).

Within the existing literatures based on MTA, the investigation of crack kinematics, crack classification and crack volume calculation have been extensively discussed. In MTA, crack types are mainly divided into tensile mode, shear mode and mixed mode. Since the understanding of the occurrence and growth of cracks under shear stress is particularly important for the evaluation of structural integrity of reinforced concrete structures, MTA can play an important role as a method for quantitative analysis of concrete cracking behaviour. However, not all recorded waveforms can be used for MTA as it requires accurate amplitude and arrival time of signals collected from at least six sensors at the same time. In that case most of work are only available for plain concrete materials or mortar blocks for testing and analysis. Reinforced concrete structure members are rarely involved because of the influence of steel bars, cracks and boundaries, etc. It is easy to cause analysis failure. This is the reason that only a small percentage of the recorded waveform set can be suitable for MTA analysis. Therefore, only limited information detected can be used in MTA analysis.

The theory of MTA will be extensively discussed in Chapter 4.

2.1.6.2 RA-AF correlation analysis

In some cases, the MTA method is not always feasible due to the strict sensor positioning requirements of experimental set-up and AE waveforms with a good signal to noise ratio. And it is even almost insurmountable in long structures monitoring like bridges. In 2003, the Federation of Construction Materials Industries from Japan published standards on estimation of concrete properties by the elastic-wave methods (Ohtsu et al. 2007). These standards contain a monitoring method for active cracks in concrete by AE (JCMS-III B5706-2003 code). The RILEM TC 212-ACD recommendation, introduced a straightforward classification method of damage modes based on AE parameter analysis in concrete. It is efficient to classify the active cracks into tensile and other type cracks including shear cracks as shown in Figure 2-12 (RILEM TC 212-ACD 2010). As shown below, the RA value and the AF value (average frequency) is applied to characterise damage source in concrete.

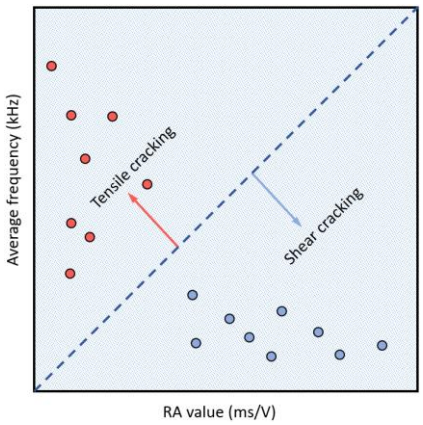

Figure 2-12. Protocol of RA-AF value based on RILEM TC 212-ACD (2010) recommendation

The AE signal signatures are very different depending on the type of movement occurring. Based on the distribution of these two indices, cracks can be directly classified into tensile and shear cracks. The crack propagation process indicates that the tensile crack will be detected when crack opening occurs. When the condition changes to sliding movements, then it will be detected as shear cracks. From the view of AE waveform characteristics, it will show low rise time and high frequency during the early stage of tensile cracks whereas the waveforms with high rise time and low

frequency will dominate the failure stage during shear movement.

However, there is no clear standard for defining the coordinate ratio between the two indices as AE measures non-linear and relatively independent random data. Therefore, it is necessary to develop a more effective classification way to collect statistics on the distribution of data.

2.2 Application of AE in reinforced concrete

In the field of civil engineering, AE technology is mainly used to find the AE wave characteristics under various damage states through experiments. The advantage of this is the direct establishment of the relationship between the material damage mechanism and AE characteristics, which is simple and straightforward. The disadvantage is that the relationship between AE signal with material properties and mechanics process is often ignored. It requires much experimental summary for different components and conditions. Because the relationship between damage mechanism and AE characteristics often show a complex nonlinear relationship, it was difficult to develop a universally applicable criterion. Although many practical engineering applications have made fruitful empirical results, this has not yet resulted in a fundamental breakthrough regarding the AE theory in this field. Therefore, researchers are increasingly focusing on AE-related theories.

Due to the complexity of the research object in the field of reinforced concrete, AE technology faces many complex issues as an NDT method. However, in terms of the purpose of detection, these problems can be summarised into three questions: Firstly, where does the damage occur? That is, the problems of AE source location; Secondly, what is the kind of damage? That is, the problems of source identification; Thirdly, what is the extent of the damage? That is, the problems of quantitative assessment of damage.

AE technology applied to concrete structures began in 1959 when Rusch did a research of the AE signals generated when the concrete was loaded (Rüsch and Van Amerongen 1960). He studied Kaiser Efect in concrete and found that the effect only

exists in the region of 70%-85% of the ultimate stress. L'Hermite (1960) studied the relationship between the cracking process and the volume change of concrete under axial compression and reported the results of AE research in the process of concrete cracking. Robinson (1968) studied the AE characteristics of concrete with different aggregate content and different aggregate size. He found that the AE signal generated from the concrete has two main frequencies, namely 2kHz and 13-14kHz. These two main frequency signals mainly occur in the load level when the sound velocity and Poisson's ratio changed. Wells (1970) developed an instrument used to record the AE signal under the deformation of concrete. The instrument can be used to measure the frequency range of 2-20kHz. Meanwhile, the mortar and concrete specimens were tested successfully, and the AE signal waveform was recorded. In the same year, Green (1969) published a more comprehensive research. By loading the top of a pressure vessel model made of pre-stressed concrete, the AE phenomenon of the loading process was tested. This is the first application of AE technology in the damage detection of concrete structures and it clearly shows the correlation of AE signals and material damage process of concrete. He also used the acoustic source location technology to determine the damage location. His work has opened up a precedent for the early warning of structural damage.

The major application of AE in structural concrete elements began in the late 1970s. Carpinteri et al. (2007). McCabe et al. (1976), Niwa et al. (1977), originally developed the AE technology which was derived from the metal materials, and enable it to be used for heterogeneous materials. Based on this study, the influence of concrete specimen size, age and loading mode on the AE signals was studied. The experiments showed that the AE rate could effectively describe the development of concrete damage.

Given that people had limited capability in AE signal processing methods and lack of understanding of the characteristics of AE source and transmission characteristic, there were many problems with the repeatability and reliability of the experiments results at the beginning of the 1980s. However, AE instruments experienced two major

improvements during the period from the 1980s to 1990s. Firstly, the modern micro-processing computer technology was introduced into the AE detection system. Then the second-generation AE source location detector with small size, light weight and fast speed was designed and applied to the promotion of AE technology in the field detection. Secondly, the third-generation digital multi-channel AE detection and analysis system is developed, which has a higher degree of computerization, smaller volume and lighter weight. In addition to the real-time measurement of AE parameters and source location, this system also can directly display and analyse the AE waveform, as well as the frequency analysis and provide a foundation of the AE technology based on waveform analysis.

After entering in the 1990s, the continuous progress of the modern AE system has created the necessary conditions for the development of AE technology. In practical application, it is concluded that the AE parameters can reflect various damage processes, and the changes of these parameters are used to judge the type of damage. In the field of reinforced concrete, commonly used AE parameters are AE hits, counts, amplitude, duration, rise time and energy (Shiotani 2008). The parameter analysis has the advantages of simplicity, real-time analysis, and low requirement for the instrument. So it is often used in the health monitoring and quantitative research of actual structure and is widely applied in the identification of source location.

Because the AE parameters only reflect partial information of AE signals, it is necessary to select the appropriate parameters or parameter combinations to analyse the characteristics of the problem. In the study of AE characteristics of concrete beams under three point bending load, Chen Bing and Zhang Lixin (2000) studied the AE characteristics of steel fibre reinforced concrete, plain concrete and mortar specimens. Based on the amplitude distribution characteristics of AE signals and setting filter value to the duration, they divided the duration time according to the amplitude of the event peak value and obtained the characteristics of AE parameters through the analysis of failure mechanism on the meso level.

In fact, even if it is a plain concrete, the properties, size, proportion and

construction technology of components would affect the mechanical properties. Therefore, it is necessary to study the influence of these factors on the AE characteristics when using AE parameters to identify the AE source. Ji Hongguang and others (2004) studied the effect of structure characteristics of concrete material on AE performance through the laboratory test of concrete specimens. At the same time, he also studied the basic characteristics of AE in concrete materials under different stress conditions, the nonlinear characteristics of AE, Kaiser effect and the relationship between AE and damage in concrete materials. It can be seen that the changes of AE parameters are affected by many factors, such as material, structure, loading condition and so on, which need to establish the relationship between various parameters and different kinds of damage mode through a large number of experiments.

In the field of reinforced concrete, cracking is the most common and basic failure form (Bamforth 2019). Therefore, it has become a direction of AE research that using fracture mechanics and AE technology to study the nature of concrete cracking and establish the relationship between AE parameters and fracture parameters. Chen et al. (1992) studied the relationship between AE and the development of cracks in mortar and concrete, and also used AE method to calculate the critical stress intensity factor and the critical notch tip opening displacement. Otsuka et al. (1998) studied the influence of aggregate size on the fracture process zone of concrete using AE method. They found that the larger the size of aggregate, the greater the fracture process zone. However, in the reinforced concrete structure, the application of fracture theory becomes more challenging due to the existence of all different kinds of rebar, and furthermore it results in more difficulties in terms of the AE characterisation of fracture mechanics.

In order to be able to use simple parameters to better reflect the damage characteristics, so as to realise the real-time monitoring of the actual structure, some scholars have made improvements to the AE parameters and bring in new AE parameters from seismology and other fields. One method that has been adapted from seismology to study AE from concrete fracture is called '*b*-value analysis', which is

originally proposed by Gutenberg and Richter (1950) and considered a qualitative method that characterises large numbers of events using an empirical log-linear frequency-magnitude distribution, from which parameters describing the distribution can be determined (such as mean occurrence time, maximum event size, relative numbers of small to large events, etc.). Although the *b*-value analysis method is well known in seismology, not too many works has been done on the area of concrete and civil engineering structures. Later on, an 'improved' *Ib*-value method was proposed and applied to the evaluation of slope failure by Shiotani (1994). Compared to *b*-value, the *Ib*-value method employs statistical parameters such as the mean and the standard deviation of the AE amplitude. It was found that the *Ib*-value analysis was in significant agreement with the progressive failure of the slope model and successful in evaluating fracture process of concrete (Shiotani et al. 2000). Colombo et al. (2003) used *b*-value analysis to study the AE signals on the test of reinforced concrete beams. The results show that the trend of *b*-value method has a good corresponding relationship with the cracking process of reinforced concrete beams. Farhidzadeh et al. (2012) studied and monitored the fracture process of large reinforced concrete shear wall under cyclic load by using AE technology. The filter-*b* value based on Gauss filter method is used to monitor the evolution of each fracture mode, and the clustering analysis based on *k*-means is proposed to automatically divide the signal into tensile and shear types. Abdelrahman et al. (2014) using the accumulation of AE energy of AE technology to evaluate the damage of pre-stressed concrete structures with different degrees of corrosion. Based on this, a revisionary damage index is proposed and the yield point of the specimen is successfully detected. Behnia et al. (2014) have made a review of the application of AE technology in the health monitoring of concrete structure and the key AE parameters of *b*-value, *Ib*-value, AE, energy and number of hit are discussed. They emphasised the limitations of these parameters in the actual detection and discussed some new parameters appeared in recent years like sifted *b*-value, minimum *b*-value and Q value.

Since 2010s, some researchers have tried to summarise the new AE parameters

which can reflect the essence of the AE source based on the signal analysis. In the identification of cracking pattern of cement-based materials by Aggelis et al. (2013), the analysis of crack mode of reinforced concrete members by Aldahdooh and Bunnori (2013), and the fatigue crack classification of reinforced concrete beams by Nor et al. (2013), both the characteristic parameters combination of Average Frequency (AF) and RA value are used to classify the active cracks (as mentioned previously in section 2.1.6.2). However, these parameters basically reflect the overall characteristics of the signal and ignore its local characteristics. When the change of AE waveform caused by the change of acoustic source mechanism is not obvious, it would be very difficult to reflect it by parameters. Therefore, the introduction of parameters which can reflect the main characteristics of the signal waveform and harmonic source is undoubted of great significance to improve the reliability of the recognition rate of the acoustic source and the AE detection.

The method of analysing the AE waveform to infer the acoustic source information is called waveform analysis. The waveform analysis can obtain more comprehensive signal information. Therefore, it is difficult to realise the acoustic source identification problem with the parameter method, which could be easier to study from the waveform analysis.

Early in the development of AE technology, people realised the important role of waveform analysis and carried out many types of research (Stephens and Pollock 1971). However, due to the limitations of the detection instrument, only moderate success was reached. From the end of the 1980s, due to the progress of AE detection system, researchers began to study the quantitative AE theory based on the signal analysis (Sachse and Kim 1987; Ono 1994). Because of the high potential of waveform-based analysis, increasingly researchers have started to study the waveform analysis to solve engineering problems in recent years (Govekar et al. 2000; Grosse and Linzer 2008). Balázs et al. (1993) used the coherence function to evaluate the similarity of two different AE signals and inferred the similar acoustic source mechanism based on similar frequency components. However, the usability of this

method is limited because it is based on the neglection of the influence of propagation medium and sensor characteristics on the waveform.

Quantitative assessment of damage is the goal of AE technology. The rule of damage evolution of material or structure is usually reflected by the change of a parameter with time or the correlation between parameters. Ohtsu (1992) used AE rate process theory to evaluate concrete AE activity. He pointed out that the AE activity of concrete is closely related to the internal defects of the material and proposed the mathematical expression the AE parameters and concrete stress. Also, he also used this method to assess the defects of existing concrete bridge structures. Nair (2006) applied the strength analysis technique of quantitative damage to the failure test of reinforced concrete beam with cyclic loading. In the experiment, the trend of strength change in the process of damaging was obtained, and an actual bridge structure was analysed by using the method of strength analysis.

In recent years, due to the continuous progress of experimental methods and the increasing demand for quantitative AE technology, research on the AE technology based on concrete materials has become more accurate and detailed. Aldahdooh and Bunnori (2013) studied the fracture mechanism of reinforced concrete beam by using AE signal and classified the crack types of reinforced concrete beams with a different thickness under four-point bending load (bending or shear cracks). Taking the number of AE hit as the parameter, the proportional relationship of the number of AE hit in the two types of cracks was obtained. The results are in good agreement with the visual observation of the crack mode. Invernizzi et al. (2013) studied the fracture and scaling ratio of AE signal strength in a combination of compression tests by using AE technology with different sizes and slenderness ratio of the concrete specimen. Then a finite element analysis model of pure compression test is presented, which can not only describe the interface crack of the aggregate material but also can describe the crack of the pure matrix material. The results show that the number of cracks in the numerical simulation and the AE count in the experiment has a good correlation with different size of specimens. Rouchier et al. (2013) studied the fibre reinforced mortar

tensile process by using digital image correlation (DIC) with AE monitoring. The evolution of the process of specimen degradation was quantified by image processing program and the correlation between AE activity, and optical measurement results were determined.

At present, most of the research on reinforced concrete structure using AE technology is based on the laboratory-scale concrete components. It is the ultimate goal of AE workers to use AE technology in practical engineering to monitor and judge the damage status of the structure. Based on a large number of laboratory studies, some scholars have made some useful attempts of NDT methods in actual engineering structures by using AE technology. Shigeishi et al. (2001) applied AE technology to detect a real bridge, a combination of stone bridge and reinforced concrete bridge. The results showed that the strong AE signal comes from the reinforced concrete structure, and the signal energy from the stone structure is small. AE could detect early crack growth and crack tip position, early than visual inspection. Vogel et al. (2006), Fricker and Vogel (2007) studied the AE analysis and monitoring method in pre-stressed concrete structures. They applied this method to an actual pre-stressed concrete bridge structure for health monitoring and the failure of the pre-stressed tendons had been successfully detected. Degala et al. (2009) did an experimental study of reinforced concrete slab with carbon fibre by using AE technology, monitoring the initiation, development and localisation of damage, using parameters, strength and principal component analysis to predict concrete cracking and carbon fibre debonding. Suzuki et al. (2010) using AE rate process theory to study the durability of concrete under the action of freeze-melting circulation. They pointed out that the relative elastic modulus of concrete under action of freeze-melting circulation have a quantitative relationship with parameters of AE rate process. Kawasaki et al. (2013) applied continuous AE monitoring to the study of corrosion defects of reinforced concrete beams and successfully determined the occurrence of corrosion and crack nucleation induced by corrosion. The analysis results of AE parameters were compared with the results of corrosion mechanism viewed by electron probe, which showed that it is

promising that using AE to make a quantitative assessment of concrete corrosion caused by the expansion of early corrosion.

In the past twenty years, AE technology has achieved remarkable development and begun to be applied in the evaluation of infrastructure such as bridges and dams. At the same time, damage quantification technology has been transferred from laboratory research to practical structures in service at this stage. Various methods of damage detection and quantification through AE-based condition assessment have been proposed and verified.

As the Kaiser effect described in section2.1.5 above, the Felicity ratio, also known as the *F*-ratio, was proposed as a method to quantify the Kaiser effect. Another two ratios to estimate the Kaiser effect are proposed and defined by Ohtsu et al. (2002) as:

(1) Ratio of load at the onset of AE activity to previous load:

$$Load\ ratio = \frac{load\ at\ the\ onset\ of\ AE\ activity\ in\ the\ subsequent\ loading}{the\ previous\ maximum\ load}$$

(2) Ratio of cumulative AE activity during the unloading process to that of the last maximum loading cycle:

$$Calm\ ratio = \frac{the\ number\ of\ cumulative\ AE\ activity\ under\ unloading}{total\ AE\ activity\ during\ the\ whole\ cycle}$$

As the Load ratio and Calm ratio are introduced in practice, the damage assessment method is proposed to classify the damage levels as illustrated in Figure 2-13. Nevertheless, the criterion of the particular values to classify these two ratios should be properly determined based on the experimental data obtained at the site or in a laboratory as it varies in different scale structures. Ohtsu et al. (2002) suggested that 0.9 of the Load ratio and 0.05 of the Calm ratio can be applied for the classification in laboratory tests. For a larger scale structure, for example a concrete bridge beams (Colombo et al. 2005a; Colombo et al. 2005b), 0.3-0.45 of the Load ratio and 0.6 of the Calm ratio can be applied.

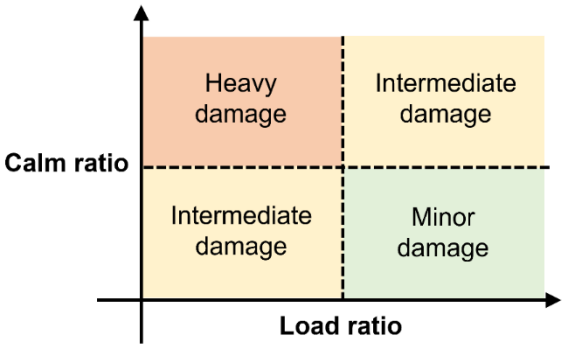

Figure 2-13. Qualification of the damages by Calm ratio and Load ratio

Given the similarities between AE phenomenon and earthquake except for in different scales, there are two main methods adapted from seismology. One is Moment Tensor Analysis (MTA) as previously introduced in section 2.1.6.1 and will be discussed in detail in Chapter 4. Another one is the *b*-value analysis as mentioned above as well. After analysing large numbers of earthquakes in the temporal as well as the spatial domain, Stein and Wysession (2009) found that the slope of the cumulative frequency-magnitude relationship is usually equal to unity, i.e., b≈1, in seismically active regions. An example of a cumulative frequency-magnitude diagram is given in Figure 2-14. The data is from USGS (1900-1990) Website titled “Frequency of occurrence of earthquakes”, and the Graph was plotted by L. Linzer (Mhamdi et al. 2015). Another example from Schumacher (2008) of a continuous estimation using *b*-values for a full-scale reinforced concrete bridge girder is given in Figure 2-15.

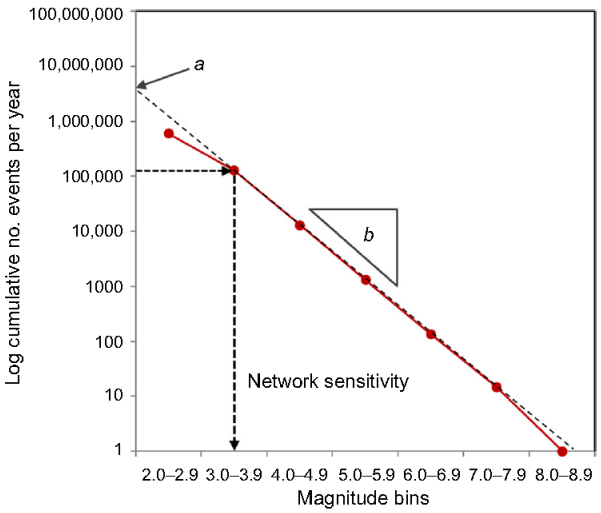

Figure 2-14. Example of cumulative frequency-magnitude diagram (or Gutenberge-Richter distribution) in seismology

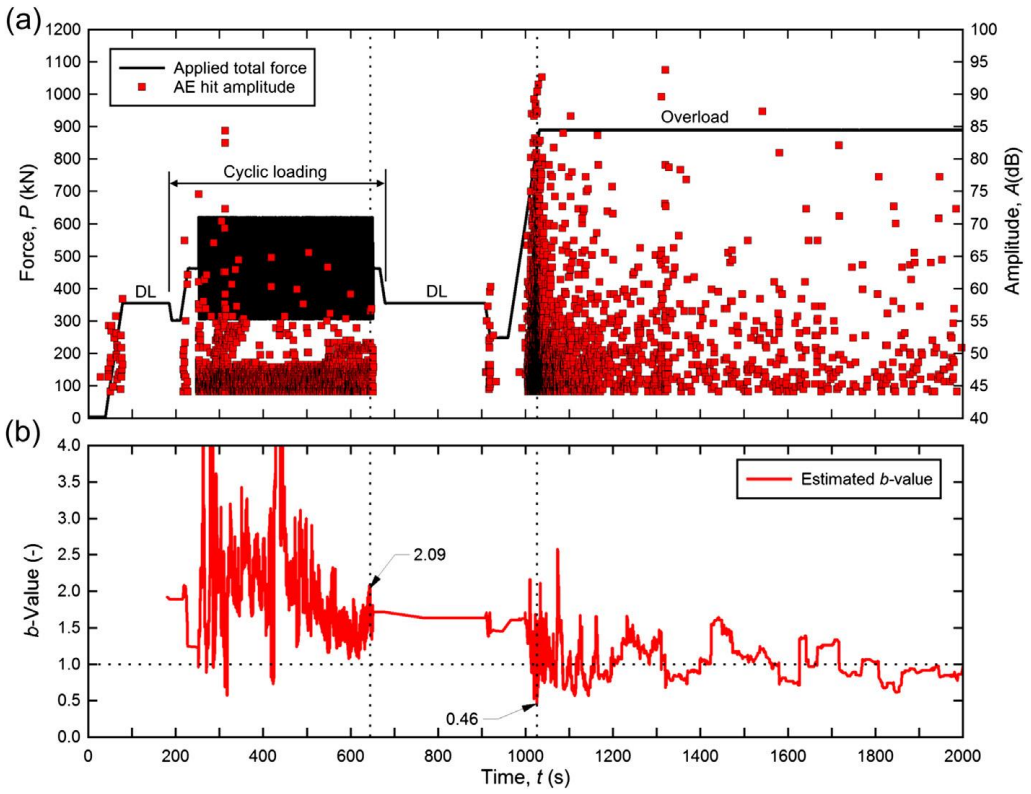

Figure 2-15. (a, b) Example of continuous *b*-value analysis for a full-scale reinforced concrete bridge girder (Schumacher 2008)

Except those method described above, there are other numerous studies regarding the application of AE in damage assessment during load tests of RC and PC structures, such as:

• Intensity analysis (IA): This method was proposed by Fowler et al. (1989) to assess damage in fibre-reinforced polymer vessels and tanks. It was used to classify the damage associated with ASR (Alkali-Silica Reaction) distress (Abdelrahman et al. 2016). Recently, the IA method was extended to material degradation mechanisms in concrete structures such as corrosion (Abouhussien and Hassan 2016);

• Relaxation ratio: A method initially proposed by Colombo (2003) in his PhD to quantify the AE energy recorded during the unloading and loading phases of a cycle test, which is based on the principle that the presence of AE energy during the unloading phase of an AE test is generally an indication of structural damage of the material and/or structure under study.

• Index of damage (ID) and modified index of damage (MID). The ID method was initially put forward by Benavent-Climent et al. (2012) for the application of damage evaluation of reinforced concrete slabs subject to seismic loads. The ID method is based on the relationship between the cumulative AE energy and plastic strain energy dissipated by concrete. However, one of the constraints of this method is that it is only applicable within lab-scale experiments as it requires the continuation of the test until the specimen surpasses the level of maximum admissible damage. Thereafter, Abdelrahman et al. (2014) made an improvement and proposed a modified index of damage (MID) to enable the field applicability.

Nevertheless, most of them have the limitation as they can only classify damage if cracking has occurred, such as *b*-value and relaxation ratio, which can classify in terms of micro- and macro-cracking (Elbatanouny et al. 2014); therefore, these are widely applied for tests with high-level AE activities but not suitable for low-level AE activities. Table 2-1 shows an overview of some typical work on the application of AE in concrete structure assessment in recent years according to different experiment scales, material types, loading, sensors and evaluation methods.

Table 2-1. An overview of application of AE assessment on RC structures

Authors and publication time	Experiment scale	Structural material	Loading method	Sensor type	Damage evaluation method
(Ohtsu et al. 2002)	Medium	Reinforced concrete	Static loading	Resonant (150kHz)	Load ratio and Calm ratio (LR & CR)
(Golaski et al. 2002)	On-site testing, full Size	Pre-stressed concrete	Static loading	Resonant (55-60kHz)	Intensity analysis
(Colombo et al. 2003)	Medium	Reinforced concrete	Static loading	Resonant (55-60kHz)	b-value
(Colombo et al. 2005b)	Medium	Reinforced concrete	Static loading	Broadband	LR & CR, relaxation ratio
(Ridge and Ziehl 2006)	Medium	Reinforced concrete	Cyclic loading	Resonant (55-60kHz)	Cumulative Signal Strength Ratio (CSS ratio)
(Lovejoy 2008)	Full Size	Reinforced concrete	Static loading	Resonant (150kHz)	Intensity analysis, LR & CR
(Ziehl et al. 2008)	On-site testing	Post-tensioned Pre-stressed concrete	Cyclic loading	Resonant (55-60kHz)	LR & CR, CSS ratio, global performance index
(Liu and Ziehl 2009)	Small	Reinforced concrete	Cyclic loading	Resonant (55-60kHz)	LR & CR, relaxation ratio
(Aggelis et al. 2009)	Small	Reinforced concrete	Step loading	Resonant (55-60kHz)	Ib-value
(Nair and Cai 2010)	On-site testing	Pre-stressed concrete	Live load by dump trucks	Resonant (55-60kHz)	Intensity analysis
(Barrios and Ziehl 2012)	Full Size	Pre-stressed concrete	Cyclic loading	Resonant (55-60kHz)	LR & CR
(Xu et al. 2013)	Medium	Pre-stressed concrete	Cyclic loading	Resonant (55-60kHz)	LR & CR, CSS ratio, relaxation ratio

As the basis of the experimental study of AE technology, the hardware system has made a great progress in recent years including the new sensing technology to improve the measurement accuracy, frequency range and stability, the wireless sensor technology for the convenience of engineering application (Lédeczi et al. 2009; Lédeczi et al. 2011), the new technology of global optical fibre sensor for reducing the number of AE sensors and convenience of large structural engineering (Verstrynge et al. 2014).

2.3 Smart material and application of NDT&E techniques in self-healing concrete

As the most commonly used construction material, the safety and durability of concrete used are always the core issues that attention needed to be paid, particularly when considering that a typical design life for a civil engineering structure is 50 years or more (Joseph et al. 2010). Normally the repair and maintenance costs account for approximately half of the total expenditure on construction (Liu et al. 2017). Under the unfavourable influences of external environment, cracking of concrete is extremely common far before the predetermined service life is reached. To prevent the threats to the structure safety caused by the cracking, currently regular maintenance and external filling methods are mainly adopted. However, those methods of filling and repairing are time-consuming and labour-consuming. Moreover, the problems of whether the supplemented materials can be well connected and combined with the original materials, whether its strength and durability and other properties meet the requirements of structural safety after recombination, and the consumption of a great deal of manpower and materials have not been well resolved. Therefore, to deal with those problems, new techniques and methods need to be explored.

2.3.1 Introduction on smart material

Since the degradation of material has been considered as an inevitable process, and a large amount of infrastructure budgets have been spent on repairs, maintenance and the replacement of existing and new structures (For example, 35-45% in the UK, 50% in EU), which points to significant inadequacies in past practice and current design and construction techniques (Gardner et al. 2018). Therefore, intelligent materials is becoming one of the major trends in the development of building materials.

Researchers have gained the inspiration from biological systems and been developing materials which have the ability to adapt and respond to their environment, including those with autogenous and autonomic self-healing and self-repairing capabilities. This fundamental change in material design philosophy has resulted in the creation of a whole host of ‘smart’ materials, including self-healing concrete.

To better understand the problems encountered during the construction of concrete structures in the UK and the degree to which concrete cracking/damage is a major problem, the research to develop biomimetic approach to the healing of concrete is being undertaken in the United Kingdom as part of the multi-disciplinary research project, Resilient Materials for Life (RM4L), a collaborative research between Cardiff University, the Universities of Bath, Bradford and Cambridge (Jefferson et al. 2010; Joseph et al. 2010; Davies et al. 2015; Al-Tabbaa et al. 2018; Belie et al. 2018). The vision of RM4L project is really to initiate the concepts of self-sensing, self-diagnosing, self-immunisation and self-reporting capabilities into cementitious systems in order to develop truly biomimetic responses in our infrastructure materials and structures.

According to a market research conducted by Gardner et al. (2018) from the M4L (Materials for Life) project, it was indicated that the main problems experienced with concrete (both old and new construction) in projects on which the respondents had worked over the last 5 years are given in Figure 2-16 below:

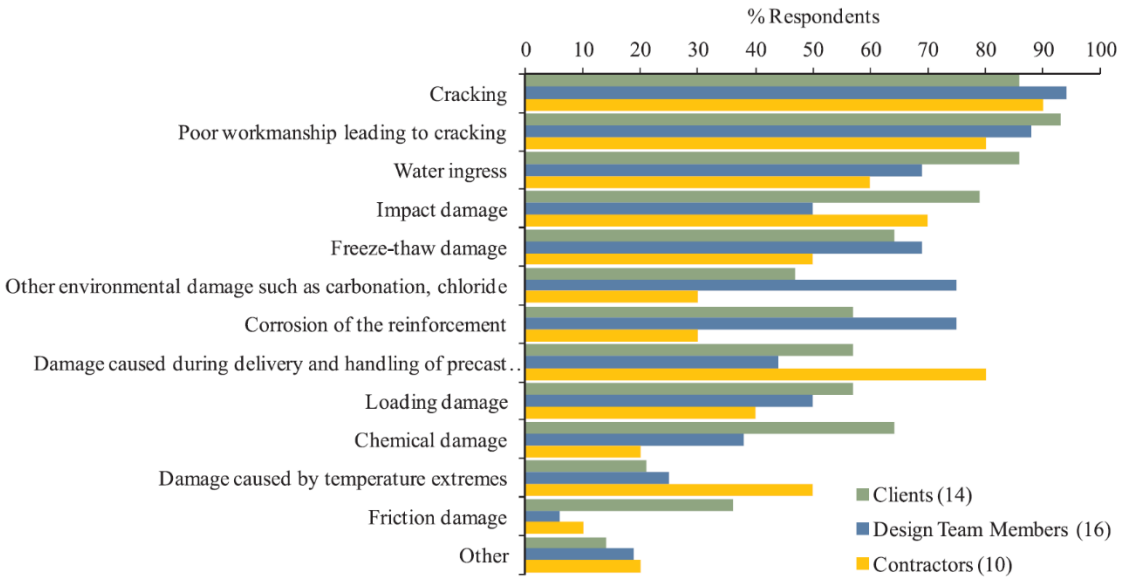

Figure 2-16. The main causes of damage in concrete structures (according to participants) (Gardner et al. 2018).

From the survey above, it can be seen that damage in the form of cracking in concrete structures is still the most common damage form and experienced by more clients, design team members and civil engineering contractors than any other problems. To find a solution to cracking of concrete, the research work of development of vascular flow networks based system and shape memory polymer based system has been undertaken at Cardiff University since 2006 (Joseph 2008; Jefferson et al. 2010; Gardner et al. 2013; Davies et al. 2015), and still under further investigation with new techniques and improvement developed both experimentally and numerically (Davies and Jefferson 2017; De Nardi et al. 2020; Selvarajoo et al. 2020). As a part of this programme, the ability to artificially create a cementitious material with autonomic healing properties has been examined.

The concept of ‘autonomic healing’ is based on the principle that crack formation in the cementitious matrix also causes fracture of the brittle adhesive-filled capsules or tubes embedded within the matrix. The contents of the capsules or tubes are thereby released into the crack plane where the agent is intended to cure and heal the damaged host matrix. This concept was originally proposed for cementitious materials by Dry (1994). Enhanced autogenic and autonomic healing techniques have been widely developed over the last few decades, and that involve the inclusion of mineral additions, crystalline admixtures, polymers, hollow fibres, encapsulation or microorganisms within structural elements (Davies et al. 2018; Al-Tabbaa et al. 2019). Generally autogenic healing refers to the natural process of crack repair that can occur in concrete in the presence of moisture and the absence of tensile stress, while autonomic healing in concrete refers to the self-healing mechanisms which are artificially triggered within the matrix through chemical or biological agents. These healing agents are usually supplied through encapsulation or vascular networks.

Selvarajoo (2020) discussed these related techniques in detail and summarised most of them developed for cementitious materials as given in Table 2-2.

Table 2-2. Summary of self-healing techniques developed for cementitious materials (Selvarajoo 2020)

Self-healing system	Self-healing technology	Ways and techniques	Healing processes
Autogenic healing	Supplementary cementitious materials	Inclusion of SCMs into the cementitious mix.	The presence of water allows the precipitation of $CaCO_3$ crystals.
	Microfibers (i.e. steel, PVA, PE)	Microfibres randomly dispersed throughout the cementitious mix.	Restricting crack widths so that autogenic healing can occur.
	Shape memory polymers (SMP)	PET strips or strands formed into tendons anchored within the cementitious matrix similar to post-tensioning. Heat activation via electric current resulting in shrinkage.	Compressive stresses help create contact between the crack surfaces and reduce crack widths which facilitates autogenic healing.
Autonomic healing	Microencapsulation	Microcapsules distributed into the cementitious matrix.	The rupture of the micro/macro capsules releases healing agent into the cementitious matrix.
	Macro encapsulation	Hollow tubes (glass or ceramic) embedded into the cementitious matrix. Usually preferred because more healing agent can be stored to achieve multiple healing.	
	Bacteria healing systems	Bacterial spores and nutrients included in the cementitious matrix.	Exposure of bacterial spores and nutrients to water promotes deposition of $CaCO_3$ crystals.
	Vascular healing systems	Hollow channels formed in the cementitious matrix as a delivery system for the healing agent into cracks. Potentially pressurised to allow multiple healing.	The healing agent flows into crack plane when cracking reaches flow channels. This system can be connected to an external reservoir to increase supply of healing agent.

2.3.2 Application of NDT&E technique in self-healing concrete

As an experimental NDT&E technique, AE has been widely applied for damage detection in infrastructure and civil engineering for decades . The advantages of AE lie in its sensitivity to damage growth and corresponding changes occurred inside material which makes it promising for detection and quantification of damage in real time. Therefore, people started to notice the potential application of AE along with other NDT&E techniques as monitoring tools in recently designed and developed innovative type of concrete.

Granger et al. (2007) conducted a three point bending test on a UHPC (Ultra-High-Performance Concrete) beam to investigate and quantify the autogenic healing phenomenon. The healing phenomenon was mainly highlighted by means of water

permeability tests while the AE monitoring was performed in order to show that the mechanical response is due to new crystals precipitating in the crack. In that study, AE energy analysis provides the insights about the cracking process of healed concrete and characterised the response to damage of the newly formed crystals and continuation of the crack propagation. Seo and Kim (2008) applied AE to characterise the fatigue damage and healing in Asphalt Concrete (AC). It has proved that the accumulative AE energy and AE counts can be used not only to assess the initiation and propagation of fatigue damage, but also to quantify the beneficial effect of rest period on the performance of AC. Shiotani et al. (2009) employed the ultrasonic pulse velocity (UPV) method to evaluate the repair effect after the injection of repair agent (grout) into boreholes on a 70-year old dam. Based on the time-of-flights measured at all wave propagation paths, a tomogram of the dam pier was created to localise the damaged area and those identified deteriorated dam structure were manually repaired. Grosse and Malm (2016) proposed that, since AE are difficult being applied at real-world structures, a combination of inspection and monitoring techniques, including ultrasonic (UT), vibrational testing and AE, is the most useful for the development of self-healing concrete. Feiteira et al. (2017) performed a study both from macro-scale (with AE and DIC) and micro-scale (with SEM) to assess the fitness of continuous monitoring methods to detect failure due to excessive strain on polymers bridging moving cracks in the context of self-healing concrete. In this study, the cumulative AE hits distribution were used to indicate the agent fracture as cracks reopen after healing. Minnebo et al. (2017) developed a vascular system as a self-healing concrete technique, carrying the healing agent. Both AE and DIC techniques were applied to investigate the mechanical behaviour of the vascular system. The AE cumulative hits distribution was used to assess the crack closure and reopening after healing, while the new cracks formed and cracks closure after healing were detected by AE source location method. Chen et al. (2021) investigated the damage and healing of cementitious materials based on fly ash (FA) under repeated loading. The effect of repeated loading on the self-healing performance is evaluated by AE analysis, water absorption measurement and SEM observation. Specifically the AE features, such as

number of hits, signal strength, amplitude and cumulative energy, are extensively discussed for assessing the healing efficiency.

In the past decade, there are a series of studies conducted in Vrije Universiteit Brussel and Magnel Laboratory for Concrete Research (Van Tittelboom et al. 2016) in Ghent University. Table 2-3 below has provided an overview of those scientific work focusing on the application of AE along with other NDT&E techniques on assessment of damage and autonomous repair on recently developed self-healing concrete.

Table 2-3. An overview of investigation of application of AE on self-healing concrete

Authors and publication time	Experiment scale	NDT&E applied	AE monitoring tool and highlights of results
(Van Tittelboom et al. 2012)	Small	AE	AE hits energy analysis detects glass capsules rupture as crack propagates
(Tsangouri et al. 2013)	Small	AE, DIC	AE hits features (i.e., energy, duration) analysis localizes in space and in time capsule breakage events; Source localization applied to detect the area where healing agent is released
(De Belie et al. 2015)	Real	AE, DIC, UPV	AE hits energy analysis detects healing activation in large-scale concrete beams
(Van Tittelboom et al. 2015)	Small	AE, DIC, X-ray radiography	AE hits energy analysis detects healing activation in concrete where multiple cracks form and interact after healing
(Van Tittelboom et al. 2016)	Real	AE, DIC, X-ray tomography, fluorescent light microscopy	AE hits energy analysis detects healing activation in large-scale concrete beams
(Karaiskos et al. 2016)	Real	AE, DIC, UPV	AE hits energy analysis detects healing activation in large-scale concrete beams
(Tsangouri et al. 2016)	Small	AE, AU, vibrational testing	Source localization applied to assess AE accuracy in presence of cracks and accuracy restoration after healing
(Tsangouri et al. 2019)	Real	AE, Tomography, UPV;	AE monitoring of high energy burst signals proving effective healing occurs locally

Although the application of AE and other NDT&E methods on concrete structures has a long history since the very beginning, its application on the recently developed

concrete technology, namely the autonomously healed and repaired concrete also shows great potentials as a promising tool of monitoring. It is beneficial to have the capabilities of tracking the location and scale as cracks to be occurred and healed in real time, which will be helpful to realise a higher efficiency and accuracy of self-triggering on the development of self-healing techniques.

2.4 Common AE signal processing methods

Signal processing is the last and indispensable link of AE detection technology, which plays the most important role in obtaining the characteristics of AE sources. As mentioned previously already, presently the signal processing methods of AE mainly include two ways: parameter analysis and waveform analysis. The parameter analysis uses features extracted from waveform as simplified characteristics to describe the AE signals, which is straightforward and efficient but will lose many details as well. The waveform analysis obtains the characteristics of AE signal by further processing the waveform in time domain, frequency domain or modal analysis to obtain signal characteristics. Figure 2-17 below shows a flow chart regarding the common approaches of processing AE data.

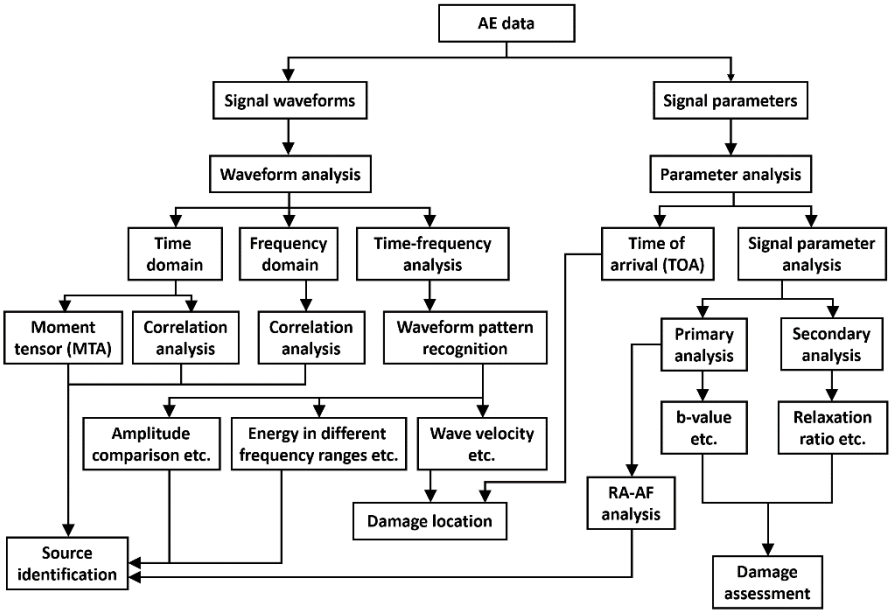

Figure 2-17. Common AE data processing approaches

2.4.1 Parameters based signal processing methods

Figure 2-18 below shows the typical AE features extracted from waveforms. Commonly used AE parameters include amplitude, energy, rise time, duration, ring counts, etc. In the early stage of AE technology development, due to the limitation of data acquisition, the hardware of AE instruments was unable to collect and save AE signals in real time and could only calculate the parameters, such as American ASME standards and national standards GB/T 181821 of China, etc. are all based on the parameter analysis to evaluate the testing objects.

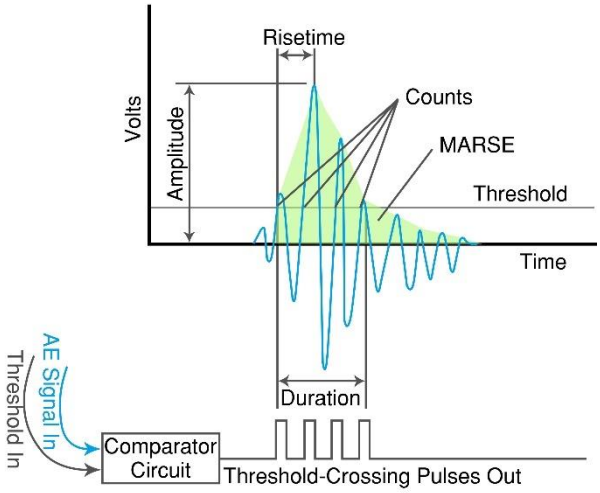

Figure 2-18. AE waveform features, figure reproduced from Pearson (2013)

Parameter analysis has been widely used in AE detection especially in the early stage of AE technology development. Daniel (1998) investigated the relationship between AE parameters and the initiation and propagation of fatigue cracks.

In the study of a tensile test on steel and welded steel specimens, Roberts and Talebzadeh (2003) found that the AE count rates has a reasonable correlation with fatigue crack propagation rate. The relationship between AE ring count and material properties in metallic material has also been studied by the scientific work from (Daniel 1998; Gong et al. 1998; Roberts et al. 1999; Talebzadeh and Roberts 2001). Li and Liu (2004) studied the AE signal characteristics of metal materials under high-frequency fatigue conditions and deduced the relationship between signal energy and the number

of fatigue cycles. Shiwa et al. (1996) and Tsamtsakis et al. (1998) performed periodic tensile tests on composite material specimens. It was found that the damage of composite materials was related to the event counts and energy of AE signals at different fatigue life stages.

Due to the advantages of simple calculation and clear physical meaning of AE parameter analysis, the standardization and commercialization of AE technology has been significantly promoted. However, it does not consider the specific details of AE waveform and a lot of useful information is lost. The main deficiencies of parameter analysis are as follows.

i. The parameter analysis is based on the assumption that the wave propagation velocity of AE signal is constant. However, the actual propagation velocity of AE wave in the medium is given in section 2.1.4.3 previously. For instance when it comes to the composite materials, the high anisotropy will result in a significant change of wave propagation velocity.

ii. It is difficult and challenging to establish a corresponding relationship between AE parameters and the mechanisms of AE sources. It is almost unlikely to directly use AE parameters to evaluate and analyse the AE source constitutionally.

iii. In the study of multi-dimensional AE signals using the parameter analysis method, it is also difficult to determine how to effectively select parameters to be applied and the correlation between them.

2.4.2 Waveforms based signal processing methods

The waveform analysis method captures AE source characteristics through time domain, frequency domain and time-frequency domain analysis of recorded and stored AE signals. At present, the spectrum analysis, time-frequency domain analysis and modal analysis are the most commonly used three kinds of waveform analysis methods.

The spectrum analysis method obtains the spectral characteristics of AE signal by

Fast Fourier Transform (FFT) and extracts the characteristics of AE signal in the frequency domain. Based on spectrum analysis, in-depth research on the extraction and processing of AE source information has been widely carried out by many researchers.

The Modal Acoustic Emission (MAE) provides a better theoretical background for AE testing, which is based on the plate wave theory (Surgeon and Wevers 1999) and aiming at the analysis of the physical mechanism of AE. In the work of fatigue damage investigation in aviation grade steel by Pullin and Holford et al. (2005), the location of the AE source can be determined through the analysis of the difference of arrival time of two dominant wave modes, symmetric (S_0) and asymmetric (A_0) in digitised AE signals, and the propagation orientation of fatigue crack can be determined by comparing the amplitude ratio of the two wave modes. Jiao et al. (2004) studied the dispersion characteristics of the modes of elastic waves propagating in thin plate through the application of wavelet transform.

Compared to the parameter analysis and the frequency spectrum analysis, the MAE has great advantages in the accuracy of source identification and source location, but to a great extent it is still in the laboratory research stage. The main reason is that the application of MAE requires researchers to be very familiar with the plate wave theory. Also the geometry of specimen and the attenuation characteristics of AE waves on the specimen will largely affect the processing accuracy of MAE as well.

Beyond those methods mentioned above, in recent years there are many time-frequency analyses methods that has emerged overcomes the shortcomings of the frequency domain analysis method based on Fast Fourier transform (FFT) and can extract the time domain and frequency domain characteristics of signal simultaneously. Specifically, those algorithms which are mainly related to SHM system have been developed to process data in association with time domain, frequency domain, or time-frequency domain, such as statistical time series (STS) models, Kalman Filter (KF), Fast Fourier transform (FFT), short-time FFT (SFFT), wavelet transform (WT), S-transform (ST), fast ST (FST), Hilbert transform (HT), Hilbert-Huang transform (HHT),

Multiple Signal Classification (MUSIC), Blind Source Separation (BSS), etc. Different features can be extracted by applying those methods on any vibration data acquired from a SHM system. The advantages and disadvantages of the models are summarized in the Table 2-4.

Table 2-4. Advantages and disadvantages of signal processing techniques (Chen et al. 2017)

Methods	Advantages	Disadvantages
STS	Linear model; Ease of implementation	Sensitive to noise; Only used for linear systems
KF	Good signal-noise ratio; Good estimation of change in time	Time consuming; Requires parameter calibration; Limited convergence speed and tracking accuracy
FFT	Nonlinear model; Model linear and nonlinear systems; Ease of implementation; Simplicity	Not applicable for complex system; Requires calibration to find model order; Sensitive to noise; Only frequency domain representation
MUSIC	High resolution in frequency domain; Closely-spaced modes can be estimated	Time consuming
SFFT	Ease of implementation; Time-frequency domain representation; Simplicity	Requires large quantity of samples; Limited time-frequency resolution; Not applicable for nonlinear and transient signals
WT	Good time-frequency resolution; Good signal-noise ratio; A mother wavelet can be used for different application	Spectral leakage; Requires several levels of decomposition; Mother wavelet will affect the result; ‘End effect’ is significant
ST	Good time-frequency resolution; Spectrum can be localized in time domain	Time consuming; Requires calibration
FST	Time saving; Good time-frequency resolution; Spectrum can be localized in time domain	The application in SHM systems need exploring
HHT	Good time-frequency resolution; High signal-to-noise ratio; Adaptive method; Ease of implementation	Mode-mixing; Requires calibration
BSS	Good signal-noise ratio; Good accuracy to separate frequency components	Require calibration Nonlinear and transient signals cannot be analysed adequately

Currently in the field of AE signal processing, wavelet transform (WT) is mainly used in signal denoising, feature extraction and AE source location. Yang and Zhou (2006) investigated the AE signal denoising method based on wavelet transform and

applied it to the AE signal in the tensile test of YSZ thermal insulation coating, which effectively removed the noise. Li et al. (1999) studied the real-time evaluation of tool wear based on wavelet analysis, which shows favourable reliability. Warren Liao et al. (2007) studied the identification method of grinding wheel wear based on wavelet transform and obtained a high recognition rate. Qi (2000) performed wavelet transform analysis on the AE signals generated during the fracture process of composite materials and extracted energy features for the identification of failure modes of specimens. Based on wavelet analysis, Staszewski and Holford (2001) realised the clustering of AE signals from the box girder of a bridge using the parameters extracted through orthogonal Daubechies wavelets. Loutas et al. (2006)conducted a quasi-static test on a centre-holed composite material and the damage state monitoring using wavelet transform was realised from collected AE signals.

2.5 Summary and main gaps declared

This chapter systematically discusses the research progress of AE technology and its extensive application in the past 70 years, including the existing research of both AE and other NDT&E techniques applied on the recently designed and developed innovative self-healing concrete. According to the review of literatures above, the main research gaps can be summarised and concluded as follows:

- In recent decades, with the development of modern signal processing techniques, the fast Fourier transform (FFT), wavelet analysis, Hilbert–Huang transform (HHT) and other techniques have been gradually applied to the field of AE signal processing and have achieved good results. The spectrum analysis is the most commonly used waveform analysis method in AE signal processing. Based on Fourier transform, the AE signal is converted from the time domain to the frequency domain. Through the study of the distribution characteristic extracted from the frequency domain of AE signal, the information of AE source can be reflected and highlighted. However, FFT is a method for overall transform, characterising the signal in either the time domain or the frequency domain. It is unable to determine when a certain frequency component appears and how it

changes from its frequency spectrum. Hence, it is mostly suitable for processing stationary signals. Usually AE, as one non-stationary signal, only the overall frequency characteristics of the signal can be obtained through spectrum analysis. Although the spectrum analysis of AE signals in early stage obtained part of the source characteristics, but the advantages of this analysis are not more prominent and obvious compared to the parameter-based analysis, especially for those materials like reinforced concrete. Therefore, to better obtain the non-stationary AE signal characteristics, it is necessary to introduce the time-frequency analysis using the joint function of time and frequency to represent the signal.

- The current AE source characterisation methods are mostly traditional statistical methods. The prerequisite is that there are large samples and fitted into the framework of the asymptotic theory (such as the RA-AF correlation analysis and other methods discussed in section2.2, 2.3 and 2.4). However, since the generation of AE signals is irreversible, it is unable to obtain a large amount of AE signals with exactly the same pattern. Therefore, the fundamental data set for the study of damage detection is always difficult to obtain. At the same time, the current AE source characterisation methods is aimed at single damage pattern recognition. In practice, multiple damage modes often occur at the same time. Therefore, it is necessary to study the AE source pattern recognition method that can simultaneously recognize multiple damage modes.

- AE, as one of the NDT&E techniques, the biggest advantage of AE lies in the monitoring of damage evolution in concrete without any extra invasion to the structures. However, due to the nature of cracking itself, it is important to remain such a monitoring process minimal destructive for the material when investigating the self-healing properties using AE and other NDT&E techniques. As discussed in section2.3.2, currently most of the methods used to evaluate the healing effectiveness are based on the evolution of parameters during the post-fracture process after healing occurred, which is against the ultimate goal of “self-healing” that enabling the materials to be able to adapt the environment and heal

themselves. Therefore, those factors above should be considered during the evaluation process to avoid ultimate destructive experimental investigation.

- When the NDT&E techniques are introduced in the assessment process of self-healing performance of the newly designed and developed types of self-healing concrete, there are still plenty of behaviours and properties needed to be studied, such as the mechanism to protect the healing agent with different encapsulation materials and techniques, the properties of the different sequestered healing agent, the distribution of the healing mechanism, triggering of the healing mechanism, and the healing efficiency or healing performance.

- Main evaluation indices of AU and UPV techniques used for evaluating the self-healing evolution properties are the signal transmission time and P wave velocities. However, since the P wave velocities is dependent on the apparent velocities calculated based on the signal transmission time, essentially only one index is critical to be measured in this evaluation method. Therefore, other independent indices should be investigated and considered toward future practical application.

Chapter 3 Acoustic Emission Characteristics of Different Basic Failure Modes in Plain Concrete Members

Characterisation of the failure mode in construction materials is always of great importance, particularly during the fracture process of any concrete structure, because a sequence of fracturing modes is generally followed (Grosse and Finck 2006; Ohno and Ohtsu 2010; Aggelis 2011; Aggelis et al. 2013). Therefore, characterisation of the dominant fracture mode is useful for identification of damage stage and indication of existing risks to make any necessary prevention or treatment measures.

In the early stage of AE technology development, there was a high level of interest in the mechanism of AE source, and many theoretical and experimental studies were conducted. However, these studies were limited to laboratory studies. In practical structure tests, researchers found that the AE phenomenon is more complex. Despite the wide application of the AE technique in the civil engineering field, there is still a need for robust theoretical support in terms of both plain and reinforced concrete structures.

One of the key points for successful application of AE technology depends on the ability to identify the relationship between the AE event and the source. Therefore, AE source location and identification has become the focus and key aspect of AE study. Nevertheless, it is not easy to establish such connections under different materials and structures. It requires abundant in-depth studies of the mechanism of different AE sources.

With respect to fracture mode identification and characterisation, the MTA has been well developed and successfully applied in lab-scale experiments (Shigeishi and Ohtsu 2001). This method was initially established under the theoretical framework and has broad application prospects in the very beginning. It can determine the damage location, fracture types and the direction of crack movement (i.e., the fault plane in seismology). A case study of this method is conducted in Chapter 4 with a comprehensive description. Nevertheless, the use of MTA is non-trivial when in real

structures due to many practical limitations. In reality, in order to cover as much volume of the structure as possible, all sensors are distributed in relatively long distance which enables the detection and evaluation on the whole scale. And the most important is to get sufficient information from AE signal, each event should be recorded by at least six individual sensors as all the directionality of the AE waves can be provided to determine all the components of moment tensor. Therefore, when using sensors of separation distances of several meters (Shiotani 2006; Shiotani Tomoki et al. 2009), it is highly unlikely to record the transient waves of the same event with the required number of sensors due to inherent material attenuation.

To accurately characterize the damage condition in concrete structures is almost impossible simply because not only the complexity of fracture mode, but also related to different loading patterns, propagation rates, material properties, environment of surroundings, etc. As most large concrete structures contain a large number of cracks either from construction or operation load, it is realized that to precisely describe the damage status and deal with the characterisation in one absolute form is highly unlikely. However, the information on the general condition plays an important role. It is understood and favourable that if information provided by any NDT&E monitoring can be used as a basis for further maintenance procedure that potentially can improve the safety of the structure and extend the service life, even an approximate evaluation can be beneficial.

For concrete components, the elemental damage modes generally include tensile, compression, shear, torsion and bending. For reinforced concrete members, the elemental damage modes include concrete cracking, failure of steel reinforcement, bond slip failure of rebar and concrete, etc. In this chapter, in order to form a systematic research method that has a comparatively clear signal processing approach and AE testing technique from elemental damage to complex damage, several analytical methods and experiments were designed to identify the corresponding AE characteristics from those different elemental damage modes.

3.1 Introduction

The fracturing behaviour of materials can be non-destructively monitored by the AE technique using sensors that detect the transient elastic waves after any crack propagation event. In addition to information relative to the total activity and the location of the cracks, certain waveform features supply detailed information on the type of cracking (Aggelis et al. 2012). The waveform of the emitted AE signal depends on the relative motion of the crack sides and therefore carries information on the mode of cracks.

The information that can be drawn concerns the crack location and the total activity, which is related to the number and the nature of cracking events (Jang and Kishi 2006; Carpinteri et al. 2010). Detailed study of qualitative parameters of the received waveforms leads to characterisation of the fracture process and sustained damage assessment (Ohtsu and Watanabe 2001; Elaqra et al. 2007).

The characterisation of AE signals generally depends on the source and, specifically, the intensity and fracturing mode. Therefore, key waveform features like amplitude, energy and frequency carry plentiful information from the damage mode and the fracture process. In general, the characterisation of cracks as to their mode provides a warning before failure. The received waveforms depend on the cracking mode, as well as on the orientation of the crack relative to the receivers and the distance between the cracking source and the sensor.

Certain AE features have been successfully correlated to the fracture process. For example, like the maximum amplitude of waveform as shown in Figure 3-1(a), it depends on the intensity of the cracking source. From the signal frequency spectrum as shown in Figure 3-1(b), the frequency with the maximum magnitude after fast Fourier transformation (FFT) of the waveform can be easily identified (Aggelis and Matikas 2012).

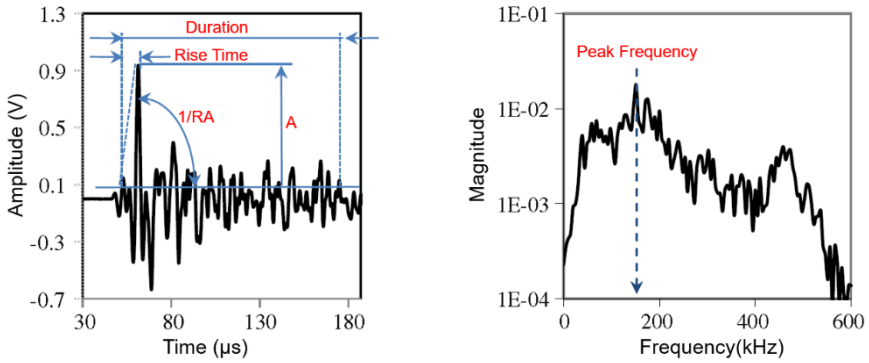

(a) (b)

Figure 3-1. (a)Main parameters from a typical AE signal; (b)A typical FFT spectrum of AE signal.

The connection between the mode of crack and the waves recorded depends on different factors like geometric conditions, relative orientation and propagation distance (Aggelis et al. 2012). When a cracking event occurs, all possible wave modes (longitudinal, transverse and Rayleigh if the crack is surface breaking as described in section 2.1.4) are excited. A tensile cracking incident excites most of the energy in the form of longitudinal waves. Therefore, most of the energy arrives in the initial part of the acquired waveform since longitudinal waves are the fastest type. When shear cracking occurs, the percentage of energy emitted in the shear wave mode is increased, resulting in a delay of the main energy cycles of the waveform (Ohtsu 2015).

The AE waveform parameters, which have been correlated with the cracking mode, are mainly the rise time and peak amplitude, used to calculate the rise angle 'RA value'. This descriptor is the duration of the first, rising part of the waveform (rise time, RT) over amplitude measured in $\mu s/V$, and has been shown to be very sensitive to the fracture mode(Soulioti et al. 2009; Aggelis 2011; Lu et al. 2011). Frequency parameters like the 'Average Frequency', F_a, are another important descriptor. The average frequency is defined as the ratio of threshold crossing (AE counts) divided by the duration time of signal, measured in kHz. Many studies have shown that tensile cracks lead to AE with higher frequency characteristics and lower RA values than shear cracks(Aggelis et al. 2009; Soulioti et al. 2009; Ohno and Ohtsu 2010; Aggelis 2011; Lu et al. 2011).

As shown in Figure 3-2, the fracture mode can be characterized by the shape of the AE waveforms. Low rise time values and high frequency are typical of tensile crack propagations that include opposing movement of the crack sides (Mode I); whereas shear cracks usually result in longer waveforms, with longer rise times and lower frequency (Mode II) (Aggelis and Matikas 2012).

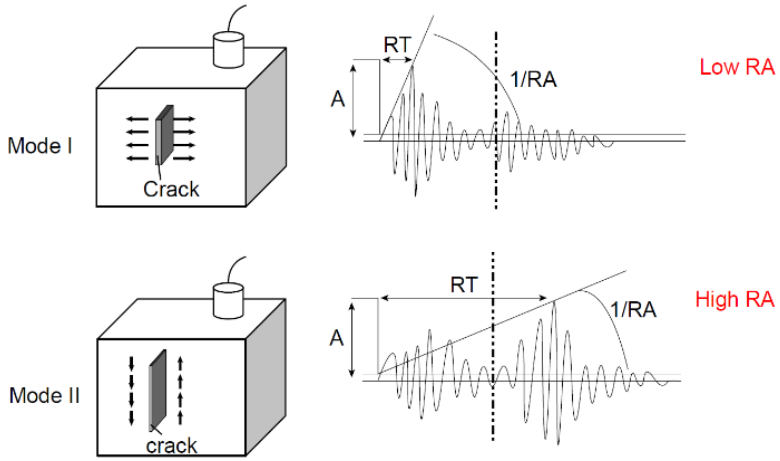

Figure 3-2. Typical waveforms of tensile and shear events (Aggelis and Matikas 2012)

As mentioned previously in section 2.4, different signal processing algorithms for time-frequency decomposition have different time-frequency resolution, accuracy, signal-to-noise ratio, and computational resource utilization characteristics (Amezquita-Sanchez and Adeli 2016). So the knowledge of characteristics of each algorithm is essential and the selection of the appropriate or convenient methods is critical to process data as well.

Huang et al. (1998) introduced the Hilbert Huang transform (HHT) as an adaptive signal processing method capable of analysing stationary, non-stationary, and transient signals. The HHT is based on two-steps: an empirical mode decomposition (EMD) followed by the Hilbert spectral transform (HT). EMD decomposes any time series data into a set of band-limited quasi-stationary functions, called Intrinsic Mode Functions (IMF). Next, the Hilbert spectral transform is applied to each IMF to obtain its amplitude and phase angle. Figure 3-3(a) shows a synthetic signal composed of two sinusoidal waves of frequency 10 Hz and 30Hz with a sampling frequency of

100Hz within a time period of 3s. Figure 3-3(b) shows the decomposition of the two constituent sinusoidal waves in their IMFs. Figure 3-3(c) displays the application of Hilbert transform to IMFs showing the evolution of the two sinusoidal waves over time. Nowadays HHT has been applied in different fields such as biomedical engineering (Zhao and Wang 2007), mechanical engineering (Antonino-Daviu et al. 2009), and earthquake engineering (Chen et al. 2010).

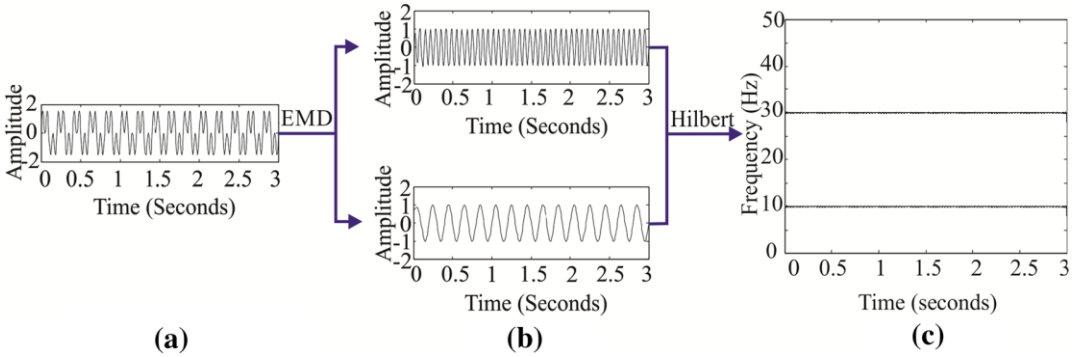

Figure 3-3. HHT procedure: (a) a synthetic signal composed of two sinusoidal waves of frequency 10 Hz and 30 Hz, (b) decomposition of the two sinusoidal waves in their IMFs, (c) application of Hilbert transform to IMFs

3.2 AE characteristics of a plain concrete beam under pure bending condition

Cracking is the most common and likely occurring damage of concrete structure which occurs almost throughout the whole failure process of concrete members (Karihaloo 1995). Normally all kinds of failure and damage of any concrete begin with cracking. Nevertheless, some minor cracks do not affect the bearing capacity of structure, while some severe cracks are often a sign of ultimate structural failure. Therefore, the study of AE on concrete cracking is not only the basis of AE study of complex failure, but also a fundamental study for AE quantitative research, because the wide differences in the degree of cracking is a common problem faced in practical engineering.

3.2.1 Specimen preparation and experiment setup

To make sure that the middle section of the testing beam is under a simple stress state of pure bending, and in order to avoid the local influence of loading area, the

specimen is tested under the three-point bending arrangement. The concrete mix of the specimen in this experiment is shown in Table 3-1. And the compressive and tensile strengths of cube and cylinder results of cube and cylinder specimens are shown in Table 3-2. The test is conducted one month after the concrete specimen is fully cured.

Table 3-1. Proportions of concrete mix

Grade/type	W/C Ratio	Cement	Water	Fine Aggregates (0-4mm)	Coarse Aggregates (4-10mm)
Origin	/	Portland-limestone cement CEM II/A-L 32,5R	Normal tap water	Crushed marine sand with limestone	Crushed limestone
C40 mix ratio	0.46	1	0.46	1.93	2.25
Concrete (kg/m^3)	/	470 kg/m^3	216.2 kg/m^3	907.1 kg/m^3	1057.5 kg/m^3

Table 3-2. Concrete strengths cured for 28 days

Cube No.	Cube compressive strength f_c(MPa)	Average (MPa)	CoV%	Cylinder No.	Cylinder splitting strength (MPa)	Average (MPa)	CoV%
1	48.9	47.6	2.4%	1	3.5	3.7	5.6%
2	46.7			2	3.8		
3	47.2			3	3.9		

The dimensions of the beam are 100mm*150mm*1500mm and the specimen setup is shown in Figure 3-4. A 12.5mm deep notch was sawn at the centre bottom of the specimen. The integrity of reinforced concrete component largely depends on the interaction between reinforcement and concrete matrix. So the bonding failure (i.e., interface debonding and slippage, etc.) is also an important form of failure. To focus on the study of AE events only coming from the concrete cracking and avoid any from the bond-slip failure, only one single steel bar (10mm) is positioned on the top of the beam to ensure that the beam won't be split apart after failure. The maximum particle size of coarse aggregate is controlled to be less than 10mm, which is smaller than the wavelength of the main AE wave in concrete, therefore the influence of the inhomogeneity of concrete regarding wave propagation is negligible.

To ensure the accuracy of frequency characteristics, four R15I-AST sensors are used in the test as the sensitive operating frequency range are from 70kHz to 200kHz,

which can cover the most main frequency ranges of AE waves in concrete. Four sensors are attached on the beam with the couplant grease used as the coupling from Electrolube company. The distance between two sensors of each pair above and below is 270mm as shown in Figure 3-4. The Digital Image Correlation (DIC) system are employed to monitor the beam and track the cracks development during loading through the whole test.

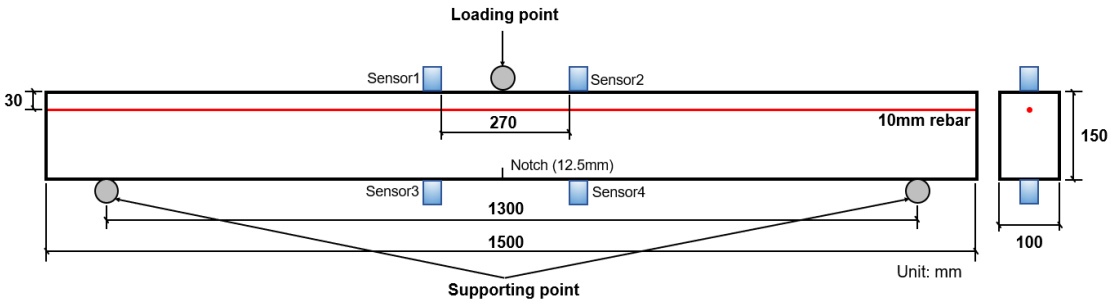

Figure 3-4. Specimen setup and dimensions for 3-point bending test

3.2.2 Testing methods and results

The experimental setup is shown in Figure 3-5. A wooden pad is placed between the roller at the loading point and beam for load transfer to prevent local failure of the beam caused by stress concentration.

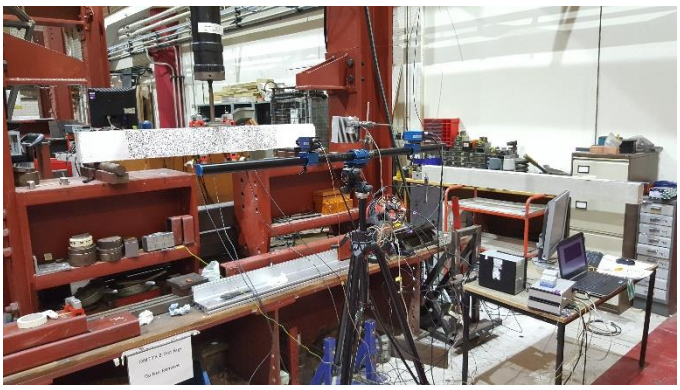

Figure 3-5. Experimental setup for four-point bending test on concrete beam

The beam is loaded incrementally with a feedback loop controlling the central displacement rate of 0.005mm/s until failure. As the experiment proceeds, the number of AE signals appears continuously and shows a stable increasing trend as shown in Figure 3-6. The bar chart in the graph below shows the distribution of energy over time. When the load reaches 3.123kN, the beam is failed and a large number of AE signals

are emitted. Meanwhile the energy released also reaches the maximum.

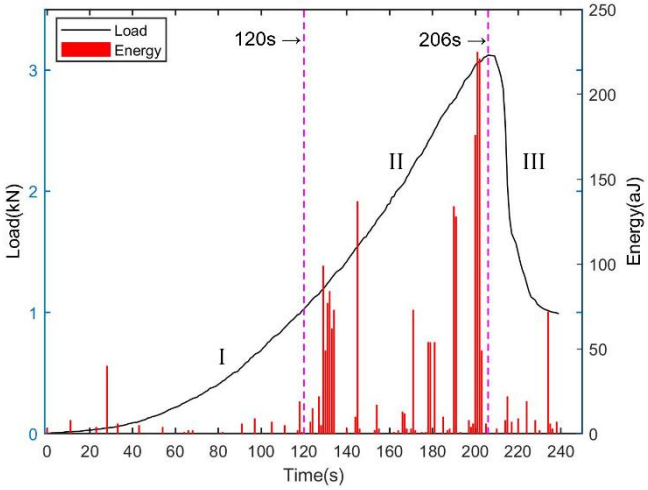

Figure 3-6. Loading curve with the distribution of AE energy in bending test (Energy refers to Absolute Energy, the time integral of the square of the signal voltage expressed in aJ (attojoules))

The three DIC figures (a), (b), and (c) in Figure 3-7 correspond to the moments selected from stage I, II, and III marked in Figure 3-6.

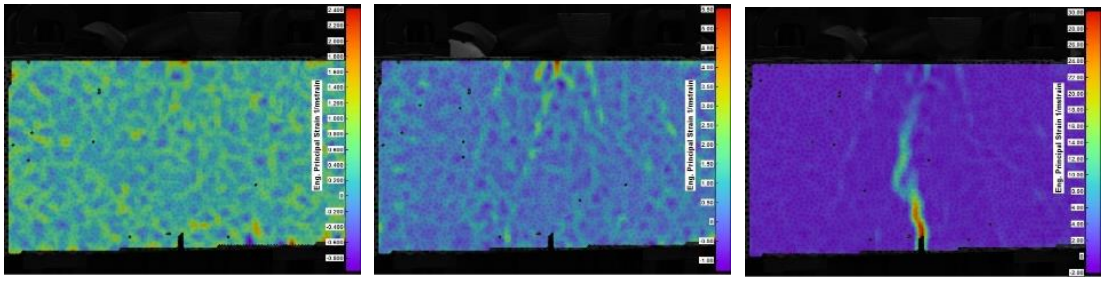

(a) (b) (c)

Figure 3-7. Evolution of crack expressed by the change of horizontal strain in DIC (a)Initial damage; (b)Formation and gathering of micro-crack; (c)After failure.

Figure 3-8. Final failure mode of the specimen in bending test

3.2.3 Analysis and discussion

The difficulties of processing data from a concrete beam test lie in the large quantity of signals and complexity of different waveforms. Therefore, signal screening and denoising of signals collected from the test are essential and necessary for further data processing and analysis.

3.2.3.1 HHT Analysis and Time-Frequency Characteristics of AE Signals

3.2.3.1.1 Screening of AE signals for waveform analysis

There is always a massive number of AE signals collected in the actual damage monitoring process of any concrete components. Therefore, it is neither realistic nor necessary to use waveform-based analysis for all the signals. In this study, the parameter analysis method is used to screen the AE signals based on the energy (or other similar parameters), and representative signals would be selected for further waveform analysis. Since the energy of different AE events may differ by several orders of magnitude, an index called 'Energy Magnitude' using the natural logarithm of energy is introduced which is defined by Gu et al. (2019) as a parameter screening tool, namely:

$$Energy\ Magnitude = \log(E) \tag{3.1}$$

Where 'E' is the energy from an AE signal acquired by the acquisition system. This concept originates from the concept 'Earthquake Magnitude' in seismology, similar to the concept 'Richter magnitude scale' initially developed by Charles F. Richter in 1935 (Richter 1935; Gutenberg and Richter 1942; Kanamori 1983), but it is intrinsically different. The Earthquake Magnitude is a measure of the strength of earthquakes in seismology, and it depends on the scale of seismic waves, whereas the Energy Magnitude here depends on the amount of energy released of the AE signal or event. This can be used to perform a preliminary classification of AE signals.

In this bending test, the AE event with the highest energy magnitude occurred at 203s, which is at the time of the ultimate failure. Its Energy Magnitude has reached 2.42. However, 81.37% of the events have Energy Magnitude less than 1.0 as shown

in Figure 3-9. Therefore, it can be seen that the Energy Magnitude of most signals is at a relatively low level.

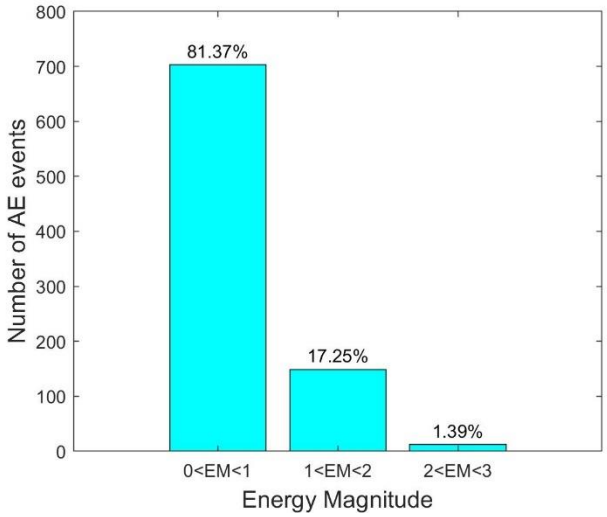

Figure 3-9. Number of AE events in different Energy Magnitude levels of bending test

3.2.3.1.2 Waveform analysis based on Hilbert-Huang Transform

After some typical AE signals are selected from different stages or different clusters, then the Empirical Mode Decomposition (EMD) is proceeded to the waveforms and then the Intrinsic Mode Functions (IMF) of each order are obtained which help to identify the physical mechanism of AE signal. Then the Hilbert spectrum reflecting the time-frequency distribution characteristics of the signal can be displayed through the Hilbert transform.

The typical AE signals selected from above three stages (shown in Figure 3-6) are analysed, which are signals from initial damage (stage I), formation of micro-cracks and macro-crack (stage II) and unstable crack development and propagation (stage III). And then the first five orders of IMF and three-dimensional time-frequency distribution of each signal are analysed and discussed.

As shown in Figure 3-10, the signals are emitted from point source, normally containing multiple point sources result from material degradation, as they all have the features like low energy and periodic reflection waves. For multiple point source signals, the superposition of these periodic reflections often results in a periodic wave packet.

In addition, the experimental signals are more likely to be influenced by other factors, so the waveform could be more complex. However, the characteristic of periodic wave packet in each IMF can be observed through EMD decomposition.

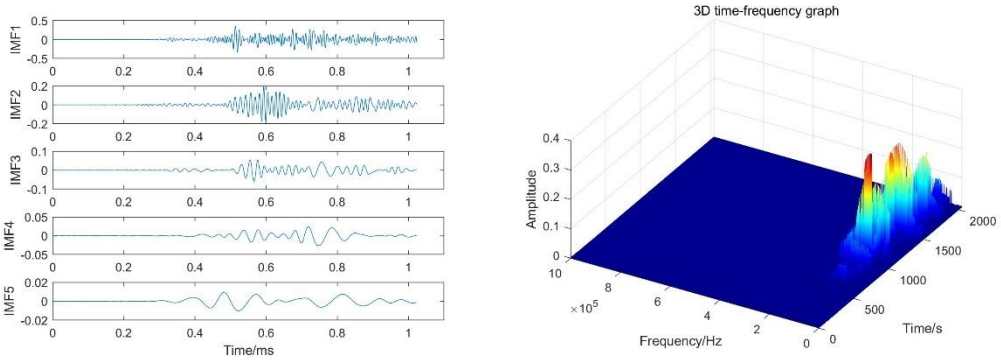

(a) Signal No.29

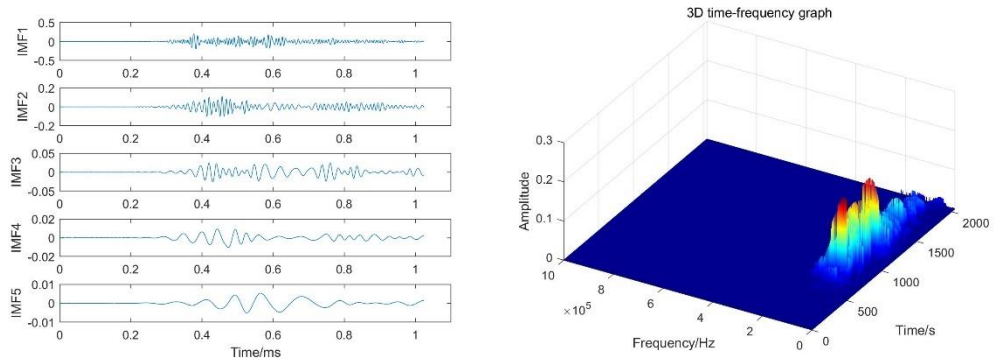

(b) Signal No.36

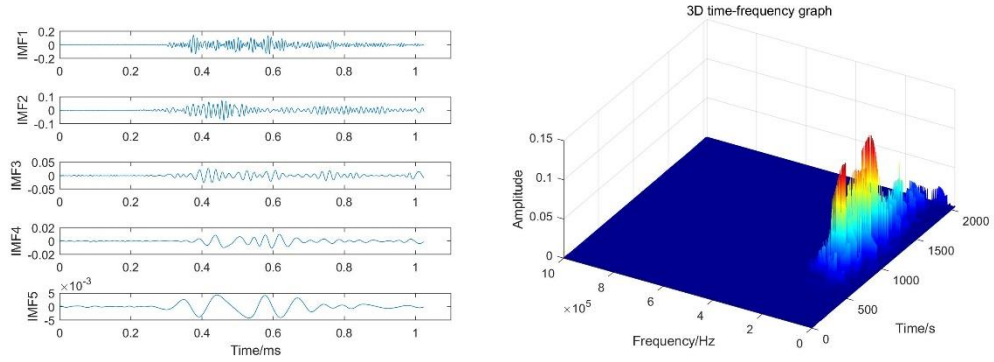

(c) Signal No.25

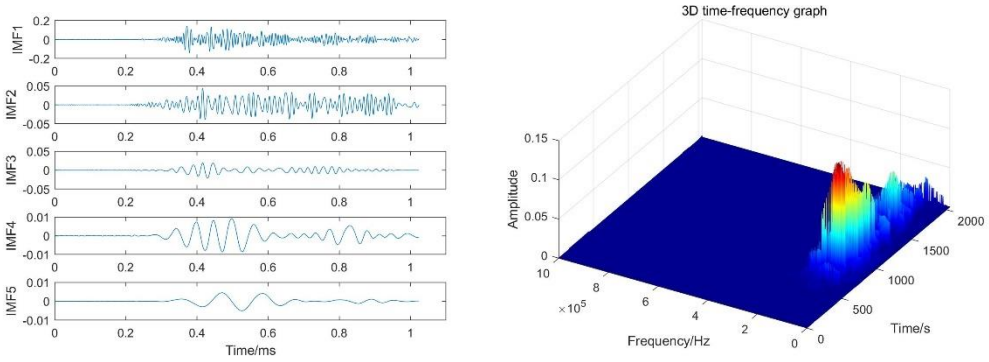

(d) Signal No.17

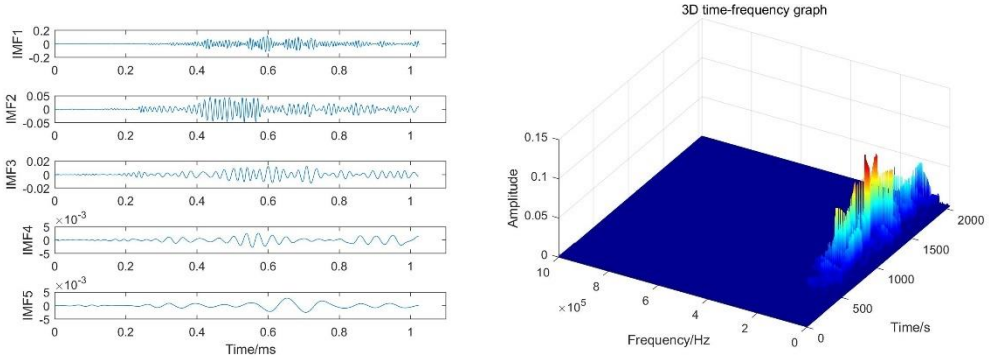

(e) Signal No.30

Figure 3-10. The first five IMFs(left) and HHT spectrum(right) of typical AE signals from initial damage

Signals shown in Figure 3-11 are from the formation of micro-crack and macro-crack stage. From the first and second order IMFs, it can be seen that several successive wave packets show that the sources are also from multi-point excitation, while the signals with higher frequency components with no attenuation can be regarded as noise. Nevertheless, it is not a system noise as it doesn't appear in all signals. So that noise could be coming from local rupture and crushing of concrete beam. The second-order IMF revealed the main characteristics of the signal, most of AE come from the continuous source emission when concrete cracking. Due to the inhomogeneity and other particular properties of concrete, cracks may occur in many places during loading and that also makes the obtained signals more complex.

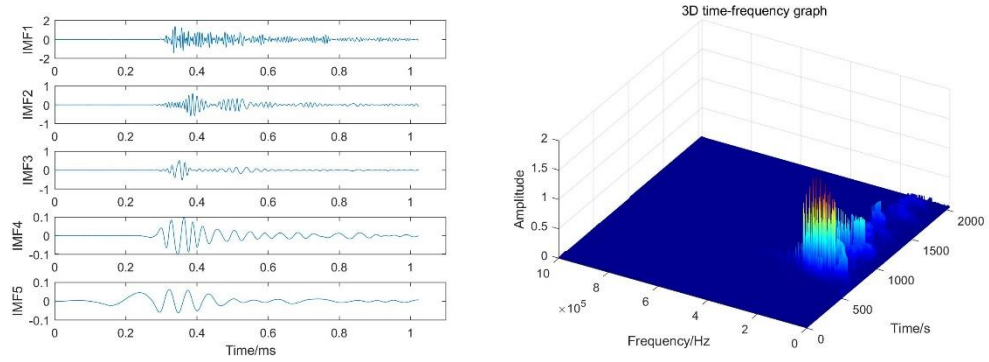

(a) Signal No.505

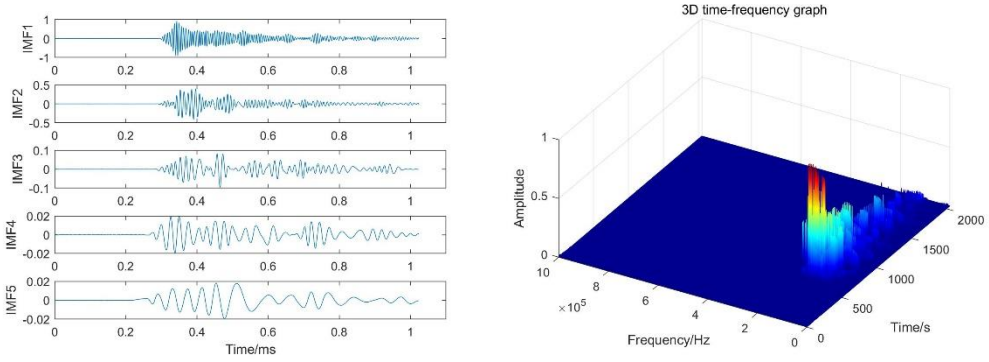

(b) Signal No.508

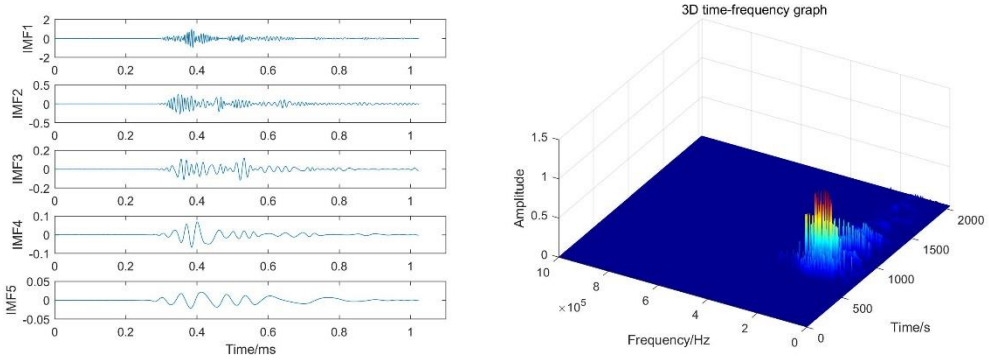

(c) Signal No.376

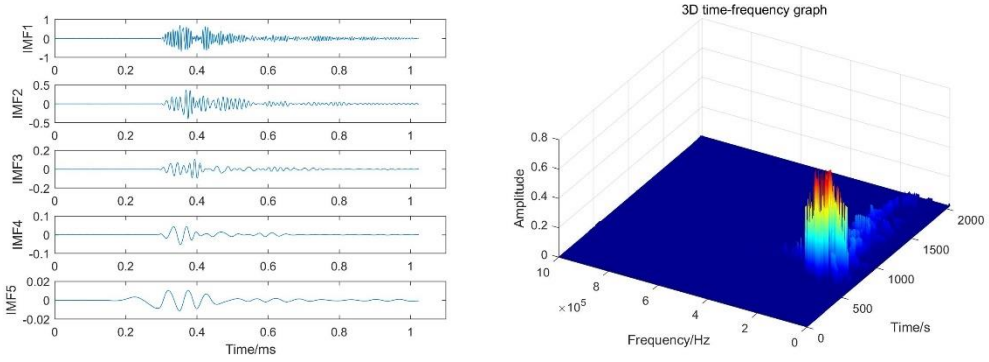

(d) Signal No.405

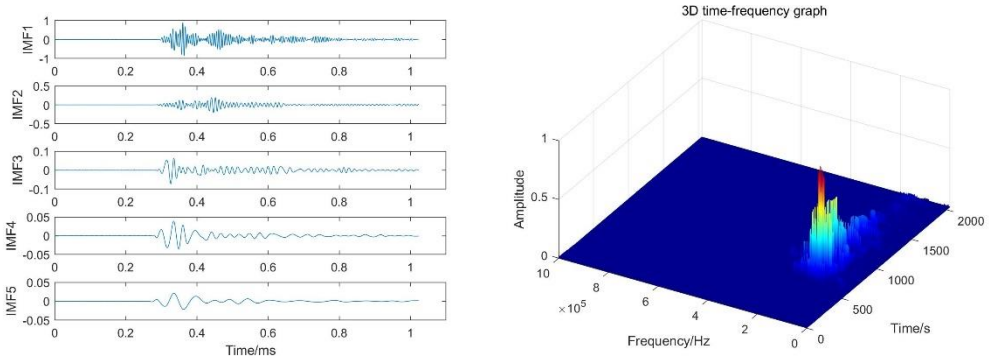

(e) Signal No.446

Figure 3-11. The first five IMFs (left) and HHT spectrum (left) of typical AE signals from the process of formation of micro-cracks and macro-crack

Signals shown in Figure 3-12 are from the unstable crack development and propagation stage. Those signals have shown similar characteristic as they all have a relatively long duration and waveforms in the time domain are similar to the micro-crack and macro-crack formation stage shown in Figure 3-11, but with higher energy and the envelope of the wave in the IMF is less regular than the signals from growth of small cracks.

This shows that those two kinds of signals have the same essence of source (both from the cracking due to tension in a form of line pattern), but the energy released is different. The multi-signal superposition produced by the larger line source cracking, which makes the waveform more complicated.

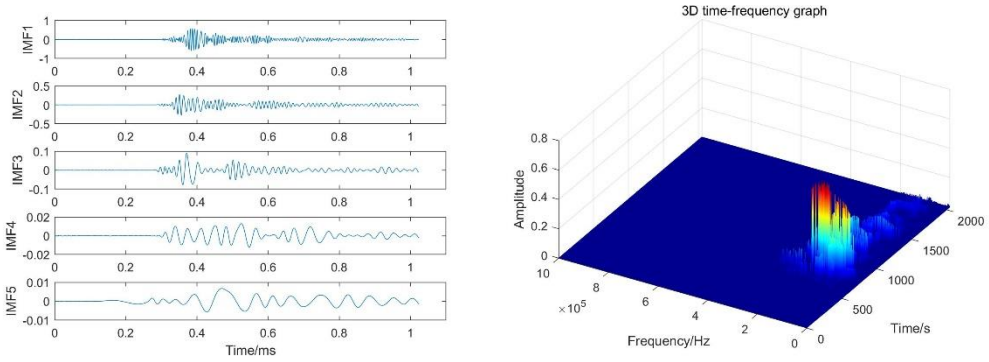

(a) Signal No.565

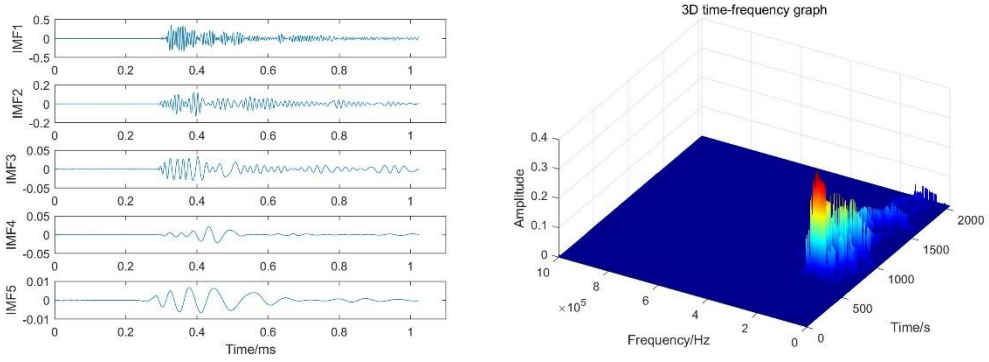

(b) Signal No.567

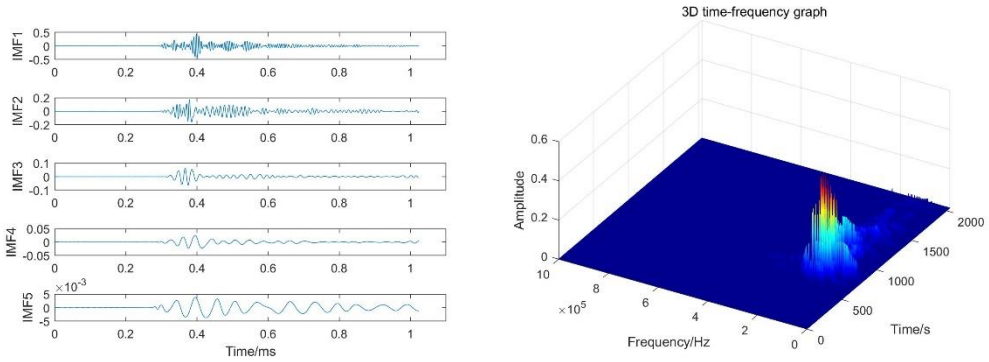

(c) Signal No.584

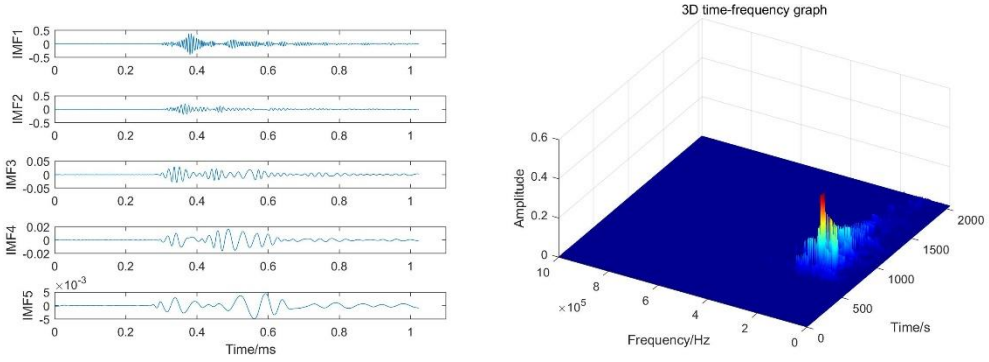

(d) Signal No.583

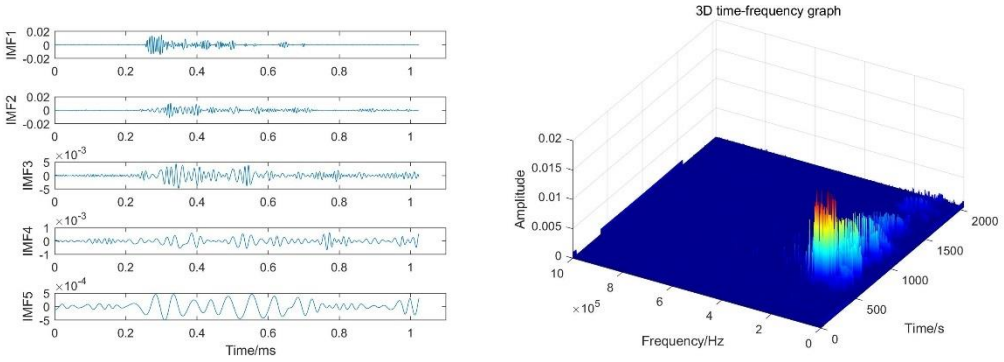

(e) Signal No.593

Figure 3-12. The first five IMFs(left) and HHT spectrum(left) of typical AE signals from the stage of unstable crack development and propagation

3.2.3.2 Maximum amplitude and characteristic instantaneous frequency of Intrinsic mode

Essentially the Energy Magnitude can actually reflect the amount of energy released by an AE event. A severe AE event may contain several AE signals. Generally the signal with the largest energy is more likely to accurately reflect the damage state of this AE event, while other signals could come from the subsequent activities or boundary reflection of the event. A single AE signal may contain multiple different source mechanisms. It can be decomposed into several IMFs by EMD decomposition, and the IMF with the highest energy can be regarded as the main source which is helpful to indicate the corresponding source characteristics.

For the convenience of comparison, two concepts are defined in this study as the energy and frequency characteristics of each signal, which are the ‘Maximum Amplitude of Intrinsic Mode’ and its corresponding ‘Characteristic Instantaneous Frequency’.

For the signal with maximum energy in an AE event, the maximum amplitude of all IMF waveforms is defined as the Maximum Amplitude of the Intrinsic Mode, represented in A_{mi}, and the corresponding instantaneous frequency is defined as the Characteristic Instantaneous Frequency, represented in f_c.

The physical meaning of A_{mi} and f_c can be explained as follows: EMD

decomposition can decouple the multi-source hybrid phenomenon in the signal, and it decomposes the original signal into IMFs which have physical meanings. The IMF with the largest amplitude (or energy) reflects the main characteristics of the signal. Therefore, A_{mi} can reflect the amplitude information of the main source in the signal. Correspondingly, the instantaneous frequency f_c corresponding to A_{mi} can reflect the frequency characteristics of the main source of the signal. In that case, the analysis process can be simplified by adopting these two parameters which can reflect the most important sound source characteristics of the AE event while ignoring the secondary factors, such as interface reflection, secondary sound source and waveform distortion.

The analysis process of A_{mi} and f_c is shown in Figure 3-13. There are always thousands of AE signals collected during an experiment and it is impossible to carry out the above analysis for every single signal. Therefore, the Energy Magnitude can be applied as the criterion of first threshold for the selection of important signals for analysis. Secondly, select the signals with the largest energy (or amplitude) in each AE event for the next step of analysis. Then the waveform selected is analysed by HHT, including EMD decomposition and time-frequency transform, and finally a time-frequency distribution map reflecting the time-frequency characteristics is obtained. The Maximum Amplitude of Intrinsic Mode can be extracted from the time-frequency spectrum and the corresponding instantaneous frequency could be calculated, that is, A_{mi} and f_c. This method would be applied in subsequent studies.

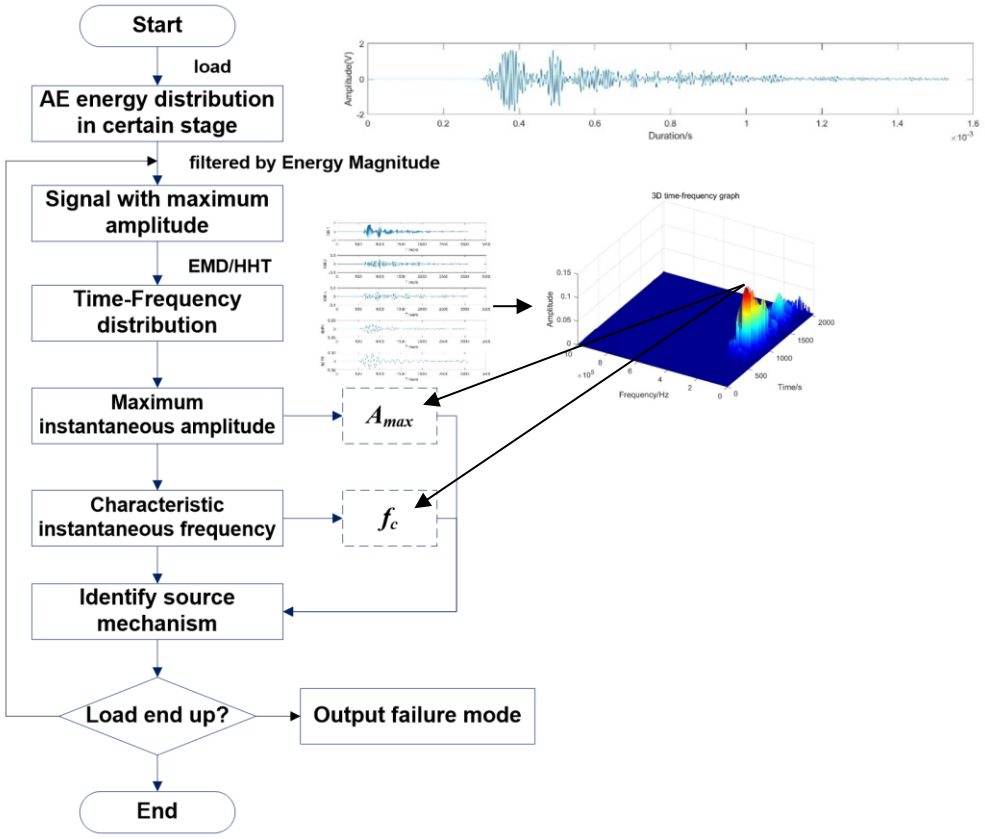

Figure 3-13. Analysis process for the extraction of A_{mi} and f_c

Table 3-3. Summary of A_{mi} and f_c of typical signals from 3 stages shown in Figure 3-10, Figure 3-11 and Figure 3-12

I. initial damage			II. formation of micro-cracks and macro-crack			III. unstable development and propagation of cracks		
No. of signal	A_{mi} (V)	f_c (kHz)	No. of signal	A_{mi} (V)	f_c (kHz)	No. of signal	A_{mi} (V)	f_c (kHz)
29	0.368	79.2	505	1.748	151.5	565	0.625	144.7
36	0.208	83.1	508	0.940	176.9	567	0.350	161.3
25	0.150	93.8	376	1.045	136.9	584	0.498	158.4
17	0.148	79.2	405	0.731	118.3	583	0.408	143.7
30	0.121	101.7	446	0.929	147.6	593	0.016	140.8

*The A_{mi} values listed in the table above are only from those selected signals, and different signals will have a certain range of variation.

It can be found from the data shown in Table 3-3, at the initial cracking stage, AE sources are mainly point source with relatively low amplitude. Nevertheless, the formation of micro-cracks and development of macro-cracks always exhibit higher amplitude as they all belong to boundary cracking. The development of macro-cracks

belongs to the continued expansion of existing cracks; therefore, the signal amplitude is slightly lower than previous stage. The frequency of signals in the initial damage stage is relatively low as the concrete is in a deterioration process. The stiffness of structure is continuously decreasing. The superposition of a large number of complex waveforms result in a higher instantaneous frequency and higher energy release.

3.3 AE characteristics of plain concrete beams under shearing condition

As a kind of quasi-brittle material, the failure mode is always ‘cracking’ regardless of any circumstances of stress states. Under certain conditions, the principal stress of structure may cause oblique cracking and result in final failure of concrete beams. This kind of failure and cracking mode always appear at the last moment when beam collapse and needs careful attention. Therefore, in this study, the plain concrete beams are used to explore the failure mode of structure under shearing condition and corresponding AE signal characteristics.

3.3.1 Specimen preparation and experiment setup

The short concrete beams for shearing test are shown in Figure 3-14. All material properties and parameters of specimens are the same as those of bending test in previous section. A 37.5mm deep notch was sawn at the centre line of both the top and bottom surface of the specimen to induce the position of cracking.

Under the stress state of the beam as shown in Figure 3-14(a) and the corresponding Shear Force Diagram (SFD) and Bending Moment Diagram (BMD) in Figure 3-14(b), the shearing force at the mid-span is at largest while the bending moment is zero. In that case, the notch tip, or cracking tip, is under a pure shear stress state.

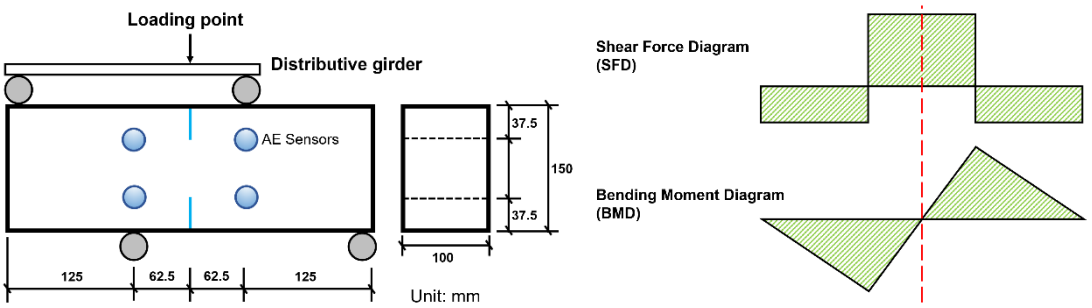

(a) (b)

Figure 3-14. Shearing test: (a) Specimen dimensions; (b) Shear Force Diagram (SFD) and Bending Moment Diagram (BMD)

The specimen is loaded on displacement-controlled based with a rate of 0.002mm/s. The loading process is monitored by four AE sensors attached on the beam surface as shown in Figure 3-15.

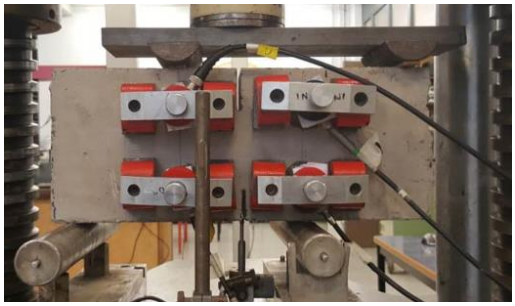

Figure 3-15. Experimental setup (from the back side)

3.3.2 Testing results

As the loading curve and the distribution of energy from the shearing test shown in Figure 3-16, it can be seen that the final destruction of beam is dominated by a sudden failure. Before the beam is failed, the load is increased gradually without any particular change, and so is the case with AE signal. Although there are a great number of AE signals generated during the loading process, the energy from final cracking signals basically occupy the absolute dominant position. When those cracking events occur, the energy they have carried immediately obliterate the energy carried by other previous AE signals, making other events almost negligible.

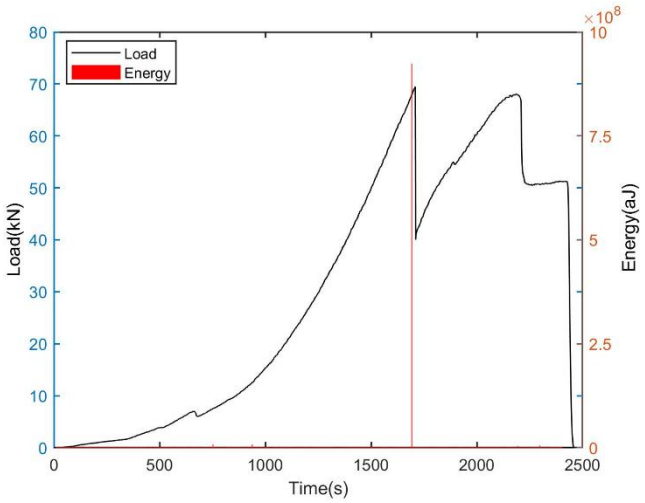

Figure 3-16. Loading curve with the distribution of AE energy in bending test

The tip of the notches is in a pure shear stress state as shown in Figure 3-17. Moreover, as concrete is a quasi-brittle material, its ultimate tensile strength is far weaker than the compression strength. Therefore, the ultimate failure mode of the beam is tensile failure as the maximum tensile stress at the crack tip is in a 45°degree direction. Thus, the initial crack starts from this direction and finally results in a sudden oblique cracking.

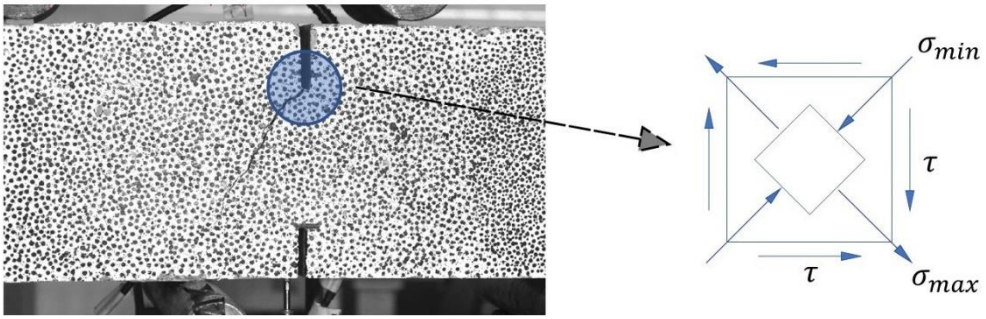

Figure 3-17. Failure mode of the shearing beam and the stress state of the crack tip

In the shearing test, the AE event with the highest Energy Magnitude (8.97) occurred at 1692s, which is around at the time of the ultimate failure. As shown in Figure 3-18, it can be seen that the number of AE events with Energy Magnitude between 2 and 3 is the largest, accounting for 40.19% of the total events. And the vast majority of events are at a relatively low Energy Magnitude level. 99.04% events have Energy Magnitude below 5. For the rest high Energy Magnitude (over 5) events, most of them occur at the time around the ultimate failure point and post-fracture stage.

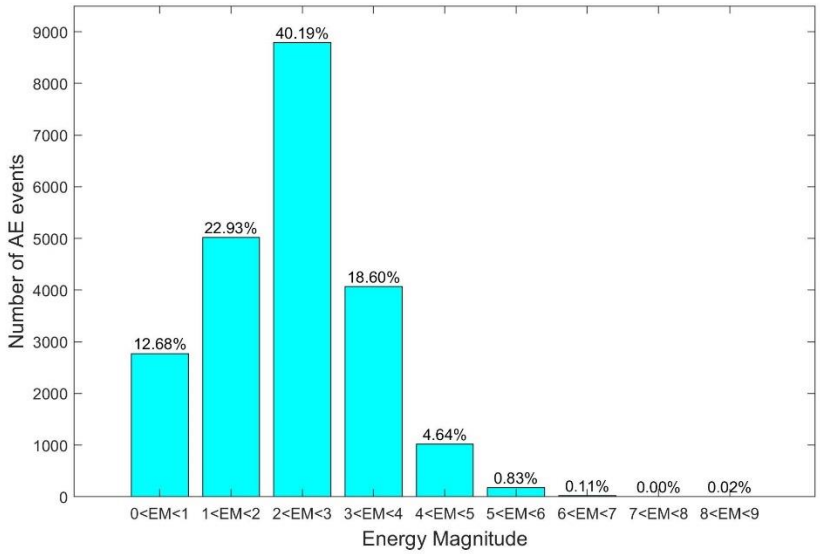

Figure 3-18. Number of AE events in different EM levels of shearing test

The events during the failure moment contain many AE signals and most of them possess high energy. Through further analysis on these events, it can be found that these signals basically all have the characteristics of wide frequency band and relatively long duration. The HHT spectrums of the AE signal with largest amplitude and following signals are shown in Figure 3-19.

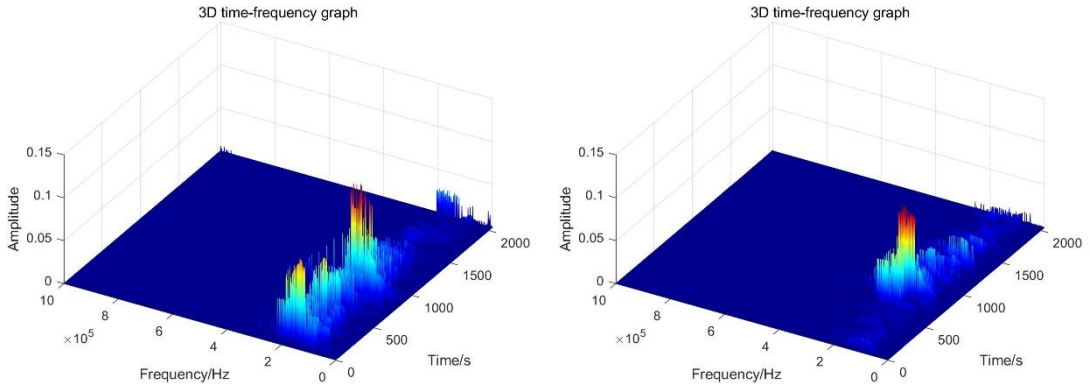

(a) (b)

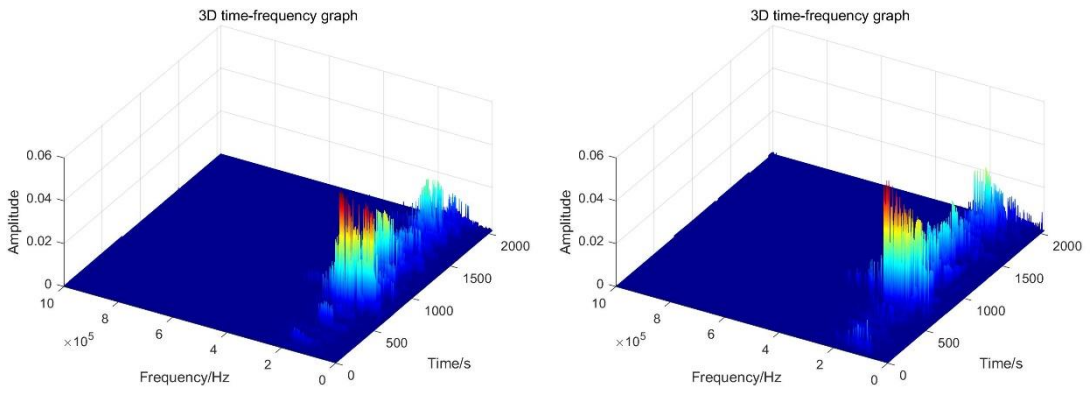

(c) (d)

Figure 3-19. The HHT spectrum of: (a)the AE signal with maximum amplitude, and (b) (c) (d) the following signals from the cracking event

The A_{mi} and f_c of typical signals from this failure cracking event is listed in Table 3-4. It can be seen from the table that the A_{mi} of those signals are both relatively high as most of cracking and damaging is occurred at this moment. Their Energy Magnitude has all reached 8 and 9.

Table 3-4. A_{mi} and f_c of typical signals from the failure cracking event

Time(s)	Channel	A_{mi}(V)	f_c(kHz)
1692.23384	4	0.1322	134.9
1692.23881	2	0.1088	157.4
1692.23782	1	0.0534	172.0
1692.23781	3	0.0596	176.1

It can be inferred from the above that although the specimen is subjected to a pure shear condition, the final failure mode still shows a cracking form and result in higher f_c (around 150-170kHz) eventually. Nevertheless, the stress state of the cracking tip (as shown in Figure 3-17) enforce the specimen to be likely to present a shear-slip failure mode and eventually leads to an overall destruction of structure.

3.4 Summary and discussion

The A_{mi}, f_c and time-frequency distribution characteristics of AE signals extracted from two basic failure modes are summarised in Table 3-5 below.

Table 3-5. The A_{mi}, f_c and time-frequency distribution characteristics of AE signals in two basic failure mode

Failure mode	Phase	A_{mi}(V)	f_c(kHz)	Time-frequency characteristics+
Concrete cracking under bending	Initiation of damage and crack	10^{-2}	Low	Low frequency; Short duration time.
	Formation of micro-crack and macro-crack	10^{-1}	Medium to high	From medium frequency to high frequency; Medium duration time.
	Unstable development and propagation of cracks*	10^{-1}	Medium to high	Low frequency; Long duration time.
Concrete cracking under shearing	Micro-crack	10^{-2}	Low	Low frequency; Short duration time.
	Unstable cracking*	10^{0}	Low	Low frequency; Short duration time.
	Final failure	10^{0}	High	Both low and high frequency; Long duration time.

*Within the same type of source, when an AE signal is 1 or 2 orders of Energy Magnitude larger than other signals, it will be regarded as a signal from 'unstable cracking' stage.

+ Low frequency refers to the frequency below 100kHz; Medium frequency refers to the frequency between 100 and 150kHz; High frequency refers to the frequency over 150kHz.

3.5 Conclusion

In this chapter, in order to intrinsically study the characteristics of different basic failure modes of concrete structure, two typical basic failure mode tests, bending and shearing, were designed and conducted. The AE characteristics of the destruction process were studied through the combined method of parametric analysis and waveform analysis. The signal characteristics of frequency, amplitude and time-frequency distribution from each source type were obtained and analysed, which now provides a basis for the study of AE characteristics under more complex failure modes.

The main conclusions of this chapter are as follows:

(1) The combination of parametric analysis and waveform analysis has both the advantages, fast and real-time features of parameter-based analysis, and

comprehensive and accurate features of waveform-based analysis. The Hilbert-Huang Transform is applied to analyse the AE waveform, and the three-dimensional energy spectrum of the signal is obtained. Two characteristic parameters, Maximum Amplitude A_{mi} and Characteristic Instantaneous Frequency f_c, that can characterize the intensity and properties of AE source are determined, which can be used to quantitatively characterize the AE signal.

(2) According to the AE characteristics under two basic damage modes, the damage identification process can be divided into three levels: ①Through the AE energy magnitude analysis, the important signals can be screened out and different damage stages can be roughly divided; ② After the A_{mi} and f_c are obtained, the f_c can be used to further determine the type of sound source, while the A_{mi} can be used to estimate the severity of damage of the source; ③Through time-frequency feature analysis, complex multi-source AE events can be further distinguished based on time-frequency distribution features.

(3) Through the above research, it can be found that the Characteristic Instantaneous Frequency f_c is highly correlated to the sound source and can better distinguish various source types. As for the Maximum Amplitude A_{mi}, it depends on the release of strain energy from material, and it's generally related to the suddenness of damage event, so it could be affected by many factors such as, material properties, loading rate and stress state. Basically the A_{mi} value varies widely in each individual test, and the difference can even be reaching one or two orders of magnitude, which enables this feature to be used to estimate the damage level and severity.

Chapter 4 Multiple Damage Monitoring and source discrimination of Reinforced Concrete Structures

In earth science, earthquake is a phenomenon that is caused by the rapid shear fracture of a fault in the crust. AE, as an NDT&E technique of inspection, are quite similar to earthquakes but on a much smaller scale. They all represent the phenomenon of stress wave propagation in a solid. Earthquakes, mining-induced seismicity, and AE are typically caused by the interaction of the earth's tectonic plates, mining activities, and fracture within a material, respectively. Figure 4-1 shows a scale regarding the typical frequency range of different phenomena.

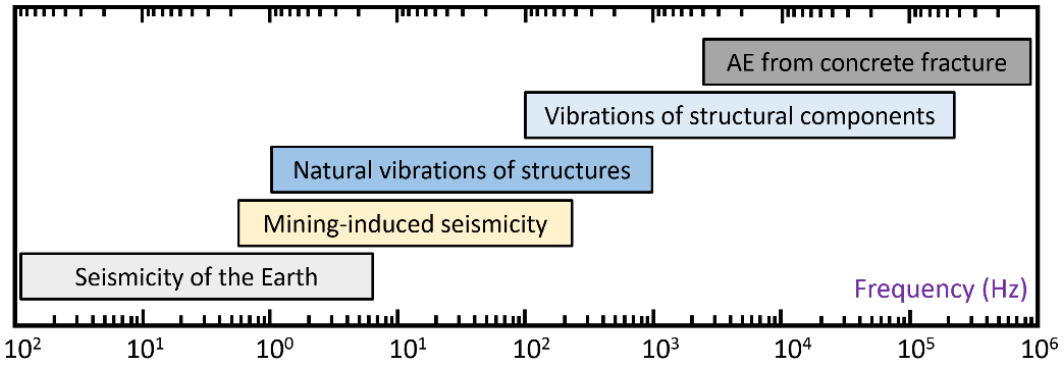

Figure 4-1. Frequency scale of stress wave phenomena), figure reproduced from Mhamdi et al. (2013)

An illustrative sketch of comparison between seismology and AE is presented in Figure 4-2. As shown below, earthquakes occur due to the sudden release of stress in the earth's crust, which results in the generation of seismic waves that propagate the released energy from the source of the earthquake along the surface of and through the earth. For AE activity, it accompanies almost all processes when a solid medium undergoes an internal stress change (mechanical, thermal, physical, etc.) resulting in a sudden release of stress. It occurs in the microscale due to the movement at the microscopic level, as well as in the macroscale due to the failure of structural components (Mhamdi et al. 2013).

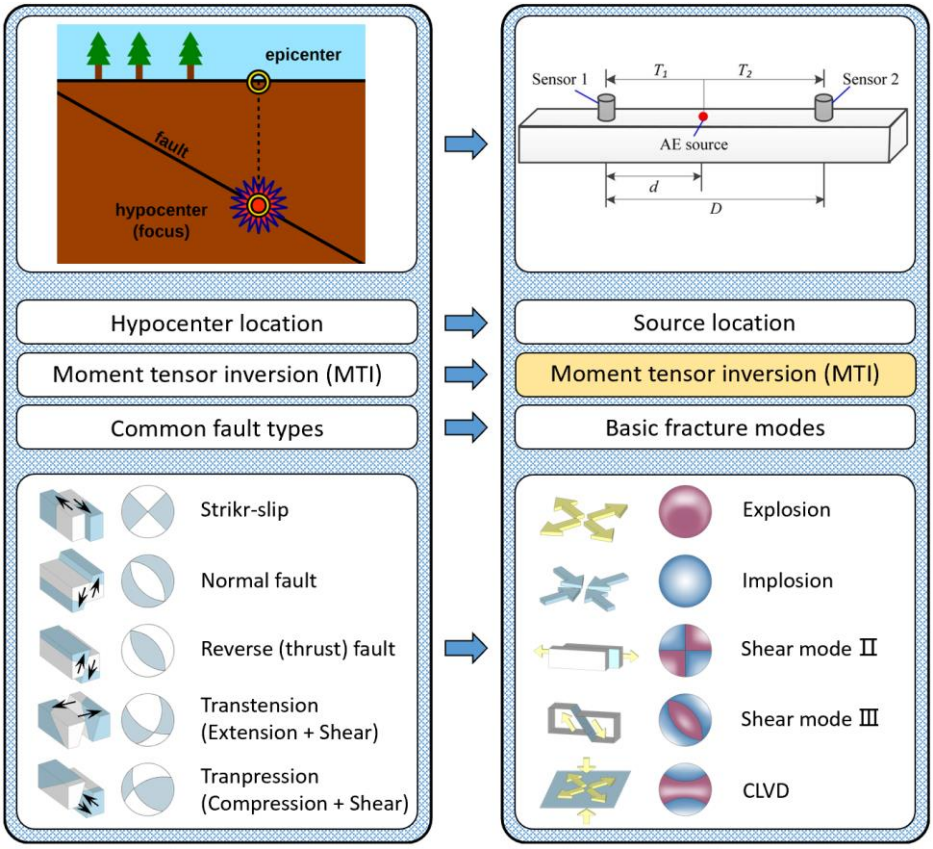

Figure 4-2. Differences between earthquake from seismology (left) and AE from concrete fracture (right), figure reproduced from Mhamdi et al. (2013)

Despite those differences above, AE and earthquakes are quite similar except there are differences in scale, geometry, loading, boundary conditions and medium. So to a certain degree, AE can be thought of as a form of micro-earthquake that occurs at much smaller scale. Some researcher's work (MOGI 1962; Scholz 1968; Bonamy 2009) has also shown that AE can be a good lab-scale model and provide support for earthquake studies.

In Earth science, seismic moment tensor inversion is an effective method to obtain the source process in earthquakes (Dost et al. 2020; Kühn et al. 2020). AE in rock and concrete materials is quite similar to an earthquake as both of them are a process of a rapid release of elastic strain energy. The moment tensor inversion method can be used in some situations to investigate and understand more information about the location and characteristics of the AE source. Moment tensor inversion (MTI) of an AE source is conducted using the first motion and amplitude of the P wave. When an AE

burst is generated by micro-fracture at small scale and the size of specimen is much larger than the AE wavelength, the far-field approximation method of P wave moment tensor analysis can be applied. In this chapter, a RC beam is designed and tested to enable different damage modes to develop to investigate the failure mechanism using AE. The aim is to be able to use the approach to understand the damage type and hence inform the appropriate process and location of healing in smart concrete structures.

To intrinsically identify the source mechanism of AE signals, the SiGMA (**Si**mplified **G**reen's functions for **M**oment tensor **A**nalysis) procedure was applied. Prior to four-point bending tests of RC beams, the whole SiGMA procedure was applied on AE waveforms excited by Hsu-Nielsen (H-N) source for a preliminary test on a concrete cube to verify the effectiveness and accuracy. Then the cracking mechanisms in four-point bending experiments on RC beam were investigated by applying both the conventional parameter analysis and the SiGMA procedure to AE waveforms.

4.1 Introduction

As the number of aged concrete structure has increased significantly worldwide, the detection and estimation methods for crack distribution have been in great demand because cracking is the major cause of failure of concrete structures. To make an evaluation of the safety and performance of the current state of concrete structures, a range of NDT&E methods are applied to estimate and determine whether the structures requires repair and maintenance.

In terms of concrete, AE is one of the most practical and helpful methods to detect and investigate the damage degree in concrete. For example, taking account of the number of AE hits and maximum amplitude of AE signal is one of the most straightforward ways to promptly estimate the damage status of concrete structure and those methods have been standardized (Ohtsu 2006). Moreover, planar and spatial source location in concrete due to crack formation can also be performed by time of arrival (TOA) method (Grosse et al. 1997; Mclaskey and Glaser 2007; Boniface et al.

2020).

To intrinsically investigate the damage mechanism and understand the cracking progress in fracture tests, one powerful technique has been developed using the simplified Green's functions for MTA procedure which is capable of quantitatively determining the crack kinematics of located sources, crack types and orientations (Ohtsu 1991).

Initially, the MTA was derived from seismology as an effective method to obtain the source process. The difficulties of earthquake prediction not only lie in the complexity of the actual physical process and the inaccessibility, but also because of its rarity. In that case, the studies and research results on strong earthquakes are accumulating tardily. The generation mechanism of AE is similar to that of earthquakes as both of them are a process of rapid release of elastic strain energy. Many characteristics of AE are similar to earthquakes such as the magnitude-frequency relationship, waveform characteristics and propagation modes, etc. In that case, under certain circumstances, AE could also be regarded as a kind of 'micro-earthquake'. Commonly used seismic research methods are also applied in AE studies in concrete such as 3D source location, *b*-value statistics analysis, fractal characteristics and frequency spectrum analysis. Nevertheless, there are no sufficient existing research methods of source mechanisms of AE in concrete, but this is evidently of great importance, not only to AE but earthquakes as well.

This chapter mainly explores the theoretical background and principles of MTA theories and verifies the effectiveness of this method for investigating the damage mechanism through experiments. Based on the results, the differences between parameter-based analysis, MTA analysis and waveform analysis are discussed with their respective advantages and disadvantages.

4.2 AE parameter analysis

At present, the post-processing analysis of AE signals for detection of concrete material mainly includes two types of methods: parameter analysis and waveform

analysis. Parameter analysis uses conventional simplified waveform characteristics to describe the AE signals. Due to its several advantages, such as real-time statistical information, clear and straightforward physical meaning, simplicity of calculation, etc., it has been widely applied in AE detection among different types of materials and promoted the standardization and commercialization of AE technology, especially during the early stage of AE study. However, it is based on many assumptions such as constant propagation velocity. Additionally, commercial techniques often result in detailed information being discarded. It is also hard to establish the correspondence between AE parameters and their sources especially in concrete material due to signal attenuation and reflections. Therefore, to evaluate the AE source characteristics directly by using AE signal parameters would not be reliable and could lead to the failure to identify damage or even identify damage that is not present. Furthermore, it is difficult to determine how to effectively select the most valid parameters for post-processing and identify their relationships as well.

As mentioned previously in literature review section 2.1.6.2, in 2003, the Federation of Construction Materials Industries from Japan published standards on estimation of concrete properties by the elastic-wave methods (Ohtsu et al. 2007). These standards contain a monitoring method for active cracks in concrete by AE (JCMS-III B5706-2003 code). Under the standardized action, the method for classification of cracks is successfully applied to investigate the damage process in concrete. Conventionally AE parameters obtained from the extraction of waveform are AE count, AE hit, AE event, peak amplitude, AE energy, rise time, duration, arrival time differences in AE sensor array and so forth as shown previously in Figure 2-18. In order to classify active cracks as introduced previously in section 2.1.6.2, AE indices of RA value, and the Averaged Frequency (F_{a} or AF) are defined from parameters as shown in equations 4.1 and 4.2, RA value is the rise time divided by the maximum amplitude and AF is defined as the ratio of threshold crossing (AE counts) divided by the duration time of signal.

$$RA = \frac{\text{rise time}}{\text{maximum amplitude}} \tag{4.1}$$

$$AF = \frac{\text{AE counts}}{\text{Duration time}} \tag{4.2}$$

By employing these two indices, cracks can be classified into tensile and shear modes as shown in Figure 4-3. During the process of crack propagation and development, crack opening will normally generate tensile cracks. Thereafter this, the condition will change to sliding movements regarded as shear movements. The AE signals generated by different types of movement will have completely different signal signatures. From the view of waveform characteristics, it will show low rise time and high frequency during the early stage of tensile cracks whereas the waveforms with high rise time and low frequency will dominate the failure stage during shear movement. However, this approach has limitations as both AE count and duration are related to the value of a user-defined threshold, AE sensors commonly have a resonance and there is a big difference of the resonance frequencies between concrete material and rock as their inherent fractures have a significant influence on their mechanical properties.

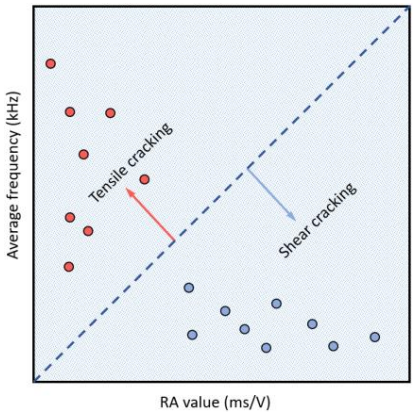

Figure 4-3. Crack type classification based on the protocol of RA-AF values (figure reproduced from RILEM TC 212-ACD (2010) recommendation)

4.3 Moment tensor inversion theories

In response to the excitation of the Earth's normal mode caused by the earthquake source, Gilbert (1971) firstly proposed the concept of moment tensor, which is defined as the first-order moment of equivalent body force acting on a point. The moment

tensor contains the information of radiant energy and nodal plane orientation, including the shear fracture component and the isotropic components.

As shown in Figure 4-4, Richards and Aki (1980) introduced the forward solution of elastic wave propagation in medium in detail, including the acquisition and processing of the source wave in elastic medium. Based on the information from obtained waveform, the source location coordinates could be determined, and the moment tensor solution was eventually obtained. Then, the solved moment tensor solution can be used to invert the focal mechanism solution, the source parameters and the source rupture energy.

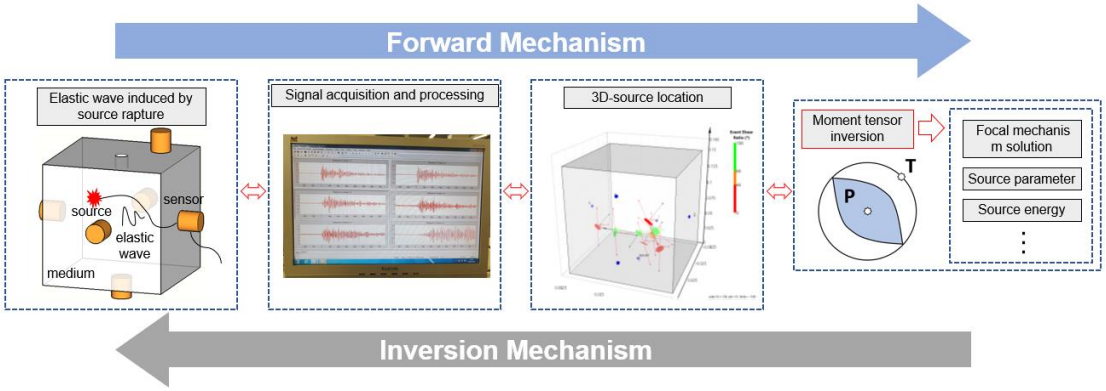

Figure 4-4. Sketch of forward problems and MTI mechanisms about focal source

The introduction of moment tensor linearizes the equations of source parameters (strike angle, dip angle and rake angle, etc., as shown in Figure 4-5), which simplifies the processing and calculation in seismological analysis. Through the inversion of moment tensor, the source mechanism of earthquake can be presented and provides important information to those who work on earthquake prediction prevention.

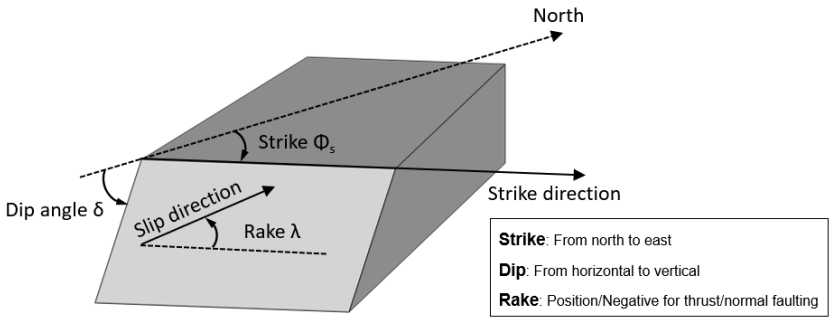

Figure 4-5. Fault orientation parameters: strike, dip and rake (Andersen 2001).

‘Inversion’ is a mathematical-based research method and it is commonly and widely used in various fields. For instance, in theoretical physics, inversion is a method of studying the symmetry properties of microscopic particles (Ghosh Roy 1994; Ni and Chen 1995). The relationship between the motion laws of the object in the original coordinate system and the inverse coordinate system is equivalent to the relationship with the image in the mirror. In remote sensing, the inversion is based on a mathematical model to infer the state parameters of the target based on the measurable parameter values, or, based on the observation information and the forward physical model, to solve or infer the application parameters / targets describing the ground truth data (Twomey 2013). In geophysics, the seismic inversion is a method of using signal data observed from earth surface, constraints from known geological laws, drilling and logging data to solve and present the spatial structure of underground rock layers or the properties of underground seismic sources when an earthquake occurs (Russell 1988; González et al. 2007; Bosch et al. 2009; Bosch et al. 2010).

The theoretical basis of moment tensor inversion is the elastic wave theory. Like seismic waves, AE also belongs to the category of elastic waves. After clarifying the differences of boundary conditions in between, the well-developed moment tensor theory in seismology could be applied on the study of AE as well. Regarding the study in this chapter, only the tensor inversion on point sources in homogeneous medium is considered.

4.3.1 Theory of moment tensor

Based on the generalized theory of AE (Ono and Ohtsu 1984), AE waves are elastic waves that occur inside a solid material by dynamic-crack (dislocation) motions. The seismic moment tensor of a real source is defined as a combination of force couples and dipoles called equivalent forces, which produce displacements at a given point identical to the displacements produced by the actual forces acting at the source, as illustrated in Figure 4-6.

$$M = \begin{bmatrix} M_{xx} & M_{xy} & M_{xz} \\ M_{yx} & M_{yy} & M_{yz} \\ M_{zx} & M_{zy} & M_{zz} \end{bmatrix} =$$

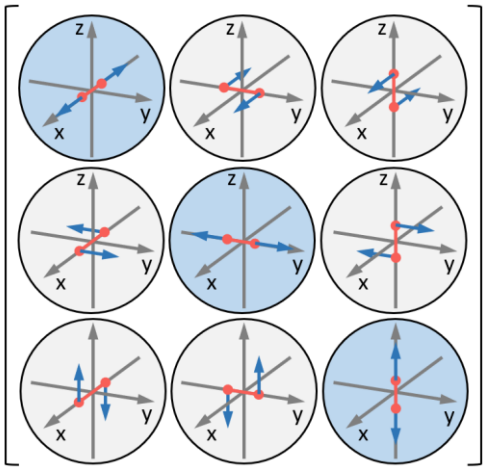

Figure 4-6. Representation of nine force-couple components in canonical and spatial forms

Figure 4-7 and Figure 4-8 shows two distinct sources, explosion and shear respectively, as explained by the moment tensor.

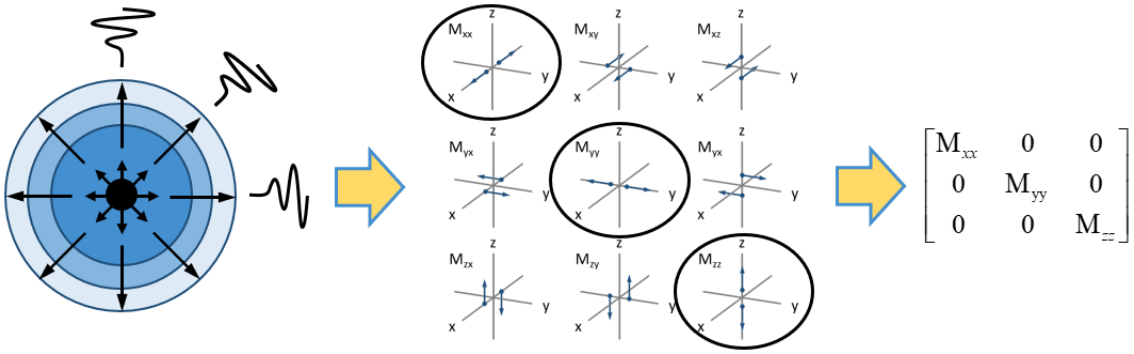

Figure 4-7. Radiation patterns and Moment Tensors of pure explosion source

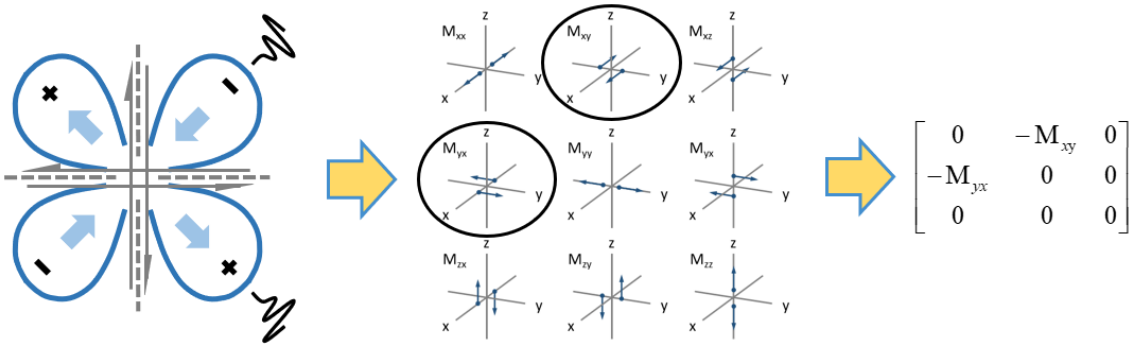

Figure 4-8. Radiation patterns and Moment Tensors of pure shear source

Different disciplines use different terms to describe cracking behaviour. Using fracture mechanics terminology as there are three different fracture mode as shown in

Figure 4-9 below, Mode II refers to in-plane shear crack, where the forces are parallel to the cracking surface, and mode III describes the out-of-plane shear cracks, where the forces are normal to the cracking surface (Linzer et al. 2013). From the perspective of seismology, shear dislocations are also regarded as double couple sources. A double couple is made up of two force couples (e.g. M_{xy} and M_{yx}) and is the preferred force system. It is based on observational and theoretical evidence and a thorough understanding of the radiation pattern of P waves and S waves generated by the two types of sources (Linzer et al. 2013). The double couple formulation also allows the simplification of some complex equations and is directly compatible with the tensor formulation for stress and strain used in rock mechanics (Richards and Aki 1980; Jaeger et al. 2009).

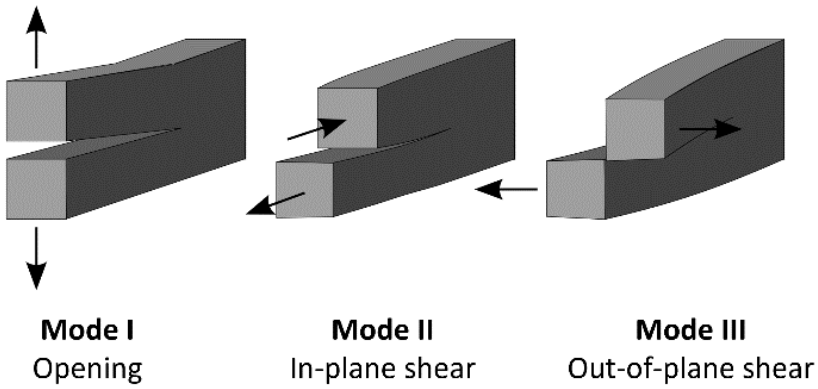

Figure 4-9. three fracture modes from fracture mechanics

According to the fault orientation theory of seismology, generally faults are expected to develop at approximately 30°to the orientation of the greatest principal stress σ_1. This results in the development of three distinct tectonic regimes, each with characteristically oriented faults as shown in Figure 4-10. Different types of sources produce characteristic patterns. For example, extension would generate a normal fault (mode II shear where the shear stress is perpendicular to the plane of fracture) and produce the pattern demonstrated in Figure 4-11. The points halfway between the nodal planes are the P- and T-axes, the compressional and tensional axes, respectively (Stein and Wysession 2009).

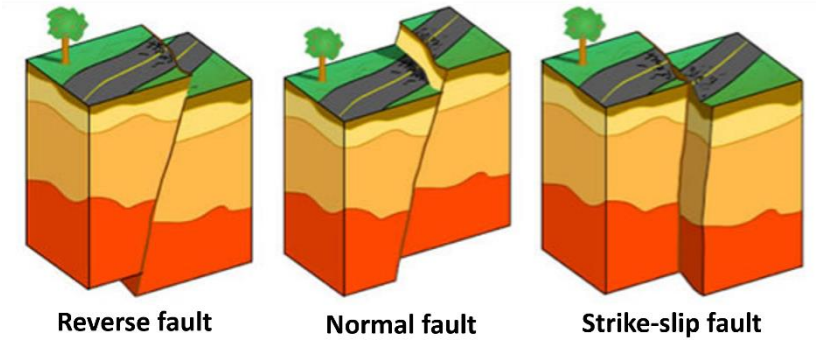

Figure 4-10. Schematic of three main tectonic faults

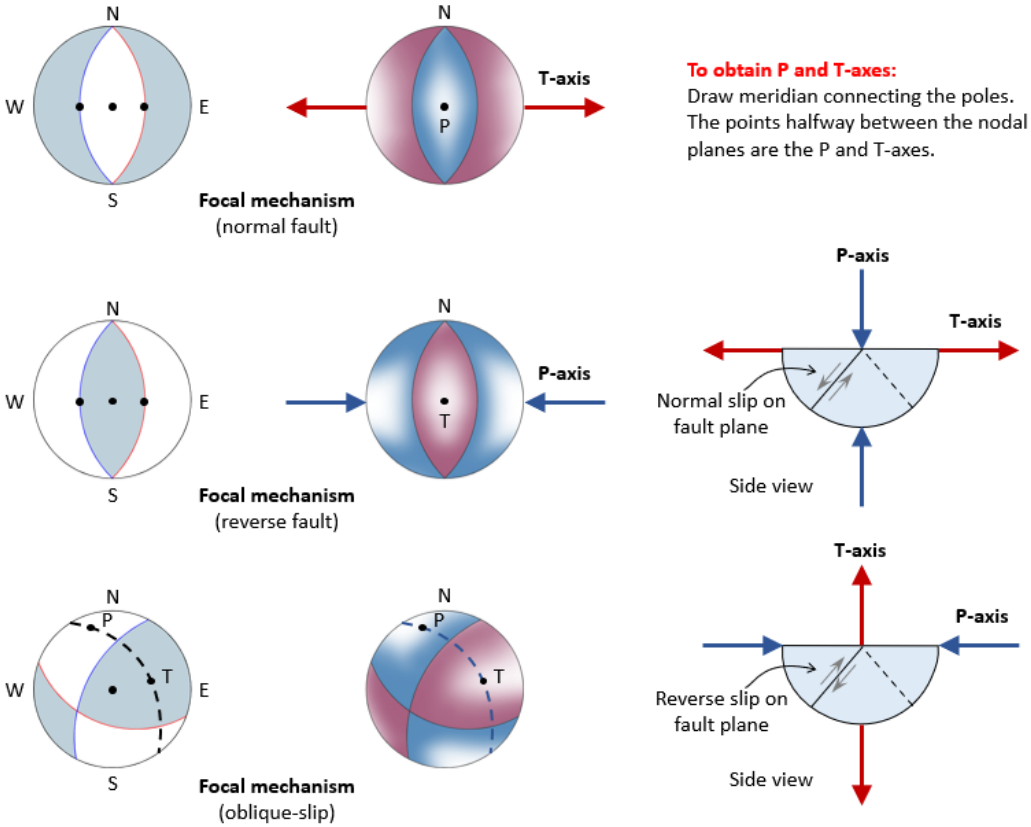

Figure 4-11. Simplified relationship between the P- and T-axes and normal, reverse, and oblique slip fault types. The P- and T-axes can be obtained by drawing a meridian line that connects the poles to the fault planes. The points halfway between the nodal planes are the P- and T-axes. Redrawn and modified from(Stein and Wysession 2009).

An important difference found by Stein and Wysession (2009) between seismology and fracture mechanics is that the maximum and minimum compressive stress directions determined by the moment tensor are at 45° to the slip plane.

However, the experimental results show that the fracture plane usually forms an angle of 25° with the direction of the maximum principal stress.

4.3.2 SiGMA procedure

Basically, the SiGMA analysis consists of a three-dimensional (3D) AE source location procedure and moment tensor analysis of AE source. Two parameters of the arrival time and the amplitude of the first motion are picked up and applied to the analysis.

In order to determine the moment tensor of an AE source, a simplified procedure has been developed. The procedure is implemented as SiGMA (Ohtsu 1991). Two parameters of the arrival time and the amplitude of the first motion are extracted and determined from the AE waveform. In the location procedure, source location is determined from the arrival time differences. Then, distance and its direction vector are determined. From the amplitudes of the first motions at more than six channels, the moment tensor is determined. Since the SiGMA code requires only relative values of the moment tensor components, the relative calibration of the sensors is adequate.

4.3.2.1 Determination of the P wave onset time and first motion amplitude

The implementation of SiGMA procedure mainly depends on an accurate measurement and calculation of the time the signal was transmitted. In that case, the detection of the actual start time of the waveform is of great importance. Traditionally the most accurate way to pick the onset time of a wave would be to do it manually. And it is largely depended on checking the signal traces based on the user's experience. In terms of the acquisition system, normally it would be triggered once the wave crosses the pre-set threshold and that crossing point will be detected and recorded as the onset time of the wave instead of the actual start. And though possibly insignificant, errors still can occur as shown in Figure 4-12.

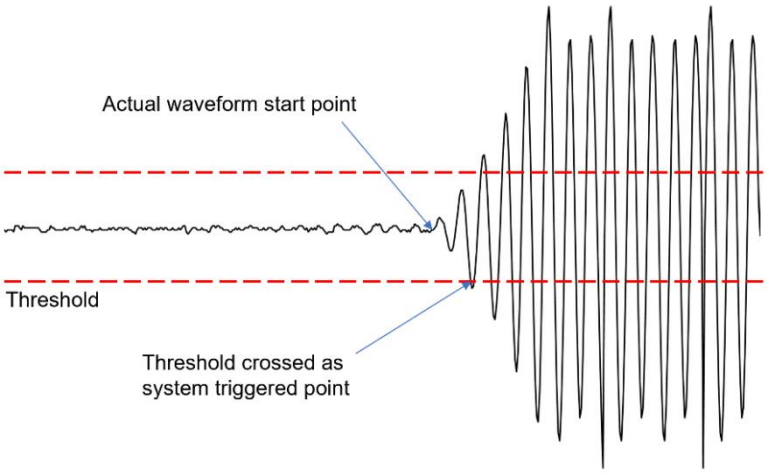

Figure 4-12. System triggered point missing the true waveform start point

An automated method was also initially proposed by Japanese scholar Naoki Maeda (Maeda, 1973) to adopt the AIC (Akaike Information Criterion) function. In this method, the onset time of a wave is determined when the AIC value becomes the global minimum. The AIC value at point $i = k$ calculated by the following Equation 4.3:

$$\mathrm{AIC}_k = k \cdot \log\{\mathrm{var}(X[1,k])\} + (N-k) \cdot \log\{\mathrm{var}(X[k,N])\} \qquad (4.3)$$

where N is the number of amplitudes of a digitized wave, X_i is an amplitude of a signal $(i = 1,2,\ldots,N)$, $\mathrm{var}(X[1,k])$ indicates the variance between X_1 and X_k, and likewise $\mathrm{var}(X[k,N])$ is also the variance between X_k and X_N.

Basically this AIC function compares two vectors which are extracted from the waveforms at a particular time for similarity, the point at which the first vector is purely noise and therefore has a high-entropy and the second is only signal with low-entropy, will return the lowest correlation and therefore identify the start of the waveform. One example of this being used to detect the start of a signal compared with the traditional threshold crossing technique can be seen in Figure 4-13.

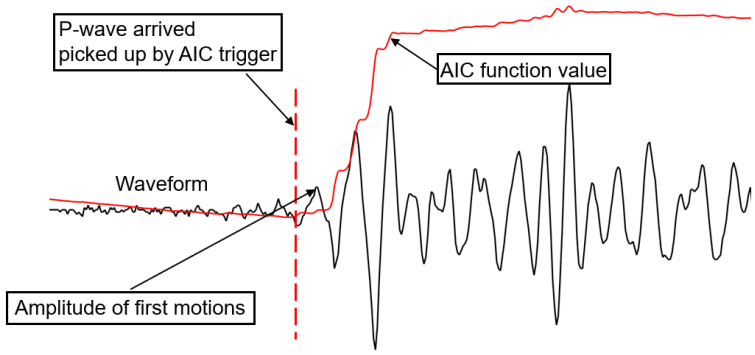

Figure 4-13. Determination of the onset time of P wave and the amplitude of first motion by Akaike Information Criterion (AIC) picker

This technique has been widely utilised by others since Kurz et al. (Kurz et al. 2005) who showed its increased accuracy for picking the start of an AE source comparing to another automatic onset detection algorithm based on the Hinkley criterion. Pearson et al. (2017) applied it to the Delta-T mapping technique (Baxter et al. 2007) to significantly improve the accuracy over the conventional Time-Of-Arrival (TOA) method. Further improvements to the technique have been made in recent years by many researchers(Eaton et al. 2012; Al-Jumaili et al. 2016; Pearson et al. 2017) as well aiming at not only to improve the accuracy but speed up the time of data processing.

4.3.2.2 Unified Decomposition of Moment Tensor

The tensor expression can be very concise under the Principal axis coordinate system and can be expressed as follows:

$$\begin{bmatrix} M_1 & 0 & 0 \\ 0 & M_2 & 0 \\ 0 & 0 & M_3 \end{bmatrix} \tag{4.4}$$

The moment tensor can be decomposed into a linear combination of several moment tensors. After decomposition, the kinetic motion mode of the hypocentre can be clearly presented and understood. Nevertheless, the decomposition of moment tensor is not unique and which decomposition method should be used depends on different physical assumptions applied.

In seismology, it is generally considered that the fault has no out-of-plane displacement under the condition of high confining pressure. Generally, the trace of seismic moment tensor is 0, which is the pure deviatoric moment tensor, that is, $M_1 + M_2 + M_3 = 0$. There are multiple decomposition schemes for pure deviatoric moment tensor. For instance, it can be decomposed into a double-couple (DC) part and a compensated linear vector dipole (CLVD) part:

$$\begin{bmatrix} M_1 & 0 & 0 \\ 0 & M_2 & 0 \\ 0 & 0 & M_3 \end{bmatrix} = \frac{M_1 - M_3}{2}\begin{bmatrix} 1 & 0 & 0 \\ 0 & 0 & 0 \\ 0 & 0 & -1 \end{bmatrix} - \frac{M_1 + M_3}{2}\begin{bmatrix} -1 & 0 & 0 \\ 0 & 2 & 0 \\ 0 & 0 & -1 \end{bmatrix} \quad (4.5)$$

Or it can be decomposed into a major double-couple and a minor double-couple:

$$\begin{bmatrix} M_1 & 0 & 0 \\ 0 & M_2 & 0 \\ 0 & 0 & M_3 \end{bmatrix} = M_1\begin{bmatrix} 1 & 0 & 0 \\ 0 & 0 & 0 \\ 0 & 0 & -1 \end{bmatrix} + M_2\begin{bmatrix} 0 & 0 & 0 \\ 0 & 1 & 0 \\ 0 & 0 & -1 \end{bmatrix} \quad (4.6)$$

Compared with earthquakes, lab-scale experiments are different as there are multiple modes of crack propagation, which enables the out-of-plane displacement and the trace of moment tensor is no longer always 0. In this case, another possible decomposition scheme can be added:

If moment tensor M

$$\boldsymbol{M} = \begin{bmatrix} M_1 & 0 & 0 \\ 0 & M_2 & 0 \\ 0 & 0 & M_3 \end{bmatrix}, \ (M_1 \geq M_2 \geq M_3) \quad (4.7)$$

rotates the coordinate system around the intermediate axis, then the moment tensor can be transformed into:

$$\begin{bmatrix} M_1 - M_2 + M_3 & 0 & \sqrt{(M_2 - M_3)(M_1 - M_2)} \\ 0 & M_2 & 0 \\ \sqrt{(M_2 - M_3)(M_1 - M_2)} & 0 & M_2 \end{bmatrix} \quad (4.8)$$

This form of moment tensor can be decomposed into a sum of two parts:

$$\begin{bmatrix} M_1 - M_2 + M_3 & 0 & 0 \\ 0 & M_2 & 0 \\ 0 & 0 & M_2 \end{bmatrix} + \begin{bmatrix} 0 & 0 & \sqrt{(M_2 - M_3)(M_1 - M_2)} \\ 0 & 0 & 0 \\ \sqrt{(M_2 - M_3)(M_1 - M_2)} & 0 & 0 \end{bmatrix} \tag{4.9}$$

The first term can be interpreted as a dislocation plus volume deformation perpendicular to the fault plane. The second term can be interpreted as a shear dislocation along the fault plane, that is, an equivalent double-couple.

In order to identify the source kinematics and classify the cracks into different type (e.g. tensile, shear or mix-mode), a unified decomposition of the eigenvalues of the moment tensor was developed by Ohtsu (1991). In general, crack motion on the crack surface consists of slip motion (shear components) and crack-opening motion (tensile components), as illustrated in Figure 4-14.

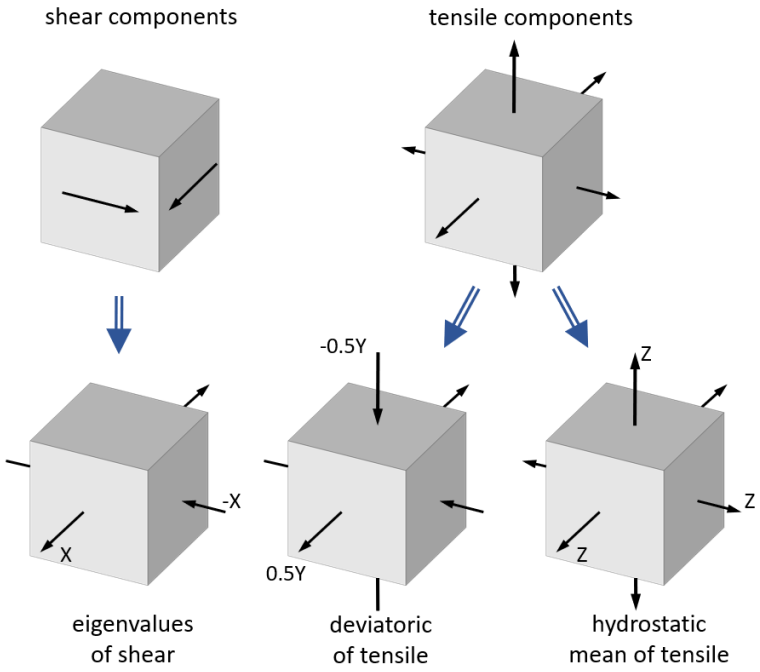

Figure 4-14. Unified decomposition of eigenvalues of the moment tensor

Thus, it is assumed that the eigenvalues of the moment tensor are the combination of those of a shear crack and those of a tensile crack, as the principal axes are identical. Then, the classification of a crack is performed by the eigenvalue analysis of the moment tensor. Setting the ratio of the maximum shear contribution as X, three

eigenvalues for the shear crack become X, 0, $-\mathrm{X}$. Likewise, the ratio of the maximum deviatoric tensile component is set as Y and the isotropic tensile component as Z. Three eigenvalues are normalized and decomposed:

Normalization

$1.0 = \mathrm{X} + \mathrm{Y} + \mathrm{Z}$, (out-of-plane direction in the figure)

the Intermediate eigenvalue/ the maximum eigenvalue

$= 0 - \mathrm{Y}/2 + \mathrm{Z}$, (vertical direction in the figure)

the minimum eigenvalue/the maximum eigenvalue

$= -\mathrm{X} - \mathrm{Y}/2 + \mathrm{Z}$, (horizontal direction in the figure)

where X, Y, and Z represent the shear ratio, the deviatoric tensile ratio, and the isotropic tensile ratio, respectively. In the present SiGMA code, AE sources of which the shear ratios are less than 40% are classified into tensile cracks. The sources of X >60% are classified into shear cracks. In between 40% and 60%, cracks are referred to as mixed mode. In the eigenvalue analysis, three eigenvectors $e1$, $e2$, and $e3$,

$$e1 = l + n$$

$$e2 = l \times n$$

$$e3 = l - n$$

Here $\times$ denotes the vector product, and the vectors l and n are interchangeable. In the case of a tensile crack, the vector l is parallel to the vector n. Thus, the vector $e1$ could give the direction of crack-opening, while the sum $e1$ + $e3$ and the difference $e1$ $-$ $e3$ give the two vectors l and n for a shear crack.

4.3.2.3 Graphic display of Acoustic Emission (AE) moment tensor

In seismology, usually a black and white source sphere can be used to represent the focal mechanism solution (FMS) of the epicentre. Specifically, the Schmidt Net and Stereographic Net (Stauder and M 1961; Cronin 2004; Liu et al. 2014) can be used to present the compression zone and expansion zone of the initial P wave to express the Focal Mechanism Solution (FMS). The compression zone (off source) is represented in black and the expansion zone (to source) is represented in white. Then the nodal

surface can be presented as the junction of black and white in between. This graphic display method can particularly well express the pure shear source of the epicentre.

In terms of most of AE tests in a lab-scale, they do not always occur under the high confining pressure conditions. It is certainly possible that the AE source could derive from a tension crack or any volume change. In order to represent the tension and volume change, this method can be slightly modified as referred from seismology. The direction and magnitude of the moment tensor can be represented by a coloured source sphere rather than the black and white source spheres.

Firstly, the moment tensor is normalized as after normalization, the moment tensor primarily presents the shape and orientation rather than the differences in absolute size. The Schmitt network is used to plot the magnitude of each moment tensor in different direction using the lower hemisphere projection method. The light green colour indicates the moment tensor is 0. The red colour indicates the moment tensor is at maximum (off-source). The blue colour indicates the moment tensor is at minimum (to-source). The colour between light green and red, and light green and blue, represents the transition area. In order to prominently present the size and direction of moment tensor, deeper colour is used for larger tensor while lighter colour is used for smaller tensor.

The comparison of two representation methods of pure shear source is shown in Figure 4-15. The black colour in the black-white sphere corresponds to red colour in the colour sphere, which represents the initial motion of P wave off the source (the T-axis of source). The white colour in the black-white sphere corresponds to blue colour in the colour sphere, which represents the initial motion of P wave toward the source (the P-axis of source).

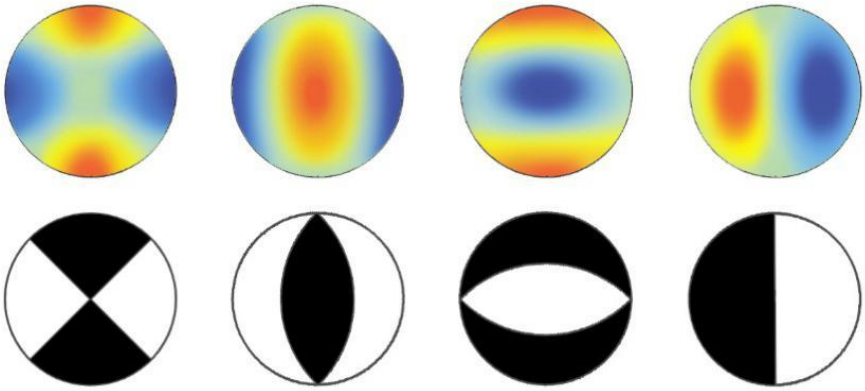

Figure 4-15. Graphical representation of pure shear source in two methods

Figure 4-16 below shows several graphical representations of non-shear sources using colour source spheres. The source of tensile crack and fracture collapse (closure) of crack are shown in Figure 4-16(a) to (f) respectively in three different principal directions. (g), (h) and (i) show the explosion source, no source, and implosion source respectively.

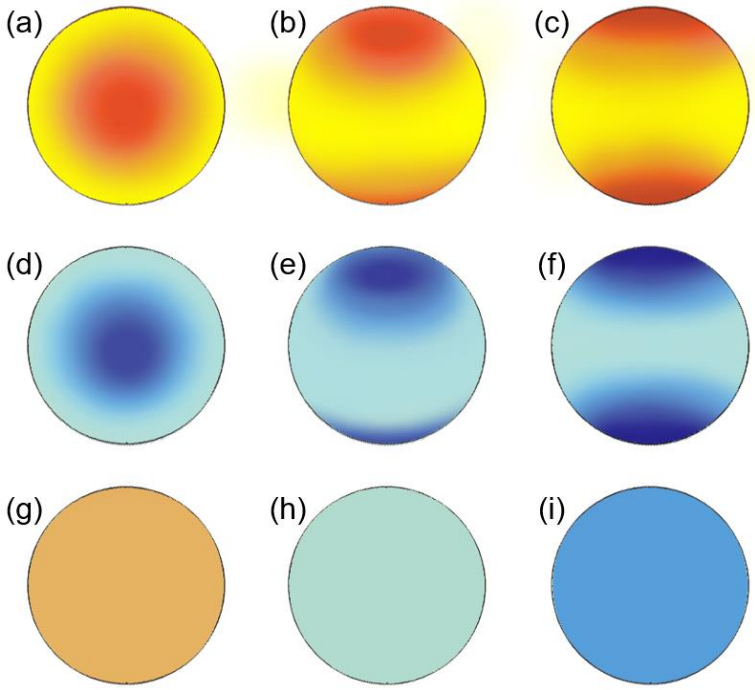

(a) (b) (c) Tensile crack, (d) (e) (f) Closure of crack,

(g) Explosion source, (d) None , (e) Implosion source

Figure 4-16. Graphical representation of non-shear source:

4.4 MTA analysis of a cube

4.4.1 Introduction and objectives

This section explains the detail of the experiments and aims to provide an understanding and evaluate the feasibility of the MTA-based technique in characterizing AE sources in concrete.

The objectives for this experiment involving the study of MTA, the experimental objectives are to produce artificial H-N source with clear and defined initial P waves as then the SiGMA-procedure can be successfully carried out. To calculate the crack type and orientation of each event from the eigenvalue analysis of each moment tensor matrix and to relate them to the failure mechanism expected during loading.

4.4.2 Hsu-Nielsen source

Hsu-Nielsen (H-N) source was used as a wideband artificial source to simulate the AE event using the fracture of pencil lead. This method was initially developed by Hsu and Breckenbridge (1981), and then named afterwards. Then this technique has been standardized for sensor calibration (ASTM 1999). Afterwards it is widely applied as a generally accepted technique within industry as well (Vallen-Systeme GmbH 2002).

As shown in Figure 4-17, the Hsu-Nielsen test is conducted mainly through breaking a 0.5 mm (or alternatively 0.3mm) diameter pencil lead at approximately 3 mm (+/- 0.5 mm) from its tip by pressing it against the surface of the object. The intense acoustic signal generated by this way is quite similar to a natural AE source and that's why it can be detected by the AE sensors as a strong burst signal. The main purpose of conducting a PLB (Pencil Lead Break) test is to ensure that the transducers are in good acoustic contact with the part being monitored. Generally, the lead breaks should register amplitudes of at least 80 dB for a reference voltage of 1 mV and a total system gain of 80 dB. Besides, it checks the accuracy of the source location setup. This involves indirectly determining the actual value of the acoustic wave velocity in that particular material of the specimen being monitored.

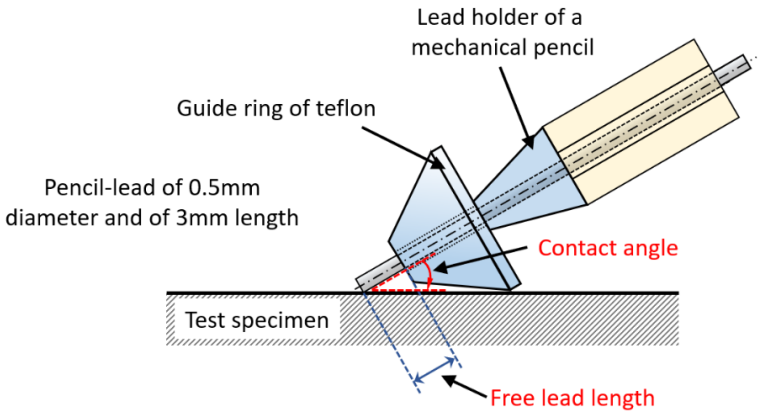

(a)

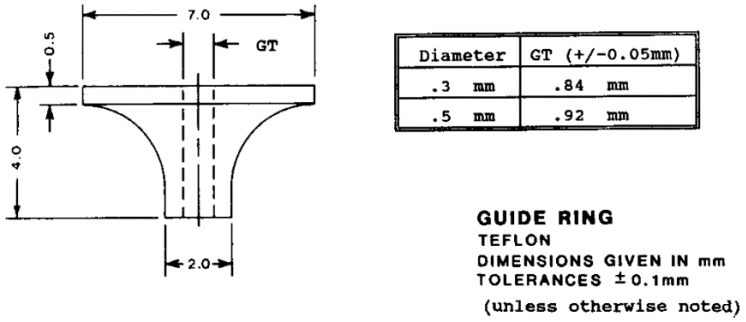

(b)

Figure 4-17. Schematic of (a) a Hsu-Nielsen pencil source and (b) dimensions of Nielsen Shoe (ASTM 1999)

After the original works of Hsu and Nielsen, Sause (2011) has conducted a further study on how differences in handling of the mechanical pencil and the lead diameter can influence the test signals as it is typically applied to investigate signal propagation in the structure under investigation, to check sensor couplings and to define threshold values for signal detection. His study has demonstrated that even slight differences in the usage of mechanical pencil can introduce large differences. This was confirmed experimentally under various contact angles and free lead lengths (indicated in Figure 4-17).

4.4.3 Experimental setup

The experiment is conducted on a solid cube made of concrete having Height x Depth x Width = 100mm x 100mm x 100mm. A 10mm-wide hole is drilled vertically in the centre of the upper surface with a depth of 10mm as well. Six sensors(R15I) are used to collect the waveforms located in specific positions on the cube shown in Figure 4-18.

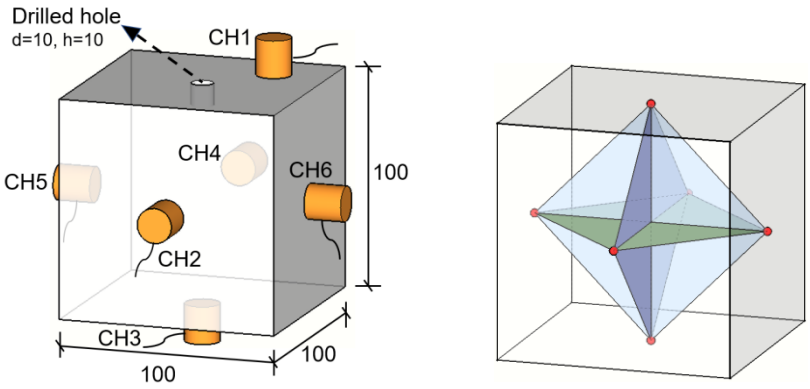

Figure 4-18. (a)Sensor arrangement on the cube specimen; (b)Sensor planes within the cube specimen.

The corresponding coordinates of all sensors used are shown in Table 4-1 below. The coordinate system used is the one supported by Noesis having all three axes parallel to corresponding edges of the cube. The origin of this system is located in the centre of the bottom surface of the cube.

Table 4-1. Coordinates of the six sensors attached on the cube

Sensor coordinates on cube specimen			
Sensor No.	x(mm)	y(mm)	z(mm)
Sensor 1	25	25	100
Sensor 2	0	-50	50
Sensor 3	0	0	0
Sensor 4	0	50	50
Sensor 5	-50	0	50
Sensor 6	50	0	50

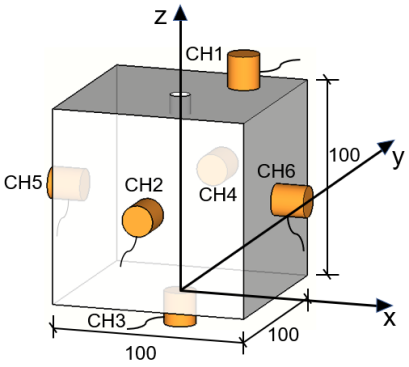

4.4.4 Experimental procedure

The premise to successfully conduct the SiGMA procedure is to determine the initial P wave amplitude and arrival time of all signals from each individual channel. Any errors in that process would affect the decomposition process of the eigenvalues of the moment tensor and eventually lead to the inaccuracies both in location and the crack kinematics. Instead of carrying out the determination of P wave amplitude and arrival time, the data analysis software Noesis developed by MISTRAS Group is introduced to perform the SiGMA procedure within the MTA module.

The experiment setup is shown in Figure 4-19. Six sensors in total are attached on each side of the specimen. Among them, sensor 1 is placed next to the hole on surface 1, and the remaining five sensors are attached exactly in the centre of each surface of the cube.

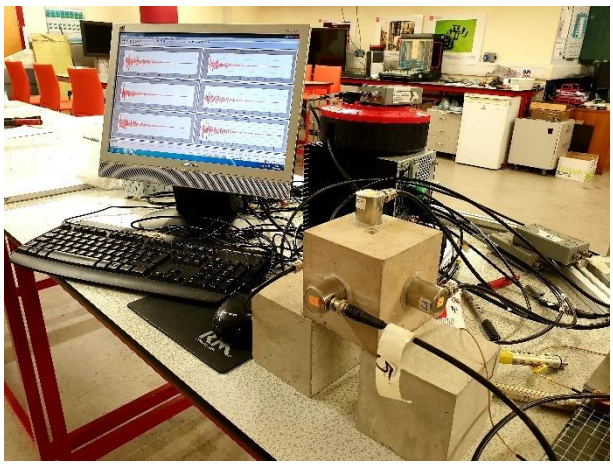

Figure 4-19. Experiment setup on the cube

The coordinates for exciting the H-N source on the concrete cube specimen are listed in Table 4-2. As shown graphically from Figure 4-20, surface 1 and 2 are selected, and totally 16 excitation points have been chosen to excite the H-N source. All excitation points are highlighted in different colour.

Table 4-2. Coordinates of H-N source excited on the cube specimen

	Set 1			**Set 2**		
	X	Y	Z	X	Y	Z
Surface 1	0	25	100	-25	25	100
	25	0	100	25	25	100
	0	-25	100	25	-25	100
	-25	0	100	-25	-25	100
Surface 2	0	-50	75	-25	-50	75
	25	-50	50	25	-50	75
	0	-50	25	25	-50	25
	-25	-50	50	-25	-50	25

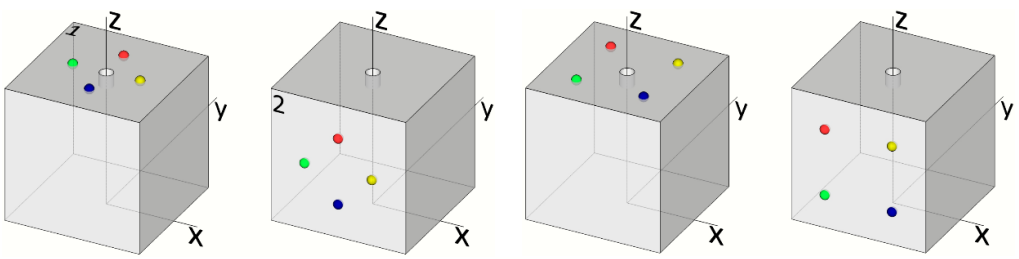

Figure 4-20. H-N source excitation location on the cube specimen

4.4.5 Results and discussion

By applying the H-N source on the concrete cube as an artificial source, it is assumed that all signals would be more reliable to be able to be detected and have a clearer initial P wave arrival time and motion picked up by each sensor. In that case the MTA should be very likely to be performed successfully on the signals with similar crack kinematics as they are all from the same excitation source. After the determination of P wave arrival time and amplitude of each signal received by all sensors, the moment tensor of each event can be calculated by performing the SiGMA procedure in the MTA module in Noesis. Then the eigen values and eigen vectors can be determined subsequently.

After performing the MTA, without any manual modification on pick-up of waveforms in advance, only 10 events out of 18 can be processed as moment tensors determined. Among them, only 5 events out of 10 is valid to be located.

Figure 4-21 displays an example of all AE waveforms from a typical event recorded where the initial P wave arrival time and amplitude can be picked up on each of the channels.

Table 4-3 presents the H-N source excitation coordinates of five located events and the corresponding location results. It can be seen that the average error of five location results is 21.5mm and the maximum absolute error reaches 31.4mm. The variation in each location can be visualized in Figure 4-22 where most of them are within a range of approximately 10mm - 20mm suggesting the location algorithm of MTA can still indicate the damage area with a lack of accuracy.

Table 4-4 presents the moment tensor components and corresponding eigenvalues and eigenvectors produced by the SiGMA procedure of the selected events.

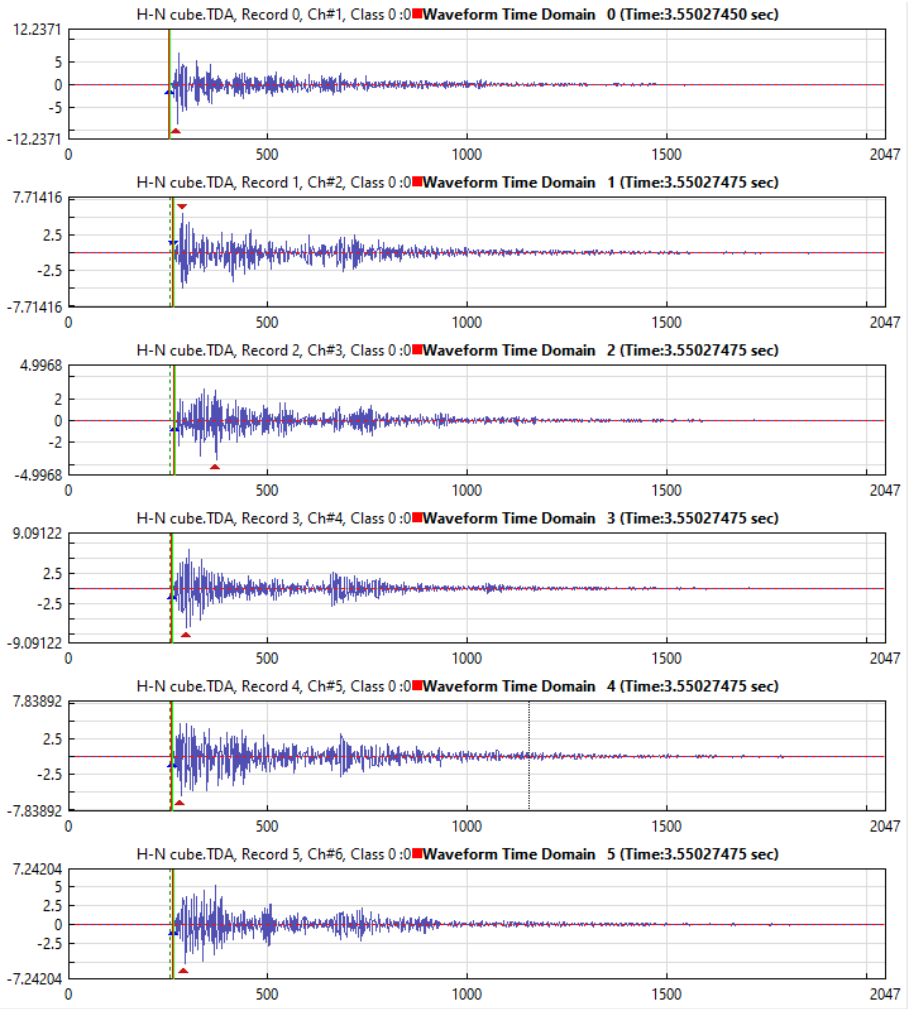

Figure 4-21. AE waveforms of an event recorded on all channels from the H-N source

Table 4-3. Coordinates of H-N sources excitation points

Event number	Coordinates of excitation (mm)			Coordinates of results (mm)			Absolute error (mm)	Average (mm)
	X	Y	Z	X	Y	Z		
1	-25	0	100	-17.8	-0.2	115.6	17.2	21.5
3	-25	-25	100	-7.5	-15.2	124.2	31.4	
6	0	-25	100	-11.4	-16.7	98.0	14.2	
8	-25	-25	100	-32.5	-29.6	129.4	30.7	
9	-25	-50	50	-20.2	-38.3	48.8	14.2	

Table 4-4. The moment tensor and corresponding eigen values and vectors produced by SiGMA procedure for the selected events

Event	Moment Tensor Components			Eigen Values and Vectors	maximum	midiate	minimum
1	-0.3818	0.3829	-0.1047	Eigen Value	1	-0.2092	-0.7451
	0.3829	0.7388	1	Eigen Vector X	0.155	-0.8943	0.4197
	-0.1047	1	-0.2933	Eigen Vector Y	0.8536	-0.0926	-0.5126
	/			Eigen Vector Z	0.4973	0.4378	0.7491
3	-0.9001	1	0.2722	Eigen Value	1	0.3896	-0.303
	1	-0.3916	0.2432	Eigen Vector X	-0.7944	0.152	0.5881
	0.2722	0.2432	-0.5355	Eigen Vector Y	0.6044	0.2941	0.7404
	/			Eigen Vector Z	0.0604	-0.9436	0.3255
6	-0.1993	1	0.2969	Eigen Value	1	-0.0002	-0.8196
	1	-0.1636	0.2044	Eigen Vector X	-0.719	0.2398	0.6524
	0.2969	0.2044	0.1493	Eigen Vector Y	0.6929	0.32	0.6461
	/			Eigen Vector Z	0.0538	-0.9166	0.3962
8	0.1924	-0.318	-0.049	Eigen Value	1	0.1092	-0.1291
	-0.318	1	0.6205	Eigen Vector X	0.2425	0.9139	-0.3257
	-0.049	0.6205	0.1915	Eigen Vector Y	-0.8609	0.0479	-0.5066
	/			Eigen Vector Z	-0.4474	0.4032	0.7983
9	-0.3193	-0.1489	1	Eigen Value	1	0.4329	-0.7342
	-0.1489	-0.4646	-0.2355	Eigen Vector X	-0.7453	0.1791	0.6422
	1	-0.2355	-0.0528	Eigen Vector Y	0.0619	0.9777	-0.2008
	/			Eigen Vector Z	0.6638	0.1099	0.7398

Table 4-5 displayed the location, crack motion vector, crack surface normal vector, and composition ratio of eigen value of each event. The results of this table are graphically presented in Figure 4-22 where each located event has been indicated on the specimen.

Table 4-5. The location, crack motion vector, crack surface normal vector, and the composition ratio of eigenvalue of all processed events

Event No.	Location (mm)			Crack Motion			Crack Surface Normal Directions			Composition Ratio of Eigenvalue (%)		
	X	Y	Z	X	Y	Z	X	Y	Z	Shear	CLVD	Mean
1	-17.817	-0.235	115.593	0.362	0.427	0.829	-0.104	0.995	-0.001	53.59	44.89	1.52
3	-7.518	-15.15	124.15	-0.115	0.953	0.279	-0.972	-0.126	-0.196	69.26	-5.48	36.22
6	-11.404	-16.738	97.989	-0.095	0.947	0.306	-0.971	0.08	-0.226	81.94	12.06	6.00
8	-32.527	-29.61	129.372	0.066	-0.997	-0.031	0.365	-0.532	-0.764	23.82	43.5	32.67
9	-20.18	-38.284	48.769	0.101	-0.129	0.986	-0.953	0.2	-0.227	36.71	40.00	23.29

In the present SiGMA procedure, AE sources of which the shear ratios are less than 40% will be classified into tensile cracks. The sources of shear ratios are greater than 60% will be classified into shear cracks. In between of 40% and 60%, cracks are referred to as mixed mode. Therefore, among the above five located events as shown in Figure 4-22, two are classified into shear mode (green), two are classified into tensile mode (red) and one is classified into mix mode (orange).

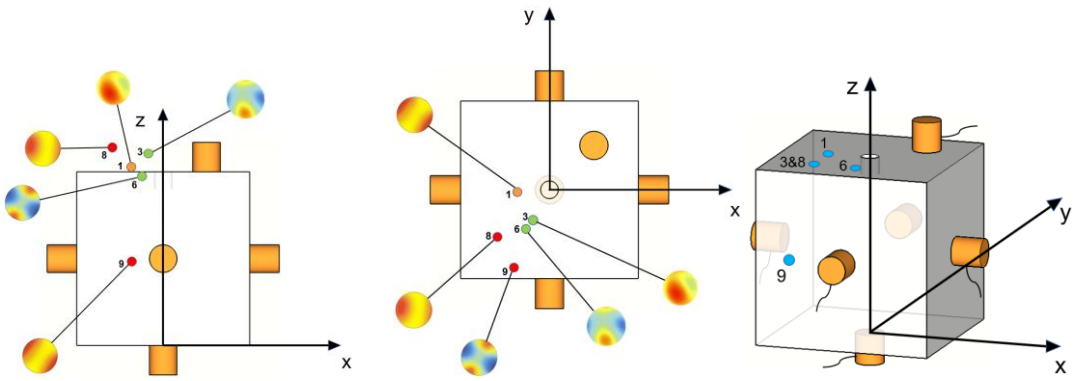

(a) (b) (c)

Figure 4-22. The location and crack types displayed by coloured source sphere on the cube (a)x-z plane, elevation view, (b) x-y plane, top view, (c) actual source location (excitation points).

Through the study above, the lack of accuracy regarding location can be result from the determination of P wave velocity. As the 3D location algorithm is based on time-of-arrival (TOA) of waveforms received from all channels, the accuracy of measured velocity is critical. Using TOA to calculate the wave propagation velocity of an emission is normally to calculate the time difference of receiving signals from an excitation produced by a H-N source between two sensors placed at a known distance. Since the TOA method determines the velocity of a waveform from the first threshold crossing while the initial P wave is produced prior to the first threshold crossing, the P wave velocity determined may be incorrect and influence the accuracy of location results.

Another difficulty to MTA is the significant lack of processed data. As described previously, inaccurate determination of initial P wave onset time and amplitude will lead to the failure of determination of moment tensor. Even if the moment tensor

components are calculated and determined, the located event will still be regarded as invalid if its location coordinates are outside the geometry of the specimen. The results from Table 4-5 and Figure 4-22 show that only five events have been successfully processed with SiGMA procedure. Among them, two events had a shear percentage below 40 and are classified as tensile, one events had a shear percentage between 40 and 60 and is classified as mixed-mode, and two events had a shear percentage above 60 and are consequently classified as shear. Initially it is assumed that all excitation produced by H-N source will present similar source mechanism. Nevertheless, the results indicate either not all pulses produced by the H-N source are the same or the inaccurate calculation process of moment tensor.

4.5 AE monitoring of RC beam

The feasibility and effectiveness of the MTA-based approach has been demonstrated from the cube test in section 4.4. The cracking mechanisms in an experiment are investigated through carrying out a four-point bending test on a RC beam.

4.5.1 Introduction and objectives

It is well known that the three most common damage mode in reinforced concrete structures are bending failure, shear failure and bond-splitting failure. Among them, the shear failures are normally occurred in a brittle nature, therefore more attention needs to be paid in the design. Nevertheless, it is found that the occurrence of the diagonal-shear failure in the RC beam highly depends on the shear span to the effective depth ratio ($\lambda = a/h_0$, where a is the length of shear span, and h_0 is the effective depth) but up to these days the cracking mechanisms of the diagonal-shear failure have not been clarified completely.

In that case, prior to any maintenance and repair of concrete structures to be conducted, a diagnostic inspection of the current degradation state is necessary and essential. The aim of this study is to detect the damage and cracks using AE, and to further evaluate the feasibility of MTA method in characterizing AE sources, especially

when it comes to the on-site AE monitoring of structure for damage detection and health monitoring.

4.5.2 Bearing capacity of diagonal section on shear span of flexural member

Diagonal section bearing capacity includes both shearing resistance and bending resistance in a diagonal section of shear span. Figure 4-23 is a scheme of typical simply supported RC beam under four-point loading, and Figure 4-24 shows the principal stress trajectories for a simply supported RC beam without web reinforcement under two symmetrical concentrated loads.

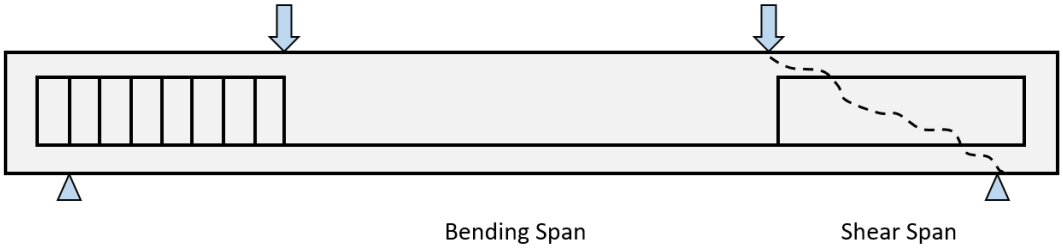

Figure 4-23. Scheme for four-point statistic bending test

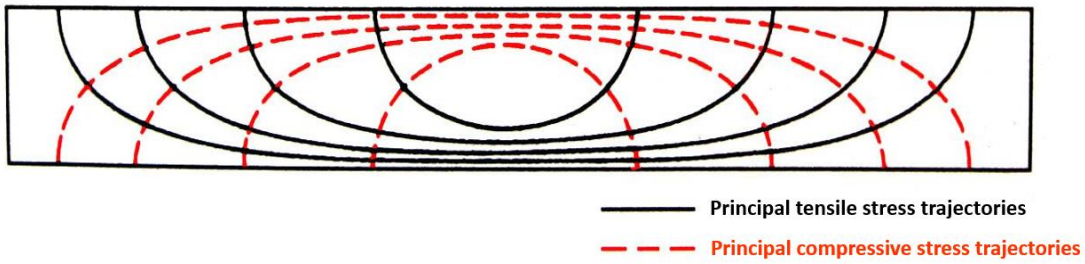

Figure 4-24. Principal stress trajectories in a homogeneous beam under four point bending arrangement

Before diagonal crack occurs, the beam is presumed as homogeneous. The principal tension stress and the principal compression stress at any point of the beam can be determined by the equations from material mechanics. Once the diagonal cracks occur, they are always along the direction of principal compressive stress trajectories as shown in Figure 4-24.

It is found that the main factors affecting shear resistance on diagonal section of bending member are the ratio of shear span to the effective depth, and strength of concrete. Normally, as the shear span to the effective depth ($\lambda = a/h_0$) ratio decreases,

the shear strength increases. (Attributed to the beneficial effect of direct load transfer to the support by arch action or so-called strut-and-tie load transfer mechanism.) The transition point between the arch action and beam action (or transfer beams and normal beams) lies between λ ratio of 1.45 to 1.78. Either side of this λ ratio, behaviour of RC beams, in terms of load resisting mechanism, failure pattern and the noise at failure, were entirely different (Londhe 2011).

Based on the range of different λ value, the diagonal failure modes can be simply classified and summarized as follows:

When $\lambda<1$, the diagonal-compression failure occurs as shown in Figure 4-25. The principal compression stress of concrete in the area near the support exceeds the compressive strength of concrete and the concrete between the support and loading point is crushed by the principal compression. In this case, the shear resistance highly depends on the compressive strength of concrete and it has a significant influence on the shear capacity of the beam.

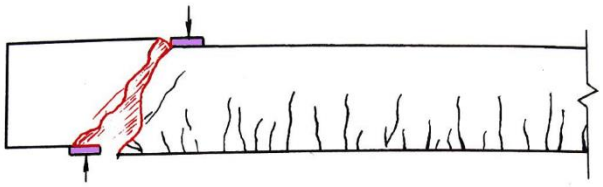

Figure 4-25. Diagonal compression failure - Shear strength depends on compressive strength of concrete

When $1<\lambda<3$, the shear-compression failure occurs. During the whole loading process many cracks could occur simultaneously. The shear-compressive zone of concrete gets smaller and the concrete stress in the residual zone is increasing under both normal stress and shear stress until the concrete strength under bi-axial loads has been exceeded. Eventually the concrete will be crushed. In this case, the shear resistance mainly depends on the concrete strength under bi-axial loads.

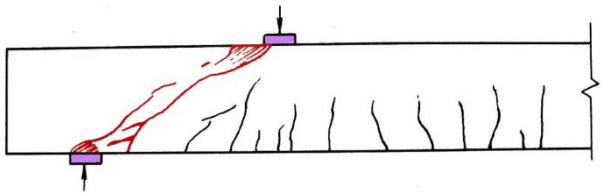

Figure 4-26. Shear compression failure - Shear strength depends on concrete strength under bi-axial loads

When $\lambda > 3$, the diagonal-tension failure occurs as shown in Figure 4-27. The shear stress increases rapidly in the residual concrete section, and the principal tensile stress in the compression zone exceeds the tensile strength of concrete at the same time. Normally there will be only one diagonal crack occurred with relatively larger width. Along two sides of the crack, concrete structure is split away into two parts. In this case, the shear resistance highly depends on the tensile strength of concrete. However, for concrete, the tensile strength does not increase proportionally as the strength level of the concrete increases, so it only has limited effect on the shear resistance of the beam.

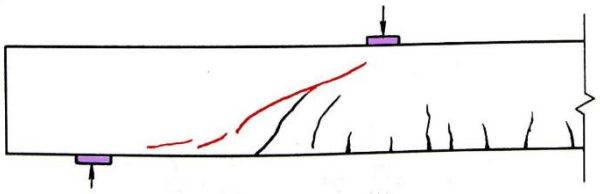

Figure 4-27. Diagonal splitting failure - Shear strength depends on tensile strength of concrete

A group of schematics of cracking and failure patterns under different shear span ratio λ is shown in Figure 4-28.

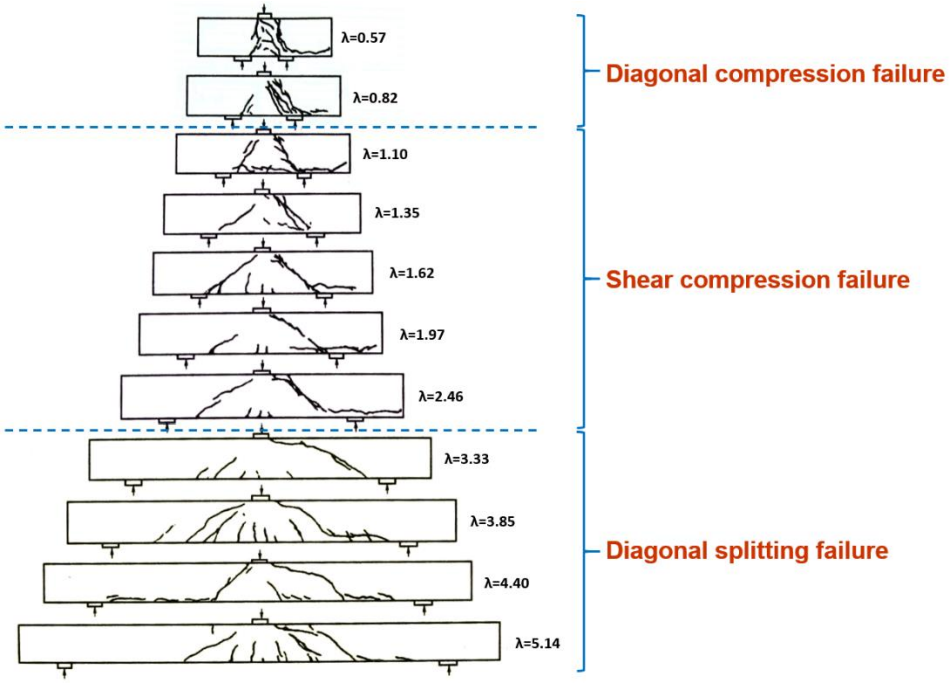

Figure 4-28. Schematic of cracking pattern under different shear span ratio λ

4.5.3 Specimen preparation

In order to make sure that the generation of the flexural failure and diagonal-shear failure could both be achieved during testing, RC beams of dimensions 100mm×150mm×1200mm were designed as shown in Figure 4-29. Seven stirrups were arranged in the shear span on the left-hand side to increase the shearing capacity and two stirrups are arranged on the right-hand side so the diagonal-shear failure could occur and be located in this region.

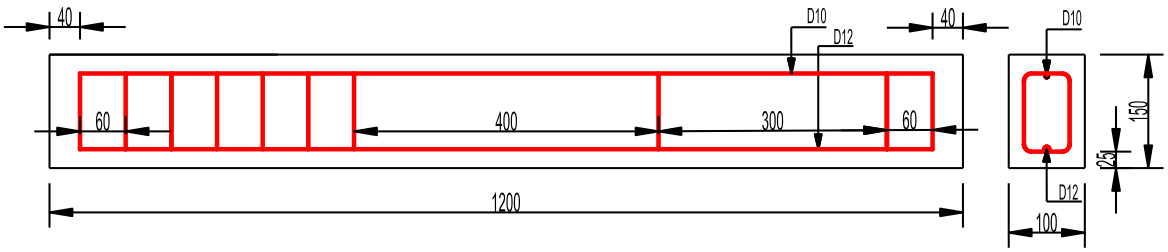

Figure 4-29 Sectional view of the specimen

As described previously, the shear span to effective depth ($\lambda = a/h_0$) ratio is set to 1.44 in this study. The reinforcements and moulds used for beam casting are shown in Figure 4-30.

Figure 4-30 Reinforcement and mould for beam casting

The concrete mix of the specimen in this experiment is shown in Table 4-6. And the mechanical properties are given in Table 4-7. These are determined from the standard cube test and cylinder test at the age of 28 days.

Table 4-6. Proportions of concrete mix

Grade	W/C	Cement	Water	Fine Agg. (0-4mm)	Coarse Agg. (4-10mm)
C40	0.46	1	0.46	1.93	2.25

Table 4-7. Mechanical properties

Cube No.	28 days cube compressive strength f_c(MPa)	Average (MPa)	Cylinder No.	28 days cylinder splitting strength (MPa)	Average (MPa)	P wave velocity (m/s)
1	50.4	53.3	1	3.8	4.0	4030
2	56.6		2	4.2		
3	52.9		3	4.1		

4.5.4 Experimental Procedure

As AE signals attenuate significantly and the wave amplitude decreases immediately in concrete as they propagate, it is essential to assure that the whole target area is covered with AE sensors in the SiGMA analysis. The sensor arrangement is shown in Figure 4-31 and the corresponding coordinates shown in Table 4-8.

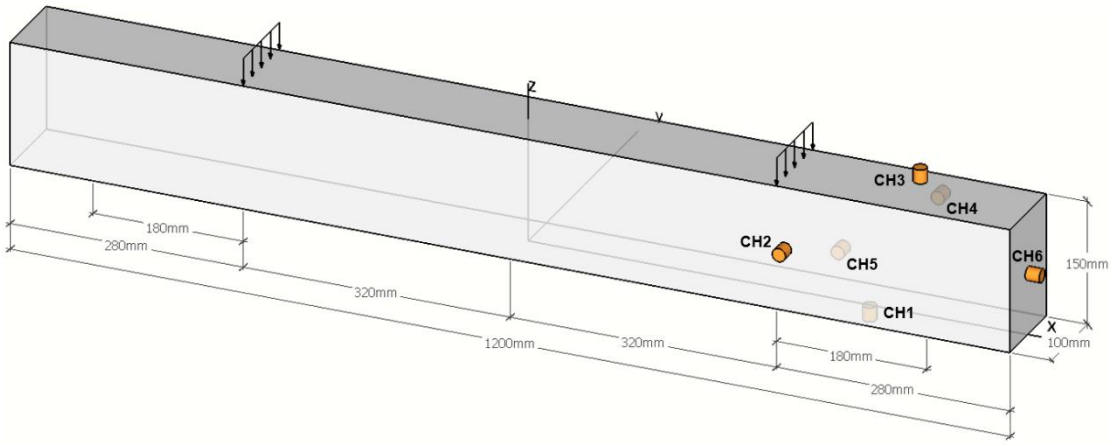

Figure 4-31. AE sensors arrangement of the beam (shear span ratio λ=1.44)

Table 4-8. Coordinates of the six sensors attached on the beam

Sensor coordinates on the beam			
Sensor No.	**x(mm)**	**y(mm)**	**z(mm)**
Sensor 1	410	0	0
Sensor 2	330	-50	75
Sensor 3	460	0	150
Sensor 4	470	50	120
Sensor 5	350	50	30
Sensor 6	600	0	75

The test of the beam subjected to a four-point bending setup is carried out, AE signals are recorded by six AE sensors of 150 kHz resonance (R15I-AST, PAC) at 2 MHz sampling frequency. The whole area of the shear span without stirrups is covered by all six AE sensors as shown above in Figure 4-31.During the test, the LVDT (Linear Variable Displacement Transducer) is applied to measure the beam central displacement.

Figure 4-32 shows the history of load versus displacement. It should be noticed that in order to ensure that the data file would not exceed the software capability to post-process, there are three pauses in between during whole loading history to split the datafile into four executable subfiles. It can be seen that the ultimate failure load of the beam is 102.6kN. The first obvious change of slope occurred at about 19.2kN and the second significant change of slope occurred at around 97.9kN. Based on these two critical points, the whole loading process was divided into three stages normally referred as elastic stage, cracking stage and failure stage.

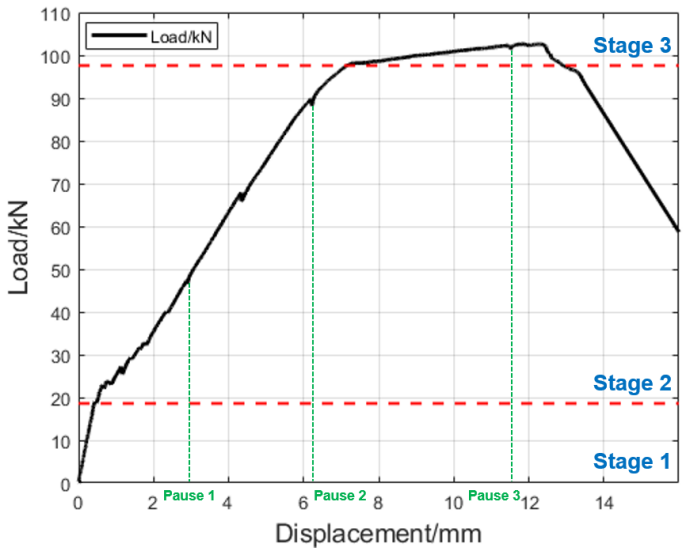

Figure 4-32. Load-displacement curve of the beam as three stages identified

The ultimate failure mode of the beam is shown in Figure 4-33, and it can be seen that several bending cracks occurred in the mid-span and the shear compression failure is occurred eventually on the side of the shear span without stirrups.

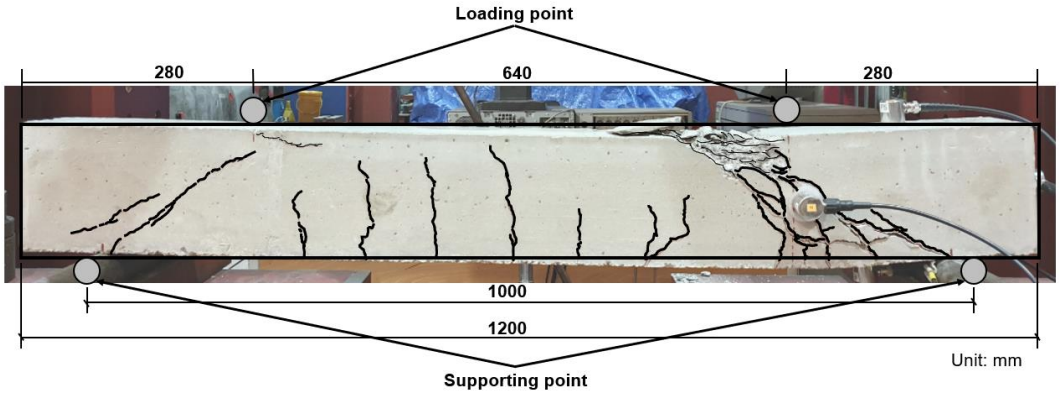

Figure 4-33. The ultimate failure mode of the beam (λ=1.44)

4.5.5 AE parameters-based analysis

As described previously, AE parameter analysis can be used to classify cracks into two types of tensile mode and shear mode (JCMS-III B5706-2003 code). Here, RA value (the rise time/the maximum amplitude) and average frequency (AE counts / the duration time) are applied to the analysis. In total, 87.4% AE hits are categorised into tensile cracks while 12.6% AE hit categorised into shear cracks. The parameter-based classification results of each channel during each stage are present in Figure 4-34. The total ratio of shear-mode cracks and tensile-mode cracks of each channel are

shown in Figure 4-35.

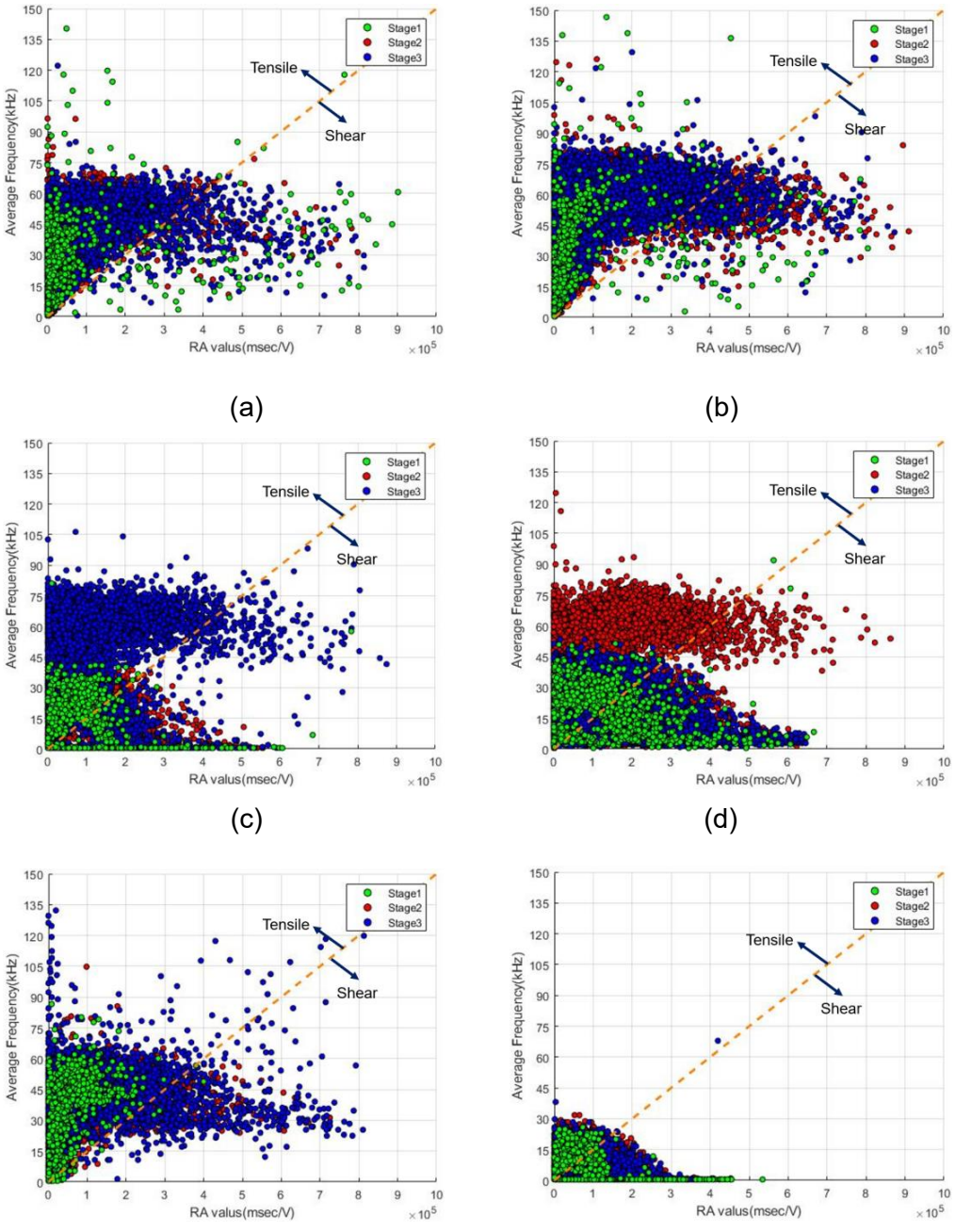

(a) Channel 1, (b) Channel 2, (c) Channel 3, (d) Channel 4, (e) Channel 5, (f) Channel 6.

Figure 4-34 Classification results based on AE parameters of three stages for each channel

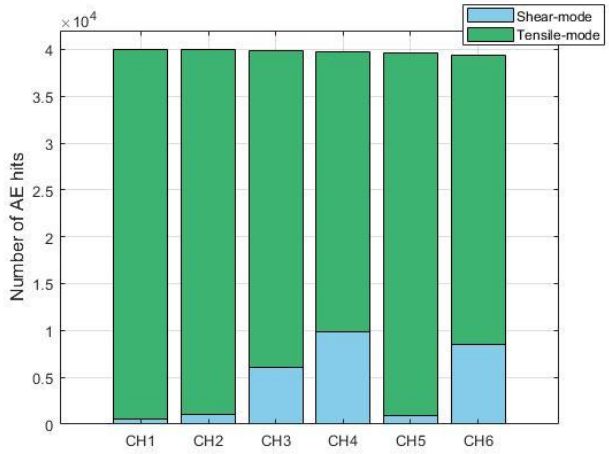

Figure 4-35 Results of AE parameter analysis for each channel from the beam

It is noticed from Figure 4-35 that the ratio of shear-mode cracks and tensile-mode cracks are all different from each channel. The shear-mode ratio from channel 3,4 and 6 are much higher than the other channels. On the contrary, the tensile-mode cracks dominate channel 1,2 and 5 while only limited shear-mode cracks shown up. It is speculated that as sensor 1 is attached on the bottom of the beam and sensor 2 and 5 are closer to the mid-span where the initiation of bending cracks occurred, more signals due to the tensile cracks from bending might be detected selectively by those three sensors than the others in the early stage of cracking.

4.5.6 SiGMA procedure-based analysis

Figure 4-36 (a) - (d) presents the MTA solution obtained in four time periods by carrying out the SiGMA procedure. Instead of presenting by the focal mechanism with source sphere, each source event is presented by a penny-shaped disk with a crack motion vector. To clearly show the source mechanism modes without interference, it is presented separately from the crack motion vector overlaid above. During each period of time presented in Figure 4-36 (a) - (d), the graph on the left shows the distribution of different source mechanism represented by the penny-shaped disks in different colour and the graph on the right shows the corresponding crack motion vectors.

The Event Definition Time (EDT) value is set to 68μs which is the maximum time difference between the TOA of two signals/waveforms caught by two different sensors (Channel 2 to Channel 6 in this study) in order to consider these signals part of the

same waveform event. It is critical to accurate source location as accurate $\triangle t$ is required.

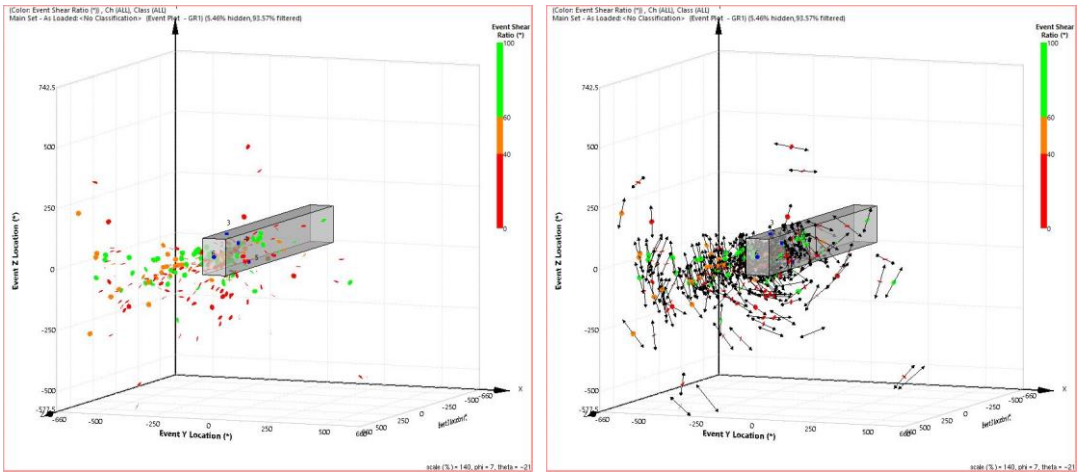

(a) During 0~352s;

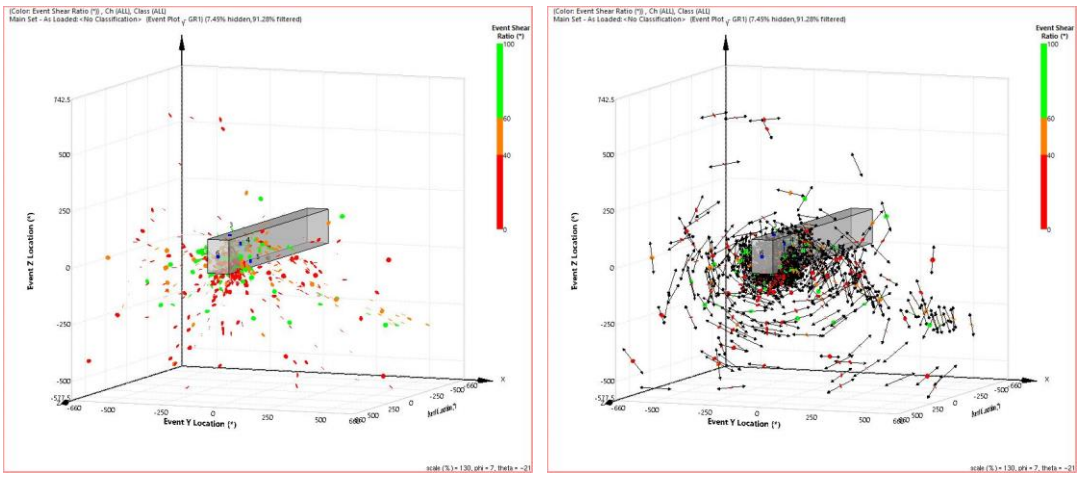

(b) During 352~658s;

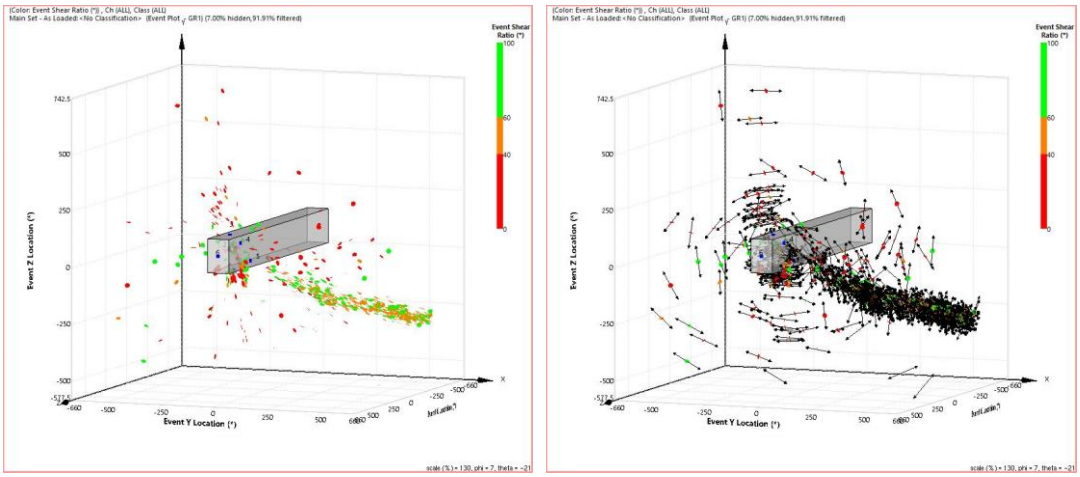

(c) During 658~1008s;

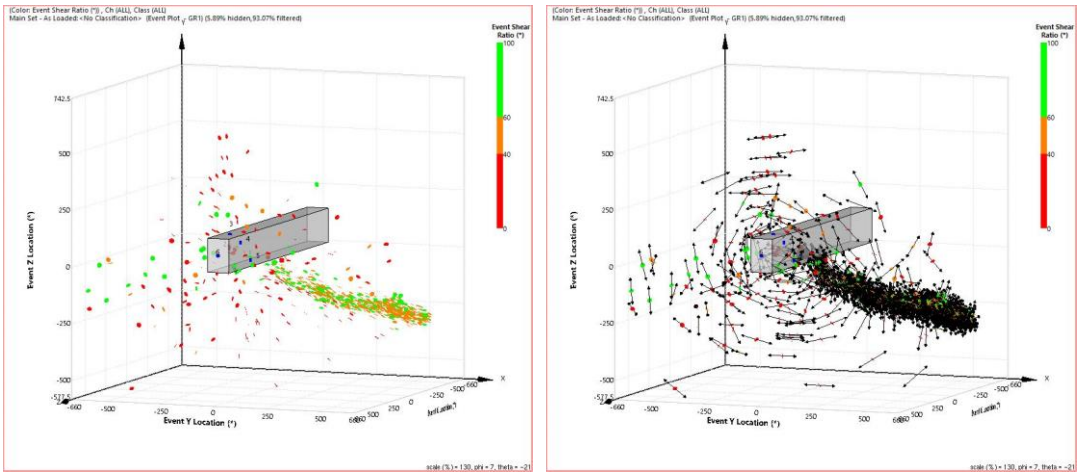

(d) During 1008~1185s.

Figure 4-36. MTA mechanism solutions of AE during four time periods in the beam under four-point bending

The results of MTA correlates to the cracks at the ultimate failure is shown in Figure 4-37, projected onto the x-z plane. Tensile cracks where the event shear ratio is less than 40% are indicated in red (●); shear cracks where the event shear ratio is greater than 60% are represented in green (●). Mixed mode cracks where the event shear ratio is between 40% and 60% are represented in orange (●).

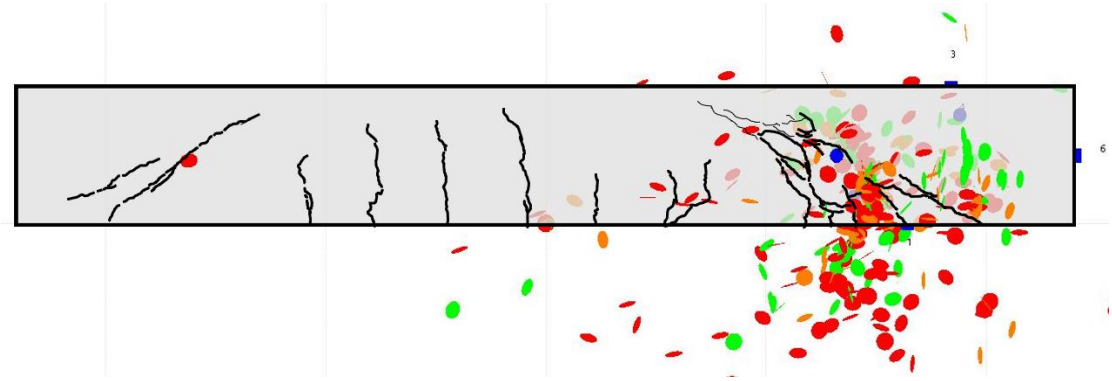

(a) During 0~352s;

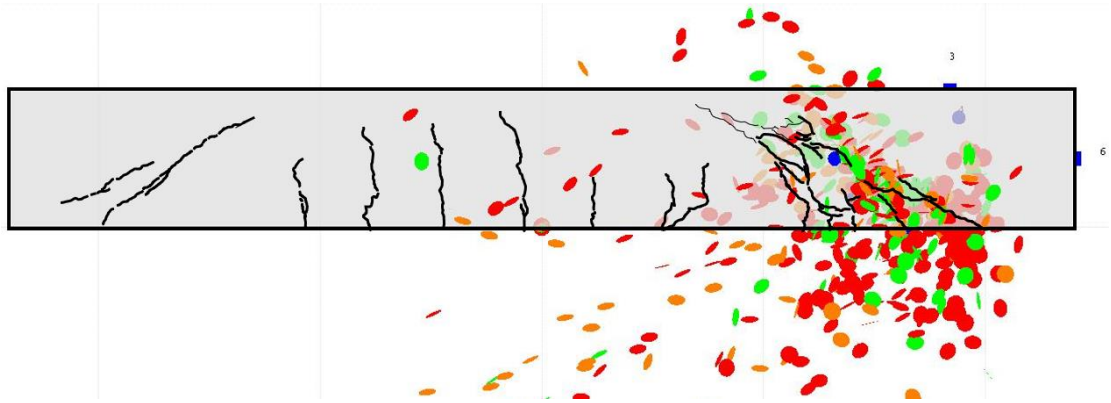

(b) during 352~658s;

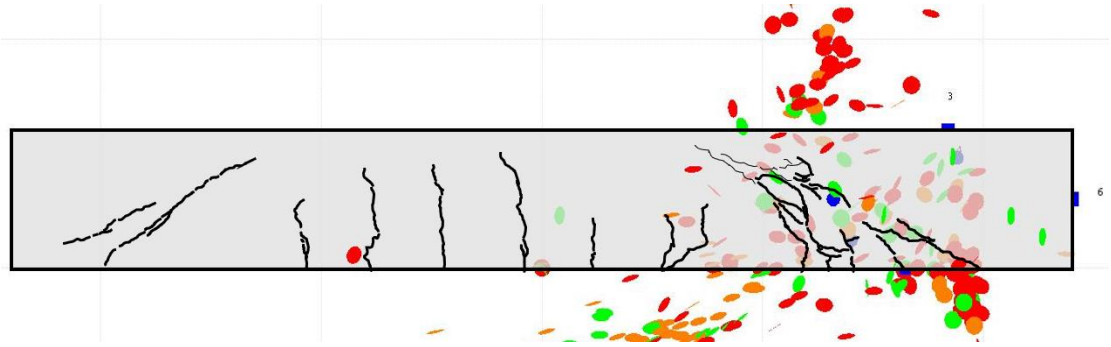

(c) During 658~1008s;

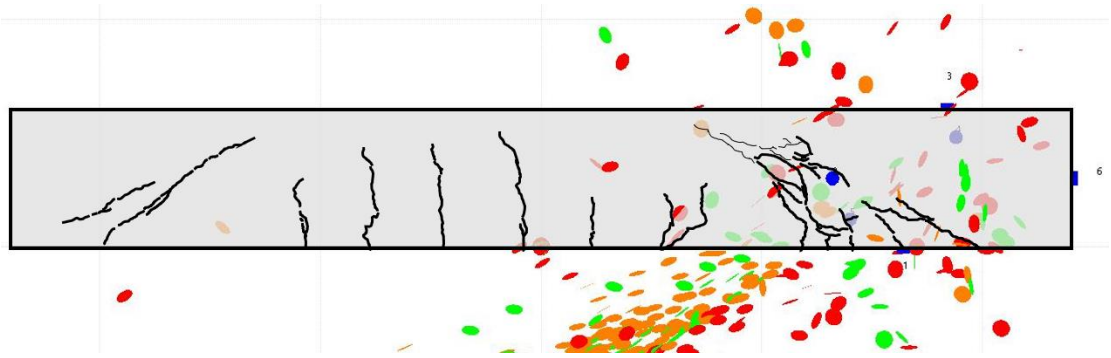

(d) During 1008~1185s

Figure 4-37. Results of crack locations and types determined of MTA

Both from Figure 4-36 and Figure 4-37, it is obvious to see that there is a significant number of events located both outside the sensor array and beam geometry, which should be discarded as invalid events. In this test, totally there are 238626 waveforms obtained and 39187 events are created. Among them, only 18101 events can be available to be processed by the SiGMA procedure for calculation of moment tensor. Further, if the determination process of moment tensor components leads to

erroneous results, or outside geometry location vector, then that particular event will be discarded as invalid event. In that case only 2460 valid events remained in total and that only accounts for approximately 6.7% of the total located events. Table 4-9 summarises the overview and details of all valid data from all the results obtained.

Table 4-9. Overview of data set from MTA processed results

Duration	Number of total hits/waveforms	Located events	Available events for executing SiGMA	Invalid	Percentage of valid events
0~352s	52326	8652	3378	2862	5.96%
352~658s	77795	12965	6812	5813	7.71%
658~1008s	51992	8665	4205	3632	6.61%
1008~1185s	56513	8905	3706	3154	6.20%
sum	238626	39187	18101	15461	Average: 6.74%

The reason that the number of signals to which the SiGMA analysis is applicable is very limited lies in most of the events does not have all six clear P wave portions to be correctly determined due to the excessive signal attenuation and noesis as well in concrete. Furthermore, the accuracy of 3D-location in SiGMA procedure depends on the TOA algorithm which require accurate $\triangle t$ (difference of arrival time), and that requires ideal geometry of specimen and depends on the signal propagation path as well. It is known that the existence of reinforcement bars, aggregates, damage and cracks, voids and irregular boundary conditions will affect the signal propagation and influence the $\triangle t$ values, resulting in the poor calculation results of 3D-source location which is necessary for the MTA analysis.

The above reasons eventually lead to only approximately 6-7% of the total events can be applicable for MTA analysis. Comparing to other people's work, most of them have encountered the same problem. For example, Beck (2004) conducted a four-point flexure test on a notched concrete beam to apply MTA. Eventually 65 events are recorded where only 17 of them are applicable for performing the SiGMA procedure.

4.5.7 Comparison of parameter-based analysis and SiGMA analysis

The difference between the AE parameter-based analysis and the SiGMA analysis could result from the fact that the parameter-based analysis is carried out for all AE hits from all channels, while the SiGMA analysis is applied to only AE events. As most of tensile-mode signals are generated from the bending cracks in the mid-span, they might be detected from any of the sensors as individual hit rather than a located event, and this could be the reason that the ratio of tensile-mode in parameter-based analysis at any particular stage could be higher.

The parameter-based analysis results in shown in Figure 4-38 while the SiGMA analysis results is shown in Figure 4-39.

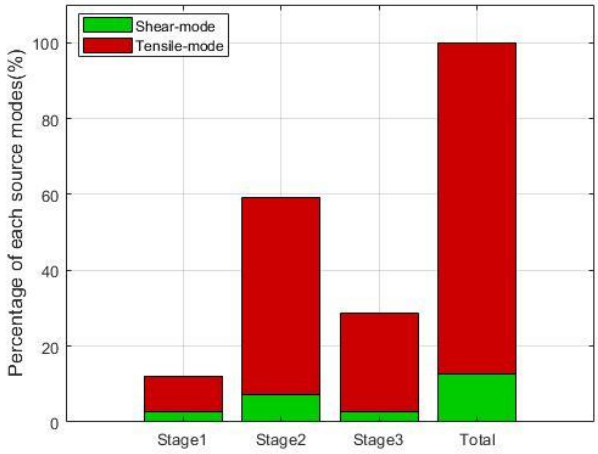

Figure 4-38. Classification results from parameter-based analysis in each stage

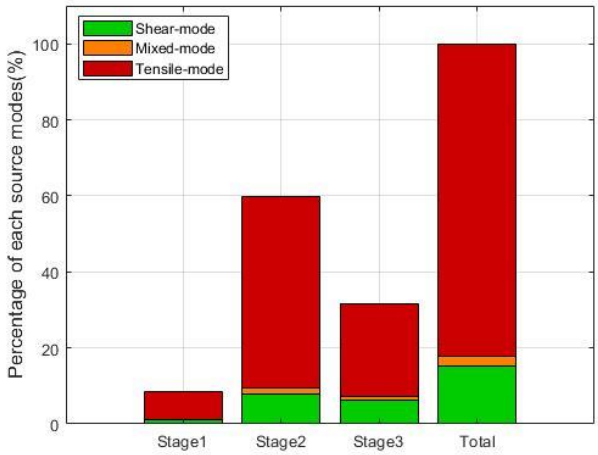

Figure 4-39. Classification results from SiGMA procedure analysis in each stage

Even there are only very limited data that are applicable to carry out the SiGMA analysis, for those successfully processed events they still show a quite reasonable and promising agreement with parameter-based results.

4.5.8 Discussion

Based on the results above, it can be summarised that there are three main reasons causing a great number of the invalid events to be carried out SiGMA procedure:

1. Lack of sufficient and effective waveforms to extract information and determine the moment tensor components.

2. Moment tensor components can be determined, but calculation regarding location vectors, motion vectors and normal vectors lead to erroneous results, such as the event location outside the geometry range of the specimen.

3. No results, or out of limits results, or negative percentages of shear ratio results shown up, even though the SiGMA procedure can be successfully carried out.

Due to those reason described above, there a significant amount of events needs to be excluded and only limited data remained for post-processing SiGMA procedure of MTA. The diagonal shear failure damage to the concrete identified by visual inspection suggested that the SiGMA procedure is still capable of determining the damage location and identifying the damage mechanisms as those limited data still shows a promising agreement with results obtained via the conventional parameter-based method.

4.6 Comparison of advantages and disadvantages of the different analysis methods

From the study of section 4.4 and section 4.5, and correlated to the waveforms-based analysis in Chapter 0, the comparison of parameter-based analysis, SiGMA analysis and waveform-based analysis are given in Table 4-10.

Table 4-10. Comparison of three AE analysis methods

Items \ Method		Parameter - based	SiGMA procedure	Waveform-based
Detection range		Wide	Limited	Wide
Location	1D (Linear)	2 sensors at least	2 sensors at least	2 sensors at least
	2D (planar)	3 sensors at least	3 sensors at least	3 sensors at least
	3D (Spatial)	4 sensors at least	4 sensors at least	4 sensors at least
Fast real-time data analysis		Yes (PC memory)	No	No
Statistical analysis		Yes (PC memory)	No	Yes (PC memory)
Amplitude analysis		Only based on statistical analysis	Require minimum resolution	Require minimum resolution
Frequency analysis		No	No	Require broadband sensors
Waveform analysis		No	Yes	Require corresponding Sampling frequency
Failure analysis	Cracking orientation	No	Yes	No
	Cracking size	No	Yes	No
	Cracking energy	No	Yes	Yes
	Cracking mode	No	Yes	No

4.7 Conclusions

This chapter has investigated the feasibility of Moment Tensor Analysis (MTA). Prior to a four-point bending failure test under static load, a preliminary test was conducted on a concrete cube to evaluate the SiGMA procedure. Even though it is assumed that clear and defined initial P waves could be produced with the excitation of artificial H-N source, due to the nature of MTA for the strict requirements regarding number of sensors, accurate information extracted from signals and high attenuation character of concrete, the results show that still many events cannot be located. Even

for those located event, still there is a significant number of them that the SiGMA procedure cannot be successfully executed and lead to erroneous results. Nevertheless, for those valid events performed with SiGMA procedure shows a promising agreement with results obtained via the conventional parameter-based method, and additionally it has been proved that its abilities to identify where those mixed mode cracking has occurred.

In order to determine where each onset time starts related to the TOA of a waveform and also to determine its amplitude (positive or negative), a secured way is to examine each individual waveform, zoom in to the area close to the pre-trigger point-in-time to identify the accurate onset time. It is crucial to the success of carrying out SiGMA procedure for MTA when examining AE waveforms. But in practice, it is neither feasible nor realistic for on-site inspection and monitoring of engineering structures when dealing with mass amount of data.

To validate the use of MTA for the characterisation of AE sources, it is recommended that the interest area is covered by the sensor array without too long propagation path to avoid significant attenuation. Applying an advanced denoising technique which is proper for AE signals from concrete, combining the improvement of existing algorithm and software could provide a clearer understanding, leading to a viable technique for assessing the source mechanisms and failure modes of concrete structure. It is also recommended that a series of similar lab-scale tests with known damage modes of failure pre-designed to be conducted for further MTA analysis to verify the accuracy and feasibility regarding location and source kinematics.

Chapter 5 Damage Detection and Evaluation of Vascular Network Based Self-Healing Concrete

The advantages of AE lie in its sensitivity to damage growth and corresponding changes occurring inside the material which makes it promising for detection and quantification of damage in real time. In that case, AE is highly capable of monitoring the internal conditions of concrete structures under load and assisting in improving the efficiency of self-healing concrete. Associated AE parameters, such as amplitude, rise time, duration, signal strength and counts, can be extracted from AE waveforms. These types of parameters have been previously analysed to provide insight of damage mechanism and failure mode.

The work in this chapter is trying to address detection of damage evolution both in concrete and self-healing concrete with focus on the mechanical properties and AE responses. The results could be utilized to provide information and guide for the design and improvements of performance end efficiency of self-healing concrete.

5.1 Specimen preparation and experimental setup

Currently there are four main self-healing techniques developed from the RM4L project (Joseph et al. 2010): (i) microcapsules releasing healing agents when damaged; (ii) bacterial healing filling cracks with calcium carbonate; (iii) shape memory polymers minimising the crack width after damage and (iv) vascular flow networks supplying healing agents due to capillary force.

This chapter aims at studying the application of AE on self-healing concrete based on using the 2D vascular network in concrete as a system for hosting the self-healing agent. Cyanoacrylates were selected as a potential self-healing agent which were injected into the polyethylene based capillary tubes after damage.

5.1.1 Concrete specimen preparation

Twelve beam specimens of size 75mm x 75mm x 255mm were cast in this study. The beam moulds contained pre-drilled holes in the end plates, four at either end of

each specimen. 4mm outer diameter capillary tubes(made of polyurethane tubing) were applied for reserving the space for the latter addition of the vascular healing network. The tubes were secured into place using crocodile clips and kept in tension to ensure no deformation or sagging occurred during casting as shown in Figure 5-1. The details of the specimen mould and concrete mix are shown in Table 5-1 and Figure 5-1.

Table 5-1. Proportions of concrete mix

Grade/type	W/C Ratio	Cement	Water	Fine Aggregates (0-4mm)	Coarse Aggregates (4-10mm)
Origin	/	Portland-limestone cement CEM II/A-L 32,5R	Normal tap water	Crushed marine sand with limestone	Crushed limestone
C40 mix ratio	0.46	1	0.46	1.93	2.25
Concrete (kg/m^3)	/	470 kg/m^3	216.2 kg/m^3	907.1 kg/m^3	1057.5 kg/m^3

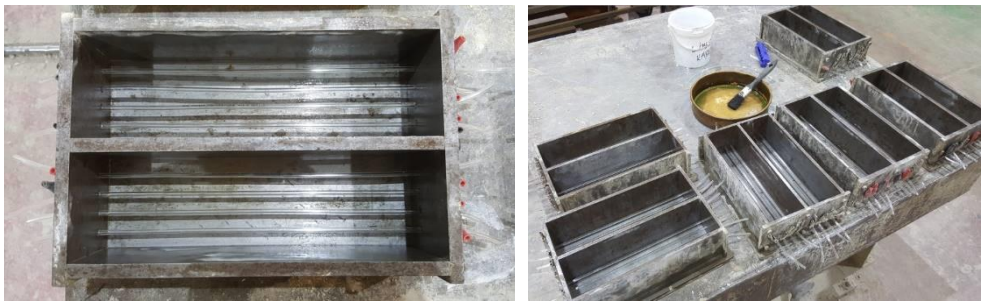

Figure 5-1. The double specimen moulds with capillary tubes placed

All the specimens were supposed to be tested on their 7-days age. In order to avoid the impact to the material properties caused by the excess water in the pore matrix, the oven was applied beforehand to remove all water content. After curing for five days in a water bath at 20°C and one day in the oven at 95°C, a 6mm rectangular notch was sawn at the centre line of the bottom surface of each beam Then all specimens were drilled at the channel openings to widen the diameter of the capillary tube hole to 6mm at a depth of 10mm; air was blown through the channels afterwards to remove any concrete dust from drilling. Polyethylene tubing, with an outer diameter of 6mm and inner diameter of 4mm, was cut to a length of 120mm and then inserted

and glued into the drilled-out channel ends. This was done in order to have continuous 4mm channel for the healing agent to flow. Two knife edges, used for the Crack Mouth Opening Displacement (CMOD) clip gauge, were glued on both sides of the notch on the bottom surface of the specimens. An aluminium, L-shaped deflection bracket, used for the LVDT (Linear Variable Displacement Transducer), was glued onto a side surface, overhanging the bottom edge (shown in Figure 5-2).

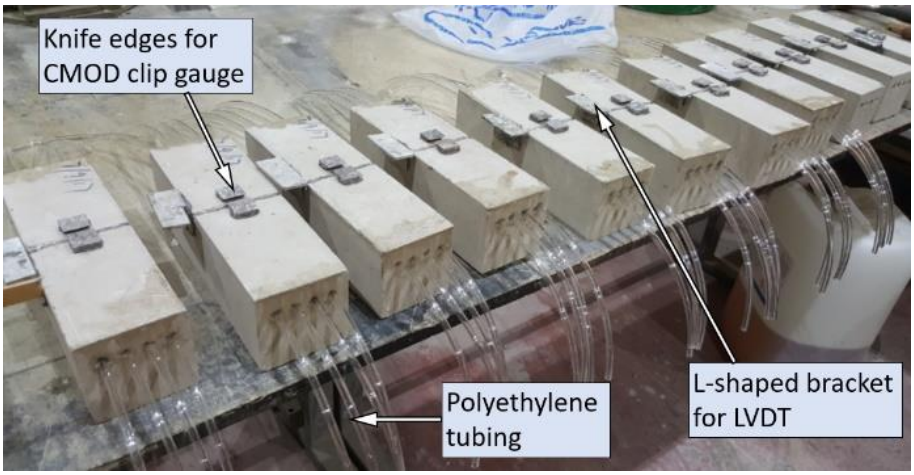

Figure 5-2. Specimen preparation and setup

5.1.2 Healing agents

More recently, researchers at Cardiff University have undertaken a substantial parametric study on self-healing cementitious materials (SHCMs) and adhesive-based self-healing of concrete beams. The main healing materials and agents that have been proposed to date and widely employed to SHCMs include polyurethane (PU), sodium silicate, methyl-methacrylate, bacteria, epoxy resins and cyanoacrylates. The techniques for storage and delivery mainly comprise the systems based on micro-encapsulation, macro-encapsulation and embedded vascular networks (Selvarajoo et al. 2020).

These healing agents have generally been “off the shelf” agents. The relatively “low cost” and readily available nature of “off the shelf” products are important assets that must be possessed by any healing agent proposed for application to a large bulk material, such as concrete. In addition to being readily available and cost effective, a

suitable agent for the autonomic healing of cementitious materials should (Ghosh 2009):

(1) have the ability to be readily encapsulated;

(2) have sufficient mobility to reach crack locations following release;

(3) have sufficient mechanical properties post-curing to resist crack reopening; and

(4) have sufficient long-term durability and compatibility with the cementitious matrix.

In this study, cyanoacrylate of type PC20 was used as the healing agent because of the main advantage of rapid curing due to acidity of glue and alkalinity of concrete (pH of approximately 13). They provide a bond strength that often exceeds the strength of the substrate, certainly in the case of concrete. Moreover, the viscosity of cyanoacrylate PC20 is less than 10 centipoise which means that it possesses the ability to heal cracks less than 100 μm in thickness efficiently. For example, water has a viscosity of 1 centipoise (1 $mP \cdot s$), milk is 3 centipoises, and grade 10 light oil is 85-140 centipoises (Joseph et al. 2010). However, if the setting time is too quick, the dispersion of the healing agent within the crack may be insufficient.

5.2 Testing methods

5.2.1 Experiment setup

The experiments consisted of four sets of three beams. Apart from one set of three control beams, each set comprise three beams tested under three-point loading with different paused time with input of self-healing agent (cyanoacrylates PC20) between 1st loading stage (initial loading) and 2nd loading (reloading) stage. The test arrangement is shown below in Figure 5-3.

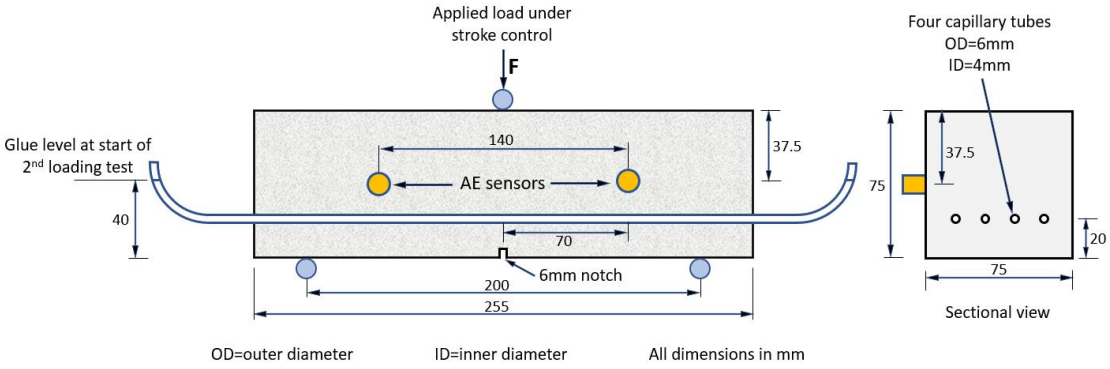

Figure 5-3. Test arrangement for self-healing experiments on notched beams

5.2.2 Instrumentation

AE signals were recorded with a MISTRAS EXPRESS-8 Eight-Channel system. A full suite of the AE Win software was installed on the PC. The acquisition parameters adopted in the study are listed in Table 5-2. The couplant grease from Electrolube company was used as the coupling. Steel pads were bonded to the concrete and magnetic clamps were used to hold the sensors on the surface of the specimens. Two R15I-AST sensors (70-200kHz) were attached on one side of the specimen with 140mm distance between each other, as shown in Figure 5-4 (a) and (b).

Table 5-2. The parameters adopted during AE data acquisition

Parameter	Value
Threshold	45 dB
Velocity	4030 m/s
Hit definition time (HDT)	800 ms
Peak definition time (PDT)	200 ms
Hit lockout time (HLT)	1000 ms

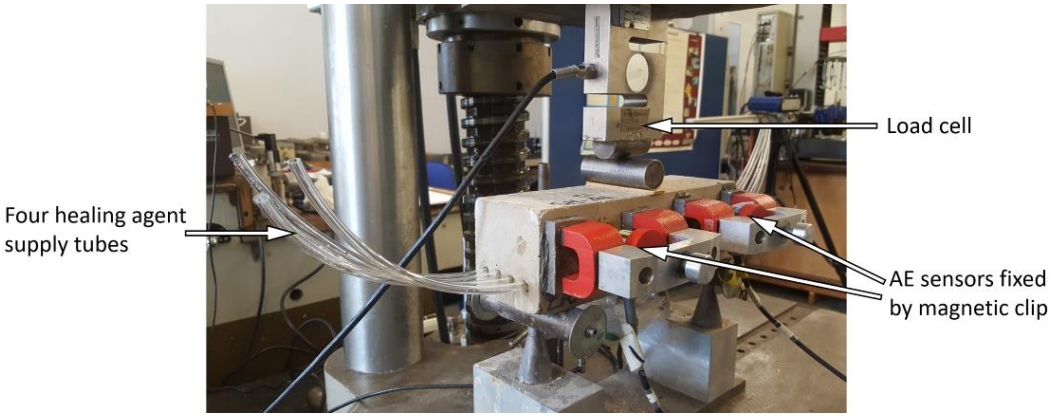

(a)

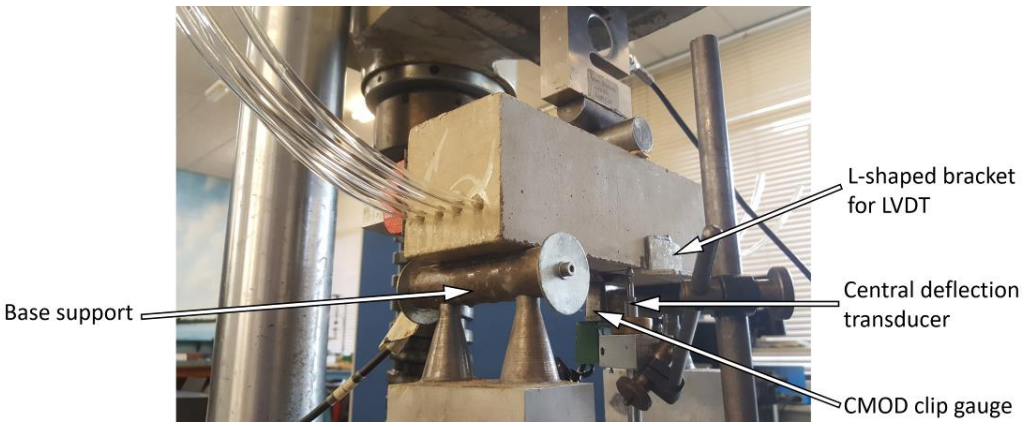

(b)

Figure 5-4. Experiment setup (a) front view; (b) back view.

5.2.3 Loading conditions

As shown in Figure 5-4, each specimen is subjected to three-point bending. The whole loading process is divided into two parts. Firstly, the load increased monotonically with a rate of 0.0002 mm/s until the CMOD reached 0.15mm. After unloading, healing agent (cyanoacrylate PC20) was injected into all tubes to the height as shown in Figure 5-3. Then the test was paused and the specimen was removed from the machine for different periods of time (1-hour, 24-hours and 3-days) before the reloading test. Secondly, after the specimen was healed, it was loaded monotonically again with the same rate of 0.0002 mm/s until the CMOD reached 0.30mm.

5.3 Results and discussion

As shown in Figure 5-5 below, the Load-CMOD curves for both reference (without healing agent, grey colour) and 24hrs-healing (blue colour) concrete beams are presented at the initial loading and reloading stages. The Roman numerals refer to the five stages that describe the progressive fracture process.

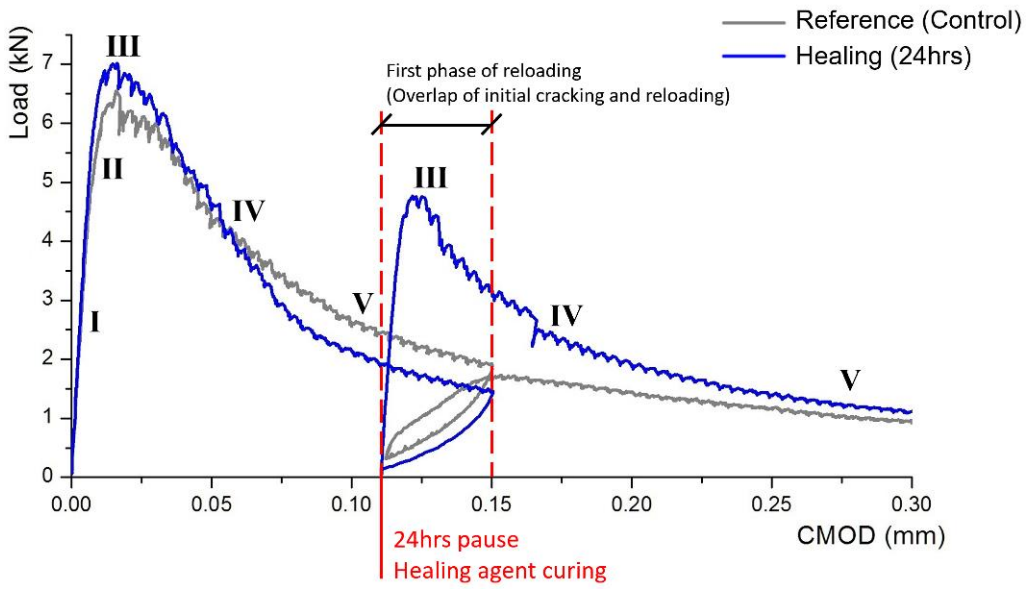

Figure 5-5. Example of the Load-CMOD graphs for control specimen (grey curve) and 24hrs self-healing (blue curve) specimen through the whole testing process.

According to the fracture theory for concrete (Mier 2017), the following crack propagation stages is highlighted (marked with Roman numerals in Figure 5-5).

I. Initially, the Load-CMOD curve evolves linearly;

II. The elastic deformation ends as micro-cracks form at the pre-crack stage and accumulate to a macro-crack;

III. The macro-crack forms as the ultimate load is reached;

IV. The crack continues to propagate;

V. The crack can no longer resist opening and widens.

5.3.1 Strength regained ratio of self-healing concrete

The results of the initial loading test (before the injection of healing agent) and the reloading test (after healing agent is injected and cracks are healed) with the peak load achieved are shown in Table 5-3. The control beams (C1 to C3) had already failed after the first three-points bending test. Therefore, the strength fell by an average of around 75% in the reloading process.

However, those specimens which were healed by cyanoacrylate with different

healing time (1-hour, 24-hours, and 3-days) carried further loading in the reloading test. Around 50%~70% original strength of specimens (batches of SH-A, SH-B and SH-C) were recovered and the maximum reached 85.8%.

The method used to measure the strength recovery from the macro-scale experiments is normally straightforward in terms of the evaluation of healing performance. The strength recovery ratio depends on a peak load (or stress), a measurement of the remaining strength (load or stress) at the time healing is initiated and the strength (load or stress) after healing has occurred(Davies 2014). Homma et al.(2009) has defined the strength recovery rate(c_γ) to compare the strength recovery due to the self-healing of FRCC (Fibre Reinforced cementitious composites) specimen, and that index is introduced and represented by c_γ in equation 5.1 and illustrated in Figure 5-6.

$$c_\gamma = \frac{P_2 - P_0}{P_1 - P_0} \times 100\% \tag{5.1}$$

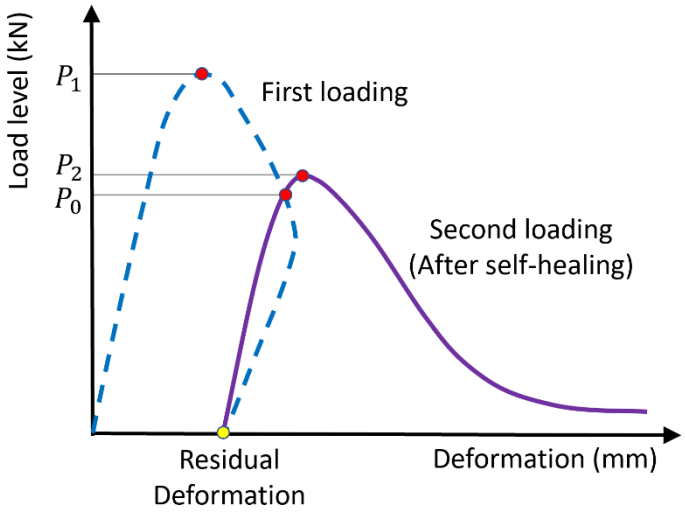

Figure 5-6. Schematic of the relationship between load and deformation of self-healing specimen

Based on the equation 5.1 above, the strength recovery (c_γ) is calculated in Table 5-3. This equation is of the same form as that presented by Homma et al.(2009) but with load (kN) replacing stress and CMOD (mm) replacing elongation (or deformation).

Table 5-3. Mechanical results of initial loading and reloading

Healing Agent	Specimen No.	1st Loading/kN	time of rest period	2nd Loading/kN	Strength Recovery/%	Average/%	CoV/%
No	C1	6.55	No	1.73	/	/	/
	C2	6.11		1.47	/		
	C3	6.13		1.59	/		
Cyanoac-rylate PC 20	SH-A1	6.67	1-hour	4.44	51.7%	48.7%	20.5%
	SH-A2	6.09		4.36	56.9%		
	SH-A3	5.98		3.72	37.6%		
	SH-B1	7	24-hours	4.81	57.1%	52.7%	12.2%
	SH-B2	7.02		4.76	55.5%		
	SH-B3	6.2		3.81	45.3%		
	SH-C1	5.27	3-days	4.71	85.8%	71.8%	20.0%
	SH-C2	6.18		4.92	72.4%		
	SH-C3	5.35		3.9	57.1%		

5.3.2 Characteristics of AE signals from damage in self-healing concrete

5.3.2.1 The amount of AE hits

Both of the four graphs in Figure 5-7 below show amplitude of the AE hits during the reloading stage for (a) control beam, (b) 1-hour healing beam, (c) 24-hours healing beam, and (d) 3-days healing beam. In those graphs, each red dot represents an AE hit. The loading curve is represented in black lines corresponding to the y-axis on the right.

One critical point worth mentioning, considering as the CMOD during reloading stage reaching 0.15mm (which is the previous unloading point), is indicated by a dotted line. Apparently, most of AE activities from healing products or consequences occur before the CMOD reached the previous maximum, which is 0.15mm, and that is why most of attention should be placed on the reloading stage just before the dotted line.

For the control beam, it can be seen that only few AE hits were found before the dotted line. This is because that there is no healing occurred and barely no new host matrix damage as well. It is only the process of crack re-opening of the original crack and consistent with the Kaiser effect as well. But plenty of AE hits show up after the dotted line in both of them. Those AE activities can be mainly attributed to the damage

of host matrix of concrete and formation of new microcracks and macrocracks.

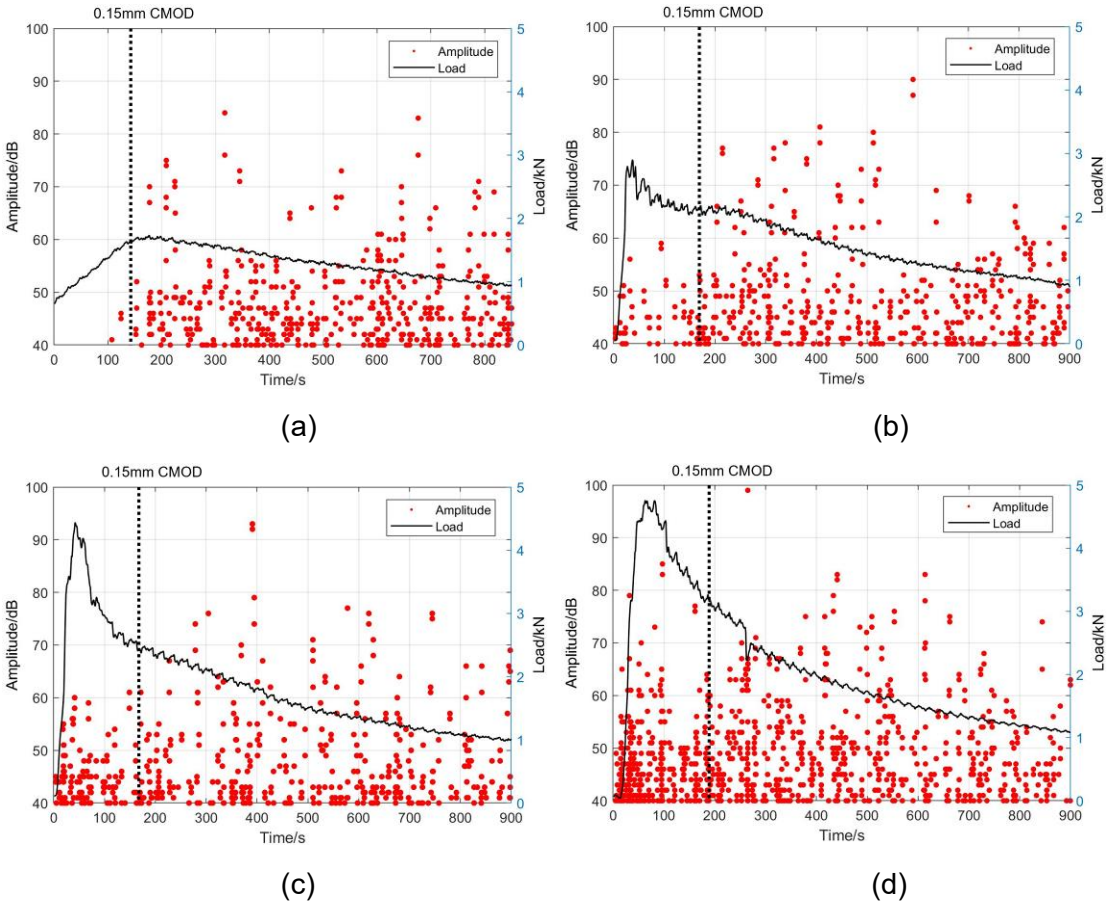

Figure 5-7. Amplitude of AE hits during the reloading stage for specimens: (a) control; (b) 1-hour healing; (c) 24-hours healing; (d) 3-days healing;

In terms of those hits before the dotted line in Figure 5-7(b), (c) and (d), it confirms that those emission are primarily attributed to the ‘healed damage’. But the difficulties lie in that it is hard to recognize whether those signals originate from the reopening of healed cracks or the formation of new cracks due to the higher strength of the bonding surface, or both processes. However, the appearance of those hits before the dotted line can still qualitatively indicate the effect of healing consequences and it can also be found that the longer pause time left for healing, the more AE hits are produced with relatively higher energy. That phenomenon matches with the mechanical response as well. Figure 5-8 gives a statistics of total number of hits before and after the 0.15mm CMOD dotted line of all specimens.

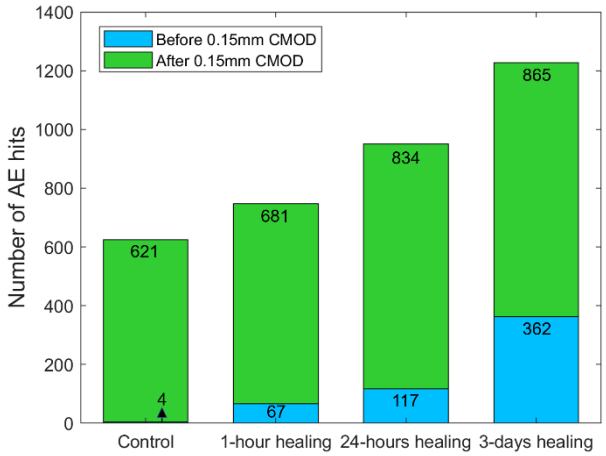

Figure 5-8. Number of AE hits in both initial loading and reloading stage for all specimens

During the stage of overlap of precracking and reloading, (indicated in Figure 5-5), theoretically the AE activities from this period of time are supposed to be coming from two different type of damage sources before the previous damage level (recognized by the value of CMOD) is exceeded after the specimens are healed. One of them is resulting from the sources of generation of new cracks formation. This is simply due to the fact that the healing effect, such as the healing agent available in the vascular network based specimen, possess a much stronger bond effect with original host matrix, which result in the bonding surface of cracked area possess higher strength than the surrounding original host material, and compel the new cracks to form in a different position. Another type is primarily the sources from the damage of healed crack surfaces. These healed cracks, result from the filling of the adhesive in the vascular network due to the capillary force when microcracks appear, can fill those tiny interspaces very well. However, in terms of the recovery of mechanical properties and the effect of healed area to the overall structure, especially for flexural strength, has been less investigated. Therefore, the bonded crack surfaces by the filling adhesive agents could still be weaker regarding the mechanical properties than that of the original host matrix. Thus, it is potentially to be damaged again before the maximum load reached.

It also presents a relative dense area of AE hits for each self-healing specimen compared with control beams before the dotted line, as discussed above, due to the

new damage after the injection of healing agent in the crack. In this case, the results during reloading stage can be explained by the self-healing phenomenon. Moreover, it can be noticed that the amounts of the AE hits were different among the specimens before the dotted line. The more hits, the better the healing effect. Therefore, from the perspective of AE hits, the level of healing effect could be qualitatively assessed in the order of healing time 1-hour < 24-hours < 3-days. These results demonstrate that the self-healing capability is indeed related to different reaction time of the adhesive and host matrix.

5.3.2.2 Evolution of AE hits

The variation and evolution of AE hits before and after different healing time are shown in Figure 5-9 to Figure 5-12. As can be seen from these graphs, a large amount of AE signals was generated both during the initial loading and reloading stages. Obviously, the amount of AE hits in the reloading stage is relatively less than that in the initial loading stage no matter for the healed beams or the control beams. For those healed beams, with the increase of load, the number of AE signals increases gradually from beginning, which is against the Kaiser Effect of AE.

This is because that although there are already loads of cracks and damage occurred after the initial loading stage, the healing agent is injected afterwards and outflow rapidly from the tubes to those macrocracks and microcracks due to capillary force. Thus, most of the cracks in the specimen have been restored as well as regained strength to return the concrete specimen to its original condition. In that case, during the reloading stage to evaluate the healing effectiveness, the healed concrete follows a similar damage process to the specimen before healing. It also can be illustrated from the AE monitoring results. More specifically, at the beginning of initial loading, the number of AE hits increase slightly due to the own properties of concrete. As a kind of porous material, there are still many micro-cavities and holes in concrete even though the concrete has cracked and damaged already. Under the action of external load, the micro-cavities and holes around the main cracks are squeezed and compacted which result in the mortar particles rub and collide with each other and will generate a small

amount of AE signals.

Subsequently, the amount of AE hits goes up significantly as the load increases, indicating that the interior structure of the specimen starts to change and produce new microcracks and damages. When the peak load is reached, the AE characteristic parameters increased dramatically because of the brittleness of concrete. Thus, the cracks will expand unstably when the load reaches the maximum value and the specimen will be failed due to the brittle fracture.

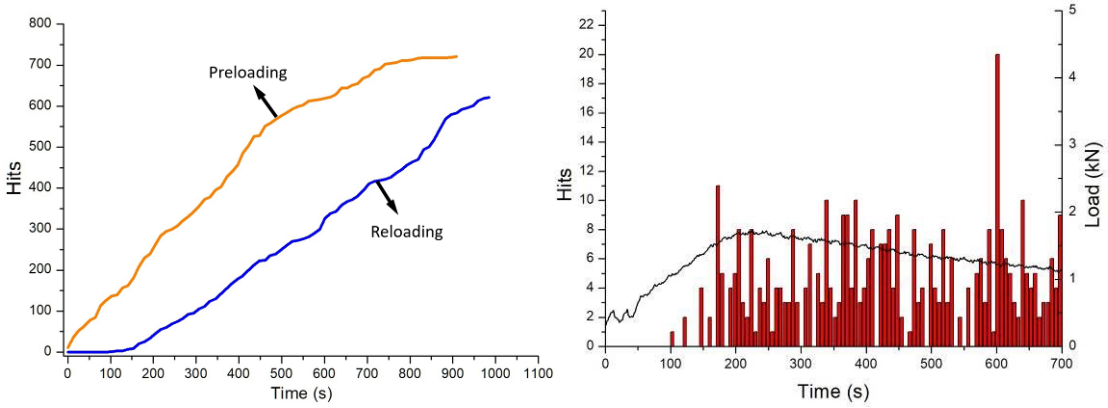

(a) (b)

Figure 5-9. Evolution of control beam, without healing: (a) Cumulative AE hits; (b) AE hits and load curve during reloading stage

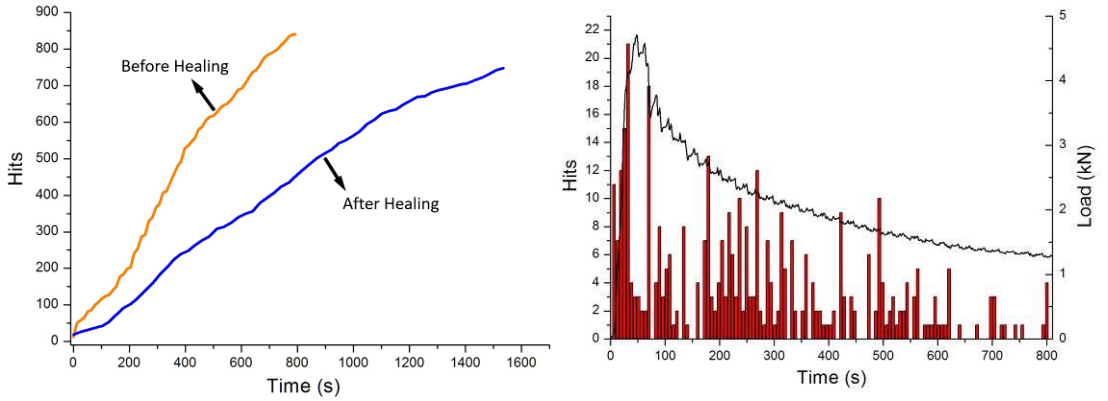

(a) (b)

Figure 5-10. Evolution of 1-hour healing: (a) Cumulative AE hits; (b) AE hits and load curve during reloading stage

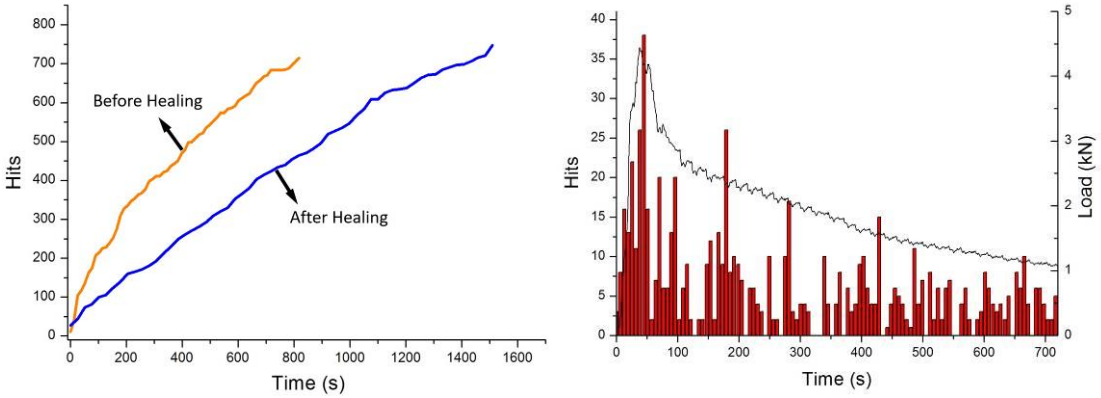

Figure 5-11. Evolution of 24-hours healing: (a) Cumulative AE hits;
(b) AE hits and load curve during reloading stage

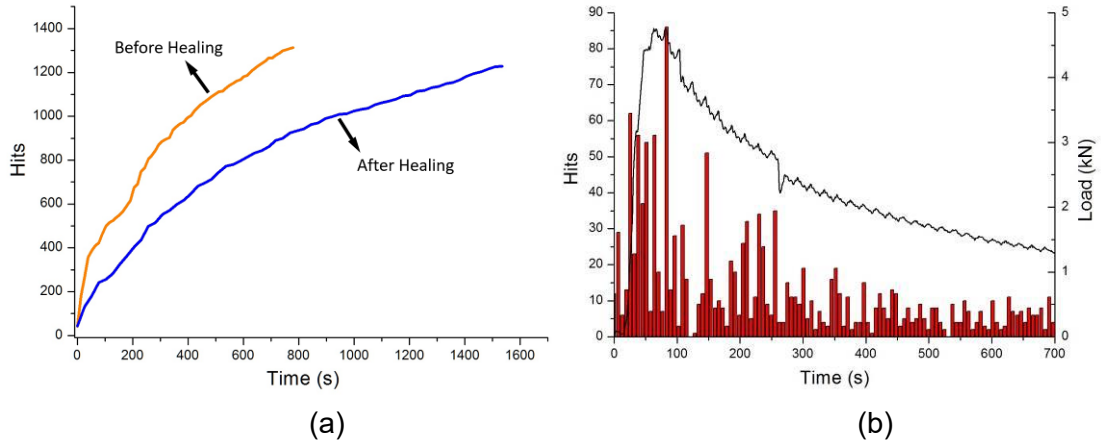

Figure 5-12. Evolution of 3-days healing: (a) Cumulative AE hits;
(b) AE hits and load curve during reloading stage

5.3.2.3 The absolute energy of AE during fracture

Figure 5-13 displays the evolution of AE hits cumulative absolute energy of both the initial loading and reloading stage for (a)control beam, (b)1-hour healing beam, (c)24-hours healing beam, and (d)3-days healing beam. The cumulative absolute energy of initial loading and reloading stage for specimen is represented in blue and red curves respectively. Again, the most important point-in-time as the CMOD value during reloading stage reaching 0.15mm (the previous unloading point), is indicated by dotted line, which is consistent with the distribution of AE hit and amplitude as discussed above.

As can be seen from Figure 5-13, a different pattern worth noting between the cumulative absolute energy generated from reloading of control beam and other self-healing beam tests after the dotted line. The energy released from control specimen during reloading increases gradually over time as similar as the initial loading stage. In terms of the self-healing specimens, however, as can be seen from both self-healing specimens, the most distinguished feature is that the energy generally stays at higher value in reloading than that of the initial loading after the previous damage was exceeded. This can be attributed to the breakage of ultimate failure caused by either the reopening of healed crack or the formation of new damage because of the higher bonding strength of the healed area.

Both the self-healing specimens show a similar pattern as there is a burst of energy. As shown in Figure 5-13, the order of magnitude is 10^6 for the control beam, and the order of magnitudes are 10^6, 10^7 and 10^8 for (b)1-hour healing beam, (c)24-hours healing beam, and (d)3-days healing beam respectively. Based on the result above, it demonstrates that the self-healing specimens have much higher cumulative energies than the control specimen, and the cumulative energies are in the order of control beam < 1-hour self-healing beam < 24-hours self-healing beam < 3-days self-healing beam, which agreed well with the results of the amounts of AE hits above as well.

On the other hand, it also demonstrates that the cumulative energy is indeed related to the healing effect and its corresponding time to some extent. Moreover, the amount of AE hits for 3-days self-healing beam is about twice than that of control specimen, but the cumulative energy for 3-days self-healing beam is about 28 times larger than that of control beam. It shows that the cumulative energy is not only related to the length of healing time, other factors such as the micropore structures of the material itself, bonding quality and healing degree, also have significant effect on the cumulative energy during the reloading stage. For instance, the higher the bonding quality is, or the less unhealed area left, the more fracture energy could be needed when cracks and damage occurred.

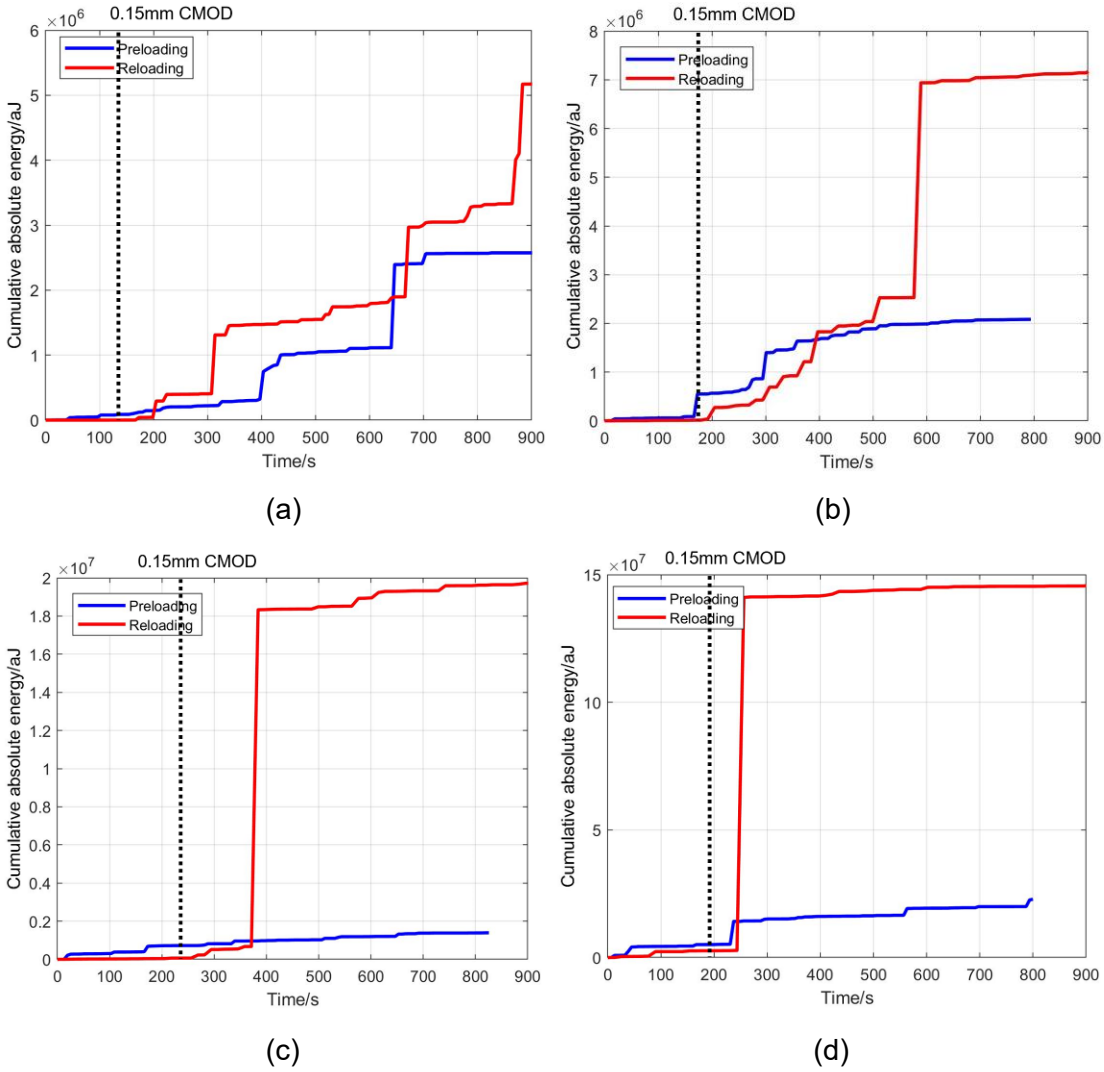

Figure 5-13. Cumulative energy of the AE hits during the initial loading and reloading stage for specimens: (a) control; (b) 1-hour healing; (c) 24-hours healing; (d) 3-days healing;

Theoretically, as shown in Figure 5-14, the healing agent would be released when damage is formed, primarily filling the macro-crack due to the capillary forces. Then micro-cracks appear as the load increases. The regained strength of damaged area, or the quality of healing highly depends on how much space of the cracked area the healing agent can fill and possess.

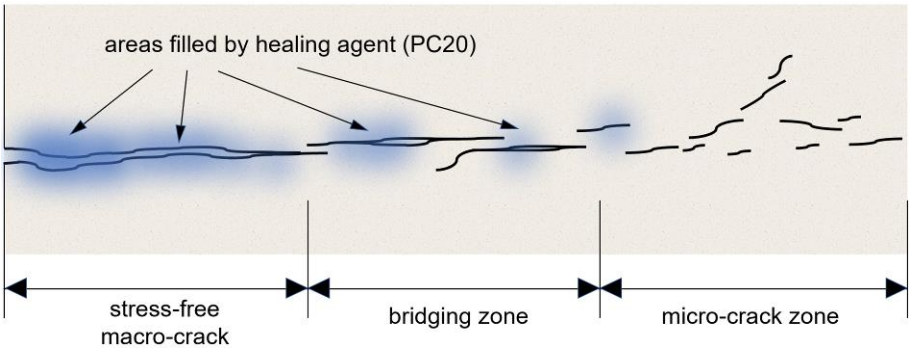

Figure 5-14. Identification of different fracture zone of concrete

One thing noticed and worth mentioning is, as shown in Figure 5-15, since the main crack occurred in the initial loading stage with a lot of microcracks surrounded, the new crack during the reloading process would initiate to the sides of the main crack after the initial cracks were healed and closed. To some extent, that phenomenon could be reflected on the graphs of the distribution of absolute energy. The distance between energy peaks of initial loading and reloading indicates that the two main cracks generated during each loading stages are not in the same place. Even some of the specimens cannot be visualized from the surface but still can be verified by the energy distribution, which would be helpful to the damage location of new cracks.

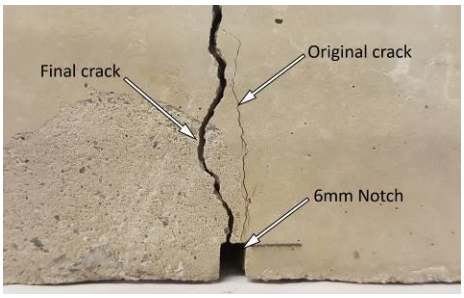

Figure 5-15. Original cracks and new crack formation on side face of Self-Healing beam

Figure 5-16 to Figure 5-18 shows the distribution of absolute energy against the X-position between two sensors mounted on each specimen. Since most of the energy is generated in the middle-notched area of each specimen, the range of X-axis of the graphs shown below has been shortened to 60mm for a more focused and clear representation. The middle of specimen is signed by a grey dotted line and the distance

from each energy peak to the centre line has been labelled.

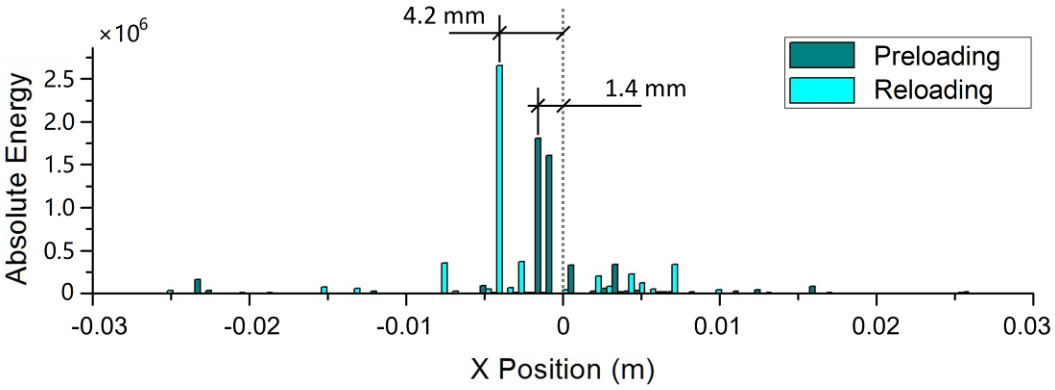

Figure 5-16. Distribution of AE absolute energy along the length between two sensors for 1-hour healing test

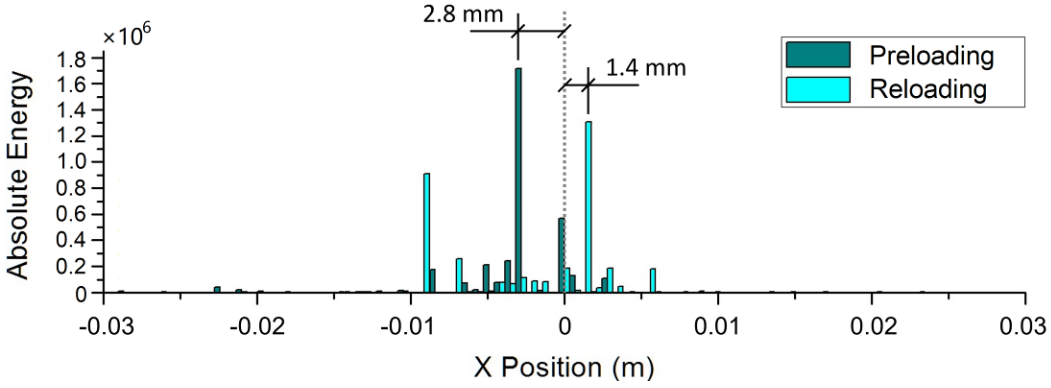

Figure 5-17. Distribution of AE absolute energy along the length between two sensors for 24-hours healing test

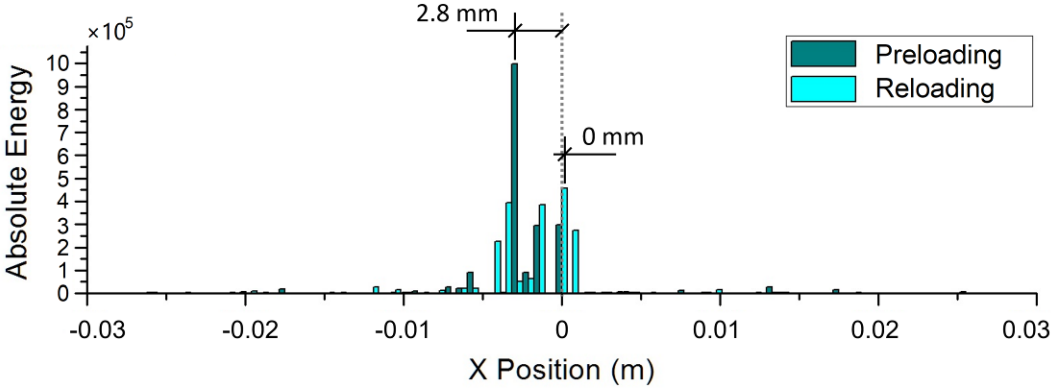

Figure 5-18. Distribution of AE absolute energy along the length between two sensors for 3-days healing test

5.3.3 Evaluation of self-healing efficiency based on AE Felicity ratio

5.3.3.1 Kaiser effect and Felicity effect

Generally, the loading path history of the material has an important impact on the AE characteristics during the repeated loading. The Kaiser effect was put forward by the German scholar Kaiser in the first place (Kaiser 1953). It was discovered in a test of loading metal materials. The Kaiser effect is manifested and defined as the absence of AE signals (or no obvious AE signals) at loads not exceeding the previous maximum load level when material undergoes repetitive loading. In other words, material has a memory for the historical load with respect to the presence of AE phenomenon. Conversely, if the material gives off significant AE signals at a lower load than the one previously reached in an increasing repeated loading, then this phenomenon is defined as the Felicity effect.

Rüsch and Van Amerongen (1960)，McCabe et al. (1976) have proved through experiments that the Kaiser effect exists in concrete, rock and masonry materials as well. Watanabe et al. (2007) found that Kaiser effect has a certain relationship with the strength of concrete. The more obvious Kaiser effect could be observed as the higher strength the concrete has. Große and Schumacher (2013) found that Kaiser effect depends on the highest stress level reached by the previous loading. When the stress level exceeds a certain range during the previous loading stage, the Kaiser effect disappears.

Hongguang and Zaoding (1997) verified the existence of the Kaiser effect and Felicity effect during the cyclic loading process of concrete materials through a series of studies and the relationship between Kaiser effect and Felicity ratio is studied in detail. It is found that the Kaiser effect of the concrete material has both the upper stress limit (about 70% - 80% of the ultimate stress) and the lower stress limit (about 30% - 40% of the ultimate stress). The upper limit of stress is determined by the failure mechanism of the concrete, and the lower limit of stress is determined by the structural characteristics of the concrete material itself.

During the two stages of loading of self-healing concrete beams, it can be observed that all the specimens generated AE signals from the very beginning until they were unloaded before the rest period. Then those specimens which were healed during the pause generated AE signals again before the unloading point (i.e., the maximum loading level during initial loading stage) was exceeded. The presence of this phenomenon is called “Felicity effect” and it can be manifested as the occurrence of “detectable and effective AE activities” during repeated loading of the material before the load level reaches the previous maximum applied load. The criteria used to determine the “effective AE signal” are discussed in the next section.

Another famous phenomenon which is known as Kaiser effect, as a widely used concept in AE signal processing as well, is demonstrated in Figure 5-19(a). Conversely, the Felicity effect observed in self-healing concrete beams is demonstrated in Figure 5-19 (b), which illustrates the cumulative AE signals emission versus the load applied. The loading path from B’ to C’ (unloading) and C’ to D’ to E’ (repeated loading) clearly indicates the absence or little of AE activities up to a loading level (D’), which is below the previous primary loading level (B’).

Compared with Figure 5-19 (b), the difference in Figure 5-19 (a) lies in the loading path from D to B where there is no new AE activities occurring until the previous loading level (B) is exceeded. It may take place if there is no healing phenomenon or strength recovery occurred at all. The Kaiser effect is literally described as when no AE activities shown up until the previous maximum load level is reached, which enables the Kaiser effect a special case of the Felicity effect (behaved as the point D’ is close enough to B’ in Figure 5-19 (b)).

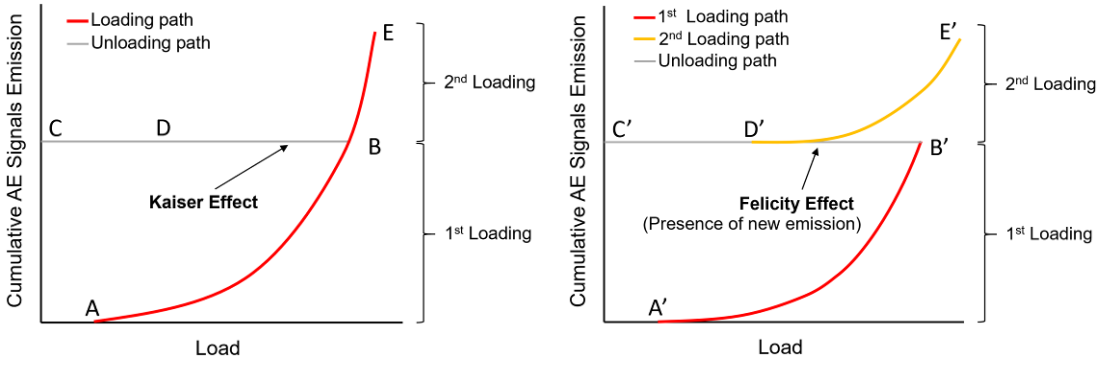

(a) (b)

Figure 5-19. Example of AE test results in a cyclically loaded specimen: (a) Presence of Kaiser effect (BCB); (b) Presence of Felicity effect (as a result of self-healing) (B'C'D')

Meanwhile, this Felicity effect can also be quantified using the Felicity ratio (FR), which is the ratio of load where considerable AE resumes during reloading, divided by the previous maximum load applied as the equation 5.2 shown below:

$$FR(i) = \frac{P_{AE}(i+1)}{P_{MAX}(i)} \tag{5.2}$$

Where

$FR(i)$ is the Felicity ratio of the i-th loading during a cyclic loading;

$P_{MAX}(i)$ is the maximum load during the i-th loading;

$P_{AE}(i+1)$ is the loading level when considerable AE resumes at the (i+1)th load.

From previous study, combination use of the Kaiser effect and Felicity effect can be efficiently used to determine whether major structural defects are present. Furthermore, Felicity ratio can become an important criterion for evaluating the severity of material defects. It is complied with Kaiser effect when Felicity ratio is greater than 1, or against the Kaiser effect when Felicity ratio is less than 1.

5.3.3.2 Determination of valid emission signals

In terms of concrete, because of its complexity and it is a kind of polyphase and

compound material, can be influenced by many factors. So many different kinds of defects, cracks and microstructural inhomogeneity are already contained inside before any load applied. In that case, some microcracks will deform and propagate even under relatively low stress condition. Therefore, it is of great importance to determine whether there are 'effective AE signal' received and corresponding loading magnitude during the process of cyclic loading. However, up to now there is no agreed definition about the concept of 'effective AE signal'. Normally researchers just distinguish the signals by using their own experience and properties of corresponding material.

During the experiments, it was observed that occasionally some cement paste caused by spalling may peel and the AE amplitude will increase significantly. But this kind of signal is very short and therefore it cannot be regarded as the valid AE signal as a sign of AE recovery. Hongguang and Zaoding (1997) conducted an experimental study with respect to the relationship of Kaiser and Felicity effect in concrete material. According to their findings shown in Figure 5-20, the following two criteria can be considered to use as the determination for "effective AE signal" in concrete:

(1) AE signals has been continuously increasing when load increases;

(2) More than 10 AE hits are received in the process of increasing the load by 10%.

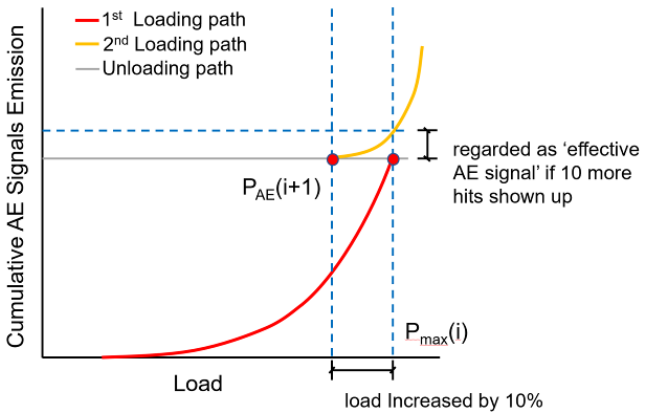

Figure 5-20. Criteria for the determination of 'effective AE signals resume'

5.3.3.3 Healing performance evaluation

To more intuitively characterize and better quantify the degree of self-healing, another index *HI*, called "Healing Index", is introduced and defined as the following

equation 5.3.

$$HI(\%) = 100 \cdot (1 - FR) \tag{5.3}$$

Where

HI is the Healing Index (%);

FR is the Felicity ratio.

According to these two criteria discussed above, the results of Felicity Ratio calculated are shown in Table 5-4 and Figure 5-21.

Table 5-4. Strength recovery and Felicity ratio

Specimen	Strength recovery(%)	Felicity ratio	Healing
C1	/	0.8135	/
C2	/	0.8221	/
C3	/	0.6989	/
SH-A1	51.7%	0.7379	26.21%
SH-A2	56.9%	0.6887	31.13%
SH-A3	37.6%	0.5738	42.62%
SH-B1	57.1%	0.0580	94.20%
SH-B2	55.5%	0.0616	93.84%
SH-B3	45.3%	0.0982	90.18%
SH-C1	85.8%	0.2385	76.15%
SH-C2	72.4%	0.1406	85.94%
SH-C3	57.1%	0.0515	94.85%

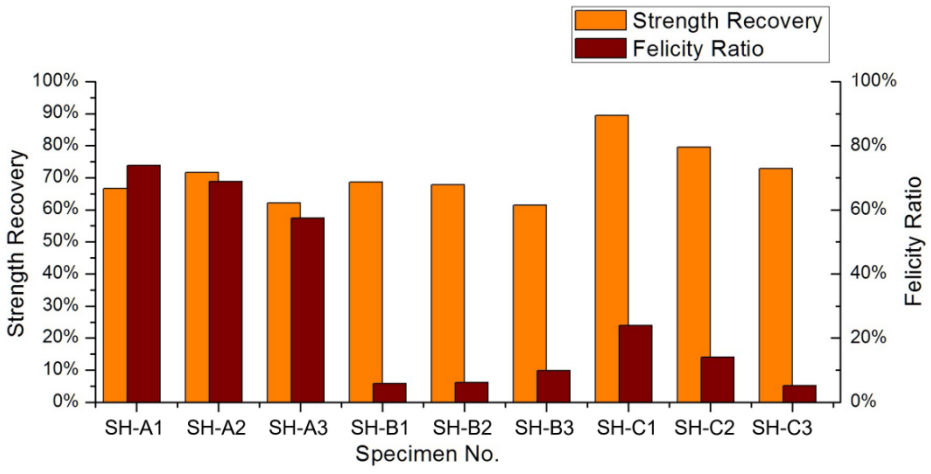

Figure 5-21. Correlation of Strength recovery and Felicity ratio

As shown in Table 5-4 and Figure 5-21, the Felicity ratio is related to different healing time and relatively decreases with the increasing strength recovery of healing. This is because the specimen is internally microcracked and damaged during the first

loading, and the healing agent will flow to the section of fracture surface due to the capillary action, which enables it to be repaired timely and promptly, so the strength of the specimen is regained and improved.

During the reloading stage, the position of crack occurred would be different according to the bonding quality of fracture surface. If the bond strength is greater than the original, it is more likely the microcracks would occur in a different location. Opposingly, if it is less than the original strength, then the previous microcrack surface will get cracked again. Therefore, the Felicity effect is shown in that case. Furthermore, it can be concluded that the use of Felicity Ratio could be promisingly used to determine and evaluate the effectiveness of healing. However, it still needs to be further studied about whether there is a quantitative relationship between the Felicity Ratio and quality of healing effectiveness.

5.4 Signal identification using PCA principal component analysis and unsupervised clustering techniques

To further investigate and differentiate signals between concrete matrix cracking and those relating to the healing process including further damage, principal component analysis (PCA) and unsupervised pattern recognition algorithms are adopted to identify different damage mechanisms.

5.4.1 Introduction

As analysed and discussed on previous work in this chapter, most of the methods used to characterise the healing behaviour using AE are based on the evolution of parameters before and after healing occurred. Nevertheless, it is challenging to identify damage mechanisms only from the AE parameters. The ability to classify these signals efficiently and automatically from different source mechanisms is definitely desirable and worth investigating.

The difficulties lie in the interpretation of transient AE signals which carry abundant information and very likely to be easily affected by source mechanisms, material properties, propagation path and sensor transfer function, etc. Hence, to increase the

accuracy of identification and classification, careful consideration of AE data is critical prior to recognising and maximising subtle differences between signals.

Grouping or classification of AE signals can be achieved through either supervised or unsupervised pattern recognition (Manson et al. 2001; Rippengill et al. 2003). Besides, the classification process requires a suitable set of features to be processed to describe each signal. Pullin et al. (2008) successfully applied the PCA to differentiate AE signals between fracture source and high level background noise in a real landing gear component subject to no load. Al-Jumaili et al. (2015) implemented unsupervised clustering techniques to classify AE signals from a carbon fibre laminate buckling test. In his work, the hierarchical clustering technique was used for AE feature extraction and selection, followed by PCA providing signal features that represent the greatest data variance while remaining linearly uncorrelated with each other, and finally two clustering analysis was performed using *k*-means and *Fuzzy C*-means techniques.

The concept of clustering refers to the geometric grouping of unknown objects whose mean values of all class variables in the database are grouped into several classes consisting of similar properties. The object features in the same cluster have great similarities while it is of relatively large differences between each cluster. Relative to clustering, classification is also a term referring to effectively identify object classes, but this process normally is costly since it requires collection and identification of a large number of different class patterns. The differences between clustering (also known as unsupervised learning) and classification (also known as supervised learning) are that the classes that clustering needs to divide is unknown. The purpose of clustering is to classify data collected using similarities into several classes with similar characteristics, which has high practical significance for dealing with a large number of objects in the database.

This section expands based on previous results using clustering techniques and PCA to further investigate the source mechanisms from self-healing behaviour.

5.4.2 Cracking modes by conventional parameter-based analysis

As described previously in section 2.1.6.2 and the application in section 4.5.5, the two descriptors, the RA value (rise time / maximum amplitude) and the Average Frequency (counts / duration time), are shown to help distinguish tensile cracks and shear cracks. Figure 5-22 below show the RA-AF index-based classification results for the control specimen. From both the preloading and reloading stage, it can be seen that most of AE signals (approximately two third) are predominately located within the upper half of the plot. This is because the control specimen subject to three-point bending arrangement keeps the tensile cracks as the dominant AE activities. For the specimens incorporating the healing agent PC20, the RA-AF plot still follows a similar trend both in preloading and reloading, as shown in Figure 5-23, as still the concrete matrix cracking is the dominant damage form subject to three-point bending test setup after the specimens are repaired.

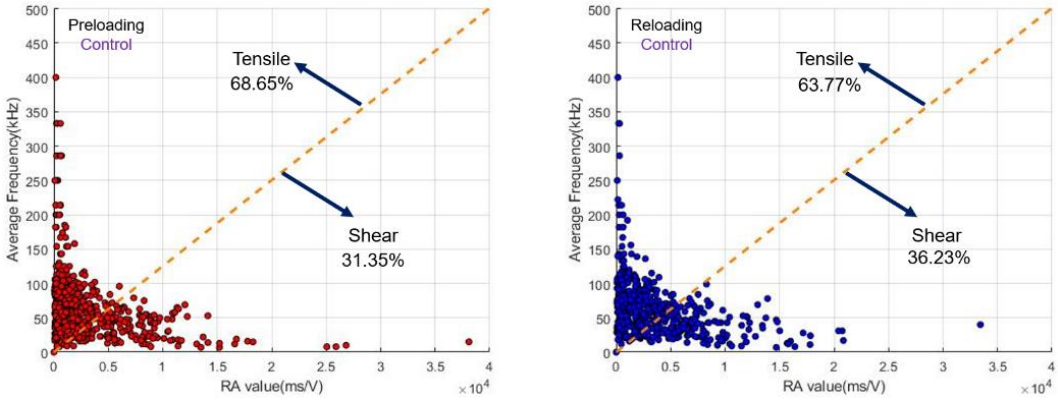

Figure 5-22. RA-AF classification result of control specimen from preloading (left) and reloading (right)

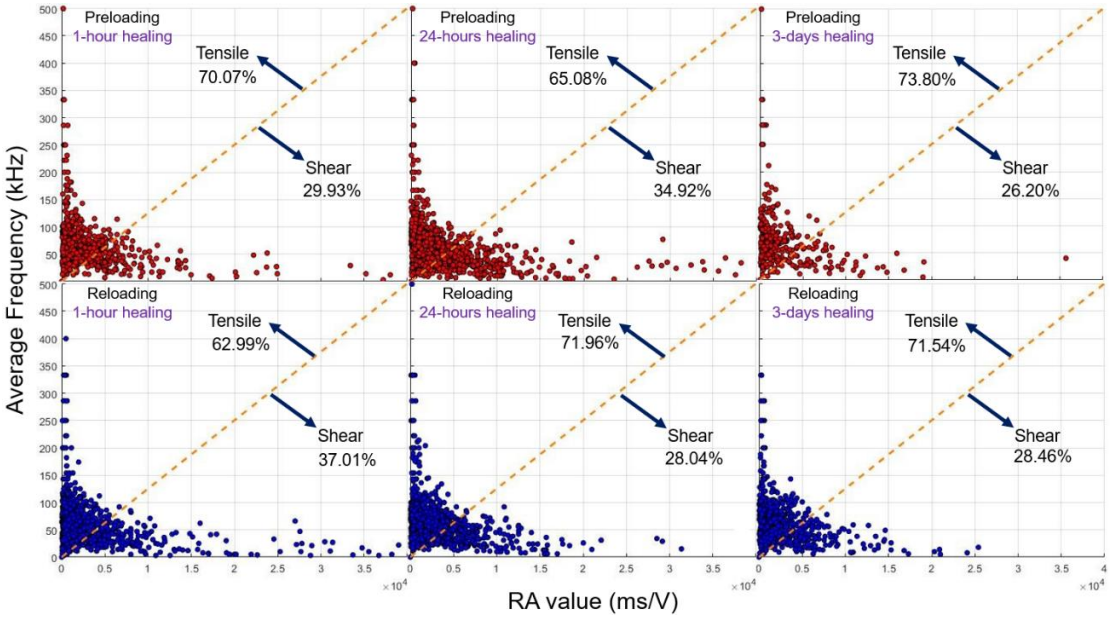

Figure 5-23. RA-AF classification result of self-healing specimens from preloading (upper) and reloading (lower)

5.4.3 Identification process

An identification procedure is proposed that includes optimum feature selection, parameter pattern recognition and dimension reduction using PCA technique. Figure 5-24 below shows the flow chart of the analysis procedure, and the individual steps are explicated in detail afterwards.

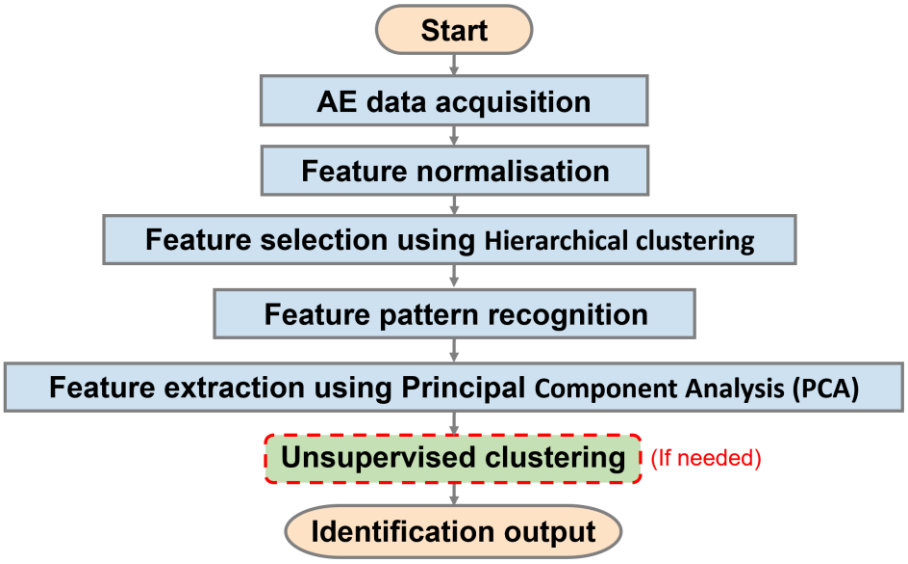

Figure 5-24. Flow chart of identification procedure

5.4.3.1 Feature normalisation

Prior to any multivariable classification or clustering process, the normalisation of data is necessary and critical to ensure that each parameter has equal weighting. When processing AE data, an individual parameter, such as amplitude, is normalised by subtracting the mean value for that parameter from each data point and dividing by the standard deviation, which result in a mean of 0 and a standard deviation of 1.

The traditional AE parameters are listed in Table 5-5 (MISTRAS Group Inc., Products & Systems Division 2011, p.4). In this work, the onward hierarchical clustering is performed based on the most common 8 AE parameters selected, which are rise time, counts, energy, duration, amplitude, average frequency, signal strength and absolute energy which are highlighted in italic in Table 5-5.

Table 5-5. Traditional AE Hit data set/parameters

No.	AE parameters	No.	AE parameters
1	*Amplitude*	8	*Rise Time*
2	*Energy*	9	Counts to Peak
3	*Counts*	10	*Average Frequency*
4	*Duration*	11	Reverberation Frequency
5	RMS	12	Initiation Frequency
6	ASL - RMS	13	*Signal Strength*
7	Threshold	14	*Absolute Energy*

5.4.3.2 Feature selection using hierarchical clustering

Hierarchical clustering is a method to identify the most correlated features and group them based on their similarity (Anderberg 2014) or correlation coefficient as proposed by other previous researchers (Moevus et al. 2008; Kontsos et al. 2011; Momon et al. 2012). The results can be visualised as a dendrogram. For a certain level of correlation coefficient, there will be a certain number of groups of features.

In this work, a complete link hierarchical clustering algorithm is applied to the 8 AE features selected of all data set to group features based on their correlation coefficient. Figure 5-25 and Figure 5-26 show the clustering results which are visualised as a dendrogram of all specimens during preloading and reloading respectively. As can be seen that, at a higher level of correlation coefficient, a great number of pairs of features exist as the features in each pair are very highly correlated and vice versa; likewise, at a lower level of correlation coefficient, a fewer number of pairs of features exist as each pair of features at that level contains less correlated information (correlation coefficient of 100 means total correlation and vice versa). In this work, considering the hierarchical clustering results both from preloading and reloading, 4 lesser correlated AE parameters, count, amplitude, average frequency and absolute energy are selected for onward analysis.

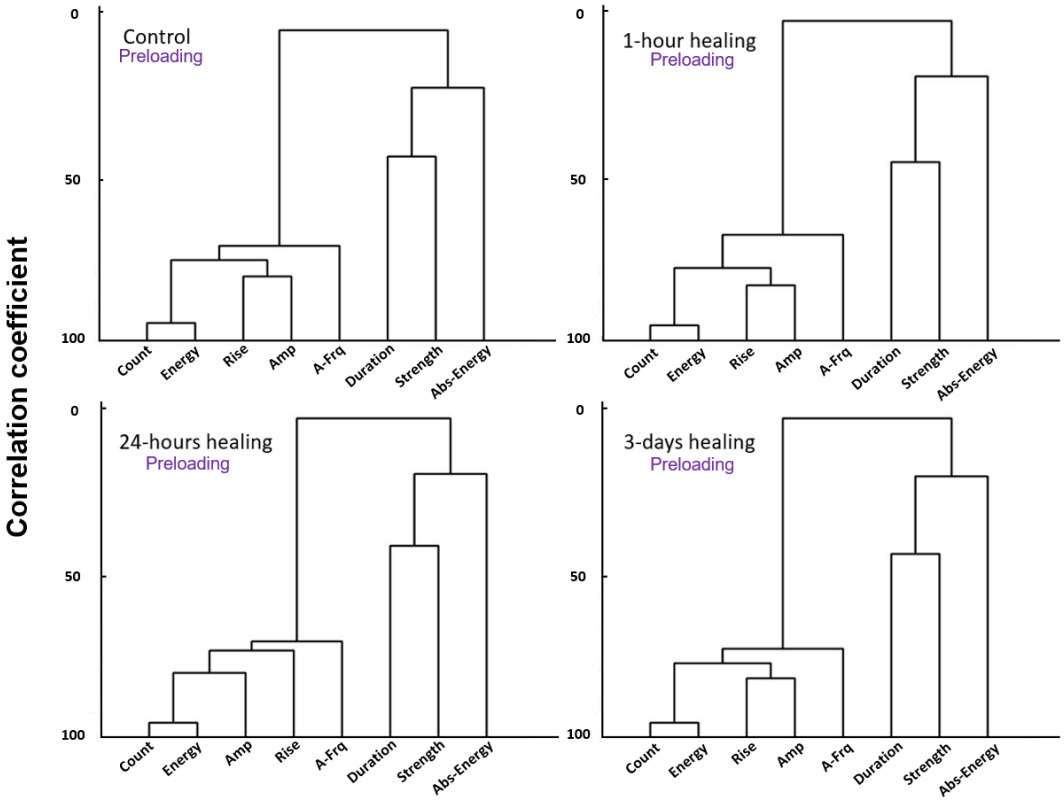

Figure 5-25. Dendrograms of 8 AE features using hierarchical clustering of all specimens during preloading

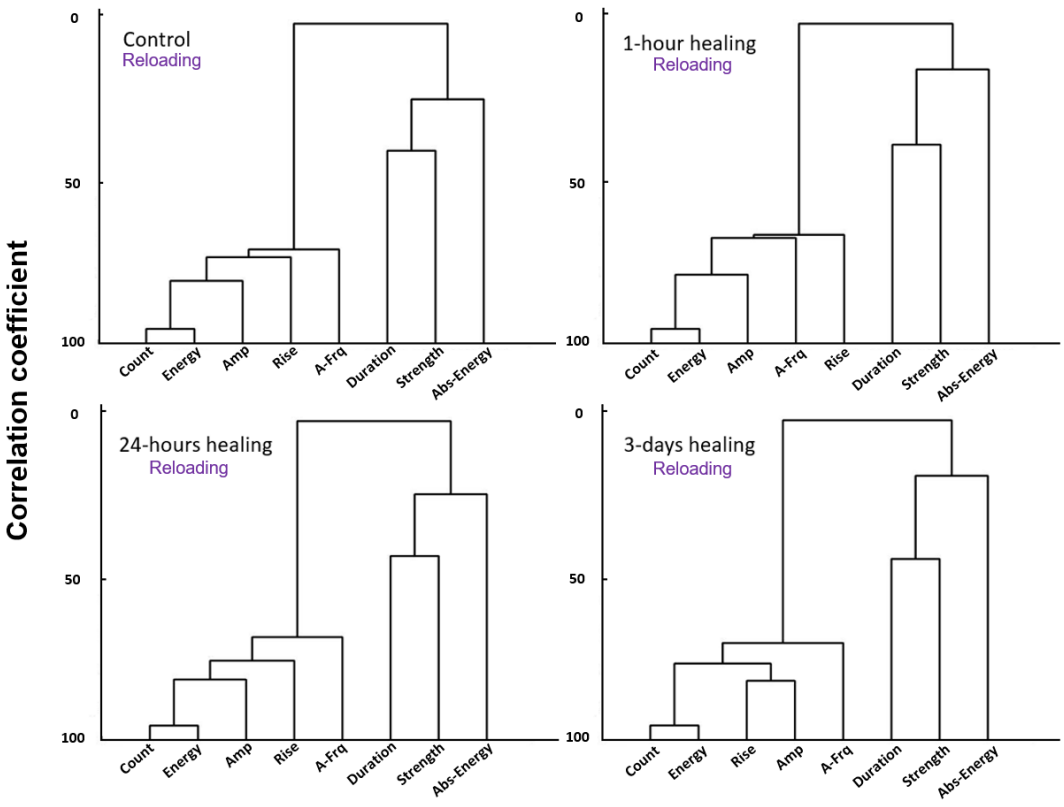

Figure 5-26. Dendrograms of 8 AE features using hierarchical clustering of all specimens during reloading

5.4.3.3 Feature pattern recognition

Based on the 4 selected AE parameters, count, amplitude, average frequency and absolute energy, the feature pattern based on each pair of AE parameters are compared to differentiate between fracture signals before and after healing occurred on all self-healing specimens. Figure 5-27 to Figure 5-32 show the 6 pairs of the 4 selected AE parameters, namely Average Frequency versus Absolute Energy, Average Frequency versus Amplitude, Average Frequency versus Count, Amplitude versus Absolute Energy, Count versus Absolute Energy, and Count versus Amplitude, of all self-healing specimens both from preloading and reloading.

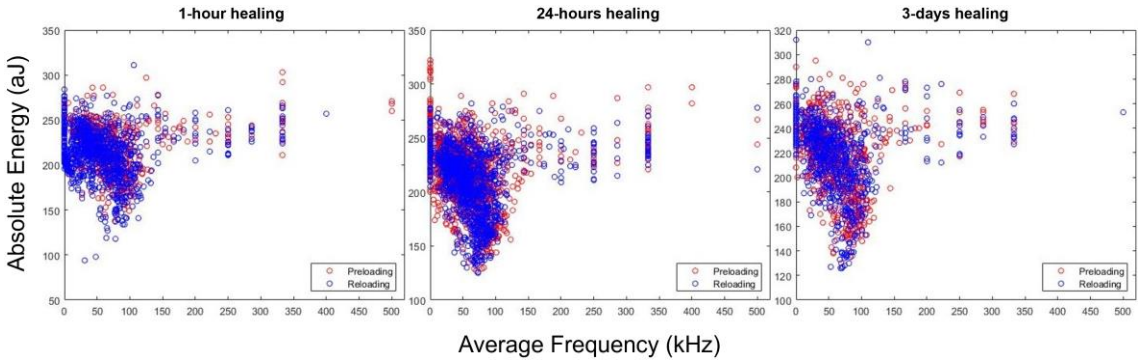

Figure 5-27. Average Frequency versus Absolute Energy for self-healing specimens

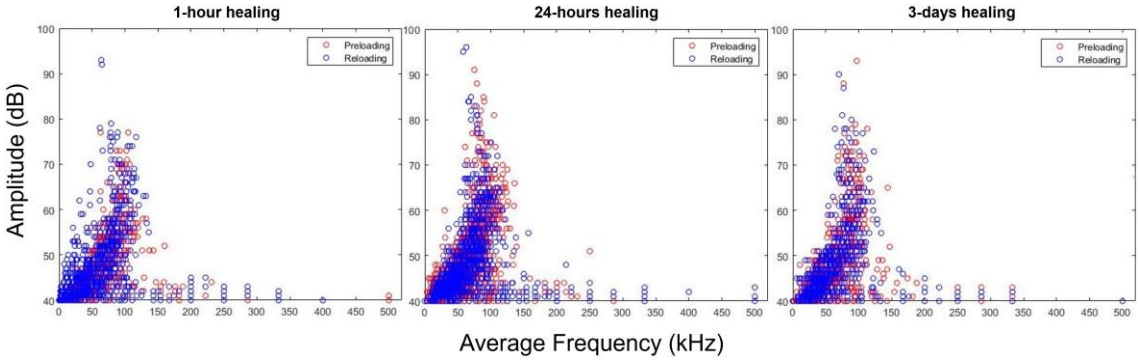

Figure 5-28. Average Frequency versus Amplitude for self-healing specimens

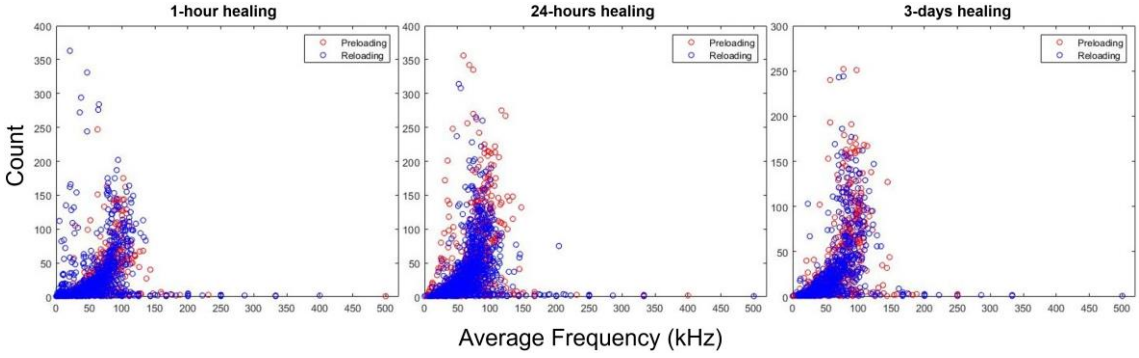

Figure 5-29. Average Frequency versus Count for self-healing specimens

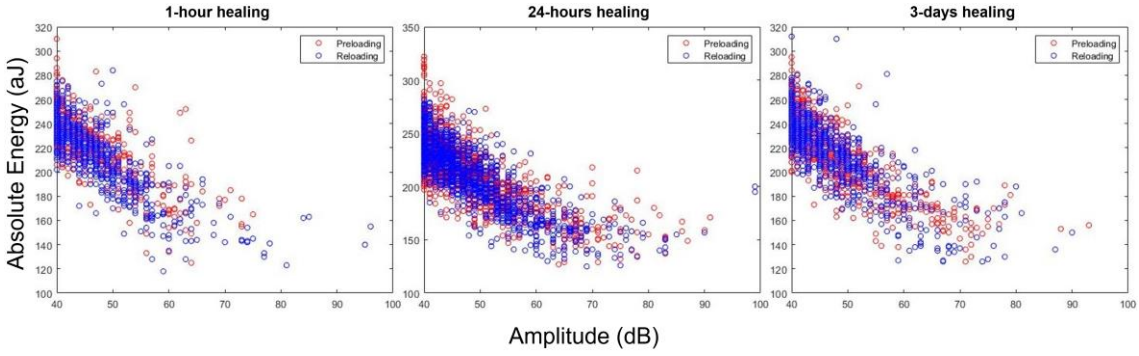

Figure 5-30. Amplitude versus Absolute Energy for self-healing specimens

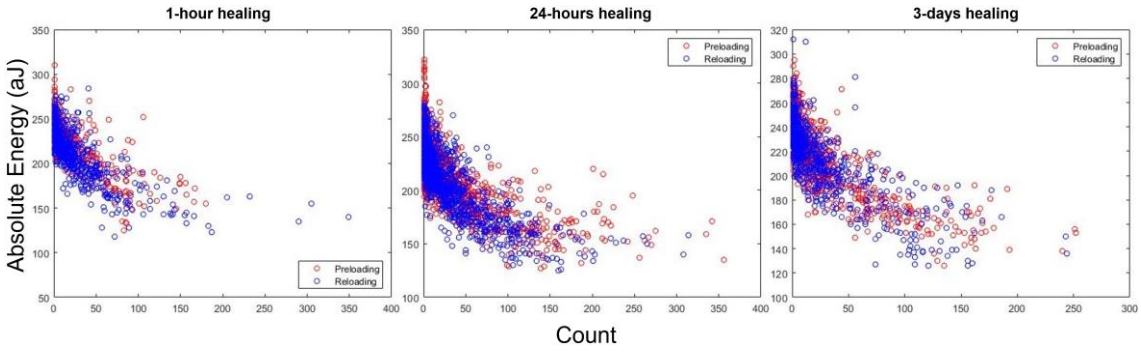

Figure 5-31. Count versus Absolute Energy for self-healing specimens

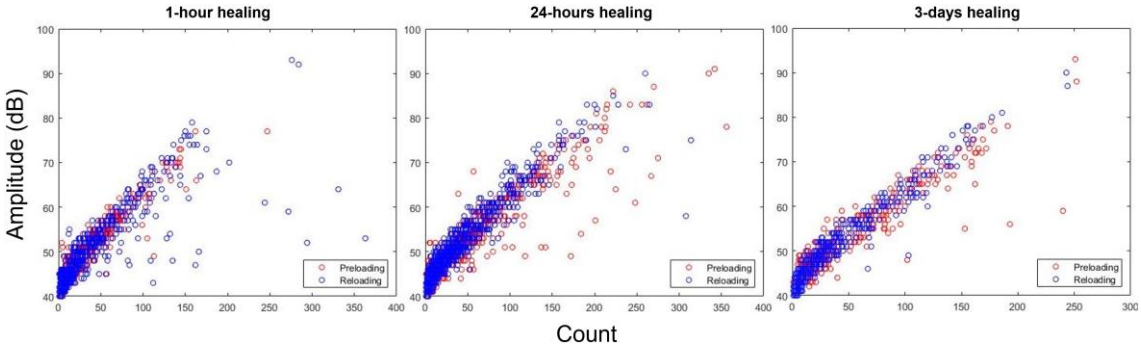

Figure 5-32. Count versus Amplitude for self-healing specimens

Overall, from those comparisons above of each pair of parameters from the self-healing specimens, it can be seen and concluded that those signals from preloading and reloading are nominally identical from the perspective of feature distribution patterns, and it can't be actually be separated from each other to identify their own source. It is indicated that even after those specimens are healed incorporating with healing agent PC20, the concrete matrix cracking is still the dominant damage form during fracture process, and re-cracking position are close to the initially cracking area as there will be an obvious change of parameters if there is a significant change of the distance from source to sensor.

Figure 5-33 to Figure 5-35 show the ultimate cracking patterns of 1-hour, 24-hours and 3-days self-healing specimens respectively after failure. As explained in section 5.3.2.3, the new crack during reloading could be initiated from the sides of the main crack occurred during preloading. This may not always be visualized from the specimen surface. As the Figure 5-33 to Figure 5-35 shown below, only two specimens have obvious re-cracking positions that can be noticed. From the physical observation

of the self-healing specimen, it also confirmed that the results of AE parameters' feature comparisons above indicating that the characteristics of signals from preloading and reloading are nominally identical, and dominantly from concrete matrix cracking. The signals from re-cracking of healing areas cannot actually be discriminated.

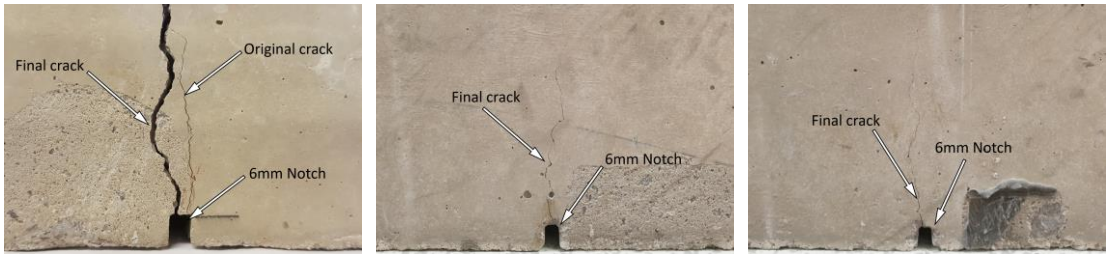

Figure 5-33. The ultimate cracking pattern of 1-hour self-healing specimens

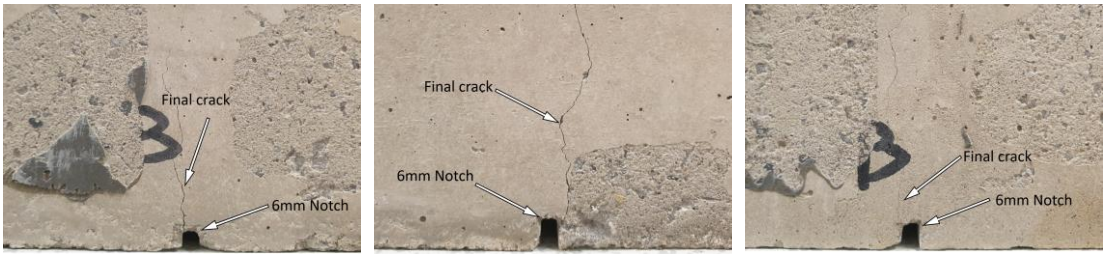

Figure 5-34. The ultimate cracking pattern of 24-hours self-healing specimens

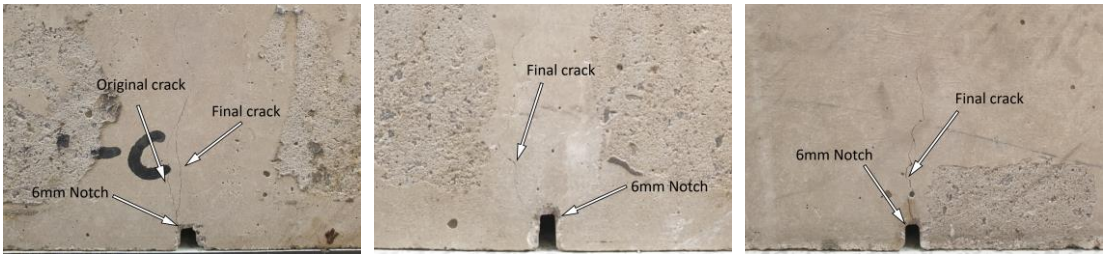

Figure 5-35. The ultimate cracking pattern of 3-days self-healing specimens

5.4.3.4 Feature extraction using PCA for dimension reduction

Since no notable feature differences can be separated from the results above, the PCA is implemented to further and automatically differentiate between AE signals from preloading and reloading of self-healing specimens. As describe previously, PCA is a method used to simplify high dimension data sets to lower dimensions to allow a simpler analysis, which enables the features grouping of AE signals can be performed under a low-dimensional framework achieving 2D or 3D visualization.

In this work, using the proposed identification procedure, 4 less correlated AE

features are selected using hierarchical clustering as the inputs of PCA. A brief introduction to the PCA methodology is given below (Al-Jumaili et al. 2015):

1. Mean subtraction – subtract the empirical mean from each column of the data set matrix;

2. Calculate the covariance matrix – find the $M \times M$ empirical covariance matrix from the M-dimension data set matrix;

3. Calculate the eigenvectors and eigenvalues from the covariance matrix – the eigenvector associated with the largest eigenvalue has the same direction as the first PC. The eigenvector associated with the second largest eigenvalue determines the direction of the second PC;

4. Visualisation – project the data from multidimensional space along the first and second PCs and plot as a two dimensional x-y plot between the two PCs.

Figure 5-36 to Figure 5-38 below present the PCA results from 1-hour healing, 24-hours healing and 3-days healing specimen respectively. It can be seen that most of the signals are overlapping. The variation observed of all signals is not large, and no distinct separation can be noticed of signals from preloading and reloading.

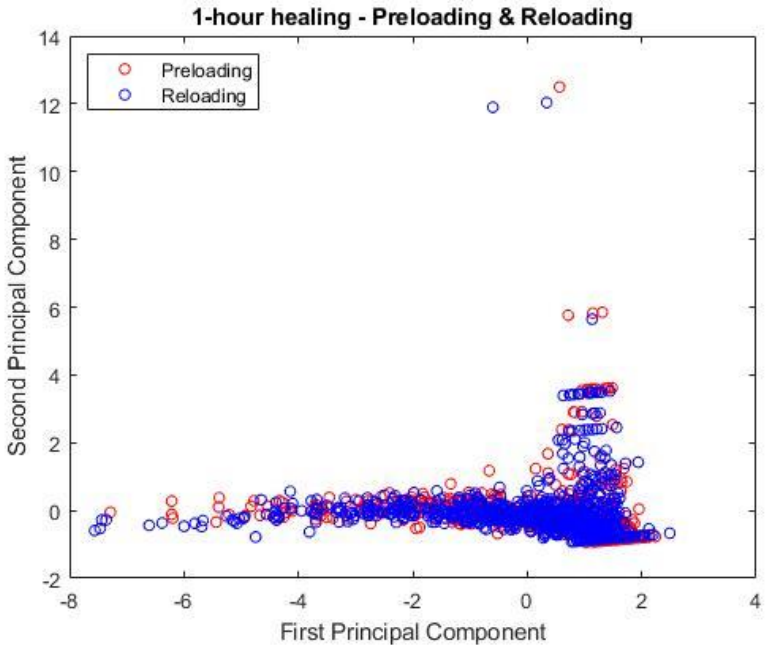

Figure 5-36. Principal component analysis of 1-hour healing specimens

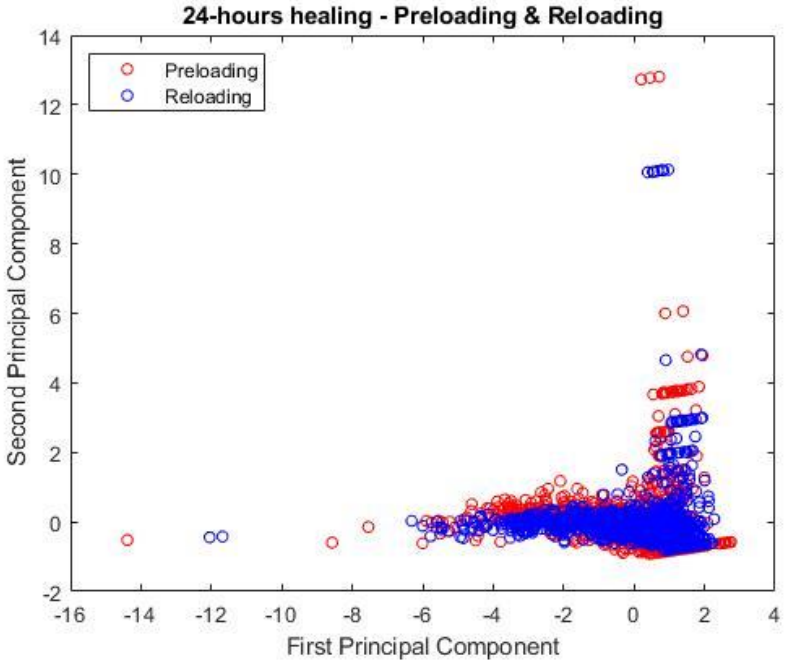

Figure 5-37. Principal component analysis of 24-hours healing specimens

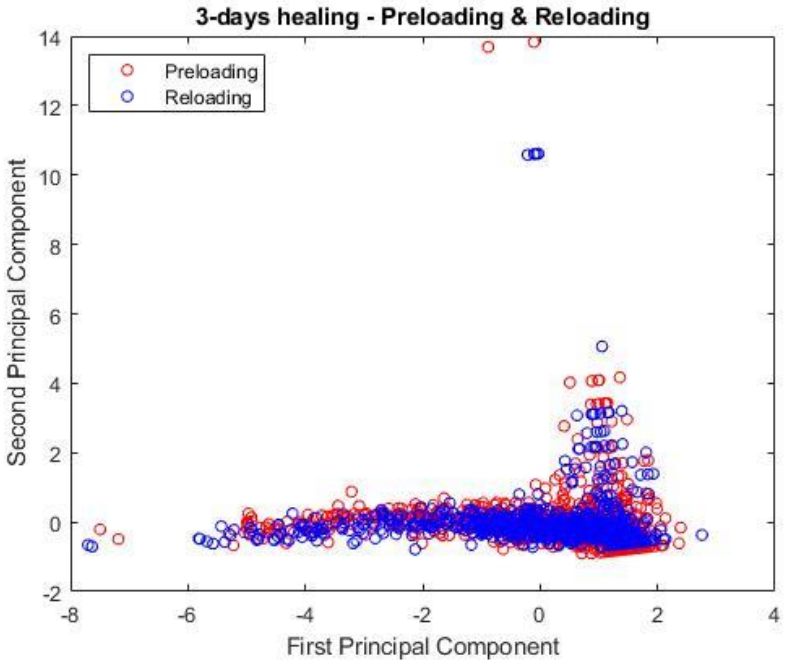

Figure 5-38. Principal component analysis of 3-days healing specimens

It is not surprising that the PCA technique is not possible to separate signals that are intrinsically very similar. In fact the purpose of PCA in this study is to identify signals generated from different sources (i.e. the re-cracking of bonding area) after the specimen is filled and healed with healing agent. Nevertheless, as the concrete

cracking is still the dominant damage from both in preloading and reloading of self-healing specimen, there is no distinct difference of signals can be automatically separated.

5.4.4 Discussion

It is confirmed again by PCA that the signals from preloading and reloading of self-healing specimen are very similar and nominally identical, which are dominantly from concrete matrix cracking. Even there exists signals from the re-cracking of healed zone of self-healing specimen, it is actually not possible to distinguish and separate those signals from the dominant concrete cracking signals regarding feature recognition and clustering. Hence, there is no foreseeable insight to conduct any further clustering given there is no distinctive differences observed both from results of feature pattern comparison, physical observation, and PCA. If a notable difference can be visualised from the output of PCA indicating the potential to discriminate data between different signals, then a further clustering analysis can be conducted through other unsupervised learning algorithms (e.g. *k*-means and *Fuzzy C*-means clustering techniques) to further identify different sources from signals.

5.4.5 Summary and conclusion

In the present investigation, AE data from control specimens and self-healing specimens were analysed. To achieve the source identification and overcome the difficulties in selection of the most uncorrelated AE parameters, the hierarchical clustering technique is implemented to select the least correlated AE parameters to maximise the variance and any subtle differences in the data. Then the selected parameters are used as the input features for onward pattern recognition and PCA process. Through the comparison of plot pattern between each pair of selected parameters, no notable or distinguishable differences are noticed between data from preloading and reloading of self-healing specimens. Further, the PCA technique is adopted to realise dimension reduction and project the data to the new features generated, namely the 1st and 2nd principal component.

In this study, those techniques that used to automatically differentiate between

signals from different sources, namely the estimation of conventional RA-AF method, feature recognition process and PCA, both indicates their potential to discriminate between fracture of concrete and signals from other sources. Nevertheless, due to the nature of the vascular network based self-healing technique used in the specimens, it is actually not possible to identify and separate those signals relating to healing process included further damage. A further investigation can be designed and conducted on scaled-up specimen with different self-healing technique implemented (e.g. versatility-enhanced microcapsule healing system, tailored bacterial healing systems, high performance shape-memory polymer (SMP) tendons based healing system, etc. (Pilegis et al. 2016)) to obtain more distinctive signals in concrete structure.

5.5 A proposal of self-healing efficiency evaluation system

Based on the features of the self-healing technique used in this chapter, combining the AE analysis methods, a multilevel self-healing efficiency evaluation system based is proposed as shown in Figure 5-39. The evaluation system is divided into three stages: (1) Kaiser effect analysis, (2) qualitative analysis of AE signals, and (3) quantitative analysis of AE signals. The three stages are presented in a progressive and intuitive way. Among them, Kaiser effect analysis is a method to directly judge whether there is any healing behaviour occurred; AE signal qualitative analysis is used as a comparative analysis for the AE parameters obtained before and after the specimen is healed, and then the signals from cement matrix damage and healing unit damage can be screened and distinguished by characteristics information extracted to find out exactly where and what kind of material is damaged again after healing. Finally, the healing efficiency can be compared horizontally through quantitative analysis of AE signals.

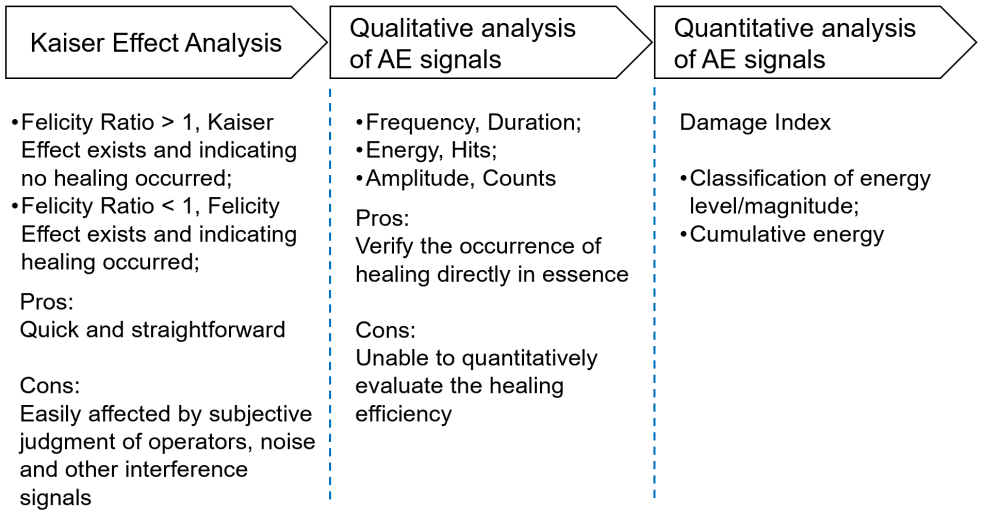

Figure 5-39. Multilevel self-healing effect evaluation system based on AE

5.6 Conclusions

In this chapter, the application of AE monitoring on the whole damage and healing process of vascular network-based self-healing system is investigated. The following conclusions can be drawn:

(1) Self-healing concrete based on vascular network is capable of restoring around 70% of the original concrete strength and bearing capacity. AE parameters could be used to highly potentially characterize the damage degree of self-healing concrete.

(2) The amount of AE hits and absolute energy before and after healing can be qualitatively assessed by AE signals. The AE results indicate that the cracked specimen after healing possessed larger amount hits and much higher energy from the ultimate failure.

(3) Kaiser effect and Felicity effect are of great potential to be applied to intuitively evaluate the severity of material defects. It provides a promising way to determine the healing efficiency regarding the self-healing materials. The higher the healing efficiency, the more obvious the Felicity effect; the lower the healing efficiency, the more obvious the Kaiser effect.

(4) PCA technique is limited of differentiating very similar AE signals in vascular

network-based self-healing concrete structure. However, as an efficient and practical technique of data dimension reduction method, PCA has the potential to automatically identify and separate distinctly different AE signals.

Chapter 6 Assessment of Concrete Using Acousto-Ultrasonics(AU)

6.1 Introduction

In the large-scale construction of modern engineering infrastructure concrete remains the most used building material. Despite the best endeavours of design engineers and modern guidance documents, such as CIRIA C766 (Bamforth 2019), cracks are still commonly found in these reinforced concrete members. Cracking occurs due to a multitude of reasons, which include restrained shrinkage of concrete and over-loading under different situation. In order to determine the hazard posed by these cracks and to develop appropriate remedies, two key information points are needed, which involve determining the crack width and depth (Shah et al. 1995). Nowadays, the measurement methods for crack width is well developed both in theory and by using surface measuring equipment (Toutanji and Deng 2003; Vidal et al. 2004; Giri and Kharkovsky 2016; Sarker et al. 2017), meanwhile the measurement of crack depth is more challenging. Ultrasonic non-destructive testing method are sometimes used to successfully determine the depth (Ohara et al. 2008; Felice et al. 2014; Her and Lin, 2014). Although there are a lot of related studies analysing the effect of AU technique on crack depth measurement, it still lacks systematic study and sufficient laboratory and on-site experimental data to provide confidence for its use with a good understanding of its accuracy and factors influencing the results.

For concrete crack depth measurement using AU technique, generally adopted methods include single-sided plan measurement, penetrating oblique measurement or borehole measurement according to the specific conditions of the cracking area on concrete structure. Among them, the single-side flat ultrasonic measurement is one of the most common, effective and fast methods that are suitable for engineering practice. The common principle of AU-related testing is expressed in slightly different ways of measurement methods and factors affecting pulse velocity in cementitious materials among the standards of different countries. According to the British Standards (BS EN 12504-4:2004), generally the main factors affecting the accuracy of crack depth measurement include design of mix ratio of concrete, degree of concrete compactness,

amount of reinforcement bars, shape of the cracks, moisture and debris content and detection method. In this study, experimental works were conducted on a range of specimen in different size with different methods, including a set of preliminary tests based on pre-notched beam to verify the effectiveness of computing methods in section 6.5; the application of single-side flat ultrasonic measurement on the monitoring of crack development in section 6.6; and the prospective investigation of AU on the newly developed technique of self-healing materials in section 6.7.

6.2 Characteristics of ultrasonic pulse transmission in concrete

Concrete is a heterogeneous material made up of different components, which means that there is a large attenuation and dispersion as they travel through the medium. It is shown that aggregate contents can considerably increase the wave velocity in wave propagation while the aggregate size could be a main factor affecting the attenuation (Philippidis and Aggelis, 2005). This is especially relevant to the high-frequency components of ultrasonic waves, which attenuates more significantly than audible sounds. Therefore, generally a lower frequency would be applied for the damage or defect detection. When the composition, manufacturing conditions, internal quality of concrete and the testing distance are generally constant, the propagation velocity, amplitude of head wave, frequency of received signal and other related acoustic parameters should be substantially the same. If there are any holes, cavities, uncompacted or cracked areas inside the concrete, the volume of air to solid ratio increases, which can be taken as a direct reflection of the integrity of the concrete. In these cases, given that the acoustic impedance of air is much smaller than concrete, the pulse wave would be reflected almost completely when it encounters the solid-air boundary. Only a part of the pulse wave can bridge the cavity or other defective areas to propagate through to the receiving transducer.

Compared to the defect-free concrete, the following aspects can be considered for assessing the quality of concrete:

(1) According to the variations of transmit time or velocity of wave, the existence

of defects and the scale of estimated defects can be evaluated.

(2) When there is a defective area in the concrete, the ultrasonic wave would be reflected and refracted during the propagation process. Relatively the high-frequency component attenuated faster than the low-frequency component, and normally the change of the frequency from received signal can be analysed for defect judgement and indication.

(3) The complex reflection and refraction occurred simultaneously at the interface between the defect and concrete matrix could result in the propagating phase of pulse waves superimposed with each other. As a result of the superposition, the received waveform would be distorted in different degrees. In that case, the presence of defects can also be discriminated according to different waveform distortion.

6.3 Factors influencing ultrasonic pulse velocity measurement

The ultrasonic pulse velocity measurement in concrete could be affected by a number of factors including age, curing conditions, moisture condition, mix proportions, type of aggregate and cement, etc. In order to provide a reliable measurement of ultrasonic pulse velocity which is repeatable and which depends essentially on the properties of the concrete under test, it is necessary to consider the various factors which can influence the ultrasonic pulse velocity and its correlation with various physical properties of concrete.

6.3.1 Influence of concrete age

Ultrasonic pulse velocity has been widely applied for the assessment of concrete properties as it increases with age as well as the compressive strength. But it is found that the mix of concrete plays an essential role in the growth rate, especially high and low w/c ratio of concrete have a significant difference at an early age (Voigt et al. 2003; Lawson et al. 2011). To clearly define the relationship between ultrasonic pulse velocity and the age of concrete with different mix proportions, it is necessary to eliminate any interferences caused by different strength growth rates.

6.3.2 Influence of water contents

The moisture content has two effects on the pulse velocity: chemical and physical. These effects are important in the production of correlations for the estimation of concrete strength. However, comparison between a fully cured cube sample and a structural element made from the same concrete, there may be a significant pulse velocity difference. Much of the difference is accounted for by the effect of different curing conditions on the hydration of the cement while some of the difference is due to the presence of free water in the voids. It is important that these effects are carefully considered when estimating strength.

6.3.3 Influence of temperature

It has been found that when the variations of concrete temperature are between 10 °C and 30 °C, there is no significant change in strength or elastic properties of concrete. When the concrete temperature is outside this range, corresponding corrections to pulse velocity measurements should be made as given in Table 6-1 (British Standards Institution 2004).

Table 6-1. Effect of temperature on ultrasonic pulse transmission

Temperature	Correction to the measured pulse velocity	
	Air-dried concrete	Water-saturated concrete
℃	%	%
60	+5	+4
40	+2	+1.7
0	0	0
0	-0.5	-1
-4	-1.5	-7.5

6.3.4 Influence of reinforcement

The pulse velocity measured in reinforced concrete in the vicinity of reinforcing bars is usually higher than in plain concrete of the same composition. This is because the pulse velocity in steel may be up to twice the velocity in plain concrete and, under certain conditions, the first pulse to arrive at the receiving transducer travels partly in concrete and partly in steel. Chung (1978) found that the effective pulse velocity is roughly between the pulse velocities in the two separate media, and varies with the

diameter of the reinforcing steel bar and the pulse velocity in the concrete. The apparent increase in pulse velocity depends upon the proximity of the measurements to the reinforcing bar, the diameter and number of bars and their orientation with respect to the propagation path (Bungey 1984; Bungey and Grantham 2006). The frequency of the pulse and surface conditions of steel bar may both also affect the degree to which the steel influences the velocity measurements. So that, wherever possible, measurements should be made in such a way that steel does not lie in or close to the direct path between transducers.

6.3.5 Influence of shape and size of specimen

The velocity of short pulses of vibrations is independent of the size and shape of specimen in which they travel, unless its least lateral dimension is less than a certain minimum value. Below this value, the pulse velocity may be reduced significantly. The extent of this reduction depends mainly on the ratio of the wavelength of the pulse vibrations to the least lateral dimension of the specimen, but it is insignificant if the ratio is less than unity. Table 6-2 (BS EN 12504-4:2004) gives the relationship between the pulse velocity in the concrete, the transducer frequency and the minimum permissible lateral dimension of the specimen.

If the minimum lateral dimension is less than the wavelength or if the indirect transmission arrangement is used, the mode of propagation changes and, therefore, the measured velocity will be different. This is particularly important in cases where concrete elements of significantly different sizes are being compared.

Table 6-2. Effect of specimen dimensions on ultrasonic pulse transmission

Transducer frequency	Ultrasonic pulse velocity in concrete (km/s)		
	v=3.5	v=4	v=4.5
	Minimum permissible lateral specimen dimension		
kHz	mm	mm	mm
24	146	167	188
54	65	74	83
82	43	49	55
150	23	27	30

6.4 Experimental apparatus and numerical methodologies

Essentially the apparatus for AU experiments consists of an electrical pulse generator, transducers, signal amplifiers and an acquisition device for measuring the time interval between the onset of a pulse generated at the exciting transducer and the onset of its arrival at the receiving transducer.

The experimental set-up used in this study is shown in Figure 6-1. Ultrasonic pulse was excited using an Agilent Technologies 33210A WaveStation (10MHz synthesized function generator). The signals were received and recorded with a MISTRAS AE acquisition system through a blocking capacitor, which is used to stop the passage of signals back from the system. The sensors used for this investigation were MISTRAS Group Ltd. (MSL) R15I-AST sensors with a 70-200kHz frequency range for recording transmitted waveforms. The integrated Auto Sensor Test (AST) capability allows these sensors to pulse as well as receive, which can enable the sensor coupling and performance to be verified at any time throughout the test. Grease from Electrolube company was used as the coupling agent to mount sensors on the surface of specimen. The source waveforms were transmitted directly from the wave generator to the AE acquisition system through a capacitor which will trigger the AE system to start recording and computing the time of arrival of signals. In order to accurately obtain the transit time from the excited source to AE sensors, the TRA acquisition mode in the AE system was applied which is a synchronized acquisition mode that the program will only process waveform data. It allows for waveforms acquisition from external/internal TTL trigger with independent or synchronized channels for special applications.

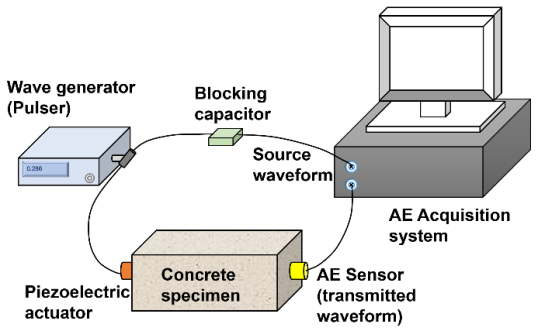

Figure 6-1. Experimental setup for AU measurement in concrete specimen

The methods used for crack depth detection in this chapter are detailed in the subsequent section 6.4.3 and 6.4.4. Those methods have been standardized in 'Technical specification for inspection of concrete defects by ultrasonic method' (CECS21:2000 code) approved by China Association for Engineering Construction Standardization in 2001. Under the standardized action, the methods for crack depth detection are widely applied to investigate the damage level in concrete (Jingfu and Eryu 1993).

6.4.1 Acousto-Ultrasonic pulse signal generation

The Agilent Technologies 33210A is a 10 MHz synthesized function generator with built-in arbitrary waveform and pulse capabilities. A piezoelectric disc with a diameter of 12mm is connected as an output exciter which makes contact with the specimen. The front panel of Agilent 33210A WaveStation is shown in Figure 6-2 and corresponding panel keys functions in Table 6-3.

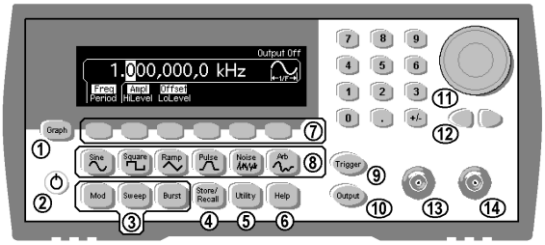

Figure 6-2. The front panel of Agilent 33210A WaveStation

Table 6-3. Panel key functions of Agilent 33210A WaveStation

1	Graph Mode/Local Key	**8**	Waveform Selection Keys
2	On/Off Switch	**9**	Manual Trigger Key
3	Modulation/Sweep/Burst Keys	**10**	Output Enable/Disable Key
4	State Storage Menu Key	**11**	Knob
5	Utility Menu Key	**12**	Cursor Keys
6	Help Menu Key	**13**	Sync Connector
7	Menu Operation Softkeys	**14**	Output Connector

6.4.2 Ultrasonic Pulse Velocity

As an effective NDT&E method, Ultrasonic Pulse Velocity (UPV) measurement has been largely applied for quality control of concrete materials and detecting damages in structural components. The UPV methods have traditionally been used for

the quality control of materials, mostly homogeneous materials such as metals and welded connections. With the recent advancement in transducer technology, the test has been widely accepted in testing concrete materials. Ultrasonic testing of concrete is an effective way for quality assessment and uniformity, and crack depth estimation. The test procedure has been standardized as “Testing concrete—Part 203: Recommendations for measurement of velocity of ultrasonic pulses in concrete (BS 1881-203: 1986)”.

6.4.3 Single-side flat measurement

In the case of that there is only one measurable surface on the cracking structure, and the crack depth is estimated to be no more than 500mm, then the single-side flat measurement method would be applicable to be employed for crack detection and evaluation.

Ultrasonic single-sided flat measurement method for detecting crack depth is based on the phenomenon of acoustic diffraction. In this method, the pulser and receiver are placed on both sides of the crack, as shown in Figure 6-3. It can be seen that the waves received by the receiver are only diffracted waves which have bypassed the crack tip.

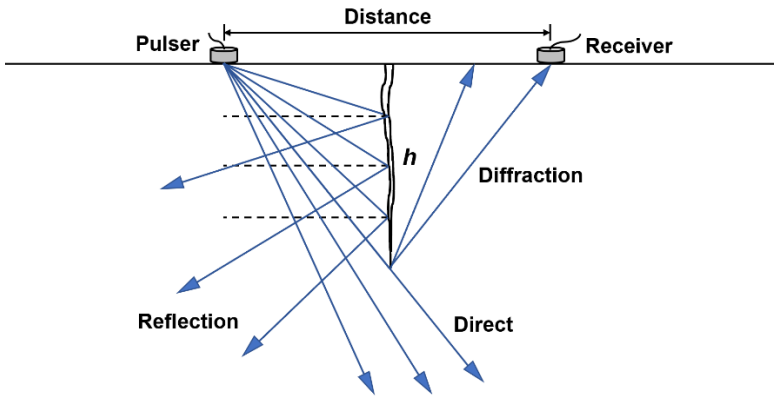

Figure 6-3. Crack depth detection using single-side flat measurement method

When acoustic waves propagate past an obstacle in a medium, the direction of waves changes, this is called diffraction and is shown in Figure 6-4. The Huygens-Fresnel principle qualitatively explains the diffraction phenomenon. It states that every point on a wavefront is itself the source of spherical wavelets and then the sum of these

spherical wavelets forms the wavefront. The Huygens-Fresnel principle theoretically explains the diffraction of wave. But for the comprehension of the changes of amplitude and phase of the diffracted wave in the single-side flat test, it is necessary to obtain an analytical expression of the space diffraction wave field.

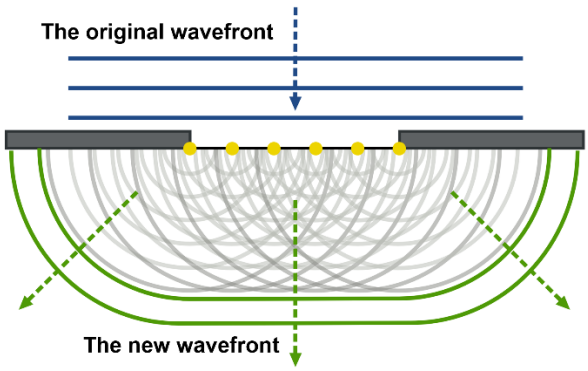

Figure 6-4. Wave diffraction in the manner of Huygens and Fresnel

6.4.3.1 Pre-measurement of initial velocity

During the flat test, the testing points should be arranged at different locations with different distances on both side of the crack using as the symmetry. The detection steps are as follows:

(1) Measuring the velocity in non-cracked surface area

Place the actuator and receiving transducer on a representative surface with a uniform quality concrete surface around the crack. Measuring the propagation time between the actuator and transducer for the distances equalling 100mm, 150mm, 200mm, 250mm, 300mm and 350mm. Then draw a 'time-distance' graph as shown in Figure 6-5, where it can be seen that all the points should be in a straight line. The slope of the straight line corresponds to the average propagation velocity of the ultrasonic pulse wave. The linear regression equation can be presented as follows:

$$l_i = a + bt_i \tag{6.1}$$

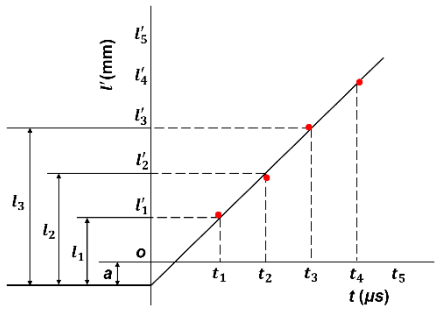

Figure 6-5. Time-distance graph under non-crack single-side flat measurement

The real propagation distance l_i of each measurement point is:

$$l_i = l' + |a| \tag{6.2}$$

Where

l_i is the real propagation distance of ultrasonic wave at measurement point i;

l' is the inner edge spacing between pulser and receiver at measurement point i;

a is the intercept of l' axis in the “Time-distance graph”, or the constant term of the linear regression equation.

The wave velocity used for flat measurement can be calculated as:

$$v = \frac{(l'_n - l'_1)}{(t_n - t_1)} \quad \left(\frac{\mathrm{km}}{\mathrm{s}}\right) \tag{6.3}$$

or

$$v = b \quad \left(\frac{\mathrm{km}}{\mathrm{s}}\right) \tag{6.4}$$

Where

l'_n and l'_1 are the distance (mm) of measurement points n and 1 respectively;

t_n and t_1 are the propagation time ($\mu\mathrm{s}$) of measurement points n and 1 respectively;

b is the regression coefficient.

(2) Placing the actuator and receiving transducer on the symmetrical sides of the crack as the axis

As shown in Figure 6-6 below, based on the wave velocity calculated in the previous step, the propagation distance of the signal can be calculated once the propagation time is determined. Thus, according to the equation (6.4) below, the crack depth h can be determined.

The actuator and receiver are placed on both sides respectively and symmetrically of the crack. Take the value of l' as 100mm, 150mm, 200mm, etc. And then take the measurements of transmitted time of each propagation paths.

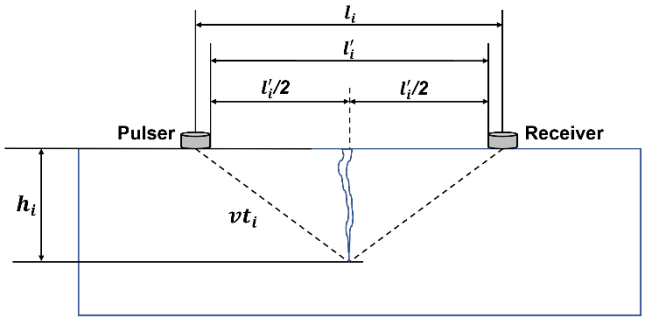

Figure 6-6. Experimental setup for single-side flat measurement (with pre-measurement of initial velocity)

The single-side flat measurement method for detecting the crack depth could be calculated as follows:

$$h_{ci} = \frac{l_i}{2} \cdot \sqrt{\left(\frac{t_i^0 v}{l_i}\right)^2 - 1} \tag{6.5}$$

$$m_{hc} = \frac{1}{n} \cdot \sum_{i=1}^{n} h_{ci} \tag{6.6}$$

Where

l_i is the real propagation distance of ultrasonic wave under non-crack flat measurement method at measurement point i;

h_{ci} is the calculated crack depth based at measurement point i;

t_i^0 is the travel time of ultrasonic wave at measurement point i;

m_{hc} is the average value of crack depth calculated from all measurement points;

n is the number of measurement points.

6.4.3.2 Without pre-measurement of initial velocity

Based on the assumption that the wave propagation in the specimen has the same velocity, and also to avoid human errors from distance measurement, system errors of velocity calculated from method in section 6.4.3.1, and other interference factors, another experimental setup for crack depth monitoring without pre-measurement of initial velocity is shown below in Figure 6-7.

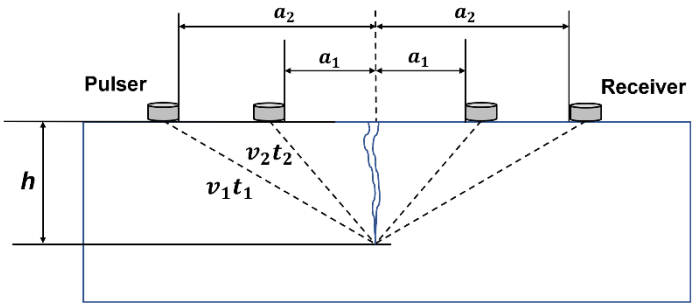

Figure 6-7. Experimental setup for single-side flat measurement (without pre-measurement of initial velocity)

Where

h is the calculated crack depth (in mm)

v is the actual ultrasonic velocity

Assuming that v_1=v_2 and a_2=2a_1,

then the crack depth can be evaluated as follow:

$$h = a_1\sqrt{\frac{4{t_1}^2-{t_2}^2}{{t_2}^2-{t_1}^2}} \tag{6.7}$$

6.4.4 Double-side oblique measurement

If the cracking region of the structure has two available parallel testing surfaces, then the double-side oblique measurement can be applied for crack or damage detection.

The measuring points arrangement is as shown in Figure 6-8. The pulser and receiver are placed on the two testing surfaces corresponding to the measuring points

1, 2, 3…8, and then according to the abrupt changes in amplitude, travel time and frequency, the depth of the crack and whether the wave has passed through the damaged section could be determined.

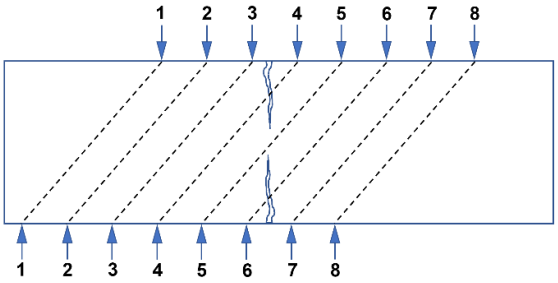

Figure 6-8. Experimental setup for Double-side oblique measurement

6.4.5 Akaike Information Criterion (AIC) for wave arrival prediction

The evaluation methods of crack development monitoring based on AU technique mainly depend on an accurate measurement and calculation of signal transmitted time. In that case, it means that the detection of actual start time of waveform is of great importance. Traditionally the most accurate way to pick the onset time of a wave would be to do it manually. And it is largely depended on checking the signal traces based on the analyst's experience. In terms of the acquisition system, normally it would be triggered once the wave crossing the pre-set threshold and that crossing point will be detected and recorded as the onset time of the wave instead of the actual start. And though possibly insignificant, errors could still occur, as shown in Figure 6-9.

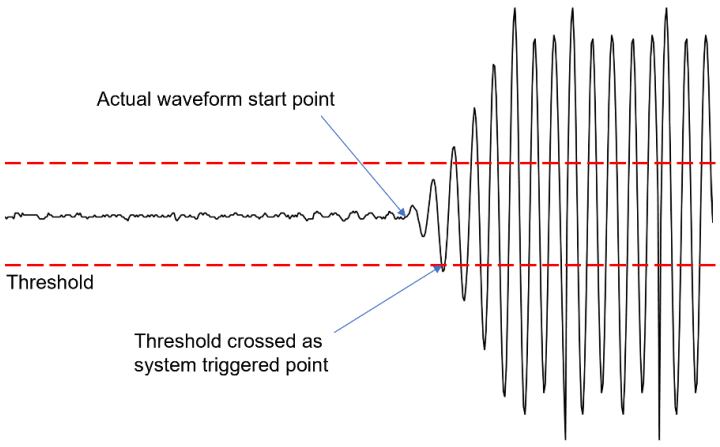

Figure 6-9. System triggered point missing the true waveform start point

One of the weakness of manually doing so is that it is considerably time demanding. It is almost unfeasible especially when handling large volumes of digital

and real-time data and completely impossible for an in-situ Structure Health Monitoring system on a concrete structure. Therefore, some processing technique is required, similar to that developed by Shah et al., where the onset time of a wave is determined by applying differences between the standard deviation of noise and the signal (Maji and Shah 1988; Li and Shah 1994).

An automated method was also initially proposed by Japanese scholar Naoki Maeda (Maeda, 1973) to adopt the AIC (Akaike Information Criterion) function. In this method, the onset time of a wave is determined when the AIC value becomes the global minimum. The AIC value at point $i = k$ calculated by the following equation:

$$\mathrm{AIC}_k = k \cdot \log\{\mathrm{var}(X[1,k])\} + (N-k) \cdot \log\{\mathrm{var}(X[k,N])\} \qquad (6.8)$$

where N is the number of amplitudes of a digitized wave, X_i is an amplitude of a signal $(i = 1,2,\ldots,N)$, $\mathrm{var}(X[1,k])$ indicates the variance between X_1 and X_k, and likewise $\mathrm{var}(X[k,N])$ is also the variance between X_k and X_N.

Basically, this function compares two vectors for similarity, the point at which the first vector is purely noise and therefore has a high-entropy and the second is only signal with low-entropy, will return the lowest correlation and therefore identify the start of the waveform. One example of this being used to detect the start of a signal compared with the traditional threshold crossing technique can be seen in Figure 6-10.

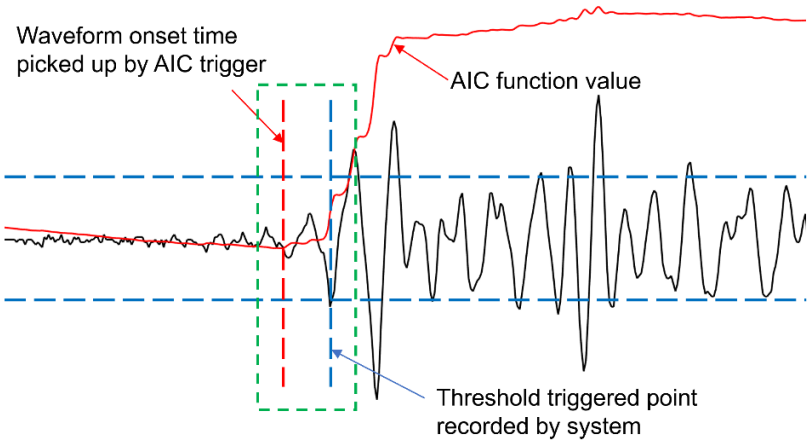

Figure 6-10. System triggered point missing the waveform start point

Work on the monitoring of the setting and hardening of concrete conducted by Kurz et al. (2005) compared the AIC-picker method with an automatic onset detection

algorithm based on the Hinkley criterion and manual picks as well as reference values. It has shown that the AIC-picker is a highly reliable tool for automatic onset detection for ultrasound signals and acoustic emissions of varying signal to noise ratio.

Further improvements have been made a variety of researchers for different purposes such as improving the accuracy and reducing the processing time. Pearson et al. (2017) utilised the Akaike Information Criterion (AIC) to greatly improve the accuracy of the triggering in terms of detecting the exact arrival time of a waveform.

6.5 Preliminary Investigation with notched specimen

In order to test the feasibility and effectiveness of the applied methods, a set of preliminary investigation was conducted. A standard notch with a known depth was created on each concrete specimen before then testing to verify the above two methods gave results within a reasonable range for practical applications.

6.5.1 Results of single-side flat measurement (with pre-measurement of initial velocity)

(1) Initial velocity measurements – for single-side flat measurement

To acquire the average wave propagation velocity, this method was tested on two specimens of size 100×100×500 (mm) with different intervals (l': 50, 100, 150, 200, 250, 300, 350 mm) of measurement points. The results and time-distance graph are shown in Table 6-4 and Figure 6-11.

Table 6-4. The results of non-cracking surface flat measurements

Distance between measurement points (mm)	Wave transit time (μs)	Calculated velocity (km/s)	Average velocity (m/s)	R^2
100	24.9	4.0373	4.1759	0.9984
150	37.4	4.0149		
200	49.2	4.0655		
250	58.5	4.2741		
300	69.6	4.3113		
350	80.4	4.3526		

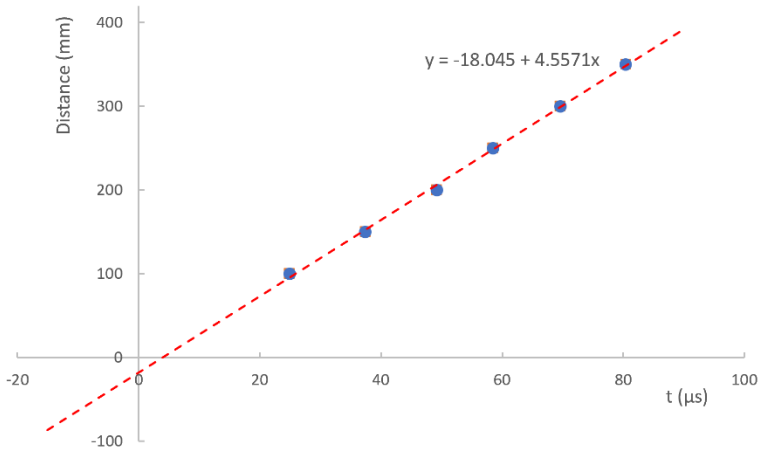

Figure 6-11. Time-distance graph under non-crack flat measurement

The time-distance regression equations are:

$$y = -18.045 + 4.5571x \tag{6.9}$$

Then the calculated velocity based on the regression equation is 4.5571 $\mathrm{km/s}$, which is the regression coefficient of the above regression equation.

Based on the measured velocity above, the results of crack depth measurement can be determined and presented in Table 6-5 according to equation (6.5) and (6.6) in section 6.4.3.

Table 6-5. The results of crack depth measurement on notched specimen – method 1

Specimen	Notch depth	Test No.	Calculated depth/mm		Absolute error/mm		Relative error/%	
			measured	average	measured	average	measured	average
Beam1	20mm	1	18.82	18.40	1.18	1.60	5.9	8.04
		2	19.14		0.86		4.3	
		3	17.26		2.74		13.7	
		4	18.11		1.89		9.5	
		5	18.65		1.35		6.8	
Beam2	40mm	1	35.68	35.39	4.32	4.61	10.8	11.54
		2	36.64		3.36		8.4	
		3	33.42		6.58		16.5	
		4	37.1		2.9		7.3	
		5	34.13		5.87		14.7	

It can be seen that the results above show that the maximum absolute error of 20mm regular notch (can be regarded as a vertical crack) depth measurement is 2.74mm, and the corresponding maximum relative error is 13.7%. For the 40mm

regular notch, the maximum absolute error of results is 6.58mm and the corresponding maximum relative error is 16.5%.

6.5.2 Results of single-side flat measurement (without pre-measurement of initial velocity)

Based on the description in section 6.4.3.2, take a_1 as 50mm and a_2 as 100mm respectively, as $a_2=2a_1$. The results are shown below in Table 6-6.

Table 6-6. The results of crack depth measurement on notched specimen – method 2

Specimen	Notch depth	Test No.	Calculated depth/mm		Absolute error/mm		Relative error/%	
			measured	average	measured	average	measured	average
Beam1	20mm	1	14.97	12.87	5.03	7.13	25.2	35.72
		2	10.77		9.23		46.2	
		3	13.27		6.73		33.7	
		4	14.67		5.33		26.7	
		5	10.65		9.35		46.8	
Beam2	40mm	1	34.85	33.95	5.15	6.05	12.9	15.14
		2	33.09		6.91		17.3	
		3	34.38		5.62		14.1	
		4	33.54		6.46		16.2	
		5	33.91		6.09		15.2	

It can be seen from the results above that this method has larger errors comparing to the previous method. Especially when measuring 20mm notch, the maximum absolute error reached 9.23mm and the corresponding relative error reached 46.2%.

By comparing and analysing the two methods above, method 1 with initial velocity measured is more sensitive and accurate to determine the depth of crack. The relative error for both 20mm and 40mm crack are all around 10%, which is within a credible range and can be accepted for practical engineering testing. For method 2, without initial velocity measured, the relative errors are relatively larger, and the largest relative error reached 46.2%.

It should be noted that those results above are based on the premise of regular cracks (notches). In an actual situation, due to the various forms of cracks and damages in field engineering inspection, the development trends of cracks are always

irregular. Additionally, the moisture content, impurities and other substances in the crack, position of transducers, restriction of working conditions, etc. could all have a huge affection to the measurement results, and eventually result in even a greater measurement error. Therefore, before the selection of testing methods for any actual engineering inspection, it has to be checked and ensured that the selected method can meet the actual engineering needs and the errors should be within an acceptable range.

6.5.3 Results of double-side oblique measurement

A prerequisite of the single-side flat measurement method is that the wave will be traveling around the cracking tip. But in most cases, when there are impurities contents, such as moisture, dust particles, exfoliated cement paste at the tip of crack, or partially filled with those things, it will become an extra channel for signal propagation. Especially when the shear-resisting mechanisms aggregate interlock exists (shown in Figure 6-12) in the structure after cracks developed, it can lead to significant errors in the measurement results.

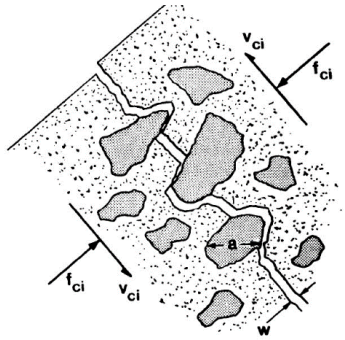

Figure 6-12. Schematic of aggregate interlock (Cescatti 2016)

Due to reasons above and as described in previous section 6.4.4, when the cracking region of structure to be tested has two available parallel surfaces, the double-side measurement method should be preferred for testing. The transducers are placed on two opposite surfaces and the measurement line is perpendicular, or obliquitous, to the testing surface. The ultrasonic wave can pass through the structure and be received by the transducer. The strength of received signal directly perpendicular should give the largest received signal strength among all positions, but is less useful to judge the structural condition, especially for perpendicular cracks.

A concrete beam of size 75mm x 75mm x 225mm is prepared for the double-side oblique measurement. To investigate and verify the impact of crack on result, a 30mm notch is manufactured at the centre line of the bottom surface. The measuring points arrangement is shown in Figure 6-13. The pulser and receiver are placed on the two testing surfaces respectively corresponding to the measuring points 1-1', 1-2',… etc.

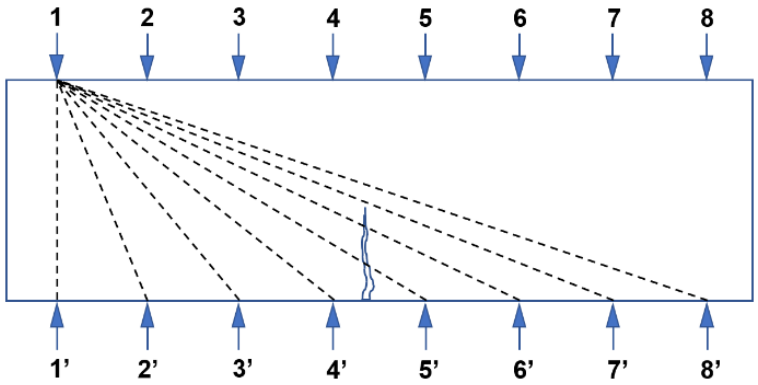

Figure 6-13. Measuring points arrangement for double-side oblique measurement

The wave propagation times of each measurement line were recorded and the corresponding velocities then are determined according to their different propagation paths. The test setup is shown in Figure 6-14 and results are shown in Table 6-7 below.

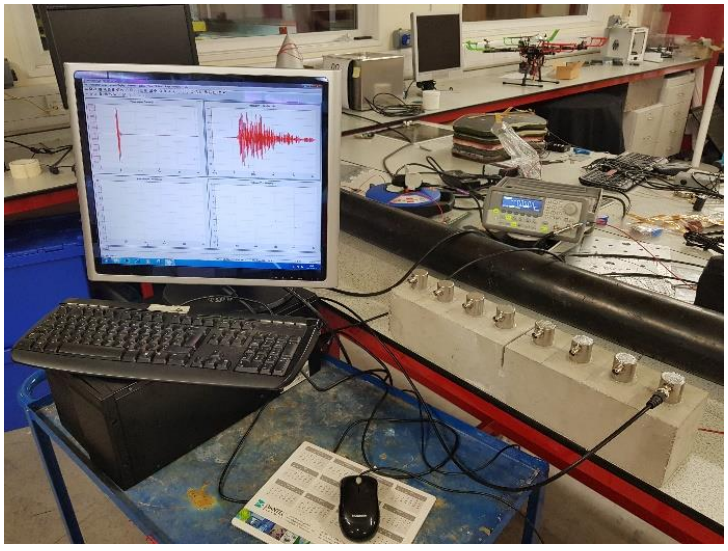

Figure 6-14. Test setup for notch depth measurement with AU

Table 6-7. Velocity of each measurement path (km/s)

Measurement points	1	2	3	4	5	6	7	8
1	4.05	3.02	2.74	2.77	2.01	1.91	2.11	2.25
2	3.11	1.38	2.17	4.00	0.98	1.69	1.96	1.60
3	2.82	1.96	1.81	2.29	0.88	1.77	1.10	1.36
4	2.89	2.61	3.23	3.45	1.87	3.46	1.83	1.34
5	2.30	1.28	4.27	4.31	3.30	3.30	3.62	2.89
6	1.91	1.65	1.44	1.26	3.85	4.62	3.85	2.93
7	1.98	1.03	1.44	0.83	1.19	2.07	2.04	2.83
8	2.23	1.78	2.16	1.43	2.57	2.00	3.99	2.88

If the wave propagates through a damaged area, then there will be a time delay which affects the apparent velocity obtained directly from the travel time. Based on the results from Table 6-7, the velocity distribution of all measurement lines can be visualized by a tomography created using MATLAB as shown in Figure 6-15 (left). Furthermore, if the tomography is presented using individual facet blocks as shown in Figure 6-15 (right), the defect area can be intuitively interpreted based on each pair of measurement lines.

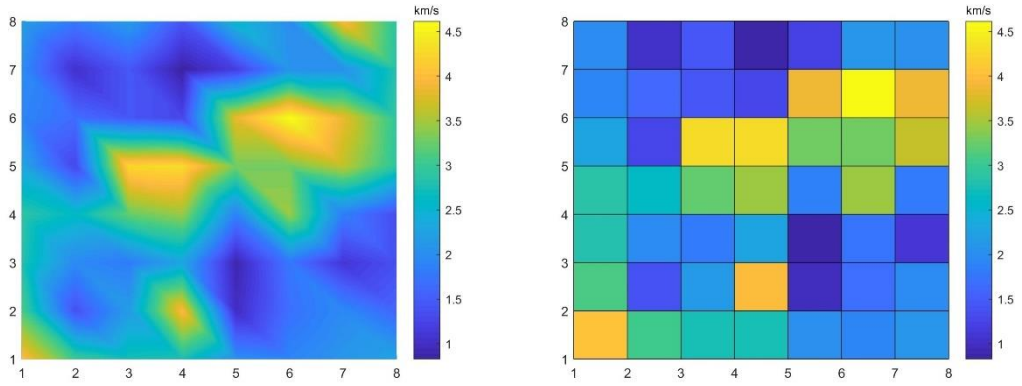

Figure 6-15. Tomography of the specimen with defectives

Theoretically, those measurement lines with the same notation number (e.g. 1-1', 1-2',…, 8-8'), as shown in Figure 6-13 previously, should have the least affected velocity, since each wave propagation path is perpendicular to the two testing surfaces. In these cases, the transducers did not have any manufactured damage in between. Furthermore the average velocities of those vertical measurement lines should be able to be used to represent the average velocity of signal propagation throughout the whole

concrete sample. As shown in Table 6-8 below, the average velocity of these eight measurement lines is 2.94 km/s.

Table 6-8. Velocity of each measurement path (km/s)

Measurement line	1-1’	2-2’	3-3’	4-4’	5-5’	6-6’	7-7’	8-8’	Average	Standard Deviation σ	CoV/%
Velocity (km/s)	4.05	1.38	1.81	3.45	3.30	4.62	2.04	2.88	2.94	1.13	38.5%

It can be considered as the ‘intact area’, or ‘unaffected area’ if the velocity is higher than the average 2.94km/s. Conversely, if it is lower than the average then it can be regarded as the ‘defect area’. Thus, the whole structure can be simply separated into two parts. In Figure 6-16 below, those ‘unaffected areas’ are highlighted in green facet block while those ‘defect areas’ are in grey. It shows a simple and effective way for displaying and evaluation of defects in structures.

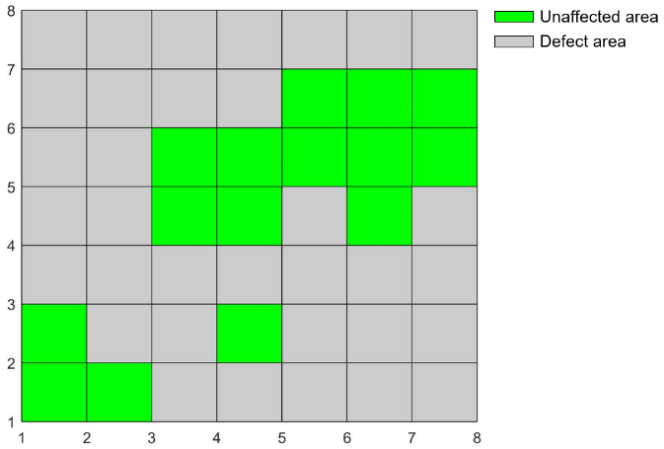

Figure 6-16. Distribution of intact areas and defect areas

It can be seen from Figure 6-16 above that the most of unaffected areas appear on the diagonal region where are the position of all vertical measurement lines, which also matches the assumption that these propagation paths have the least affected velocity.

It was proved that the double-side oblique measurement is an effective way to determine the location of defect areas and quantify the damage degree to a certain extent in concrete structure. But there may be still misjudgements as the velocity spectrogram could show an enlarged defect region and result in errors. Because this

is not only related to structure defects, but also mainly related to the inhomogeneity and density of concrete, coupling condition between transducers and specimen and all possible factors mentioned in section 6.3.

6.5.4 Discussion

For all the methods mentioned above, one critical parameter used is the wave velocity of ultrasonic signal propagating in concrete structure. The velocity used for crack depth measurement in the single-side flat measurement method is obtained by the flat measurement (see in section 8.4.1). However, it was found by actual inspection of structure that there was a big difference in wave velocity between non-crack crossing measurement and crack crossing measurement. If the velocity gained directly from the non-crack crossing flat measurements and applied for the evaluation and calculation of crack depth, it will cause a significant error.

The ultrasonic pulse waves used for damage detection include longitudinal waves, transverse waves, and more complex surface waves (Rayleigh waves). Among them, the longitudinal waves travel with the fastest velocity and the smallest amplitude. The transverse waves propagate with a slower velocity and higher amplitude than longitudinal waves. The surface wave travel with the slowest velocity and the largest amplitude. Therefore, the wave propagation time measured from the single-side flat measurement (section 6.4.3) is based on the arrival of longitudinal waves, and it should be also used when calculating the crack depth.

Among the ultrasonic pulse waves used for detecting concrete structures, there are longitudinal waves, transverse waves, and more complex surface waves. Among them, the speed of longitudinal waves is the fastest, followed by the speed of transverse waves with the smallest amplitude, the amplitude of which is larger than that of longitudinal waves, while the speed of surface waves is the slowest and the amplitude is the largest. Therefore, the first wave of sound measured during the horizontal crack measurement must be the sound of the longitudinal wave, and the velocity of the longitudinal wave should also be used when calculating the crack.

The velocity obtained from non-crack crossing measurement (described in section 8.4.1) is not from the longitudinal wave but the transverse wave, as the longitudinal wave propagates and vibrates parallel to the testing surface and perpendicular to sensing direction of the piezoelectric element in the receiving transducer. Thus, the receiving transducer is not able to receive the longitudinal wave. Conversely, the transverse wave propagates and vibrates perpendicular to the testing surface, and it has the same direction to the piezoelectric sensing element in the receiving transducer and can be properly received. In that case, the detected wave from receiving transducer should be the transverse wave in non-crack crossing measurement. So, theoretically the velocity based on that propagation time should be the velocity of transverse wave rather than the longitudinal wave. This is the essential reason for the large difference between the wave velocity measured from non-crack crossing measurement and crack crossing measurement.

Therefore, the longitudinal wave velocity should be used instead of the velocity measured from non-crack crossing measurement when evaluating and calculating the crack depth. However, in practice the structure to be tested only has only one available testing surface, and then it is not possible to measure ultrasonic wave velocity by using double-side measurement method.

In the case that the testing conditions cannot be satisfied, the wave velocity obtained have to be modified accordingly before being applied in the calculation. Shou-Xing and Gen-Huo (2007, 2008, 2010) conducted a large number of experiments to determine the ratio of the velocity measured by single-side flat measurement method compared to those measured by double-side measurement method. They have proved that by substituting the modified wave velocity into the equation for calculations, to a certain extent the accuracy of measurement results can be improved, which is desirable for a more accurate detection in real situation if the testing site conditions can be met.

6.6 AU inspection and monitoring of crack development in plain concrete

Based on the previous preliminary experiments, the single-side flat measurement method is selected to monitor the crack development of concrete beam subjected to bending in this study. Two measurement methods as described in section 6.4.3 and shown in Figure 6-17 below are applied for the computation of estimated experimental results.

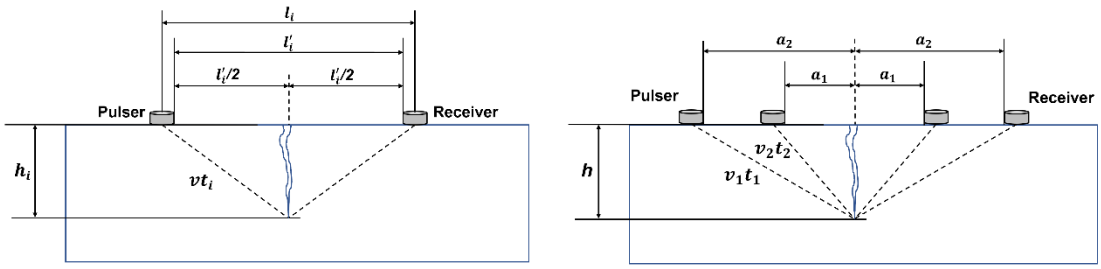

(a) (b)

Figure 6-17. Two methods of propagating and receiving ultrasonic pulses for monitoring the crack development: (a) Method 1 - with initial velocity measured; (b) Method 2 - without initial velocity measured.

6.6.1 Specimen preparation

In this study, four concrete beam specimens of size 100mm x 100mm x 500mm are prepared and all the specimens were cast from the same batch in order to ensure the accuracy of comparative tests. All the beams had full 28 days curing period before they are tested. The details of concrete mix used are shown in Table 6-9.

Table 6-9. Concrete mix used for all specimens

Grade	W/C Ratio	Cement	Water	Fine Agg. (0-4mm)	Coarse Agg. (4-10mm)
C40	0.46	1	0.46	1.93	2.25

Prior to tests, all specimens were notched to a depth of 6mm at the central of the bottom surface with a rotating diamond blade to ensure that the crack will occur exactly from the middle and captured by DIC cameras. Two knife edges were glued on both sides of the notch to take the clip gauge for monitoring the crack mouth opening displacement (CMOD) during testing. The front surface of all specimens was painted with a black speckled pattern after curing for the purpose of DIC testing.

6.6.2 Experimental Setup and test arrangement

The experimental setup is shown in Figure 6-18 below. Ultrasonic pulse with a frequency of 100kHz was excited by the actuators using the wave generator (Agilent 33210A). For recording the transmitted signals, two R15I-AST sensors with were amounted on the bottom of the specimen.

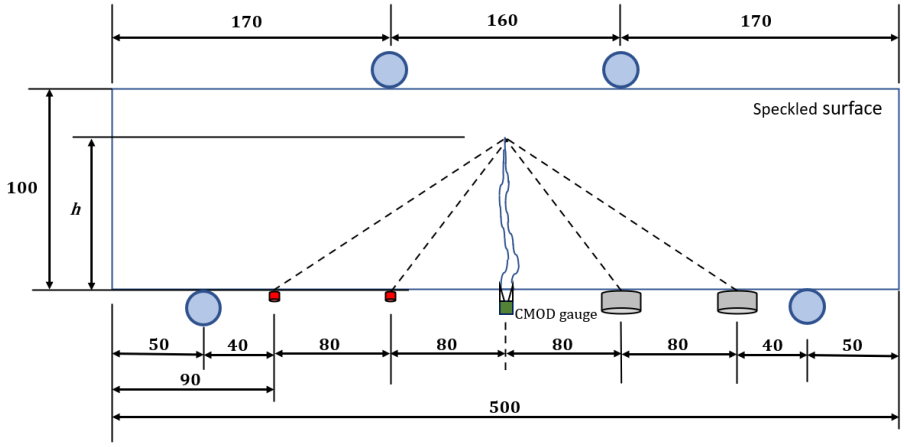

Figure 6-18. Sensors arrangement for crack depth measurements under a four-point bending arrangement

6.6.3 Loading conditions

As shown in Figure 6-19, beam1 and beam2 are subjected to three-point bending and beam3 and beam4 are subjected to four-point bending, both loaded over a span of 400 mm. The load is controlled by CMOD and increased monotonically with a rate of 0.002 mm/s. During the test, there is a pause for every 0.02mm increased in CMOD until it reaches 0.50mm in the end. Therefore, there are 25 pauses in total in the testing process for each specimen. During each pause, a pulse was applied in five 5-cycle square burst pulses, excited from two actuators and received by the two sensors on the right. Simultaneously, two DIC images were captured (every 0.01mm CMOD increase) during each pause for monitoring the crack propagation.

Four beam specimens were tested in this study and the tests conducted in two groups. As shown below, Figure 6-19(a) is the test setup for Beam 1&2 and Figure 6-19(b) is the test setup for Beam 3&4.

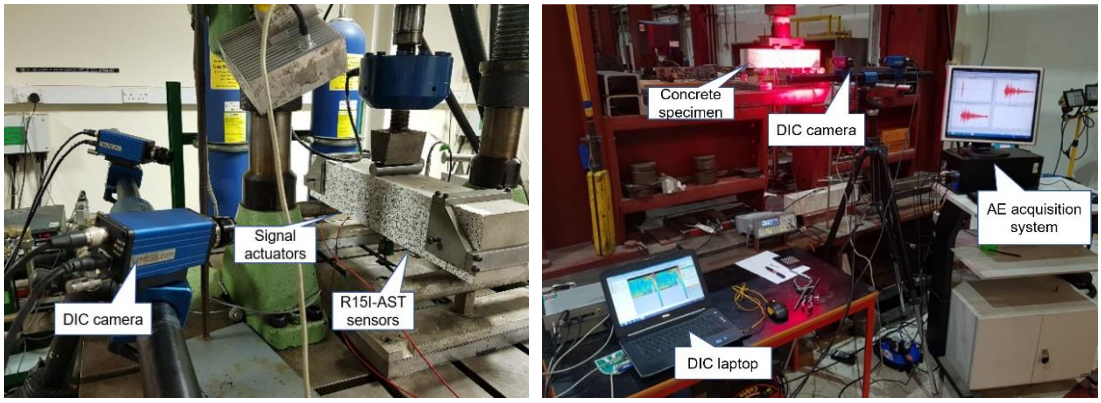

(a) Test setup of Beam 1&2 (b) Test setup of Beam 3&4

Figure 6-19. Test setup for crack monitoring with AU and DIC

6.6.4 Results

The complete data obtained from two methods for the crack depth measurement are attached in Appendices (Table 8-1 to

Table 8-4) and graphically presented in Figure 6-20 below. The orange and red curves in each graph are the results of crack development trajectories from method-1 and method-2 corresponding to the y-axis on the right. The loading history is recorded in blue curves corresponding to the y-axis on the left. The dotted purple line indicates the height of beam and the black line is the crack depth development trajectory obtained visually by DIC cameras.

It should be mentioned that, in Figure 6-20 (a) and (b), due to the set-up and focus issues, the whole images of cracking region of specimen are not fully contained in the DIC cameras and recorded. The DIC data is not included when the beam height exceeds 76mm and replaced by the dotted line for clearness and cross-checks. This problem has been solved in Figure 6-20 (c) and (d).

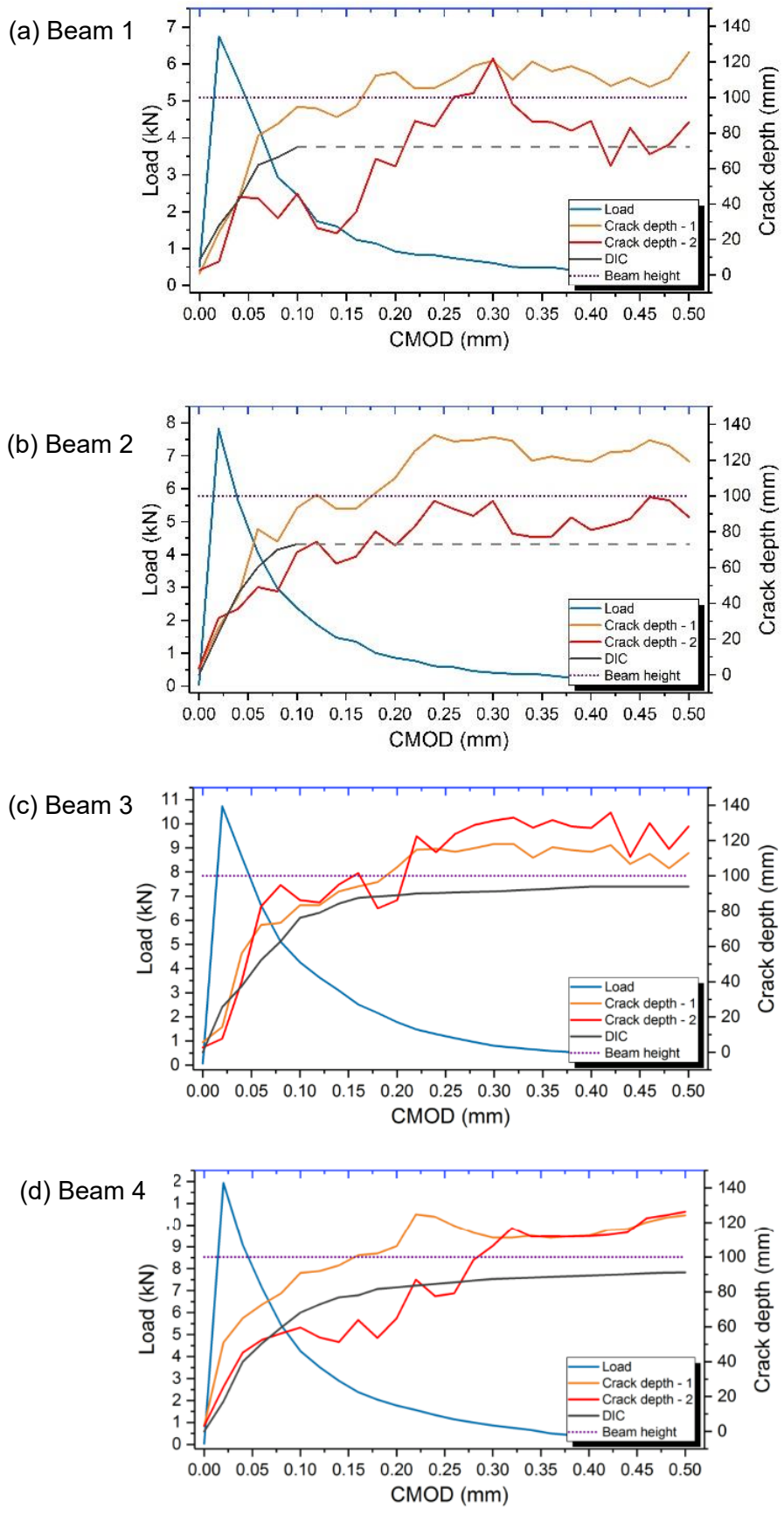

Figure 6-20. Crack development trajectories of each specimen

Figure 6-21 shows the DIC image indicating the principal strain distribution from Beam3. In order to clearly distinguish the crack developed throughout the test from DIC data, the image scale upper limit has been set as 30 microstrain to get a clear resolution for tracking the crack dip through all the images captured during test.

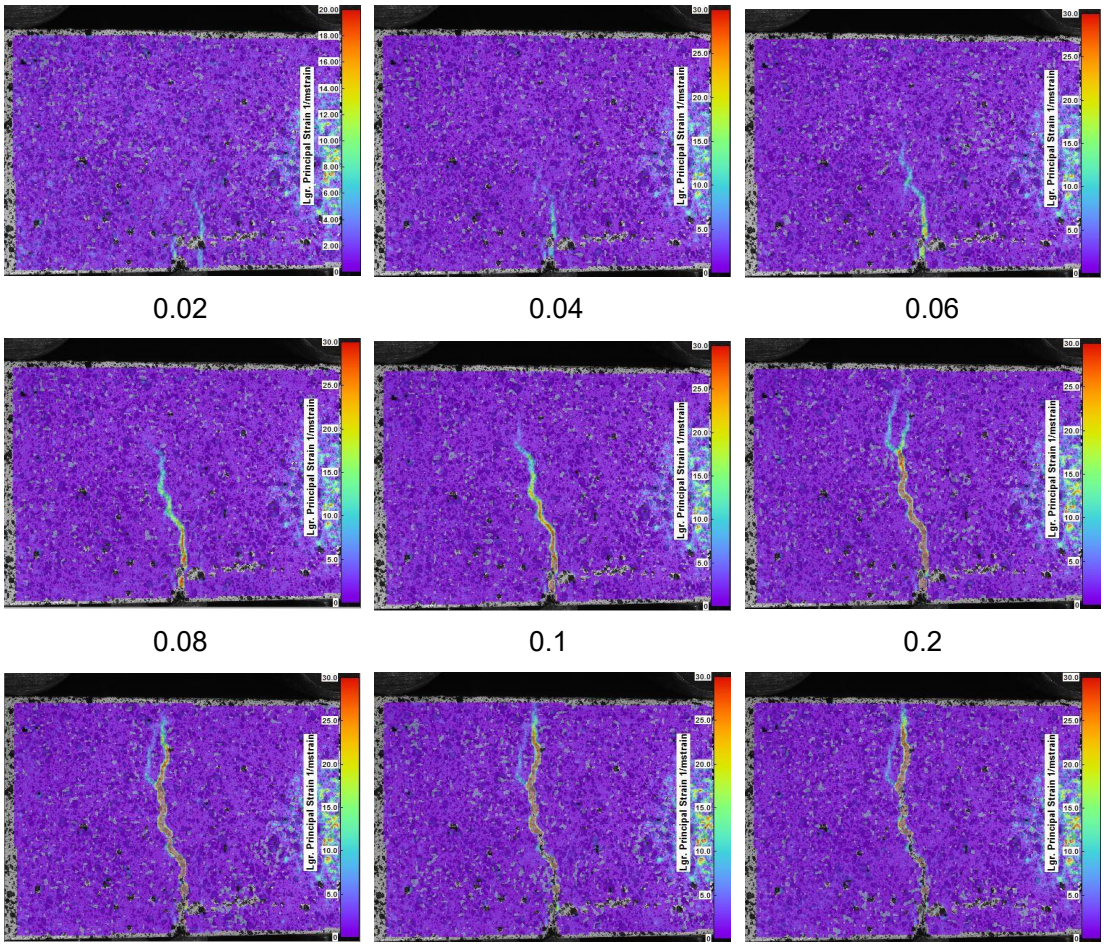

Figure 6-21. The crack evolution based on DIC principal strain profiles at different CMOD (mm) values as projected on the X–Y plane

It should be noted that, in this study, the results acquired from DIC images are experimental values rather than theoretical values. It is used as the actual values to provide a reference when plotting the results in Figure 6-20.

Through analysing the data above from four sets of test data and calculation results, it can be seen that the maximum absolute error of measurement is 1.7cm and the relative error is 5.2%.

The above data shows that the ultrasonic single-side flat measurement method

has relatively high accuracy of crack depth measurement and reliable test results. However, the impurities, loading condition, testing environment, water content and all possible factors mentioned in section 6.3 can cause a certain influence on the accuracy. From the results it can be seen that the absolute error is 4cm before the crack develops to half the height of the beam, which is around 50-60mm, and that stage of results can be considered to be much more reliable compared with the subsequent measurements. To a certain degree, this testing method can be recognized as an effective and feasible way for crack depth measurement to meet the engineering requirement.

6.6.5 Discussion

From the results shown in Figure 6-20, it can be seen that both method 1 and method 2 are promising as the overall trend are met with the DIC results. Even there are some significant errors at several measuring points (e.g. the red curve in Figure 6-20 (a)), it can still provide useful information regarding a rough idea about the depth of crack(s) or degree of damage, and be satisfied to meet the practical engineering needs in most of cases.

With respect to the causes of errors, one hypothesis of the flat measurement method is that the ultrasonic wave will travel around the crack tip. In summary, the possible reasons can be mainly concluded as follows:

1. The relationship between ultrasonic wave velocities obtained from the single-side flat measurement and double-side measurement. As discussed in previous section 6.5.4, the velocity applied in method-1 will have a big impact on the results. To acquire a more accurate results, the relationship between two velocities should be investigated experimentally beforehand and the correlation coefficients determined.

2. During the test, the cracks are developing accompanied by the splitting of the concrete matrix and other different types of damages occurred simultaneously as the load increased. In the process of formation of cracks, it could be filled by any impurities contents, such as moisture, dust particles, exfoliated cement paste, etc. inside the crack, especially when the aggregate interlock exists during crack development, and

create an extra tunnel for wave propagation and result in the reduction of propagation path. Eventually the measurement will present a shallower result than the real crack depth.

3. The reading of crack depth from DIC images are experimental values and treated as the actual values in Figure 6-20. But it is obtained visually and only from the specimen surface. So, it can neither be used to represent the situation of entire specimen, nor can it be used as a theoretical value. It can only be used to provide a reference value when comparing with the other measurement results. In that case, it can be regarded as a system error as it correlates to all measurement results and will have insignificant effects to the comparison of two methods.

4. As the Akaike Information Criterion (AIC) is introduced to pick the onset time of a wave, any abnormal data should be examined manually just in case the AIC picker miss-reads the starting point.

6.7 Investigation of the impact of healing agent in self-healing concrete

Condition of concrete may be affected by the quality of a design, manufacturing, loads applied to a structure, character of the loads, environmental deterioration, or aging. The condition of concrete is essential for the safety of a structure. The AU method is a frequently-used technique in civil engineering and the wave velocity largely depends on the medium properties. Therefore this method is considered for the investigation of properties of the healing agent as the glued bonding layer in this study to investigate how it will affect the signal propagation and reflect the healing effect.

Propagation velocity of the longitudinal wave (P wave) through the material (v_p) can be calculated as:

$$v_p = \sqrt{\frac{E_d}{\rho}\frac{1-v}{\rho(1+v)(1-2v)}} \tag{6.10}$$

where E_d is dynamic Young's modulus, v is the Poisson's ratio, and ρ is the material density.

In this preliminary study, six concrete cubes of size 100mm×100mm×100mm were

cast for the test. All the cubes were cast from the same batch in order to keep the consistency and increase the accuracy of comparative tests. Specimens were left for 24 hours in open air after casting. And then all the specimens were demoulded and placed in the water tank for 28 days curing.

6.7.1 Individual cubes study

A schematic diagram of the test setup for the individual cubes study is shown in Figure 6-22. Excitation piezo-disc was mounted on one side on the specimen and the receiving sensor was mounted on the other side. The sensors used for this investigation were MISTRAS Group Ltd. (MSL) R15I-AST sensors with a resonant frequency of 75 kHz. Data acquisition was via a 4-channel MISTRAS system using the AEwin software with the sampling frequency of 2 MHz.

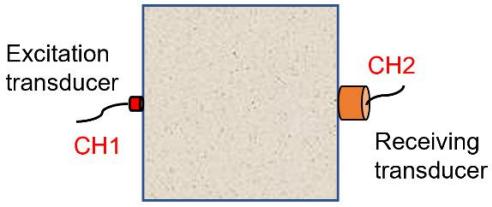

Figure 6-22. Excitation/receiving transducers setup for individual cube specimen

The pulse signals were generated using an Agilent 33210A WaveStation registering as a 6Vpp square wave signal. A frequency of 100kHz was excited as a 5-cycle burst. A total of 5 waves were excited and received for each specimen. The results of signal travel time and corresponding apparent velocity are shown in Table 6-10 and Table 6-11 respectively.

Table 6-10. Signal travel time of each pulse for the 6 specimens (unit: microsecond)

Pulse No. / Cube No.	Pulse 1	Pulse 2	Pulse 3	Pulse 4	Pulse 5	Average	CoV/%
Cube 1	22.5002	21.0000	21.0000	21.0000	21.0000	21.2838	3.1%
Cube 2	21.4998	21.9998	21.9998	21.9998	21.9998	21.8981	1.0%
Cube 3	20.8616	20.4994	20.9061	20.9061	21.1497	20.8625	1.1%
Cube 4	21.8885	21.4998	21.0000	21.0000	21.8885	21.4482	2.1%
Cube 5	21.0473	21.0473	21.0473	20.9837	20.9837	21.0221	0.2%
Cube 6	22.5002	21.0000	21.0000	21.0000	21.0000	21.2838	3.1%

Table 6-11. Velocity of each ultrasonic pulse for the 6 specimens (unit: m/s)

Pulse No. / Cube No.	Pulse 1	Pulse 2	Pulse 3	Pulse 4	Pulse 5	Average	CoV/%
Cube 1	4444.4	4761.9	4761.9	4761.9	4761.9	4698.4	3.0%
Cube 2	4651.2	4545.5	4545.5	4545.5	4545.5	4566.6	1.0%
Cube 3	4793.5	4878.2	4783.3	4783.3	4728.2	4793.3	1.1%
Cube 4	4568.6	4651.2	4761.9	4761.9	4568.6	4662.4	2.1%
Cube 5	4751.2	4751.2	4751.2	4765.6	4765.6	4756.9	0.2%
Cube 6	4761.9	4761.9	4761.9	4761.9	4761.9	4761.9	0.0%

6.7.1.1 Attenuation

As an important characteristic of AE, the amount of attenuation of a signal as it travels through the material mainly controls the detectability of an AE sensor. Ideally to analyse the attenuation, the proper way is to apply an excitation source at different designated places on the structure and then calculate the attenuation curve as the example previously shown in Figure 2-11 in chapter 2. However in this study, it only shows the amplitude loss of the signal through the length of 100mm cube from the excitation to the receiving sensor instead of calculating a complete attenuation curve. This is considered to be providing a basic attenuation parameter for the further investigation on the impact of healing agent layer.

As described above, the input signals (100kHz square pulse) were excited from one side of the cube. The amplitude responses were measured at the receiving sensor (channel 2) on the other side. For the attenuation study the amplitudes are normalized with respect to maximal value of each signal. In the Figure 6-23 below, (a) the signal received from Channel 1 was regarded as the initial input signal and (b) presents the corresponding received signal from Channel 2. The normalized amplitude responses for the cube specimens 1 to 6 are presented in Table 6-12.

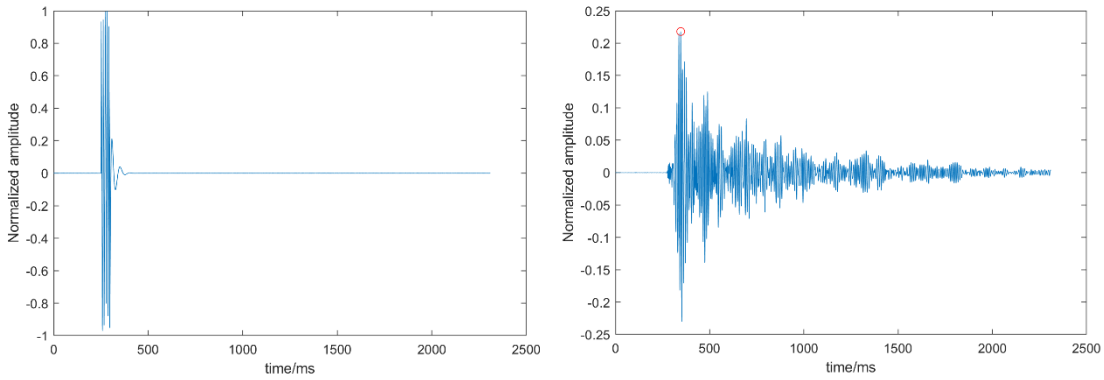

(a) (b)

Figure 6-23. Normalized amplitude for the pulse signal emitted and received of cube 3: (a)received at Channel 1 (b) received at receiving sensor

Table 6-12. The response of normalized amplitude to signals received at Channel 2

	Pulse 1	Pulse 2	Pulse 3	Pulse 4	Pulse 5	Average of amplitude drop	CoV/%
Response at Cube 1	0.1761	0.1696	0.1698	0.1688	0.1683	82.95%	1.9%
Response at Cube 2	0.1564	0.1519	0.1518	0.1528	0.1575	84.59%	1.7%
Response at Cube 3	0.2301	0.2420	0.2384	0.2384	0.2458	76.11%	2.4%
Response at Cube 4	0.1949	0.1905	0.1902	0.1928	0.1989	80.65%	1.9%
Response at Cube 5	0.2251	0.2231	0.2266	0.2311	0.2251	77.38%	1.3%
Response at Cube 6	0.1277	0.1301	0.1322	0.1314	0.1320	86.93%	1.4%

(Average：81.44%)

Results from Table 6-12 shows slight differences in attenuation among the six cube specimens. Due to the regular geometry and nature of concrete material, it is supposed that the AU signal attenuation, likes its velocity, is independent on signal transmission orientation in concrete.

6.7.1.2 Frequency contents

Generally the ultrasonic frequencies that resonate with concrete structure are between 75kHz to 200kHz and to make the best selection of sensors, that range of frequencies should be covered. The source excites a 100kHz of frequency as shown in Figure 6-24(a) for ultrasonic testing experimentations in order to ensure the signals could be well received and recorded.

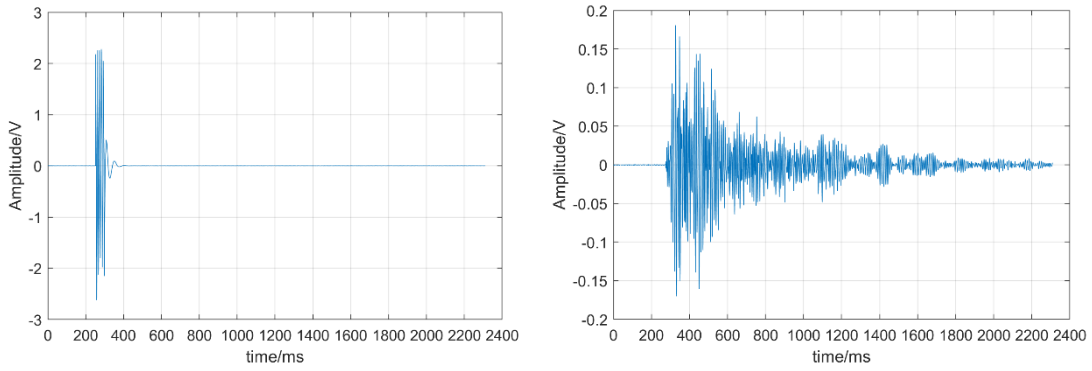

(a) (b)

Figure 6-24. Examples of waveforms (a) received at Channel 1 (b) received at receiving sensor

To assess the response of the frequency components of received signal, the frequency spectrum is given in Figure 6-25. It can be observed that the first peak occurs at a frequency of 100.4kHz which accord with the excitation frequency. The second peak occurs at a frequency of 149.8kHz and the third peak occurs at a frequency of 131.2kHz.

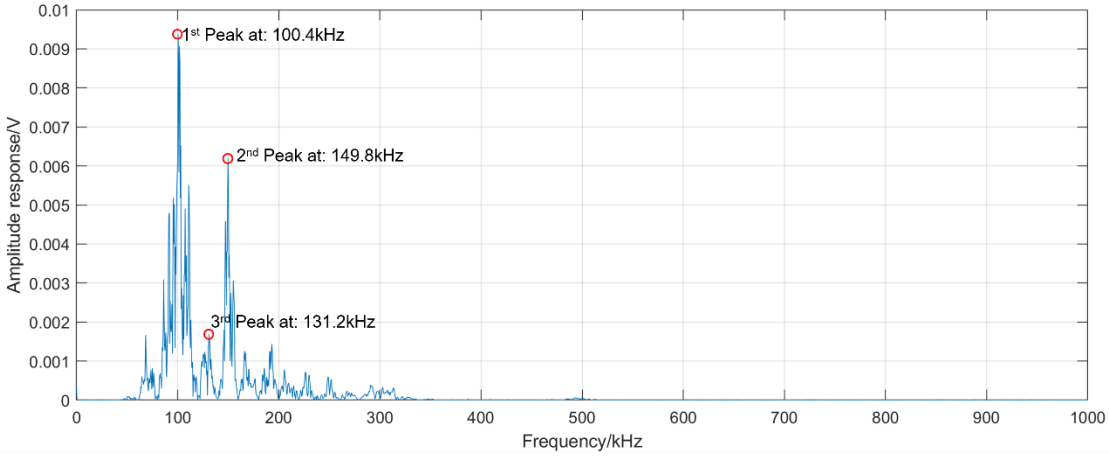

Figure 6-25. Frequency response for the pulse received at the receiving sensor

To assess how the specimen interacts with propagating wave, a wavelet transform was performed using Vallen Wavelet. Vallen are an AE-Suite system and software manufacturing and have developed specialized software for calculating wavelet transforms. Unlike FFT that can only present frequency domain and sensitive to noise, a wavelet transform can provide a good time-frequency resolution and good signal-noise ratio. Specifically, the wavelet transform enables the scaling of the signal window to achieve good time resolution at higher frequencies and good frequency resolution

at lower frequency, rather than a fixed time and frequency resolution. Furthermore, different mother wavelets for wavelet transformation can be used for different applications. The mother wavelet used in Vallen for wavelet transform is Gabor wavelet and it has been extensively used for AE characterisation and location.

Figure 6-26 shows a wavelet transform of a signal received by the receiving transducer at channel 2. It shows the arrival of first peak frequency of 100.4kHz at around 577.25μs, and the second and third peak frequency of 149.8 kHz and 131.2 kHz has arrived at basically the same time, around 598.75μs and 598.25μs respectively.

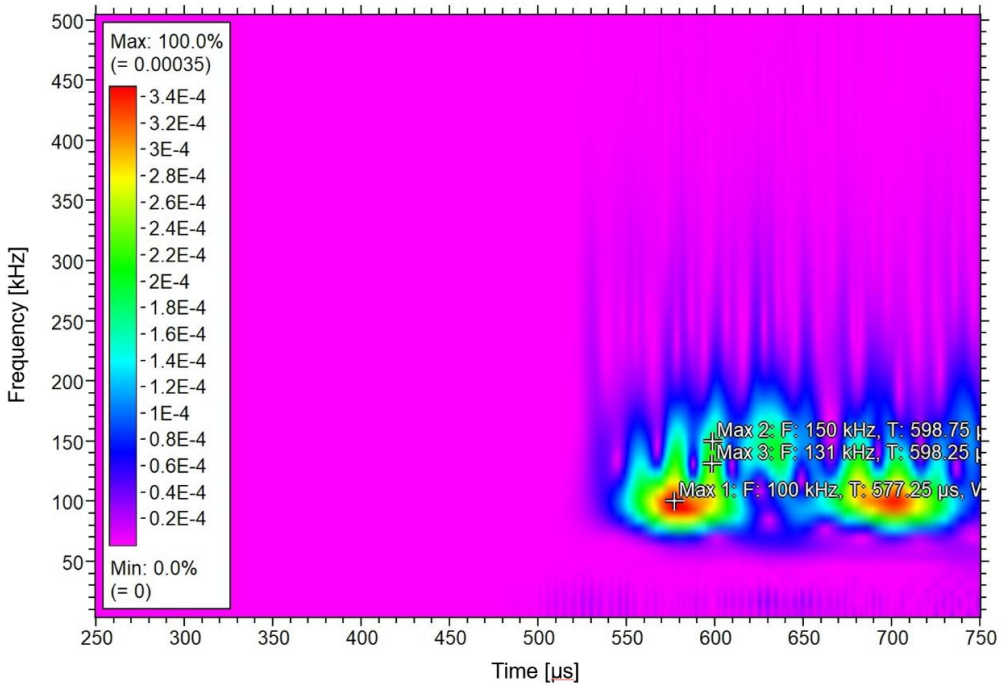

Figure 6-26. Wavelet transform of the received signal

6.7.2 Glued-cubes study

6.7.2.1 Single receiving transducer

Following on from the individual cube study, it is considered to conduct a glued-cubes study to investigate the impact of the bonding layer with healing agent between two cubes. To create the bonding layer using cyanoacrylate PC20, the healing agent was evenly spread on the surface of one cube, and then the excess glue was gently squeezed from the joint with another cube to ensure a good bond. The thickness of

the bonding layer was not particularly controlled.

Similarly, ultrasonic pulse sources were produced as a 5-cycle square burst on one surface of the glued-cube specimen and received on the other side. A schematic diagram of the test setup for the glued-cubes study is shown in Figure 6-27.

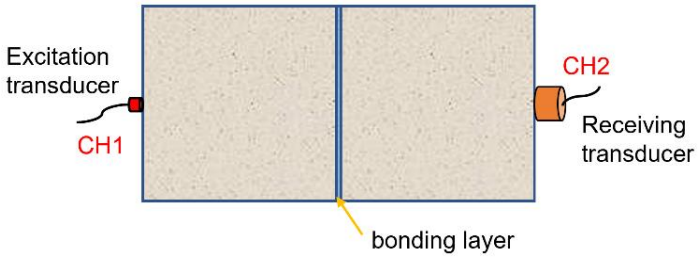

Figure 6-27. Excitation/receiving transducers setup for glued-cubes specimen

A total of 5 pulses were excited and received for the glued-cubes specimen. The results of signal travel times and corresponding apparent velocities are shown in Table 6-13 and Table 6-14 respectively.

Table 6-13. Signal travel time of each pulse (unit: microsecond)

Specimen No	Pulse 1	Pulse 2	Pulse 3	Pulse 4	Pulse 5	Average	CoV/%
Glued cube 1&2	45.0005	45.0005	43.9996	43.5000	44.4998	44.4000	1.5%

Table 6-14. Velocity of each ultrasonic pulse for the bonding specimens (unit: m/s)

Specimen No	Pulse 1	Pulse 2	Pulse 3	Pulse 4	Pulse 5	Average	CoV/%
Glued cube 1&2	4444.4	4444.4	4545.5	4597.7	4494.4	4505.28	1.5

This attenuation study is mainly investigated to determine how ultrasonic signal propagate through the bonding layer filled with healing agent, cyanoacrylate (type PC20), of the glued-cubes specimen and its impact. As described above, the input signals (100kHz square pulse) are created from one side of the cube. The amplitude responses were measured at the receiving sensor (Channel 2) on the other side. For the attenuation study the amplitudes are normalized with respect to maximal value of each signal.

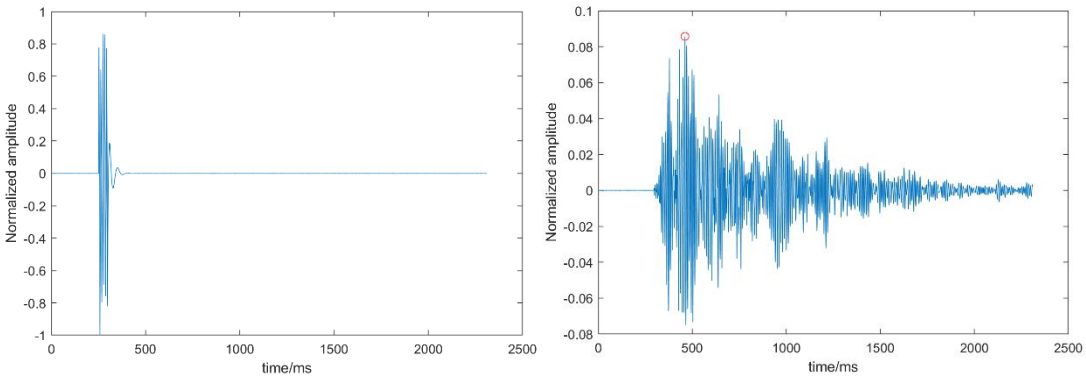

(a) (b)

Figure 6-28. Normalized amplitude for the pulse signal emitted and received of glued-cube 1&2: (a)received at Channel 1 (b) received at receiving sensor

In the Figure 6-28 (a), the signal received from Channel 1 was regarded as the initial input signal and (b) presents the corresponding received signal from Channel 2. The normalized amplitude responses for the glued-cubes specimen are presented in Table 6-15.

Table 6-15. The response of normalized amplitude to signals received at Channel 2

	Pulse 1	Pulse 2	Pulse 3	Pulse 4	Pulse 5	Average	CoV/%
Response at glued-cube 1&2	0.0823	0.0825	0.0857	0.0856	0.0845	0.0841	2.0%
Percentage of amplitude drop	91.77%	91.75%	91.43%	91.44%	91.55%	91.59%	0.2%

Results from Table 6-15 shows slight differences in attenuation among the five pulses emitted to the glued-cubes specimen. It is evident that the signal sufficiently attenuated down through the cyanoacrylate-bonded glued-cubes specimen as the amplitude drops off significantly. As five pulses were created at excitation and the averaged responses for the amplitude was 91.59%. Obviously, the attenuation increases as the signal propagation path increased as well. To identify the independent influence of the bonded layer, another attenuation study with two receiving transducers was conducted in the next section.

6.7.2.2 Double receiving transducer

To investigate the differences of signals received from different location, another attenuation study is conducted as placing another receiving transducer on the same side of the excitation. A schematic diagram of the test setup is presented in Figure 6-29.

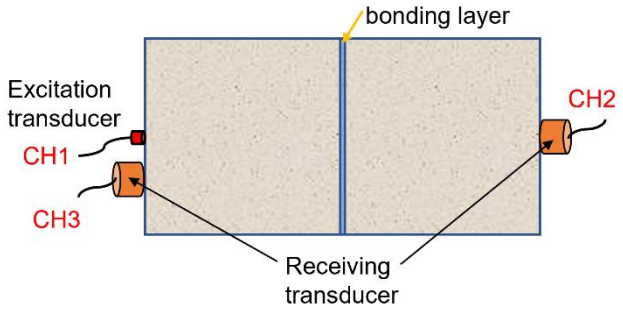

Figure 6-29. Excitation/receiving transducers setup for glued-cubes specimen

A total of 5 pulses were excited and received by two receiving transducers on each side of the glued-cubes specimen. The results from Channel 2 of signal travel time and apparent velocity are shown in Table 6-16 and Table 6-17 respectively.

Table 6-16. Signal travel time (received by Channel 2) (unit: microsecond)

Specimen No	Pulse 1	Pulse 2	Pulse 3	Pulse 4	Pulse 5	Average
Glued-cube 1&2	44	44.5	44.5	44.5	44.5	44.4

Table 6-17. Signal Velocity (received by CH2) (unit: m/s)

Specimen No	Pulse 1	Pulse 2	Pulse 3	Pulse 4	Pulse 5	Average
Glued-cube 1&2	4545.5	4494.4	4494.4	4494.4	4494.4	4504.5

To assess the response of the frequency components of received signal, the waveforms received from channel 2 and channel 3 and their frequency spectrum are given in Figure 6-30 and Figure 6-31 respectively.

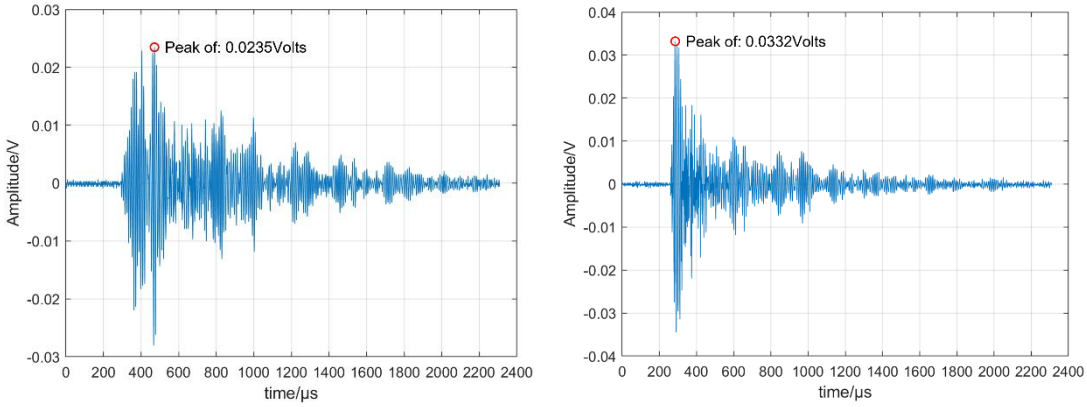

(a) (b)

Figure 6-30. Examples of signal (a)received at Channel 2 (b) received at Channel 3

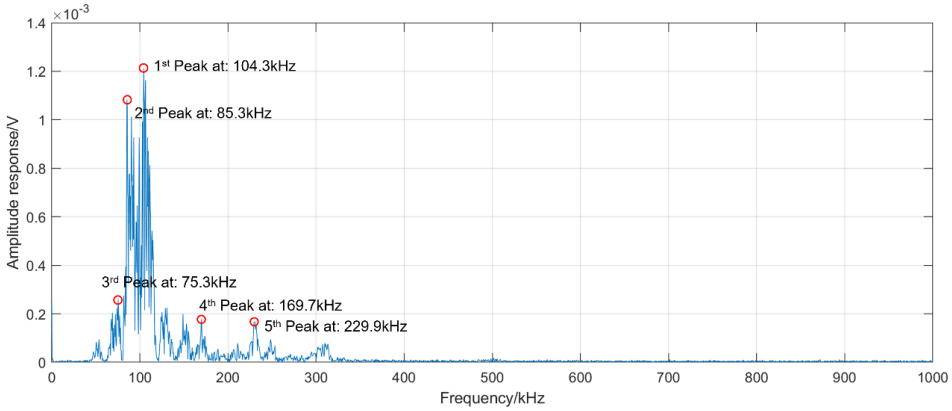

Figure 6-31. Frequency spectrum for the signal received at Channel 2

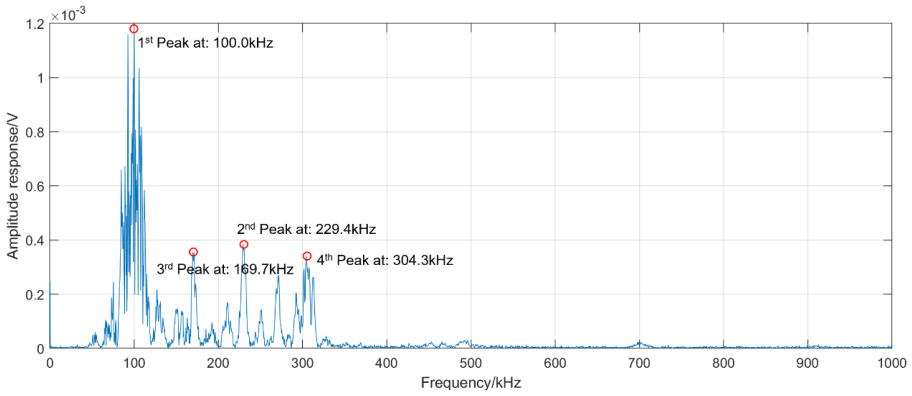

Figure 6-32. Frequency spectrum for the signal received at Channel 3

Figure 6-33 and Figure 6-34 shows a wavelet transform of a signal received by the receiving transducer at channel 2 and channel 3 respectively.

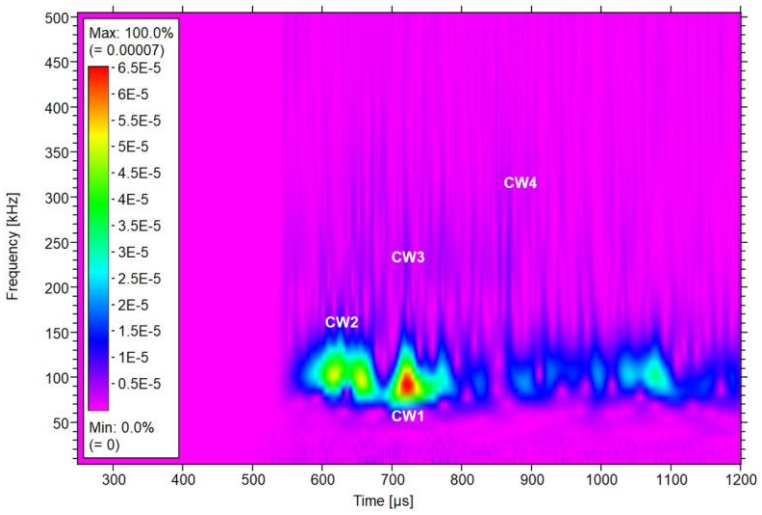

Figure 6-33. Wavelet transform of the signal received at Channel 2

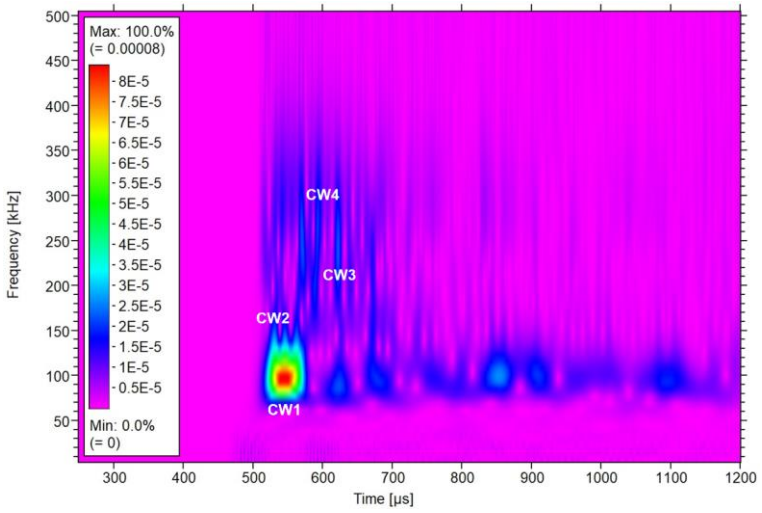

Figure 6-34. Wavelet transform of the signal received at Channel 3

6.7.3 Discussion and conclusion

The preliminary investigation of the impact of healing agent described in this section mainly explored the attenuation characteristics and change of frequency components. From the individual cube study, it shows the average drop through the attenuation study is 81.44%, and three main frequency components, 100.4kHz, 149.8kHz, and 131.2 kHz, appear at 577.25µs, 598.75µs and 598.25µs respectively. From the Glued-cubes study, it shows the average drop through the attenuation study is 91.59%, and the first main frequency component remains at around 100 kHz which is the excitation frequency. The subsequent main frequencies varies both from different receiving sensors and at different time. The difference in attenuation and frequency

variation between the individual cube and glued-cubes is mainly due to the increase of signal propagation distance. However, the influences caused by the healing agent filled bonding layer remain not clear and require further studies.

To study the impact of bonding layer filled by healing agent and how it will affect the signal propagation using AU technique, a recommendation of future work will be discussed in the subsequent section 7.3 in chapter 7.

6.8 Conclusion

In this chapter, the application of Acousto-Ultrasonics (AU) technique on a range of specimen in different size with different methods is investigated. The following conclusions can be made:

(1) Generally, there are still many factors affecting the accuracy and reliability of using AU technique in the damage detection, location and assessment, such as the calculation methods, coupling conditions between the transducer and structure, the anisotropy properties of concrete, etc., all have an impact on the quantitative defects detection and damage assessment.

(2) Compared to actual engineering structures, the experimental studies conducted in this work can still be recognised as the idealized models without many uncertainties and interference due to structure geometry and material inhomogeneity. However, there are still many problems need to be improved in single-variable experimental study using the AU detection method. Therefore, the impact analysis on the defect detection of concrete structure is not perfect, and abundant experimental investigation and analysis are still required.

(3) The results of flat measurement (both single-side and double-side) applied in this study are promising in the crack depth detection and measurement. It can be investigated to further improve the accuracy in quantitative damage detection and make the application more extensive in the field of civil engineering structure.

(4) As an efficient and straightforward NDT method, the potential application of the AU technique as a monitoring tool for the behaviour of the recently designed and developed innovative self-healing materials and structure worth further investigating.

Chapter 7 Overarching discussion, conclusions and future work

7.1 Discussion

Due to the unique dynamic, real-time and high sensitivity advantages of AE technology, its application in the field of civil engineering is extensively expanded in recent decades. Along with other NDT&E technologies, this thesis conducted several research investigations into key technologies which form the SHM system.

Compared to the existed parameter-based analysis methods, although waveform-based analysis can reveal the source mechanisms from the nature of time-frequency characteristics of the source, the fast real-time online analysis is still challenging to be achieved. The two characteristic parameters introduced in this work has been extracted to quantitatively reflect the signal energy and source characteristics through the HHT, the complexity of AE signals is decomposed and reflected from each IMFs. It has shown its advantages compared to other conventional statistical parameter-based methods as the characterisation of complex concrete damaging is enabled using parameterized indicators of basic failure mode from waveform-based analysis, but its limitations cannot be ignored. Other more effective AE indices and methods used to characterize and classify damage failure modes of concrete structure need to be explored.

The limitations of the current NDT&E techniques for the evaluation on self-healing concrete are discussed and a case study regarding the application of AE on the vascular network based self-healing system was conducted. The current technical application of AE mainly lies in the parameter-based evaluation methods for the fracture process monitoring before and after healing occurred. And the AU technique highly depends on the variability of measured data. Although the AU and UPV techniques have an advantage with respect to convenience and efficiency, there are still some limitations on its use in practical applications as the velocity-based parameters are significantly affected by material properties and environmental conditions.

The analysis results of the applicability and limitation of the NDT&E techniques discussed in this thesis suggested that the development of correlation model between self-healing indices (e.g., strength and stiffness regained, crack size, permeability, etc.) and NDT&E parameters (e.g., ultrasonic pulse velocity, attenuation and frequency characteristics, etc.) should be systematically investigated and examined, then followed by experimental tests towards verification.

Furthermore, supplementary evaluation methods, such as the image-based DIC technique, are necessary to be introduced as a physical view to validate and confirm the findings and results from other NDT&E methods.

In the light of present studies, NDT&E techniques using AE and AU (UPV) are still the preferred technologies to evaluate the mechanical properties in the field of civil engineering. However, there are still uncertainties as other NDT&E methods might be possessing more potential and sensitive to internal change of materials. And this is mainly due to the lack of existing research examining the same problems in conjunction with other NDT&E characteristics, which needs further notice and investigation.

7.2 Conclusion

Overall, this thesis has examined the role of the AE and AU techniques in the field of damage detection and monitoring of concrete structures, further the potential of application on self-healing concrete has been explored and evaluated. Given the current research status describe in the Chapter 2, the aims and objectives of this research are to investigate the application of AE techniques for use in structural monitoring of concrete damage, to describe, characterise and evaluate damage source more precisely, and eventually to explore the potential and prospect of application on recently designed and developed innovative self-healing materials and structures. Throughout this thesis, four key themes have been investigated which, between them, have demonstrated the ability of AE and AU to detect, evaluate and characterise signals occurring in the tested concrete specimens.

- The two extracted characteristic parameters, Maximum Amplitude A_{mi} and Characteristic Instantaneous Frequency f_c, can characterize the intensity and properties of AE source are determined, which can be used to quantitatively characterize the AE signal.

- Even only limited events were applicable to successfully perform the SiGMA procedure for MTA analysis, for those valid events still showed a promising agreement with results obtained via the conventional parameter-based method, additionally it has been proved that its abilities to identify where those mixed mode cracking has occurred rather than the only two failure mode identified from the conventional parameter-based analysis.

- When dealing with mass amount of data, MTA is not recommended for the analysis of damage identification and characterisation as the high requirements of signals obtained from on-site inspection and monitoring of engineering structures due to the nature of SiGMA procedure .

- Vascular network-based self-healing beam is capable of restoring around 70% of the original concrete strength and bearing capacity. AE parameters can be used to characterize the behaviour of damage and healing process. The evaluation of AE hits and absolute energy before and after healing can be qualitatively assessed by AE signals, which indicates that the cracked specimen after healing possessed larger amount hits and much higher energy from the ultimate failure.

- Kaiser effect and Felicity effect can be applied to intuitively determine the healing efficiency. The higher the healing efficiency, the more obvious the Felicity effect; the lower the healing efficiency, the more obvious the Kaiser effect.

- PCA technique is limited of differentiating very similar AE signals in vascular network-based self-healing concrete structure. However, as an efficient and practical technique of data dimension reduction method, PCA has the

potential to automatically identify and separate distinctly different AE signals.

- Many factors can affect the accuracy and reliability using AU technique in the damage detection, location and assessment. Therefore, it is recommended to combine other methods when performing structural inspections on site.
- The AU testing flat measurement was found to be a useful tool for monitoring and measuring the crack development especially when the structure has only one available surface. When the structure has two available surfaces, the tomography-based oblique measurement can be applied to effectively evaluate the damage condition of structure.

7.3 Future work

In light of the discussion and conclusion from this thesis above, the following areas are recommended for further study:

- Based on the framework presented in Chapter 3, as only two fundamental damage modes are investigated, the theoretical system needs to be further improved with comprehensive fundamental studies of various damage mechanisms (such as the yield of steel bars, slip of debonding, the effect of inhomogeneity in materials, etc.) to systematically form a set of AE evaluation methods in RC structure;
- Although a parameter screening method is used to selectively perform waveform analysis to obtain its time-frequency energy spectrum, the process so far has no way to be automatically completed, which make it impossible to achieve real-time monitoring and display.
- The impact of sensor selection will significantly affect the data processing result. Ideally a comprehensive study should be investigated on different type of sensors (such as the differences of results from resonant sensors and broadband sensors) to assure that the conclusions can be standalone and will not be affected by these factors.

- A further investigation into the use of MTA on signals from Hsu-Nielsen source. The factors affecting the classification results of source mechanisms needed to be further investigated.
- Development of a more advanced software package to largely increase the data processing capacity and accuracy of determination of the initial P wave arrival time and amplitude. Eventually improve the applicability of MTA processing massive data and feasibility of monitoring of in-service concrete structures.
- Development of improved method to evaluate healing efficiency without destructing the structure again as the conventional way to calculate the healing index.
- PCA and unsupervised pattern recognition techniques are of great potential in AE signal clustering and identification. A further exploration can be conducted based on the scale-up self-healing specimens with different technique developed.
- Exploration of more reasonable AE parameters to approach direct quantitative detection.
- To study the impact of healing agent using AU technique with respect to the characteristics of attenuation and frequency components, a schematic diagram is provided below in Figure 7-1. The signal propagation properties in the original specimen can be investigated from the test arrangement in Figure 7-1(a). The impacts of healing agent, such as the mechanism of different healing agent, thickness of bonding layer, chemical interference, etc., can be investigated from the test arrangement in Figure 7-1(b).

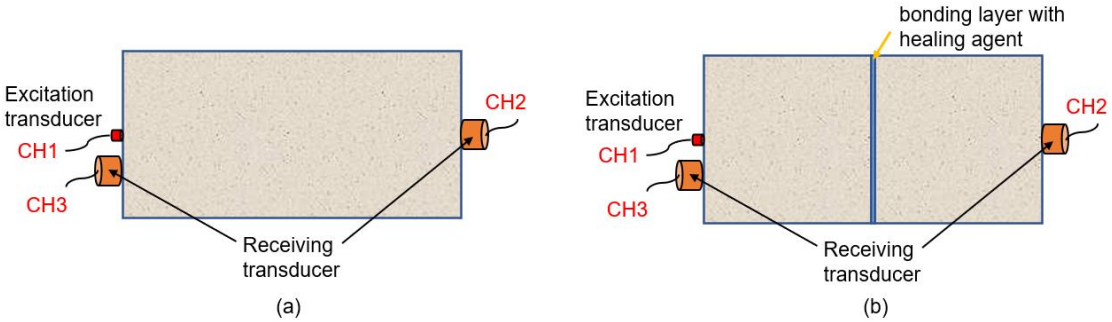

Figure 7-1. Recommended test setup for self-healing specimen: (a) Original specimen; (b) After the specimen are cut and glued back again with the healing agent

- Based on the suggested investigation above, suitable indicators to characterise the impacts caused by the healing agent and effective indices to evaluate self-healing performance worth exploring.

Appendices

Appendix A - Results of crack development monitoring in section 6.6.4

Table 8-1. Results from Beam1

Pulse	CMOD	Load	LVDT	Method-1	Method-2	DIC	Beam height
Unit	mm	kN	mm	mm	mm	mm	mm
0	0	0.51965	0.00206	0.98	2.73	8.289	
1	0.02	6.74376	0.04801	24.35	7.65	28.18	
2	0.04	5.54446	0.06613	42.88	44.02	42.14	
3	0.06	4.29066	0.08287	78.51	43.26	62.03	
4	0.08	2.92621	0.09844	85.20	32.06	66.36	
5	0.1	2.44815	0.11624	94.81	45.94	72.18	
6	0.12	1.73927	0.13195	93.69	26.58	\	
7	0.14	1.60491	0.15013	88.88	23.50	\	
8	0.16	1.23314	0.16673	95.09	35.66	\	
9	0.18	1.14111	0.1846	112.30	65.39	\	
10	0.2	0.92329	0.2019	114.13	61.19	\	
11	0.22	0.84024	0.22115	105.01	86.76	\	
12	0.24	0.82296	0.23868	105.26	83.66	\	100
13	0.26	0.74014	0.2564	110.82	100.32	\	
14	0.28	0.66837	0.27425	117.75	102.47	\	
15	0.3	0.60602	0.292	120.68	121.90	\	
16	0.32	0.50525	0.30984	110.06	96.27	\	
17	0.34	0.48887	0.32942	120.19	86.53	\	
18	0.36	0.4915	0.34729	114.79	86.02	\	
19	0.38	0.41964	0.36538	117.50	81.30	\	
20	0.4	0.39245	0.38483	113.31	86.74	\	
21	0.42	0.37263	0.40258	106.53	61.51	\	
22	0.44	0.37478	0.42112	111.07	82.85	\	
23	0.46	0.32214	0.43976	106.03	68.13	\	
24	0.48	0.33221	0.4587	110.82	73.59	\	
25	0.5	0.31322	0.47734	125.27	86.14	\	

Table 8-2. Results from Beam2

Pulse	CMOD	Load	LVDT	Method-1	Method-2	DIC	Beam height
Unit	mm	kN	mm	mm	mm	mm	mm
0	0	0.05084	0.00271	3.23	3.86	0.00	
1	0.02	7.81766	0.04344	26.46	31.72	23.59	
2	0.04	5.62155	0.05949	43.71	37.56	45.50	100
3	0.06	4.05592	0.07444	81.43	49.31	60.17	
4	0.08	2.96846	0.09025	74.56	46.71	70.01	

5	0.1	2.37259	0.10693	93.41	68.55	73.11
6	0.12	1.88103	0.12299	100.59	74.38	\
7	0.14	1.47616	0.13992	92.85	62.24	\
8	0.16	1.35973	0.15597	92.85	66.07	\
9	0.18	1.01018	0.17167	101.67	80.09	\
10	0.2	0.86319	0.18897	109.94	72.42	\
11	0.22	0.77349	0.20733	125.03	82.89	\
12	0.24	0.60475	0.22388	134.09	97.22	\
13	0.26	0.57583	0.24178	130.54	92.74	\
14	0.28	0.46013	0.25969	131.25	88.92	\
15	0.3	0.40741	0.27807	132.91	97.11	\
16	0.32	0.37743	0.2974	130.77	78.97	\
17	0.34	0.37448	0.31447	119.70	77.09	\
18	0.36	0.31804	0.33222	122.13	77.32	\
19	0.38	0.25289	0.35128	120.19	88.05	\
20	0.4	0.22633	0.3695	119.21	81.06	\
21	0.42	0.23012	0.38813	124.55	83.58	\
22	0.44	0.18851	0.40678	125.03	87.24	\
23	0.46	0.17195	0.42558	131.25	99.40	\
24	0.48	0.1571	0.44427	127.91	97.58	\
25	0.5	0.15784	0.4624	119.46	88.15	\

Table 8-3. Results from Beam3

Pulse	CMOD	Load	LVDT	Method-1	Method-2	DIC	Beam height
Unit	mm	kN	mm	mm	mm	mm	mm
0	0	0.064	0.01	5.75	2.73	0.00	100
1	0.02	10.724	0.37	14.38	7.65	25.68	
2	0.04	8.638	0.33	56.06	40.23	37.53	
3	0.06	6.619	0.3	72.21	82.76	52.32	
4	0.08	5.119	0.28	73.39	94.83	62.78	
5	0.1	4.26	0.27	83.36	86.25	76.15	
6	0.12	3.628	0.26	83.36	84.94	79.12	
7	0.14	3.094	0.26	91.16	95.00	84.25	
8	0.16	2.515	0.27	93.97	101.50	87.52	
9	0.18	2.163	0.26	96.47	81.50	88.23	
10	0.2	1.778	0.27	104.90	86.21	88.93	
11	0.22	1.473	0.28	114.80	122.45	90.00	
12	0.24	1.282	0.28	115.27	113.40	90.29	
13	0.26	1.118	0.29	113.62	123.79	90.58	
14	0.28	0.95	0.3	115.74	128.81	90.87	
15	0.3	0.805	0.31	118.09	151.32	91.16	
16	0.32	0.723	0.32	118.09	143.03	91.70	
17	0.34	0.647	0.33	112.20	117.31	92.23	

18	0.36	0.581	0.34	116.21	131.52	92.77
19	0.38	0.534	0.36	114.56	127.92	93.30
20	0.4	0.5	0.37	113.62	127.21	93.84
21	0.42	0.436	0.38	117.39	139.87	93.84
22	0.44	0.397	0.4	106.72	114.84	93.84
23	0.46	0.348	0.41	112.44	129.85	93.85
24	**0.48**	0.319	0.42	104.3105101	115.2405126	93.85
25	**0.5**	0.256	0.43	112.89	127.9899445	93.85

Table 8-4. Results from Beam4

Pulse	CMOD	Load	LVDT	Method-1	Method-2	DIC	Beam height
Unit	mm	kN	mm	mm	mm	mm	mm
0	0	0.044	0	3.23	3.20	0.00	
1	0.02	11.935	0.43	51.05	25.49	17.24	
2	0.04	9.086	0.37	64.85	45.20	39.90	
3	0.06	7.126	0.34	72.74	52.59	50.47	
4	0.08	5.423	0.3	79.22	56.23	59.62	
5	0.1	4.251	0.29	90.86	59.62	68.12	
6	0.12	3.521	0.29	91.94	53.89	72.83	
7	0.14	2.894	0.28	95.17	51.22	76.92	
8	0.16	2.379	0.27	100.99	63.92	78.00	
9	0.18	2.039	0.28	102.04	53.54	81.68	
10	0.2	1.775	0.28	106.20	64.90	82.63	
11	0.22	1.569	0.3	124.80	87.03	83.57	
12	0.24	1.342	0.31	123.38	77.55	84.52	100
13	0.26	1.14	0.32	118.15	79.16	85.47	
14	0.28	0.997	0.33	114.07	98.30	86.41	
15	0.3	0.864	0.34	111.16	106.35	87.36	
16	0.32	0.758	0.35	111.16	116.80	87.76	
17	0.34	0.659	0.36	112.38	111.87	88.16	
18	0.36	0.503	0.37	111.16	111.98	88.57	
19	0.38	0.435	0.38	111.89	111.79	88.97	
20	0.4	0.342	0.39	112.38	112.07	89.37	
21	0.42	0.279	0.4	115.75	112.83	89.77	
22	0.44	0.247	0.41	116.24	114.34	90.17	
23	0.46	0.201	0.43	120.30	122.66	90.58	
24	0.48	0.163	0.44	122.91	124.31	90.98	
25	0.5	0.135	0.45	124.33	126.35	91.20	

Appendix B - Safety and technical datasheets of Cyanoacrylates PC20

CYANOTEC Creating Bonds

PROCURE PC20

TECHNICAL DATA SHEET FOR PROCURE PC20

TYPICAL APPLICATIONS

PC 20 is specially formulated for the bonding of plastics, rubbers, wood, metals and other common substrates. Recommended for use on assemblies with very close fitting parts and smooth, even surfaces.
Can be used as a post-assembly adhesive to wick into parts.

PRODUCT DESCRIPTION

Procure PC 20 is a very low viscosity (5cPs) modified Ethyl Cyanoacrylate adhesive.
PC 20 is suitable for bonding a very wide range of materials, including some porous ones, where very fast cure speed is required.

PROPERTIES OF UNCURED MATERIAL

Chemical type		Ethyl
Appearance		Clear
Specific Gravity		1.06
Viscosity cPs[1]		
– range		2-5
– typical value		4
Tensile Strength[2]	(N/mm^2)	21
Fixture Time	(secs)	1-20
Full Cure	(hours)	24
Flash Point	(°C)	> 85
Shelf Life @ 5°C	(months)	12
Max Gap Fill	(mm)	0.05
Operating Temperature Range	(°C)	-50 to +80

[1] ISO 3104/3105
[2] ISO 6922

TYPICAL CURING PERFORMANCE

Typical Speed:

Steel/steel	<15 seconds
ABS/ABS	<5 seconds
Rubber/Rubber	<5 seconds
Wood (balsa)	<3 seconds

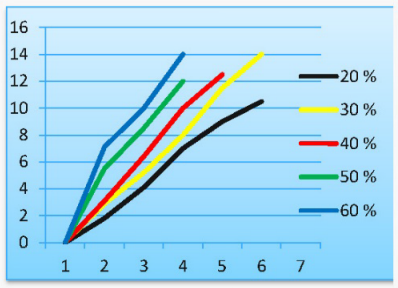

CURE VS. HUMIDITY

CURE SPEEDS VS. ENVIRONMENTAL CONDITIONS

Cyanoacrylates require surface moisture on the substrates in order to initiate the curing mechanism. The speed of cure is reduced in low-humidity conditions. Low temperatures will also reduce cure speed. All figures relating to cure speed are tested at 21°C.

CURE SPEED VS. SUBSTRATE

The speed of cure of cyanoacrylates varies according to the substrates to be bonded. Acidic surfaces such as paper and leather will have longer cure times than most plastics and rubbers. Some plastics with very low surface energies, such as polyethylene, polypropylene and Teflon® require the use of Procure 77 Primer
(See PC 77 TDS for further info).

CURE SPEED VS.ACTIVATOR

Activators 780 and 750 may be used in conjunction with cyanoacrylates where cure speed needs to be accelerated.

Cure speeds of less than 2 seconds can be obtained with most cyanoacrylates.

The use of an activator can reduce the final bond strength by up to 30% Testing on the parts to measure the effect is recommended.

CURE SPEED VS. BOND GAP

PROCURE / REACT cyanoacrylates give best results on close fitting parts. The product should be applied in a very thin line in order to ensure rapid polymerisation and a strong bond. Excessive bond gaps will result in slower cure speeds. PROCURE / REACT cyanoacrylate activators may be used to greatly increase cure speeds (see PC780 and PC750 TDS for further info).

CYANOTEC LTD
Bay 2, Building 62, Third Avenue, Pensnett Trading Estate, Kingswinford DY6 7XT
TEL 0845 618 3120 FAX 0845 618 3121 EMAIL sales@cyanotec.com

PC 20
V1.3
JUN 16

References

Abdelrahman, M., ElBatanouny, M., Serrato, M., Dixon, K., Larosche, C. and Ziehl, P. 2016. Classification of alkali-silica reaction and corrosion distress using acoustic emission. *AIP Conference Proceedings* 1706(1), p. 140001. doi: 10.1063/1.4940610.

Abdelrahman, M., ElBatanouny, M.K. and Ziehl, P.H. 2014. Acoustic emission based damage assessment method for prestressed concrete structures: Modified index of damage. *Engineering Structures* 60, pp. 258–264.

Abouhussien, A.A. and Hassan, A.A.A. 2016. The Use of Acoustic Emission Intensity Analysis for the Assessment of Cover Crack Growth in Corroded Concrete Structures. *Journal of Nondestructive Evaluation* 35(3), p. 52. doi: 10.1007/s10921-016-0369-1.

Aggelis, D.G. 2011. Classification of cracking mode in concrete by acoustic emission parameters. *Mechanics Research Communications* 38(3), pp. 153–157. doi: 10.1016/j.mechrescom.2011.03.007.

Aggelis, D.G. and Matikas, T.E. 2012. Effect of plate wave dispersion on the acoustic emission parameters in metals. *Computers & Structures* 98–99, pp. 17–22. doi: 10.1016/j.compstruc.2012.01.014.

Aggelis, D.G., Mpalaskas, A.C. and Matikas, T.E. 2013. Investigation of different fracture modes in cement-based materials by acoustic emission. *Cement and Concrete Research* 48, pp. 1–8.

Aggelis, D.G., Mpalaskas, A.C., Ntalakas, D. and Matikas, T.E. 2012. Effect of wave distortion on acoustic emission characterization of cementitious materials. *Construction and Building Materials* 35, pp. 183–190. doi: 10.1016/j.conbuildmat.2012.03.013.

Aktan, A.E., Catbas, F.N., Grimmelsman, K.A. and Tsikos, C.J. 2000. Issues in Infrastructure Health Monitoring for Management. *Journal of Engineering Mechanics* 126(7), pp. 711–724. doi: 10.1061/(ASCE)0733-9399(2000)126:7(711).

Aldahdooh, M.A.A. and Bunnori, N.M. 2013. Crack classification in reinforced concrete beams with varying thicknesses by mean of acoustic emission signal features. *Construction and Building Materials* 45, pp. 282–288.

Alexander Quon 2020. Video shows moment when steel truss bridge near Canso, N.S., collapsed - Halifax | Globalnews.ca. 7 July. Available at: https://globalnews.ca/news/7150678/steel-truss-bridge-near-canso-n-s-collapses/?fbclid=IwAR3ZBz1mWn_aGvl-Ly5WuMYIplbEIIpEchFviyM7f7HLrSrJVFIIjz5oK7A [Accessed: 24 December 2020].

Al-Jumaili, S.K., Holford, K.M., Eaton, M.J., Mccrory, J.P., Pearson, M.R. and Pullin, R. 2015. Classification of acoustic emission data from buckling test of carbon fibre panel using unsupervised clustering techniques. *Structural Health Monitoring* 14(3), pp. 241–251. doi:

10.1177/1475921714564640.

Al-Jumaili, S.K., Pearson, M.R., Holford, K.M., Eaton, M.J. and Pullin, R. 2016. Acoustic emission source location in complex structures using full automatic delta T mapping technique. *Mechanical Systems and Signal Processing* 72–73, pp. 513–524. doi: 10.1016/j.ymssp.2015.11.026.

Al-Tabbaa, A., Lark, B., Paine, K., Jefferson, T., Litina, C., Gardner, D. and Embley, T. 2018. Biomimetic cementitious construction materials for next-generation infrastructure. *Proceedings of the Institution of Civil Engineers - Smart Infrastructure and Construction* 171(2), pp. 67–76. doi: 10.1680/jsmic.18.00005.

Al-Tabbaa, A., Litina, C., Giannaros, P., Kanellopoulos, A. and Souza, L. 2019. First UK field application and performance of microcapsule-based self-healing concrete. *Construction and Building Materials* 208, pp. 669–685. doi: 10.1016/j.conbuildmat.2019.02.178.

Amezquita-Sanchez, J.P. and Adeli, H. 2016. Signal Processing Techniques for Vibration-Based Health Monitoring of Smart Structures. *Archives of Computational Methods in Engineering* 23(1), pp. 1–15. doi: 10.1007/s11831-014-9135-7.

Anderberg, M.R. 2014. *Cluster Analysis for Applications: Probability and Mathematical Statistics: A Series of Monographs and Textbooks*. Academic Press.

Antonino-Daviu, J.A., Riera-Guasp, M., Pineda-Sanchez, M. and Perez, R.B. 2009. A Critical Comparison Between DWT and Hilbert–Huang-Based Methods for the Diagnosis of Rotor Bar Failures in Induction Machines. *IEEE Transactions on Industry Applications* 45(5), pp. 1794–1803. doi: 10.1109/TIA.2009.2027558.

ASTM 1999. Determining the Reproducibility of Acoustic Emission Sensor Response.

Balázs, G.L., Grosse, C., Koch, R. and Reinhardt, H.W. 1993. Titel: Acoustic emission monitoring on steel-concrete interaction Zeitschriftentitel: Otto-Graf-Journal. *Otto-Graf-Journal* . Available at: http://mediatum.ub.tum.de/1121201 [Accessed: 5 December 2016].

Bamforth, P.B. 2019. *Control of cracking caused by restrained deformation in concrete*. CIRIA.

Barrios, F. and Ziehl, P.H. 2012. Cyclic Load Testing for Integrity Evaluation of Prestressed Concrete Girders. *ACI Structural Journal* 109(5)

Baxter, M.G., Pullin, R., Holford, K.M. and Evans, S.L. 2007. Delta T source location for acoustic emission. *Mechanical systems and signal processing* 21(3), pp. 1512–1520.

BBC News 2019. Brazil bridge collapses in Pará state after ferryboat crash. *BBC News* 7 April. Available at: https://www.bbc.com/news/world-latin-america-47843419 [Accessed: 24 December 2020].

Beck, P. 2004. *Quantitative damage assessment of concrete structures using Acoustic Emission*. Cardiff University. Available at: http://ethos.bl.uk/OrderDetails.do?uin=uk.bl.ethos.583398 [Accessed: 28 November 2016].

Behnia, A., Chai, H.K. and Shiotani, T. 2014. Advanced structural health monitoring of concrete structures with the aid of acoustic emission. *Construction and Building Materials* 65, pp. 282–302.

Belie, N.D., Gruyaert, E., Al-Tabbaa,A., Antonaci, P. and Baera, C. 2018. A Review of Self-Healing Concrete for Damage Management of Structures. *Advanced Materials Interfaces* 5(17), p. 1800074. doi: https://doi.org/10.1002/admi.201800074.

Benavent-Climent, A., Gallego, A. and Vico, J.M. 2012. An acoustic emission energy index for damage evaluation of reinforced concrete slabs under seismic loads. *Structural Health Monitoring* 11(1), pp. 69–81. doi: 10.1177/1475921711401128.

Bonamy, D. 2009. Intermittency and roughening in the failure of brittle heterogeneous materials. *Journal of Physics D: Applied Physics* 42(21), p. 214014. doi: 10.1088/0022-3727/42/21/214014.

Boniface, A., Saliba, J., Sbartaï, Z.M., Ranaivomanana, N. and Balayssac, J.-P. 2020. Evaluation of the acoustic emission 3D localisation accuracy for the mechanical damage monitoring in concrete. *Engineering Fracture Mechanics* 223, p. 106742. doi: 10.1016/j.engfracmech.2019.106742.

Bosch, M., Carvajal, C., Rodrigues, J., Torres, A., Aldana, M. and Sierra, J. 2009. Petrophysical seismic inversion conditioned to well-log data: Methods and application to a gas reservoir. *GEOPHYSICS* 74(2), pp. O1–O15. doi: 10.1190/1.3043796.

Bosch, M., Mukerji, T. and Gonzalez, E.F. 2010. Seismic inversion for reservoir properties combining statistical rock physics and geostatistics: A review. *GEOPHYSICS* 75(5), pp. 75A165-75A176. doi: 10.1190/1.3478209.

British Standards Institution 2004. *Testing concrete: part 4 : determination of ultrasonic pulse velocity.* London: British Standards Institution.

BS EN 12504-4:2004 2004. *BS EN 12504-4:2004 - Testing concrete. Determination of ultrasonic pulse velocity – BSI British Standards*. Available at: https://shop.bsigroup.com/ProductDetail?pid=000000000030102823 [Accessed: 2 December 2020].

Bungey, J.H. 1984. The Influence of Reinforcement on Ultrasonic Pulse Velocity Testing. *Special Publication* 82, pp. 229–246. doi: 10.14359/6557.

Bungey, J.H. and Grantham, M.G. 2006. *Testing of Concrete in Structures: Fourth Edition*. CRC Press.

Cailleux, E. and Pollet, V. 2009. Investigations on the development of self-healing properties in protective coatings for concrete and repair mortars. In: *Proceedings of the 2nd International Conference on Self-Healing Materials*. Chicago, IL, USA., p. 4.

Carpinteri, A., Cardone, F. and Lacidogna, G. 2010. Energy Emissions from Failure Phenomena: Mechanical, Electromagnetic, Nuclear. *Experimental Mechanics* 50(8), pp. 1235–1243. doi: 10.1007/s11340-009-9325-7.

Carpinteri, A., Lacidogna, G. and Pugno, N. 2007. Structural damage diagnosis and life-time assessment by acoustic emission monitoring. *Engineering Fracture Mechanics* 74(1), pp. 273–289.

Catbas, F.N., Gul, M. and Burkett, J.L. 2008. Conceptual damage-sensitive features for structural health monitoring: Laboratory and field demonstrations. *Mechanical Systems and Signal Processing* 22(7), pp. 1650–1669. doi: 10.1016/j.ymssp.2008.03.005.

Cescatti, E. 2016. *Behaviour of RC beams strengthened in shear with NSM FRP reinforcement*. doi: 10.13140/RG.2.1.2546.4565.

Chen, C.-H., Wang, C.-H, Liu, J.-Y., Liu, C., Liang, W.-T. Yen, H.-Y., Yeh, Y,-H, Chia, Y.-P., and Wang, Y. 2010. Identification of earthquake signals from groundwater level records using the HHT method. *Geophysical Journal International* 180(3), pp. 1231–1241. doi: 10.1111/j.1365-246X.2009.04473.x.

Chen, H.L., Cheng, C.T. and Chen, S.E. 1992. Determination of fracture parameters of mortar and concrete beams by using acoustic emission. *Materials evaluation* 50(7), pp. 888–894.

Chen, Z., Zhou, X., Wang, X., Dong, L. and Qian, Y. 2017. Deployment of a Smart Structural Health Monitoring System for Long-Span Arch Bridges: A Review and a Case Study. *Sensors* 17(9), p. 2151. doi: 10.3390/s17092151.

Chen, Z.-Y., Li, W. and Yu, Q.-Q. 2021. Characterization of Damage and Healing of Cement Matrices Based on Fly Ash under Repeated Loading. *Journal of Materials in Civil Engineering* 33(1), p. 04020408. doi: 10.1061/(ASCE)MT.1943-5533.0003516.

Chung, H.W. 1978. Effects of embedded steel bars upon ultrasonic testing of concrete. *Magazine of Concrete Research* 30(102), pp. 19–25. doi: 10.1680/macr.1978.30.102.19.

Colombo, I.S., Main, I.G. and Forde, M.C. 2003. Assessing damage of reinforced concrete beam using “b-value” analysis of acoustic emission signals. *Journal of materials in civil engineering* 15(3), pp. 280–286.

Colombo, S. 2003. *Feasibility study of the application of the acoustic emission technique to concrete bridges*. The University of Edinburgh.

Colombo, S., Forde, M.C., Main, I.G., Halliday, J. and Shigeishi, M. 2005a. AE energy

analysis on concrete bridge beams. *Materials and Structures* 38(9), pp. 851–856. doi: 10.1007/BF02481658.

Colombo, S., Forde, M.C., Main, I.G. and Shigeishi, M. 2005b. Predicting the ultimate bending capacity of concrete beams from the “relaxation ratio” analysis of AE signals. *Construction and Building Materials* 19(10), pp. 746–754. doi: 10.1016/j.conbuildmat.2005.06.004.

Cronin, V. 2004. A draft primer on focal mechanism solutions for geologists. *Texas. Baylor University* , p. 14.

Daniel, I.M. 1998. ACOUSTIC EMISSION MONITORING OF FATIGUE DAMAGE IN METALS. 14((1-2)), pp. 71–87.

Davies, R., Teall, O., Pilegis, M., Kanellopoulos, A., Sharma, T., Jefferson, A., Gardner, D., Paine, K., and Lark, R. 2018. Large Scale Application of Self-Healing Concrete: Design, Construction, and Testing. Available at: http://uhra.herts.ac.uk/handle/2299/20590 [Accessed: 26 September 2018].

Davies, R. and Jefferson, A. 2017. Micromechanical modelling of self-healing cementitious materials. *International Journal of Solids and Structures* 113–114(Supplement C), pp. 180–191. doi: 10.1016/j.ijsolstr.2017.02.008.

Davies, R., Jefferson, A., Lark, R. and Gardner, D. 2015. A NOVEL 2D VASCULAR NETWORK IN CEMENTITIOUS MATERIALS. Available at: http://orca-mwe.cf.ac.uk/86643/1/Davies.pdf [Accessed: 9 November 2016].

Davies, R.E. 2014. *Micromechanical modelling of self-healing cementitious materials*. phd, Cardiff University. Available at: http://orca.cf.ac.uk/70424/ [Accessed: 4 January 2020].

De Belie, N., Van Tittelboom, K., Tsangouri, E., Karaiskos, G., Snoeck, D., Wang, J., and Van Hemelrijck, D. 2015. Autonomous regeneration of concrete structures by incorporation of self-healing mechanisms. In: *International Conference on the Regeneration and Conservation of Concrete Structures (RCCS)*., pp. 1–10.

De Nardi, C., Gardner, D. and Jefferson, A.D. 2020. Development of 3D Printed Networks in Self-Healing Concrete. *Materials* 13(6), p. 1328. doi: 10.3390/ma13061328.

Degala, S., Rizzo, P., Ramanathan, K. and Harries, K.A. 2009. Acoustic emission monitoring of CFRP reinforced concrete slabs. *Construction and Building Materials* 23(5), pp. 2016–2026.

Dimitrios G. Aggelis, Tomoki Shiotani, Shouhei Momoki and Akinobu Hirama 2009. Acoustic Emission and Ultrasound for Damage Characterization of Concrete Elements. *ACI Materials Journal* 106(6). Available at: http://www.concrete.org/Publications/ACIMaterialsJournal/ACIJournalSearch.aspx?m=details&ID=51663333 [Accessed: 28 August 2019].

Dominique Alzéari 2019. Pont effondré de Mirepoix-sur-Tarn : le poids lourd pesait plus de 50 tonnes. Available at: https://www.ladepeche.fr/2019/11/18/un-pont-suspendu-seffondre-dans-la-riviere-au-nord-de-toulouse,8547999.php [Accessed: 24 December 2020].

Dost, B., van Stiphout, A., Kühn, D., Kortekaas, M., Ruigrok, E. and Heimann, S. 2020. Probabilistic Moment Tensor Inversion for Hydrocarbon-Induced Seismicity in the Groningen Gas Field, the Netherlands, Part 2: Application. *Bulletin of the Seismological Society of America* 110(5), pp. 2112–2123. doi: 10.1785/0120200076.

Drouillard, T.F. 1979. *Acoustic emission: A bibliography with abstracts. ed. Laner FJ*. New York: Plenum Publ.

Dry, C. 1994. Matrix cracking repair and filling using active and passive modes for smart timed release of chemicals from fibers into cement matrices. *Smart Materials and Structures* 3(2), p. 118. doi: 10.1088/0964-1726/3/2/006.

Dunegan, H.L., Harris, D.O. and Tatro, C.A. 1968. Fracture analysis by use of acoustic emission. *Engineering Fracture Mechanics* 1(1), pp. 105–122. doi: 10.1016/0013-7944(68)90018-0.

Eaton, M. 2007. *Acoustic Emission (AE) monitoring of buckling and failure in carbon fibre composite structures.* phd, Cardiff University. Available at: http://orca.cf.ac.uk/54625/ [Accessed: 14 June 2018].

Eaton, M.J., Pullin, R. and Holford, K.M. 2012. Acoustic emission source location in composite materials using Delta T Mapping. *Composites Part A: Applied Science and Manufacturing* 43(6), pp. 856–863.

Elaqra, H., Godin, N., Peix, G., R'Mili, M. and Fantozzi, G. 2007. Damage evolution analysis in mortar, during compressive loading using acoustic emission and X-ray tomography: Effects of the sand/cement ratio. *Cement and Concrete Research* 37(5), pp. 703–713. doi: 10.1016/j.cemconres.2007.02.008.

Elbatanouny, M.K., Ziehl, P.H., Larosche, A., Mangual, J., Matta, F. and Nanni, A. 2014. Acoustic emission monitoring for assessment of prestressed concrete beams. *Construction and Building Materials* 58, pp. 46–53. doi: 10.1016/j.conbuildmat.2014.01.100.

Farhidzadeh, A., Dehghan-Niri, E., Salamone, S., Luna, B. and Whittaker, A. 2012. Monitoring crack propagation in reinforced concrete shear walls by acoustic emission. *Journal of Structural Engineering* 139(12), p. 04013010.

Farrar, C.R., Duffey, T.A., Doebling, S.W. and Nix, D.A. 1999. A statistical pattern recognition paradigm for vibration-based structural health monitoring. *Structural Health Monitoring* 2000, pp. 764–773.

Feiteira, J., Tsangouri, E., Gruyaert, E., Lors, C., Louis, G. and De Belie, N. 2017. Monitoring crack movement in polymer-based self-healing concrete through digital image correlation, acoustic emission analysis and SEM in-situ loading. *Materials & Design* 115, pp. 238–246. doi: 10.1016/j.matdes.2016.11.050.

Felice, M.V., Velichko, A. and Wilcox, P.D. 2014. Accurate depth measurement of small surface-breaking cracks using an ultrasonic array post-processing technique. *NDT & E International* 68, pp. 105–112. doi: 10.1016/j.ndteint.2014.08.004.

Feng, H. and Yi, W. 2017. Propagation characteristics of acoustic emission wave in reinforced concrete. *Results in Physics* 7, pp. 3815–3819. doi: 10.1016/j.rinp.2017.09.060.

Fowler, T.J., Blessing, J.A., Conlisk, P.J. and Swanson, T.L. 1989. The MONPAC system. *Journal of acoustic emission* 8(3), pp. 1–8.

Fricker, S. and Vogel, T. 2007. Site installation and testing of a continuous acoustic monitoring. *Construction and Building Materials* 21(3), pp. 501–510.

G. Manson, K. Worden, K. Holford and R. Pullin 2001. Visualisation and Dimension Reduction of Acoustic Emission Data for Damage Detection. *Journal of Intelligent Material Systems and Structures* 12(8), pp. 529–536. doi: 10.1177/10453890122145375.

Gardner, D., Lark, R., Jefferson, A. and Davies, R. 2018. A survey on problems encountered in current concrete construction and the potential benefits of self-healing cementitious materials. *Case Studies in Construction Materials* 8, pp. 238–247. doi: Gardner, Diane <http://orca.cf.ac.uk/view/cardiffauthors/A042134C.html>, Lark, Robert <http://orca.cf.ac.uk/view/cardiffauthors/A026660Y.html>, Jefferson, Anthony <http://orca.cf.ac.uk/view/cardiffauthors/A042118C.html> and Davies, Robert <http://orca.cf.ac.uk/view/cardiffauthors/A028922R.html> 2018. A survey on problems encountered in current concrete construction and the potential benefits of self-healing cementitious materials. Case Studies in Construction Materials 8 , pp. 238-247. 10.1016/j.cscm.2018.02.002 <http://dx.doi.org/10.1016/j.cscm.2018.02.002> file <http://orca.cf.ac.uk/109127/7/1-s2.0-S2214509517302206-main.pdf>.

Gardner, D.R., Herbert, D.M., Jayaprakash, M. and Jefferson, A.D. 2013. Autonomic self-healing concrete: the capillary flow of cyanoacrylate in discrete cracks. Available at: http://orca.cf.ac.uk/id/eprint/57166 [Accessed: 30 May 2017].

Ghosh Roy, D.N. 1994. An Overview of Some Inverse Problems and Techniques. In: von Geramb, H. V. ed. *Quantum Inversion Theory and Applications*. Lecture Notes in Physics. Berlin, Heidelberg: Springer, pp. 1–13. doi: 10.1007/978-3-662-13969-1_1.

Ghosh, S.K. 2009. *Self-healing materials: fundamentals, design strategies, and applications*. Wiley Online Library.

Gilbert, F. 1971. Excitation of the Normal Modes of the Earth by Earthquake Sources. *Geophysical Journal International* 22(2), pp. 223–226. doi: 10.1111/j.1365-

246X.1971.tb03593.x.

Giri, P. and Kharkovsky, S. 2016. Detection of Surface Crack in Concrete Using Measurement Technique With Laser Displacement Sensor. *IEEE Transactions on Instrumentation and Measurement* 65, pp. 1–3. doi: 10.1109/TIM.2016.2541358.

Golaski, L., Gebski, P. and Ono, K. 2002. Diagnostics of reinforced concrete bridges by acoustic emission. *Journal of acoustic emission* 20(2002), pp. 83–89.

Gong, Z., DuQuesnay, D.L. and McBride, S.L. 1998. Measurement and Interpretation of Fatigue Crack Growth in 7075 Aluminum Alloy Using Acoustic Emission Monitoring. *Journal of Testing and Evaluation* 26(6), pp. 567–574. doi: 10.1520/JTE12114J.

González, E.F., Mukerji, T. and Mavko, G. 2007. Seismic inversion combining rock physics and multiple-point geostatistics. *GEOPHYSICS* 73(1), pp. R11–R21. doi: 10.1190/1.2803748.

Govekar, E., Gradišek, J. and Grabec, I. 2000. Analysis of acoustic emission signals and monitoring of machining processes. *Ultrasonics* 38(1), pp. 598–603.

Graff, K.F. 2012. *Wave Motion in Elastic Solids*. Courier Corporation.

Granger, S., Loukili, A., Pijaudier-Cabot, G. and Chanvillard, G. 2007. Experimental characterization of the self-healing of cracks in an ultra high performance cementitious material: Mechanical tests and acoustic emission analysis. *Cement and Concrete Research* 37(4), pp. 519–527. doi: 10.1016/j.cemconres.2006.12.005.

Green, A.T. 1969. *STRESS WAVE EMISSION AND FRACTURE OF PRESTRESSED CONCRETE REACTOR VESSEL MATERIALS.* Aerojet-General Corp., Sacramento, Calif. Available at: http://www.osti.gov/scitech/biblio/4736758 [Accessed: 5 December 2016].

Green, A.T., Lockman, C.S. and Steele, R.K. 1964. Acoustic verification of structural integrity of polaris chambers. *Modern Plastics* 41(11), pp. 137–139.

Grosse, C. and Malm, F. 2016. Combination of inspection and monitoring techniques for the detection of fractures in concrete with self-healing properties. In: *Proceedings of the 9th International Conference on Fracture Mechanics of Concrete and Concrete Structures*. IA-FraMCoS. Available at: http://framcos.org/FraMCoS-9/Full-Papers/235.pdf [Accessed: 5 November 2020].

Grosse, C., Reinhardt, H. and Dahm, T. 1997. Localization and classification of fracture types in concrete with quantitative acoustic emission measurement techniques. *NDT and E International* 30(4), pp. 223–230. doi: 10.1016/S0963-8695(96)00060-6.

Große, C. and Schumacher, T. 2013. Anwendungen der Schallemissionsanalyse an Betonbauwerken. *Bautechnik* 90(11), pp. 721–731. doi: 10.1002/bate.201300074.

Grosse, C.U. and Finck, F. 2006. Quantitative evaluation of fracture processes in concrete using signal-based acoustic emission techniques. *Cement and Concrete Composites* 28(4), pp. 330–336.

Grosse, C.U. and Linzer, L.M. 2008. Signal-based AE analysis. In: *Acoustic emission testing*. Springer, pp. 53–99. Available at: http://link.springer.com/chapter/10.1007/978-3-540-69972-9_5 [Accessed: 5 December 2016].

Gu, A., Sun, L., Liang, J. and Han, W. 2019. Acoustic Emission Characteristics Based on Energy Mode of IMFs. In: Shen, G., Zhang, J., and Wu, Z. eds. *Advances in Acoustic Emission Technology*. Springer Proceedings in Physics. Cham: Springer International Publishing, pp. 119–129. doi: 10.1007/978-3-030-12111-2_11.

Gutenberg, B. and Richter, C.F. 1942. Earthquake magnitude, intensity, energy, and acceleration. *Bulletin of the Seismological Society of America* 32(3), pp. 163–191.

Gutenberg, G. and Richter, C.F. 1950. Seismicity of the earth and associated phenomena, Howard Tatel. *Journal of Geophysical Research* 55, p. 97. doi: 10.1029/JZ055i001p00097.

Harris, D.O. and Dunegan, H.L. 1972. Verification of Structural Integrity of Pressure Vessels by Acoustic Emission and Periodic Proof Testing. *Testing for Prediction of Material Performance in Structures and Components* . Available at: http://www.astm.org/DIGITAL_LIBRARY/STP/PAGES/STP34682S.htm [Accessed: 21 October 2020].

Her, S.-C. and Lin, S.-T. 2014. Non-Destructive Evaluation of Depth of Surface Cracks Using Ultrasonic Frequency Analysis. *Sensors* 14(9), pp. 17146–17158. doi: 10.3390/s140917146.

Homma, D., Mihashi, H. and Nishiwaki, T. 2009. Self-Healing Capability of Fibre Reinforced Cementitious Composites. *Journal of Advanced Concrete Technology* 7(2), pp. 217–228. doi: 10.3151/jact.7.217.

Hongguang, J. and Zaoding, L. 1997. Experimental study on the relationship of Kaiser and Felicity effect in concrete material. *Applied Acoustics* 16(6), pp. 30–33.

Hsu, N.N. and FR, B. 1981. Characterization and calibration of acoustic emission sensors.

Huang, N. E., Shen, Z., Long, S. R., Wu, M. C., Shih, H. H., Zheng, Q., Yen, N. -C., Tung, C. C. and Liu, H. H. 1998. The empirical mode decomposition and the Hilbert spectrum for nonlinear and non-stationary time series analysis. *Proceedings of the Royal Society of London. Series A: Mathematical, Physical and Engineering Sciences* 454(1971), pp. 903–995. doi: 10.1098/rspa.1998.0193.

Ida, N. and Meyendorf, N. 2019. *Handbook of advanced nondestructive evaluation*. Springer International Publishing.

Invernizzi, S., Lacidogna, G. and Carpinteri, A. 2013. Scaling of fracture and acoustic emission in concrete. *Magazine of Concrete Research* 65(9), pp. 529–534. doi: 10.1680/macr.12.00112.

Jaeger, J.C., Cook, N.G.W. and Zimmerman, R. 2009. *Fundamentals of Rock Mechanics*. John Wiley & Sons.

Jang, B.-K. and Kishi, T. 2006. Mechanical properties of TiNi fiber impregnated CFRP composites. *Materials Letters* 60(4), pp. 518–521. doi: 10.1016/j.matlet.2005.09.027.

Jefferson, A., Joseph, C., Lark, R., Isaacs, B., Dunn, S. and Weager, B. 2010. A new system for crack closure of cementitious materials using shrinkable polymers. *Cement and Concrete Research* 40(5), pp. 795–801.

Jerrold Colten and Sonia Sirletti 2019. Another Bridge Collapse Highlights Italy's Infrastructure Crisis. *Bloomberg.com* 24 November. Available at: https://www.bloomberg.com/news/articles/2019-11-24/viaduct-on-italy-s-a6-highway-collapses-during-landslide [Accessed: 24 December 2020].

Jiao, J., He, C., Wu, B., Fei, R. and Wang, X. 2004. Application of wavelet transform on modal acoustic emission source location in thin plates with one sensor. *International Journal of Pressure Vessels and Piping* 81(5), pp. 427–431.

Jingfu, K. and Eryu, Z. 1993. APPLICATION OF ULTRASONIC STRENGTH TESTING METHOD IN QUALITY DETECTION ON CAST-IN-SITU CONCRETE PILES. *Industrial Construction* (12), p. 6.

Joseph, C. 2008. *Experimental and numerical study of the fracture and self-healing of cementitious materials*. phd, Cardiff University. Available at: http://orca.cf.ac.uk/54913/ [Accessed: 21 June 2017].

Joseph, C., Gardner, D., Jefferson, T., Isaacs, B. and Lark, B. 2010. Self-healing cementitious materials: a review of recent work. *Proceedings of the Institution of Civil Engineers-Construction Materials* 164(1), pp. 29–41.

Kaiser, E.J. 1953. *A study of acoustic phenomena in tensile tests [Ph. D]*. PhD Thesis, Dissertation. Technische Hochschule Munchen, Munich, FRG.

Kaiser, J. 1950. *Untersuchungen über das Auftreten von Geräusen biem Zugversuch*. thesis, Technische Hochschule, München, W. Germany.

Kanamori, H. 1983. Magnitude scale and quantification of earthquakes. *Tectonophysics* 93(3), pp. 185–199. doi: 10.1016/0040-1951(83)90273-1.

Karaiskos, G., Tsangouri, E., Aggelis, D.G., Van Tittelboom, K., De Belie, N. and Van Hemelrijck, D. 2016. Performance monitoring of large-scale autonomously healed concrete beams under four-point bending through multiple non-destructive testing methods. *Smart*

Materials and Structures 25(5), p. 055003.

Karihaloo, B.L. 1995. Fracture mechanics & structural concrete. *Longman Scientific and Technical*

Kawasaki, Y., Wakuda, T., Kobarai, T. and Ohtsu, M. 2013. Corrosion mechanisms in reinforced concrete by acoustic emission. *Construction and Building Materials* 48, pp. 1240–1247.

Keoni Everington 2019. Update: 6 Filipino, Indonesian workers perish after NE Taiwan bridge collapse | Taiwan News | 2019/10/02. Available at: https://www.taiwannews.com.tw/en/news/3788721 [Accessed: 24 December 2020].

Kontsos, A., Loutas, T., Kostopoulos, V., Hazeli, K., Anasori, B. and Barsoum, M.W. 2011. Nanocrystalline Mg–MAX composites: Mechanical behavior characterization via acoustic emission monitoring. *Acta Materialia* 59(14), pp. 5716–5727. doi: 10.1016/j.actamat.2011.05.048.

Kühn, D., Heimann, S., Isken, M.P., Ruigrok, E. and Dost, B. 2020. Probabilistic Moment Tensor Inversion for Hydrocarbon-Induced Seismicity in the Groningen Gas Field, The Netherlands, Part 1: Testing. *Bulletin of the Seismological Society of America* 110(5), pp. 2095–2111. doi: 10.1785/0120200099.

Kurz, J.H., Grosse, C.U. and Reinhardt, H.-W. 2005. Strategies for reliable automatic onset time picking of acoustic emissions and of ultrasound signals in concrete. *Ultrasonics* 43(7), pp. 538–546.

Landini, G.S., Francesca 2020. Road bridge in north Italy collapses, two suffer minor injuries. *Reuters* 8 April. Available at: https://www.reuters.com/article/us-italy-bridge-idUSKBN21Q1E0 [Accessed: 24 December 2020].

Lawson, I., Danso, K.A., Odoi, H.C., Adjei, C.A., Quashie, F.K., Mumuni, I.I. and Ibrahim, I.S. 2011. Non-Destructive Evaluation of Concrete using Ultrasonic Pulse Velocity., p. 7.

Lédeczi, Á., Hay, T., Volgyesi, Pé., Hay, D.R., Nádas, A. and Jayaraman, S. 2009. Wireless acoustic emission sensor network for structural monitoring. *IEEE Sensors Journal* 9(11), pp. 1370–1377.

Lédeczi, Á., Völgyesi, P., Barth, E., Nádas, A., Pedchenko, A., Hay, T. and Jayaraman, S. 2011. Self-sustaining Wireless Acoustic Emission Sensor System for Bridge Monitoring. In: *New Developments in Sensing Technology for Structural Health Monitoring*. Springer, pp. 15–39. Available at: http://link.springer.com/chapter/10.1007/978-3-642-21099-0_2 [Accessed: 6 December 2016].

L'Hermite, R. 1960. *What do we know about plastic deformation and creep of concrete?* Waterways Experiment Station.

Li, G. and Liu, Z. 2004. AE monitoring of high frequency fatigue in metallic material. *Chinese Journal of Mechanical Engineering* 15(13), pp. 1205–1209.

Li, H.-N., Ren, L., Jia, Z.-G., Yi, T.-H. and Li, D.-S. 2016. State-of-the-art in structural health monitoring of large and complex civil infrastructures. *Journal of Civil Structural Health Monitoring* 6(1), pp. 3–16. doi: 10.1007/s13349-015-0108-9.

Li, X., Dong, S. and Yuan, Z. 1999. Discrete wavelet transform for tool breakage monitoring. *International Journal of Machine Tools and Manufacture* 39(12), pp. 1935–1944. doi: 10.1016/S0890-6955(99)00021-8.

Li, Z. and Shah, S.P. 1994. Localization of Microcracking in Concrete Under Uniaxial Tension. *Materials Journal* 91(4), pp. 372–381. doi: 10.14359/4052.

Linzer, L., Schumacher, T. and Mhamdi, L. 2013. The Application Of Moment Tensor Inversion Methods To Fracture Monitoring Of Civil Engineering Materials. European Association of Geoscientists & Engineers, p. cp-378-00072. Available at: https://www.earthdoc.org/content/papers/10.3997/2214-4609-pdb.378.SAGA2013_DAY3_SESSION_9B_Linzer [Accessed: 3 April 2020].

Liu, P.X., Chen, S.Y., Guo, Y.S. and Li, P.C. 2014. Moment tensor inversion of acoustic emission. *Chin. J. Geophys* 57, pp. 858–866.

Liu, S., Pearson, M.R., Eaton, M. and Pullin, R. 2017. Correlation between acoustic emission distribution and stress variation through the depth of RC beam cross sections. *Construction and Building Materials* 150(Supplement C), pp. 634–645. doi: 10.1016/j.conbuildmat.2017.06.001.

Liu, Z. and Ziehl, P. 2009. Evaluation of RC beam specimens with AE and CLT criteria. *ACI Structural Journal* 106(3), pp. 1–12.

Londhe, R. 2011. Shear strength analysis and prediction of reinforced concrete transfer beams in high-rise buildings. doi: 10.12989/sem.2011.37.1.039.

Loutas, T.H., Kostopoulos, V., Ramirez-Jimenez, C. and Pharaoh, M. 2006. Damage evolution in center-holed glass/polyester composites under quasi-static loading using time/frequency analysis of acoustic emission monitored waveforms. *Composites Science and Technology* 66(10), pp. 1366–1375. doi: 10.1016/j.compscitech.2005.09.011.

Lovejoy, S.C. 2008. Acoustic Emission Testing of Beams to Simulate SHM of Vintage Reinforced Concrete Deck Girder Highway Bridges. *Structural Health Monitoring* 7(4), pp. 329–346. doi: 10.1177/1475921708090567.

Lu, Y., Li, Z. and Liao, W.-I. 2011. Damage monitoring of reinforced concrete frames under seismic loading using cement-based piezoelectric sensor. *Materials and Structures* 44(7), pp. 1273–1285. doi: 10.1617/s11527-010-9699-0.

Maji, A. and Shah, S.P. 1988. Process zone and acoustic-emission measurements in concrete. *Experimental Mechanics* 28(1), pp. 27–33. doi: 10.1007/BF02328992.

Marks, R. 2016. *Methodology platform for prediction of damage events for self-sensing aerospace panels subjected to real loading conditions*. phd, Cardiff University. Available at: http://orca.cf.ac.uk/93486/ [Accessed: 4 March 2019].

McCabe, W.M., Koerner, R.M. and Lord, A.E. 1976. Acoustic emission behavior of concrete laboratory specimens. *Journal of the American Concrete Institute* 73(7), pp. 367–71.

McCrory, J. 2016. *Advanced Acoustic Emission (AE) monitoring techniques for aerospace structures*. phd, Cardiff University. Available at: http://orca.cf.ac.uk/89212/ [Accessed: 14 June 2018].

Mclaskey, G.C. and Glaser, S.D. 2007. Temporal evolution and 3D locations of acoustic emissions produced from the drying shrinkage of concrete. *Journal of Acoustic Emission* 25(1), pp. 52–57.

Mhamdi, L., Schumacher, T. and Linzer, L. 2013. Development of seismology-based acoustic emission methods for civil infrastructure applications. *AIP Conference Proceedings* 1511(1), pp. 1363–1370. doi: 10.1063/1.4789201.

Mhamdi, L., Schumacher, T. and Linzer, L. 2015. 5 - Seismology-based acoustic emission techniques for the monitoring of fracture processes in concrete structures. In: Ohtsu, M. ed. *Acoustic Emission and Related Non-Destructive Evaluation Techniques in the Fracture Mechanics of Concrete*. Woodhead Publishing Series in Civil and Structural Engineering. Oxford: Woodhead Publishing, pp. 79–111. Available at: https://www.sciencedirect.com/science/article/pii/B9781782423270000052 [Accessed: 8 February 2018].

Mier, J.G.M. van 2017. *Fracture Processes of Concrete*. CRC Press. Available at: https://www.taylorfrancis.com/books/9780203756768 [Accessed: 9 July 2019].

Minnebo, P., Thierens, G., De Valck, G., Van Tittelboom, K., De Belie, N., Van Hemelrijck, D. and Tsangouri, E. 2017. A Novel Design of Autonomously Healed Concrete: Towards a Vascular Healing Network. *Materials* 10(1), p. 49.

MISTRAS Group Inc., Products & Systems Division 2011. *AEwin SOFTWARE User's Reference Manual - Rev.4*. NJ, USA.

Mobley, R.K. 2002. *An Introduction to Predictive Maintenance*. Elsevier.

Moevus, M., Godin, N., R'Mili, M., Rouby, D., Reynaud, P., Fantozzi, G. and Farizy, G. 2008. Analysis of damage mechanisms and associated acoustic emission in two SiCf/[Si–B–C] composites exhibiting different tensile behaviours. Part II: Unsupervised acoustic emission data clustering. *Composites Science and Technology* 68(6), pp. 1258–1265. doi: 10.1016/j.compscitech.2007.12.002.

MOGI, K. 1962. Study of elastic shocks caused by the fracture of heterogeneous materials and its relations to earthquake phenomena. *Bull. Earthq. Res. Inst.* 40(1), pp. 125–173.

Momon, S., Godin, N., Reynaud, P., R'Mili, M. and Fantozzi, G. 2012. Unsupervised and supervised classification of AE data collected during fatigue test on CMC at high temperature. *Composites Part A: Applied Science and Manufacturing* 43(2), pp. 254–260. doi: 10.1016/j.compositesa.2011.10.016.

MumbaiMarch 15, D.S., March 15, 2019UPDATED: and Ist, 2019 21:57 2019. BMC blames negligence for Mumbai CST bridge collapse, suspends 2 engineers. Available at: https://www.indiatoday.in/india/story/mumbai-cst-bridge-collapse-bmc-report-engineers-suspended-1479166-2019-03-15 [Accessed: 24 December 2020].

Muravin, B. 2009. Acoustic emission science and technology. *Journal of Building and Infrastructure Engineering of the Israeli Association of Engineers and Architects* . Available at: http://muravin.com/downloads/Muravin%20-%20Acoustic%20Emission%20Science%20and%20Technology.pdf [Accessed: 5 December 2016].

Nair, A. 2006. *Acoustic emission monitoring and quantitative evaluation of damage in reinforced concrete members and bridges*. Citeseer. Available at: http://citeseerx.ist.psu.edu/viewdoc/download?doi=10.1.1.528.1761&rep=rep1&type=pdf [Accessed: 5 December 2016].

Nair, A. and Cai, C.S. 2010. Acoustic emission monitoring of bridges: Review and case studies. *Engineering Structures* 32(6), pp. 1704–1714. doi: 10.1016/j.engstruct.2010.02.020.

Nam, B.H., Kim, J., An, J. and Kim, B. 2013. A Review on the Effects of Earthborne Vibrations and the Mitigation Measures. *International Journal of Railway* 6. doi: 10.7782/IJR.2013.6.3.095.

Ni, G. and Chen, S. 1995. Relation between space-time inversion and particle-antiparticle symmetry and the microscopic essence of special relativity. *arXiv:hep-th/9508069* . Available at: http://arxiv.org/abs/hep-th/9508069 [Accessed: 2 March 2020].

Niwa, Y., Kobayashi, S. and Ohtsu, M. 1977. Studies of AE in concrete structures. In: *Proc. JSCE*., pp. 101–112.

Nor, N.M., Ibrahim, A., Bunnori, N.M. and Saman, H.M. 2013. Acoustic emission signal for fatigue crack classification on reinforced concrete beam. *Construction and Building Materials* 49, pp. 583–590.

Ohara, Y., Yamamoto, S., Mihara, T. and Yamanaka, K. 2008. Ultrasonic Evaluation of Closed Cracks Using Subharmonic Phased Array. *Japanese Journal of Applied Physics* 47(5S), p. 3908. doi: 10.1143/JJAP.47.3908.

Ohno, K. and Ohtsu, M. 2010. Crack classification in concrete based on acoustic emission. *Construction and Building Materials* 24(12), pp. 2339–2346. doi: 10.1016/j.conbuildmat.2010.05.004.

Ohtsu, M. 1991. Simplified moment tensor analysis and unified decomposition of acoustic emission source: Application to in situ hydrofracturing test. *Journal of Geophysical Research: Solid Earth* 96(B4), pp. 6211–6221. doi: 10.1029/90JB02689.

Ohtsu, M. 2006. Quantitative AE Techniques Standardized for Concrete Structures. Available at: https://www.scientific.net/AMR.13-14.183 [Accessed: 28 February 2020].

Ohtsu, M. 2015. *Acoustic Emission and Related Non-destructive Evaluation Techniques in the Fracture Mechanics of Concrete: Fundamentals and Applications*. Woodhead Publishing.

Ohtsu, M., Isoda, T. and Tomoda, Y. 2007. Acoustic Emission Techniques Standardized for Concrete Structures. (25), p. 12.

Ohtsu, M., Uchida, M., Okamoto, T. and Yuyama, S. 2002. Damage Assessment of Reinforced Concrete Beams Qualified by Acoustic Emission. *Structural Journal* 99(4), pp. 411–417. doi: 10.14359/12109.

Ohtsu, M. and Watanabe, H. 2001. Quantitative damage estimation of concrete by acoustic emission. *Construction and Building Materials* 15(5), pp. 217–224. doi: 10.1016/S0950-0618(00)00071-4.

Ono, K. 1994. Trends of recent acoustic emission literature. *Journal of acoustic emission* 12(3–4), pp. 177–198.

Ono, K. and Ohtsu, M. 1984. A generalized theory of acoustic emission and Green's functions in a half space. *Journal of Acoustic Emission* 3, pp. 27–40.

Otsuka, K., Date, H. and Kurita, T. 1998. Fracture process zone in concrete tension specimens by X-ray and AE techniques. *Fracture mechanics of concrete structures, proceedings FraMCoS-3. Freiburg: AEDIFICATIO Publishers* , pp. 3–16.

Ou, J. and Li, H. 2010. Structural Health Monitoring in mainland China: Review and Future Trends. *Structural Health Monitoring* 9(3), pp. 219–231. doi: 10.1177/1475921710365269.

Pearson, M. 2013. *Development of lightweight structural health monitoring systems for aerospace applications*. phd, Cardiff University. Available at: http://orca.cf.ac.uk/47104/ [Accessed: 14 June 2018].

Pearson, M.R., Eaton, M., Featherston, C., Pullin, R. and Holford, K. 2017. Improved acoustic emission source location during fatigue and impact events in metallic and composite structures. *Structural Health Monitoring: An International Journal* 16(4), pp. 382–399. doi: 10.1177/1475921716672206.

Philippidis, T.P. and Aggelis, D.G. 2005. Experimental study of wave dispersion and attenuation in concrete. *Ultrasonics* 43(7), pp. 584–595. doi: 10.1016/j.ultras.2004.12.001.

Pilegis, M., Davies, R., Lark, R., Gardner, D. and Jefferson, A. 2016. Challenges of Self-healing Concrete Scale-up and Site Trials. IA-FraMCoS. Available at: http://framcos.org/FraMCoS-9/Full-Papers/283.pdf [Accessed: 9 November 2016].

Pollock, A.A. 1986. Classical wave theory in practical AE testing. *Progress in Acoustic Emission III-JAP Society of Non-Destructive Testing* , pp. 708–721.

Pullin, R., Eaton, M.J., Hensman, J.J., Holford, K.M., Worden, K. and Evans, S.L. 2008. A Principal Component Analysis of Acoustic Emission Signals from a Landing Gear Component. *Applied Mechanics and Materials* 13–14, pp. 41–47. doi: 10.4028/www.scientific.net/AMM.13-14.41.

Pullin, R., Holford, K.M. and Baxter, M.G. 2005. Modal Analysis of Acoustic Emission Signals from Artificial and Fatigue Crack Sources in Aerospace Grade Steel. *Key Engineering Materials* . Available at: https://www.scientific.net/KEM.293-294.217 [Accessed: 12 November 2020].

Qi, G. 2000. Wavelet-based AE characterization of composite materials. *NDT & E International* 33(3), pp. 133–144. doi: 10.1016/S0963-8695(99)00037-7.

Rddad, Y. 2019. PHOTOS: Truck driver was following GPS before Arkansas bridge collapse, official says. Available at: https://www.arkansasonline.com/news/2019/jan/31/truck-bridge-collapse-Arkansas-county/ [Accessed: 24 December 2020].

Reddy, P.N., Kavyateja, B.V. and Jindal, B.B. 2020. Structural health monitoring methods, dispersion of fibers, micro and macro structural properties, sensing, and mechanical properties of self-sensing concrete—A review. *Structural Concrete* n/a(n/a). Available at: https://onlinelibrary.wiley.com/doi/abs/10.1002/suco.202000337 [Accessed: 8 December 2020].

Reuters Staff 2019. China bridge collapse kills three, injures two. *Reuters* 11 October. Available at: https://www.reuters.com/article/us-china-bridge-collapse-idUSKBN1WQ021 [Accessed: 24 December 2020].

Richards, P.G. and Aki, K. 1980. *Quantitative Seismology: Theory and Methods*. Freeman.

Richter, C.F. 1935. An instrumental earthquake magnitude scale. *Bulletin of the Seismological Society of America* 25(1), pp. 1–32.

Ridge, A.R. and Ziehl, P.H. 2006. Evaluation of strengthened reinforced concrete beams: cyclic load test and acoustic emission methods. *ACI Structural Journal* 103(6), p. 832.

RILEM, T. 2010. 212-ACD, Test method for classification of active cracks in concrete

structures by acoustic emission. *Materials and Structures* 9, pp. 1187–1189.

Rindorf, H.J. 1981. *Acoustic emission source location in theory and in practice*. Brüel & Kjær.

Rippengill, S., Worden, K., Holford, K.M. and Pullin, R. 2003. Automatic Classification of Acoustic Emission Patterns. *Strain* 39(1), pp. 31–41. doi: 10.1046/j.1475-1305.2003.00041.x.

Roberts, T.M., Davies, A.W. and Holford, K.M. 1999. Structural Integrity of Welded Steel Structures. *Key Engineering Materials* . Available at: https://www.scientific.net/KEM.167-168.142 [Accessed: 12 November 2020].

Roberts, T.M. and Talebzadeh, M. 2003. Acoustic emission monitoring of fatigue crack propagation. *Journal of Constructional Steel Research* 59(6), pp. 695–712. doi: 10.1016/S0143-974X(02)00064-0.

Robinson, G.S. 1968. Methods of detecting the formation and propagation of microcracks in concrete. Available at: https://trid.trb.org/view.aspx?id=98847 [Accessed: 5 December 2016].

Rouchier, S., Woloszyn, M., Foray, G. and Roux, J.-J. 2013. Characterisation of concrete and mortar cracking by digital image correlation and acoustic emission. *European Journal of Environmental and Civil Engineering* 17(6), pp. 467–477.

Rüsch, H. and Van Amerongen, C. 1960. *Physical problems in the testing of concrete*. Cement and Concrete Association.

Russell, B.H. 1988. *Introduction to Seismic Inversion Methods*. Society of Exploration Geophysicists. Available at: https://library.seg.org/doi/abs/10.1190/1.9781560802303 [Accessed: 2 March 2020].

Sachse, W. and Kim, K.Y. 1987. Quantitative acoustic emission and failure mechanics of composite materials. *Ultrasonics* 25(4), pp. 195–203.

Sarker, M., Ali, T., Abdelfatah, A., Yehia, S. and Elaksher, A. 2017. A COST-EFFECTIVE METHOD FOR CRACK DETECTION AND MEASUREMENT ON CONCRETE SURFACE. *ISPRS - International Archives of the Photogrammetry, Remote Sensing and Spatial Information Sciences* XLII-2/W8, pp. 237–241. doi: 10.5194/isprs-archives-XLII-2-W8-237-2017.

Sause, M.G. 2011. Investigation of pencil-lead breaks as acoustic emission sources. *Journal of Acoustic Emission* 29, pp. 184–196.

Scholz, C.H. 1968. The frequency-magnitude relation of microfracturing in rock and its relation to earthquakes. *Bulletin of the Seismological Society of America* 58(1), pp. 399–415.

Schumacher, T. 2008. *Acoustic emission techniques applied to conventionally reinforced concrete bridge girders.* Oregon. Dept. of Transportation. Research Unit.

Selvarajoo, T. 2020. *Characterisation of a vascular self-healing cementitious material system*. phd, Cardiff University. Available at: http://orca.cf.ac.uk/130332/ [Accessed: 17 March 2020].

Selvarajoo, T., Davies, R.E., Gardner, D.R., Freeman, B.L. and Jefferson, A.D. 2020. Characterisation of a vascular self-healing cementitious material system: Flow and curing properties. *Construction and Building Materials* 245, p. 118332. doi: 10.1016/j.conbuildmat.2020.118332.

Seo, Y. and Kim, Y.R. 2008. Using Acoustic Emission to monitor fatigue damage and healing in Asphalt Concrete. *KSCE Journal of Civil Engineering* 12(4), pp. 237–243. doi: 10.1007/s12205-008-0237-3.

Shah, S.P., Swartz, S.E. and Ouyang, C. 1995. *Fracture Mechanics of Concrete: Applications of Fracture Mechanics to Concrete, Rock and Other Quasi-Brittle Materials*. John Wiley & Sons.

Shen Gongtian 2015. *Acoustic emission Technology and application*. Science Press.

Shigeishi, M., Colombo, S., Broughton, K.J., Rutledge, H., Batchelor, A.J. and Forde, M.C. 2001. Acoustic emission to assess and monitor the integrity of bridges. *Construction and building materials* 15(1), pp. 35–49.

Shigeishi, M. and Ohtsu, M. 2001. Acoustic emission moment tensor analysis: development for crack identification in concrete materials. *Construction and Building Materials* 15(5), pp. 311–319. doi: 10.1016/S0950-0618(00)00079-9.

Shiotani, T. 1994. Evaluation of progressive failure using AE sources and improved b-value on slope model tests. *Progress in Acoustic Emission VII, JSNDI* , pp. 529–534.

Shiotani, T. 2006. Evaluation of long-term stability for rock slope by means of acoustic emission technique. *NDT & E International* 39(3), pp. 217–228. doi: 10.1016/j.ndteint.2005.07.005.

Shiotani, T. 2008. Parameter analysis. In: *Acoustic emission testing*. Springer, pp. 41–51. Available at: http://link.springer.com/10.1007/978-3-540-69972-9_4 [Accessed: 5 December 2016].

Shiotani, T., Momoki, S., Chai, H. and Aggelis, D.G. 2009. Elastic wave validation of large concrete structures repaired by means of cement grouting. *Construction and Building Materials* 23(7), pp. 2647–2652. doi: 10.1016/j.conbuildmat.2009.01.005.

Shiotani, T., Yuyama, S., Li, Z.W. and Othsu, M. 2000. Quantitative evaluation of fracture process in concrete by the use of improved b-value. *5th Int. Symposium Non-Destructive*

Testing in Civil Engineering , pp. 293–302. doi: 10.1016/B978-008043717-0/50031-3.

Shiotani Tomoki, Aggelis Dimitrios G. and Makishima Osamu 2009. Global Monitoring of Large Concrete Structures Using Acoustic Emission and Ultrasonic Techniques: Case Study. *Journal of Bridge Engineering* 14(3), pp. 188–192. doi: 10.1061/(ASCE)1084-0702(2009)14:3(188).

Shiwa, M., Carpenter, S. and Kishi, T. 1996. Analysis of Acoustic Emission Signals Generated during the Fatigue Testing of GFRP. *Journal of Composite Materials* 30(18), pp. 2019–2041. doi: 10.1177/002199839603001804.

Shou-Xing, T. 2007. Detecting and verifying the quality of concrete-steel pipe by ultrasonic testing. *Nondestructive Testing* 29(12), pp. 731–732.

Shou-Xing, T. 2008. Contrast Experiments of Ultrasonic Velocity Between Digital and Analog Ultrasonic Detectors. *Nondestructive Testing* 2

Shou-Xing, T. and Gen-Huo, W.U. 2010. The Relationship Between the Ultrasonic Head Wave Amplitude Difference and the Measured Sonic Time Value. *Nondestructive Testing* 5

Sohn, H., Farrar, C.R., Hunter, N.F. and Worden, K. 2001. Structural Health Monitoring Using Statistical Pattern Recognition Techniques. *Journal of Dynamic Systems, Measurement, and Control* 123(4), pp. 706–711. doi: 10.1115/1.1410933.

Soulioti, D., Barkoula, N.M., Paipetis, A., Matikas, T.E., Shiotani, T. and Aggelis, D.G. 2009. Acoustic emission behavior of steel fibre reinforced concrete under bending. *Construction and Building Materials* 23(12), pp. 3532–3536. doi: 10.1016/j.conbuildmat.2009.06.042.

Staff, R. 2020. Russia's rail link to port of Murmansk severed by bridge collapse. *Reuters* 2 June. Available at: https://www.reuters.com/article/us-russia-bridge-idUSKBN2390X7 [Accessed: 24 December 2020].

Staszewski, W.J. and Holford, K.M. 2001. Wavelet Signal Processing of Acoustic Emission Data. In: *Key Engineering Materials*. Available at: https://www.scientific.net/KEM.204-205.351 [Accessed: 12 November 2020].

Stauder, W. and M, A.W. 1961. A comparison of some S-wave studies of earthquake mechanisms. *Bulletin of the Seismological Society of America* 51(2), pp. 277–292.

Stein, S. and Wysession, M. 2009. *An Introduction to Seismology, Earthquakes, and Earth Structure*. John Wiley & Sons.

Stephens, R.W.B. and Pollock, A.A. 1971. Waveforms and frequency spectra of acoustic emissions. *The Journal of the Acoustical Society of America* 50(3B), pp. 904–910.

Sun, L., Shang, Z., Xia, Y., Bhowmick, S. and Nagarajaiah, S. 2020. Review of Bridge

Structural Health Monitoring Aided by Big Data and Artificial Intelligence: From Condition Assessment to Damage Detection. *Journal of Structural Engineering* 146(5), p. 04020073. doi: 10.1061/(ASCE)ST.1943-541X.0002535.

Surgeon, M. and Wevers, M. 1999. Modal analysis of acoustic emission signals from CFRP laminates. *NDT & E International* 32(6), pp. 311–322. doi: 10.1016/S0963-8695(98)00077-2.

Suzuki, T., Ogata, H., Takada, R., Aoki, M. and Ohtsu, M. 2010. Use of acoustic emission and X-ray computed tomography for damage evaluation of freeze-thawed concrete. *Construction and Building Materials* 24(12), pp. 2347–2352.

Talebzadeh, M. and Roberts, T.M. 2001. Correlation of Crack Propagation and Acoustic Emission Rates. Available at: https://www.scientific.net/KEM.204-205.341 [Accessed: 12 November 2020].

Tatro, C.A. 1971. Experimental Considerations for Acoustic Emission Testing. *Materials Research and Standards* . Available at: https://trid.trb.org/view.aspx?id=110396 [Accessed: 5 December 2016].

Toutanji, H. and Deng, Y. 2003. Deflection and crack-width prediction of concrete beams reinforced with glass FRP rods. *Construction and Building Materials* 17(1), pp. 69–74. doi: 10.1016/S0950-0618(02)00094-6.

Tsamtsakis, D., Wevers, M. and de Meester, P. 1998. Acoustic Emission from CFRP Laminates during Fatigue Loading. *Journal of Reinforced Plastics and Composites* 17(13), pp. 1185–1201. doi: 10.1177/073168449801701304.

Tsangouri, E., Lelon, J., Minnebo, P., Asaue, H., Shiotani, T., Van Tittelboom, K., De Belie. N., Aggelis, D.G., and Van Hemelrijck, D. 2019. Feasibility study on real-scale, self-healing concrete slab by developing a smart capsules network and assessed by a plethora of advanced monitoring techniques. *Construction and Building Materials* 228, p. 116780. doi: 10.1016/j.conbuildmat.2019.116780.

Tsangouri, E., Aggelis, D.G., Van Tittelboom, K., De Belie, N. and Van Hemelrijck, D. 2013. Detecting the activation of a self-healing mechanism in concrete by acoustic emission and digital image correlation. *The Scientific World Journal* 2013. Available at: http://www.hindawi.com/journals/tswj/2013/424560/abs/ [Accessed: 14 December 2016].

Tsangouri, E., Karaiskos, G., Deraemaeker, A., Van Hemelrijck, D. and Aggelis, D. 2016. Assessment of Acoustic Emission localization accuracy on damaged and healed concrete. *Construction and Building Materials* 129, pp. 163–171. doi: 10.1016/j.conbuildmat.2016.10.104.

Twomey, S. 2013. *Introduction to the Mathematics of Inversion in Remote Sensing and Indirect Measurements*. Elsevier.

Vallen-Systeme GmbH 2002. AE Testing Fundamentals,Equipment, Applications. Available at: https://www.ndt.net/article/v07n09/05/05.htm [Accessed: 30 April 2020].

Van der Auweraer, H. and Peeters, B. 2003. International Research Projects on Structural Health Monitoring: An Overview. *Structural Health Monitoring* 2(4), pp. 341–358. doi: 10.1177/147592103039836.

Van Tittelboom, K., Wang, J., Araújo, M., Snoeck, D., Gruyaert, E., Debbaut, B., Derluyn, H., Cnudde, V., Tsangouri, E., Van Hemelrijck, D. and De Belie, N. 2016. Comparison of different approaches for self-healing concrete in a large-scale lab test. *Construction and Building Materials* 107, pp. 125–137. doi: 10.1016/j.conbuildmat.2015.12.186.

Van Tittelboom, K., De Belie, N., Lehmann, F. and Grosse, C.U. 2012. Acoustic emission analysis for the quantification of autonomous crack healing in concrete. *Construction and Building Materials* 28(1), pp. 333–341.

Van Tittelboom, K., Tsangouri, E., Van Hemelrijck, D. and De Belie, N. 2015. The efficiency of self-healing concrete using alternative manufacturing procedures and more realistic crack patterns. *Cement and Concrete Composites* 57, pp. 142–152. doi: 10.1016/j.cemconcomp.2014.12.002.

Verstrynge, E., Pfeiffer, H. and Wevers, M. 2014. A novel technique for acoustic emission monitoring in civil structures with global fiber optic sensors. *Smart Materials and Structures* 23(6), p. 065022.

Vidal, T., Castel, A. and François, R. 2004. Analyzing crack width to predict corrosion in reinforced concrete. *Cement and Concrete Research* 34(1), pp. 165–174. doi: 10.1016/S0008-8846(03)00246-1.

Vogel, T., Schechinger, B. and Fricker, S. 2006. Acoustic emission analysis as a monitoring method for prestressed concrete structures. *Institute of Structural Engineering, ETH. Zurich, Switzerland. ECNDT* . Available at: http://citeseerx.ist.psu.edu/viewdoc/download?doi=10.1.1.159.159&rep=rep1&type=pdf [Accessed: 5 December 2016].

Voigt, T., Akkaya, Y. and Shah, S.P. 2003. Determination of Early Age Mortar and Concrete Strength by Ultrasonic Wave Reflections. *Journal of Materials in Civil Engineering* 15(3), pp. 247–254. doi: 10.1061/(ASCE)0899-1561(2003)15:3(247).

Wang, Y., Pullin, R., Pearson, M., Davies, R. and Holford, K. 2021. Detection and Evaluation of Vascular Network Based Self-healing Concrete Using Acoustic Emission. In: Shen, G., Zhang, J., and Wu, Z. eds. *Advances in Acoustic Emission Technology*. Springer Proceedings in Physics. Singapore: Springer, pp. 299–311. doi: 10.1007/978-981-15-9837-1_25.

Warren Liao, T., Ting, C.-F., Qu, J. and Blau, P.J. 2007. A wavelet-based methodology for grinding wheel condition monitoring. *International Journal of Machine Tools and*

Manufacture 47(3), pp. 580–592. doi: 10.1016/j.ijmachtools.2006.05.008.

Watanabe, T., Nishibata, S., Hashimoto, C. and Ohtsu, M. 2007. Compressive failure in concrete of recycled aggregate by acoustic emission. *Construction and Building Materials* 21(3), pp. 470–476. doi: 10.1016/j.conbuildmat.2006.04.002.

Wells, D. 1970. An acoustic apparatus to record emissions from concrete under strain. *Nuclear engineering and design* 12(1), pp. 80–88.

Willberg, C., Duczek, S., Vivar-Perez, J.M. and Ahmad, Z.A.B. 2015. Simulation Methods for Guided Wave-Based Structural Health Monitoring: A Review. *Applied Mechanics Reviews* 67(010803). Available at: https://doi.org/10.1115/1.4029539 [Accessed: 30 December 2020].

Worden, K., Farrar, C.R., Manson, G. and Park, G. 2007. The fundamental axioms of structural health monitoring. *Proceedings of the Royal Society A: Mathematical, Physical and Engineering Sciences* 463(2082), pp. 1639–1664. doi: 10.1098/rspa.2007.1834.

Xu, J., Barnes, R.W. and Ziehl, P. 2013. Evaluation of Prestressed Concrete Beams based on Acoustic Emission Parameters. *Materials evaluation* 71(2)

Yang, L. and Zhou, Y. 2006. Wavelet analysis of acoustic emission signals from thermal barrier coatings. *Transactions of Nonferrous Metals Society of China* 16, pp. s270–s275. doi: 10.1016/S1003-6326(06)60189-1.

Yao, J.T.P. and Wong, F.S. 2012. Structural Health Monitoring and Symptom-Based Reliability., pp. 314–320. doi: 10.1061/40571(304)18.

You, T. 2019. Busy highway bridge suddenly collapses during rush hours in China. Available at: https://www.dailymail.co.uk/news/article-7558889/Busy-highway-bridge-suddenly-collapses-rush-hours-China.html [Accessed: 7 January 2021].

Zhao, Z.-D. and Wang, Y. 2007. Analysis of Diastolic Murmurs for Coronary Artery Diseasebased on Hilbert Huang Transform. In: *2007 International Conference on Machine Learning and Cybernetics*., pp. 3337–3342. doi: 10.1109/ICMLC.2007.4370724.

Ziehl, P.H., Galati, N., Nanni, A. and Tumialan, J.G. 2008. In-Situ Evaluation of Two Concrete Slab Systems. II: Evaluation Criteria and Outcomes. *Journal of Performance of Constructed Facilities* 22(4), pp. 217–227. doi: 10.1061/(ASCE)0887-3828(2008)22:4(217).